공학박사 학위논문

Nanostructured Ni-Gd doped Ceria Anode by Co-Sputtering for a Direct Methane Solid Oxide Fuel Cells operated under 500℃

500℃ 이하 작동 직접 메탄 고체산화물 연료전지를 위한 코스퍼터링 니켈-가돌리늄 도핑 세리아 나노구조 연료극

2020년 2월

서울대학교 대학원

기계항공공학부

유 원 종

Nanostructured Ni-Gd doped Ceria Anode by Co-Sputtering for a Direct Methane Solid Oxide Fuel Cells operated under 500℃

By

Wonjong Yu

A Dissertation Submitted in Partial Fulfillment of the

Requirements for the Degree of

Doctor of Philosophy

Department of Mechanical and Aerospace Engineering

Seoul National University

February 2020

Nanostructured Ni-Gd doped Ceria Anode by Co-Sputtering for a Direct Methane Solid Oxide Fuel Cells operated under 500 ℃

지도교수 차 석 원

이 논문을 박사 학위논문으로 제출함
2019년 10월

서울대학교 대학원
기계항공공학부
유 원 종

유원종의 박사 학위논문을 인준함
2019년 12월

위 원 장 _____ (인)

부위원장 _____ (인)

위 원 _____ (인)

위 원 _____ (인)

위 원 _____ (인)

Abstract

Nanostructured Ni-Gd doped Ceria Anode by Co-Sputtering for a Direct Methane Solid Oxide Fuel Cells operated under 500 ℃

Solid oxide fuel cells (SOFCs) are promising energy conversion device converting chemical energy to electric energy with excellent fuel flexibility, high efficiency, and low pollutant. For the commercialization of SOFC, several breakthroughs should be achieved in structure and fuel sections. For example, in terms of structure, electrolyte thickness should be thin enough to reduce the operating temperature down to below 600℃. In these operating temperature region, SOFC technology issues such as high degradation rate, the use of expensive materials, and slow start-up time can be resolved. In addition, in terms of fuel, direct use of hydrocarbon fuel (methane, butane, propane, etc.) to low-temperature SOFCs could eliminate the problem of hydrogen storage and large system size due to external reformer. However, thin-film deposition techniques for fabricating electrolyte is highly dependent on deposition conditions and surface structure of the

substrate. Detailed studies on the correlation between sputtering structure and deposition parameters are essential for commercially applying thin-film deposition techniques for fabricating electrolyte and electrode. In addition, at low operating temperatures, direct electrochemical oxidation and reforming of hydrocarbon fuel are extremely sluggish. Therefore, a highly active thermal catalyst structure at low operating temperatures should be designed and studied.

Due to the nano-sized grain structure of the thin-film layer deposited by sputtering, other than reducing the thickness of electrolyte, sputtering for thin-film fabrication could be utilized for designing highly active electrode. Furthermore, since the requirement for a highly active thermally catalytic reforming layer is providing high density of triple-phase boundary (TPB), co-sputtering for fabricating reforming layer could satisfy the requirement for low-temperature direct hydrocarbon SOFCs. In this study, co-sputtering technique was applied to fabricate high-performance nanostructured Ni-GDC anode and Ru-GDC reforming layer for the development of direct methane SOFCs operated under 500°C.

Anodic aluminum oxide (AAO) has been used as a substrate for thin-film SOFC (TF-SOFC) fabricated by sputtering due to a uniform nano-hole array, high thermo-

mechanical stability, and scalability. Due to electrically non-conductive characteristics of AAO, electrochemical performance is greatly affected by anode nanostructure on AAO. Typical current collecting resistance in anode supported SOFC is negligible to the ohmic resistance of SOFC. In AAO supported TF-SOFC, however, the electron pathway is in-plane direction of nanostructured anode, which results in substantial loss in electron current collecting. Therefore, understanding the nanostructure effect on electrochemical performance is necessary to design high-performance Ni-GDC anode structure on AAO. Various deposition parameters such as deposition chamber pressure, target to substrate distance (TSD), and substrate rotation speed were studied for anode thickness, porosity, and column structure. Experimental results showed that these physical properties of the anode nanostructure are critical factors for determining the electrochemical performance of TF-SOFC.

Thermally catalytic reforming layer fabricated by co-sputtering on AAO depends on composition and porosity. It is noteworthy that the composition of Ru-GDC fabricated by co-sputtering is correlated with the porosity of the nanostructure. It is possible that large difference in deposition rate of Ru and GDC (over 90%) could be attributed to porosity change with composition change. However, a detailed

mechanism is not in this thesis boundary. Nevertheless, Ru 3 volumetric percent showed successful reforming performance at 500℃. The structure analysis indicated that the nano-sized grain structure of Ru-GDC enables the direct methane operation with extremely low contents of Ru.

The integration of high-performance Ni-GDC anode and Ru-GDC nanostructured reforming layer (NRL) could produce substantial power density at 500℃ with nearly dry methane (3% H_2O). Furthermore, operation time is extended to over 12 hours, which is longer than any other experimental data reported in the literature. Although the cell showed 4.9% per hour degradation rate, the platinum (Pt) based cathode is largely attributed to the degradation. Post analysis showed that carbon coking on Ni-GDC anode is negligible, which indicates that the carbon coking is not the main contribution to degradation.

Keyword: low-temperature solid oxide fuel cell, direct methane, co-sputtering, nickel-gadolinium doped ceria (Ni-GDC), ruthenium-gadolinium doped ceria (Ru-GDC)

Student Number: 2014-21846

Acknowledgments

First and foremost, I would like to thank my advisor, Professor Suk Won Cha, who has been a great mentor to me for six years of Ph.D. course. I am deeply indebted to his support and guide during the course of my research and project.

Secondly, I would like to thank the fuel cell group members, Sanghoon Lee, Sangbong Ryu, Inwon Choi, Wonyeop Jeong, Myungsuk Lee, and Jaewon Hwang. Also, I am very thankful to the hybrid vehicle group members, Changbum Kang, Bonhyun Gu, Changhee Song, Donghwan Sung, Jaehyuk Yang, Kyunghyun Kim, and Sunghyun Jang. When I had trouble with the research, the group member gave me a lot of strength and reminded me of the purpose of the Ph.D. course.

I am deeply indebted to my family, father who taught me how to deal with a difficult problem, a mother who improves my mood and mental well-being, and sister who inspire me to further efforts.

Lastly, I would like to give my warmest thanks to my wife Minjae Gil. Without her support and understanding, it would not be possible for me to achieve the goal of my thesis work.

Table of Contents

List of Figures

List of Tables

Chapter 1. Introduction

1.1. Fuel Cell Fundamentals

A fuel cell is an energy conversion device capable of converting chemical species energy to electric energy with high efficiency [1]. The principle of fuel cell operation is similar to battery system. Reactant chemical species are electrochemically oxidized and reduced at anode and cathode, respectively. Electrons produced by electrochemical reaction at electrodes is released to external circuit, and active charge carrier is conducted through electrolyte. The difference between the battery and fuel cell systems is the fuel source. Unlike battery, fuel for the fuel cell is supplied from the external source. Therefore, a fuel cell does not need recharging. With well-designed fuel storage, fuel cells can operate much longer than battery systems at the same weight condition [2,3].

There are various types of fuel cell depending on the chemical properties of the electrolyte. Polymer exchange membrane fuel cell (PEMFC) uses electrolyte fabricated by polymer materials conducting proton through the electrolyte. Solid oxide fuel cells (SOFCs) use solid oxide electrolyte for oxygen ion-conducting. Among many fuel cell type, PEMFC and SOFC are the most advanced fuel cell types close to the commercialization[4,5]. However, there are still critical issues for ensuring economic feasibility.

The fuel cell consists of three mechanical parts: anode, electrolyte, and cathode. Anode and cathode are porous structures so that gaseous fuel passes through the structure. To be electrochemically active, electron conductive solid phase, ionic conducting solid phase, and gas species should be contacted at one boundary, which is called triple-phase boundary (TPB)[6–8]. The electrochemical reactions such as

oxygen reduction or hydrogen oxidation reactions occur in the presence of TPB. Designing the electrode with high density of TPB is important to reduce overall activation loss in fuel cells. On the other hand, the electrolyte structure should be dense enough to block electron. Depending on the electrolyte material and structure, conducting charge carrier species and conductivity are widely varied.

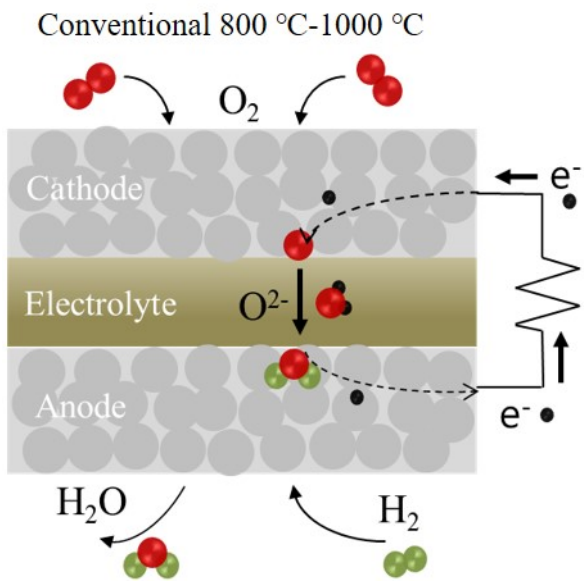

Figure1.1 Demonstration of solid oxide fuel cells working principle.

In the thermodynamic perspective, the maximum energy potential that can be exploited from the electrochemical reactions is theoretically expected by calculating a change in Gibbs free energy of chemical species. The change in the Gibbs free energy change is directly related to electrical work (E).

$$\Delta \hat{g}_f = \ -n \cdot F \cdot E$$

n represents the number of electrons involved in the reaction. F is Faraday's constant. The reversible voltage under standard conditions can be denoted as E^o.

$$E^0 = \frac{-\hat{g}_f}{n \cdot F}$$

However, fuel cells operated under non-standard conditions. Nernst equation accounts for concentration effect on reversible voltage and written by:

$$\mathrm{E} = E^o - \frac{RT}{nF} ln \frac{\Pi a_{products}^{vi}}{\Pi a_{reactants}^{vi}}$$

T is temperature. R is gas constant. *a* is the activity of the gas (for ideal gas, $a_i = p_i/p^o$, p_i is the partial pressure, p^o is the standard pressure).

As fuel cells operate, the ideal voltage can not be sustained due to the various losses from reaction kinetics and activation energy for conduction, and mass transport resistance.

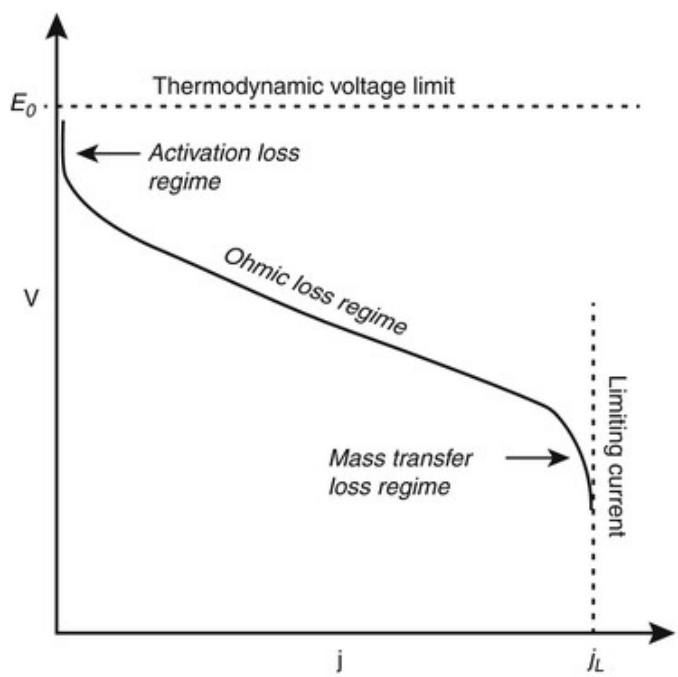

Figure1.2 Schematic of fuel cell i-V curve and three major losses that affect ideal thermodynamic voltage during the operation.

The actual voltage of the fuel cell is affected by three major losses: activation loss (η_{act}), ohmic loss(η_{ohm}), and mass transport loss (η_{mass}). The real voltage is written by:

$$V = E - \eta_{act} - \eta_{ohm} - \eta_{mass}$$

Activation loss is caused by an activation energy barrier from the charge transfer of the electrochemical reaction. Typically, activation loss is dominating at low current region, which is in low over-potential region. The reason for this is because of the activation barrier in reaction kinetics affected by the magnitude of the over-potential. Butler-Volmer equation explains how voltage loss is related to the current produced by the electrochemical reaction in fuel cell and written as:

$$j = j_o^o \left(\frac{C_R^*}{C_R^o} e^{\frac{\alpha n F \eta}{RT}} - \frac{C_P^*}{C_P^o} e^{-\frac{(1-\alpha) n F \eta}{RT}} \right)$$

j is the current density of fuel cells. C_R^* and C_P^* represent actual concentration at the electrode. j_o^o is an exchange current density at standard condition (reference concentration : C_R^o and C_P^o). α is called a transfer coefficient. η represents over-potential in fuel cell operation.

Ohmic loss is originated from charge transport through the electronic path and ionic path. In most cases, electron conduction resistance is negligible compared to ionic conduction. The charge transport resistance follows ohmic's law and can be written as:

$$V = i \left(\frac{L}{A\sigma} \right) = iR$$

L represents the thickness of the electrolyte, length of the ionic conduction path. And A means the area for ionic conduction. σ is the ionic conductivity of the electrolyte.

Last, mass transport loss is caused by depletion of reactant at reaction sites. As the reaction rate increases consuming rate of the reactants at the electrode should

increase. When reactant gas diffusion rate is lower than reaction rate, the current can not be further increased. The relationship between limiting current density (j_L) and diffusivity is presented below:

$$j_L = nFD^{eff}\frac{C_R^o}{\delta}$$

D^{eff} is the effective diffusivity of the reactant gas in the electrode layer. δ is the diffusion layer thickness. This concentration phenomenon affects the Nernst voltage and the expression is written below:

$$\eta_{conc} = \frac{RT}{nF} ln \frac{j_L}{j_L - j}$$

Typically, mass transport is considered as a critical factor for PEMFC system due to the need for water management. Channel design is one of the key aspects for achieving high performance of PEMFC. However, in SOFC system, due to high operating temperature, water management or flow system is considered as less important.

1.2. Solid Oxide Fuel Cells

Oxygen ion conduction through the solid electrolyte is dominated by the hoping mechanism, which is sluggish at low-temperatures (under 600℃). For this reason, operating temperature of conventional SOFCs is in the range between 800 and 1000℃. The unduly high operating temperature (800-1000℃) of conventional SOFCs induces several critical issues such as limited material selection, severe degradation of the cell, and high cost of balance of plant (BOP)[9–11]. For resolving these issues, many research has been focusing on reducing the operating temperature of SOFCs. Major losses of SOFC can be categorized into three parts: activation loss,

ohmic loss, and mass transport loss. Since gas diffusivity at high temperature is sufficiently high, the mass transport loss is typically negligible for SOFCs[12]. Therefore, reducing the activation and ohmic losses is important to achieve high performance of SOFCs at low temperatures.

1.3. Thin-film Solid Oxide Fuel Cells

Thin-film SOFCs (TF-SOFCs) are now one category of SOFCs research field. TF-SOFCs has been drawn significant attention for a decade due to the superior performance enhancement at low operating temperatures [13–16]. As mentioned above, reducing the ohmic and activation resistances is the key factor for SOFCs to be operated at the low-temperature region (under 600℃). Thin-film electrolyte thickness ranging from a few nanometers to micrometer is known to be suitable for lowering ohmic resistance with short ionic conduction path. From the equation related to charge transport resistance, it is clear that electrolyte thickness is proportional to ohmic resistance. Other than reducing the thickness of the electrolyte, thin-film structure has superior characteristics in fabricating the high density of TPB. The thin-film structure typically constitutes of the nano-sized grain structure, which is much smaller than conventional SOFC structure fabricated by chemical sintering methods [17].

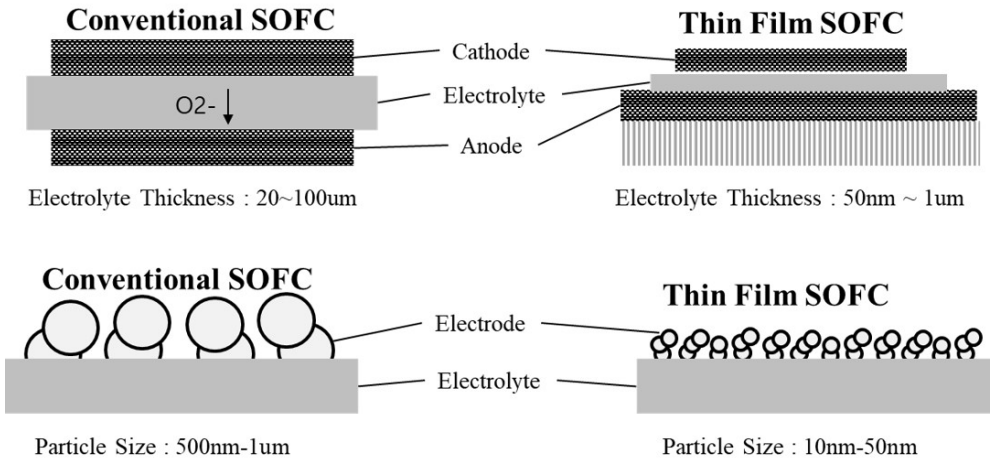

Figure 1.3. Comparative schematics of thin-film SOFC and conventional SOFC.

As the grain size of the electrode reduces, the effective surface area of the electrode, which is potential TPB density for electrochemical reaction, increases. This phenomenon is confirmed from the experimental data reported in the literature. Figure 1.4 represents the working temperature of SOFCs as a function of electrolyte thickness. Black points indicating the reported experimental data of thin-film electrolyte (electrolyte deposited by thin-film deposition techniques: physical or chemical vapor deposition) are clearly located in the low operating temperature compared to the SOFCs with conventional electrolyte (electrolyte fabricated by conventional techniques: sintering process) [10–52].

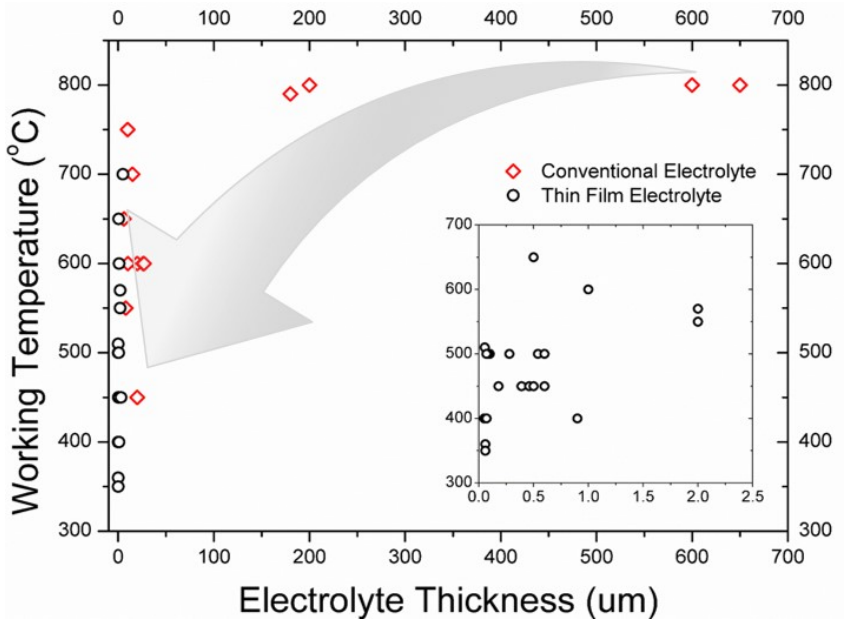

Figure 1.4 Literature experimental data of the working temperature of SOFCs varied with electrolyte thickness. Red: electrolyte fabricated by a conventional process including high-temperature sintering. Black: electrolyte deposited by thin-film deposition techniques including physical or chemical vapor deposition.

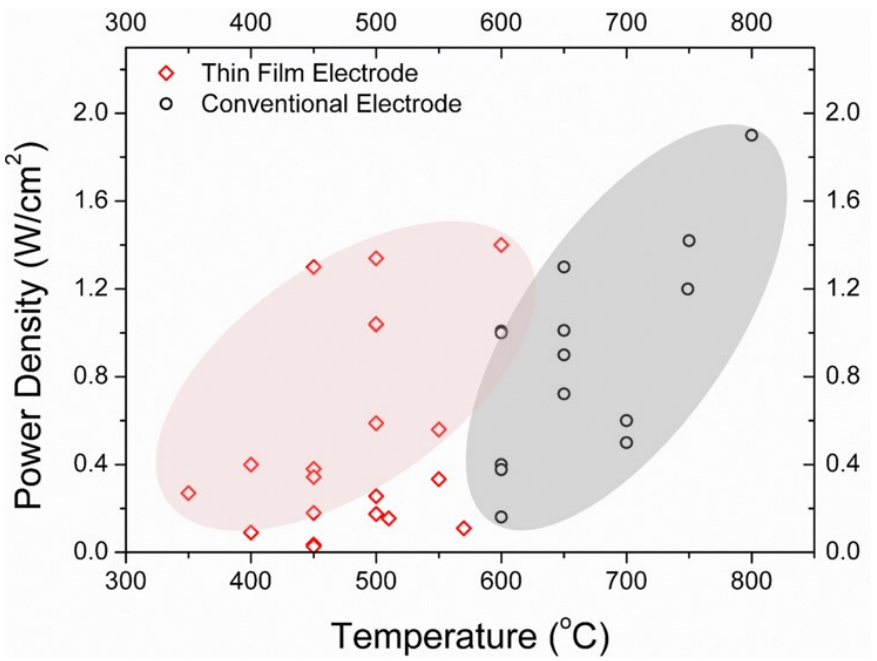

Figure 1.5 Literature experimental data of power density of SOFCs varied with temperature ranging from 350 to 800℃. Red points represent SOFCs with a thin-film electrode fabricated by physical or chemical vapor deposition). Black points represent SOFCs with conventional electrode fabricated by a sintering process.

Figure 1.5 also confirms that SOFCs with thin-film electrode design clearly show high performance in low-temperature regions. Statistic information from the literature indicates that using a thin-film deposition technique for electrode fabrication is beneficial for achieving high performance at low temperatures.

1.3.1 Thin-film Deposition Techniques

Various kinds of thin-film deposition techniques have been used for the fabrication of SOFC components. Magnetron sputtering, pulsed laser deposition (PLD), and thermal evaporation, which are physical vapor deposition (PVD), have been demonstrated as deposition methods for nanostructure fabrication[16]. Chemical vapor deposition (CVD) and atomic layer deposition (ALD) are also extensively used for ultrathin electrolyte and nano-thin surface coating for a nanostructured electrode. Among those techniques, magnetron sputtering has shown superior properties for nanostructure fabrication due to easy control of porosity and nanoscale thickness control[61]. Furthermore, it is already proved that sputtering is commercially viable because of uniform deposition for large area and variety of material selection. The principle of the sputtering is simple. As the large electric potential difference is applied between the target and substrate, a plasma is created by ionizing the sputtering gas species around target materials. Simultaneously, positively charged ionized gas species is dragged into the target surface. The bombardment of the gas species takes off the target material at atomic scale. Ejected atoms from the target flow directly to the substrate. The nucleation and accumulation of the ejected atoms from the target materials result in formation of the nano-sized grain structure of the film on the substrate[62,63].

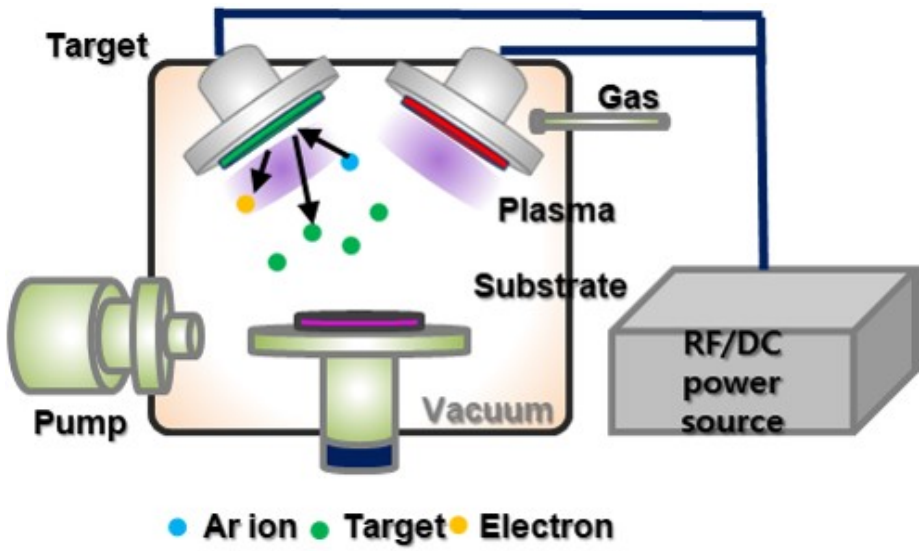

Figure 1.6 Schematic of the sputtering system.

Sputtering has a number of features for controlling the nanostructure of the deposited film. The most dominant and controllable variables for sputtering are sputtering gas species, chamber pressure, target to substrate distance (TSD), sputtering incident angle, and substrate rotation speed. These variables are sensitive for determining the characteristics of the nanostructure such as porosity and column structure. Other than these variables, sputtering power, substrate temperature, and bias voltage can affect the crystallinity and the chemical composition of the deposited film[64].

Thin-film electrolyte fabricated by sputtering has been widely used to reduce the ohmic resistance of SOFC. Meanwhile, nanostructured anode fabricated by sputtering is also promising structure for high performance at low operating temperature due to the high density of triple-phase boundary (TPB) stemmed from

nano-sized grain structure of sputtering layer[65]. However, nanostructure fabricated by sputtering is highly dependent on deposition parameters and substrate structure conditions. To achieve high performance of TF-SOFC fabricated by sputtering, detailed studies on nanostructured sputtering anode affected by deposition parameters are essential. Therefore, various electrode materials such as nickel-gadolinium doped ceria (Ni-GDC) should be studied with various deposition conditions of co-sputtering on the nanoporous substrate.

1.3.2 Types of Thin-film Solid Oxide Fuel Cells

Electrode and electrolyte deposited by the thin-film technique require support (substrate) to be mechanically sustained at nanoscale level. In addition, thin-film structure is highly dependent on surface structure of the support. Therefore, considering the type of substrate for thin-film deposition is the important step for fabricating TF-SOFCs. Type of TF-SOFCs can be categorized into 4: silicon-based freestanding structure, anodic aluminum oxide (AAO) supported structure, anode pellet supported structure, and porous metallic substrate. Si wafer is used as a support for thin-film structure with the lithography etching process. This structure is frequently called as free-standing TF-SOFC due to the characteristic of electrolyte structure. After electrolyte deposition on si wafer, the wafer is etched from the backside to the electrolyte by lithography. Consequently, the electrolyte is sustained by itself without any supporting mechanical structure. For this reason, this type of TF-SOFC suffers severe thermo-mechanical degradation at operating temperature.

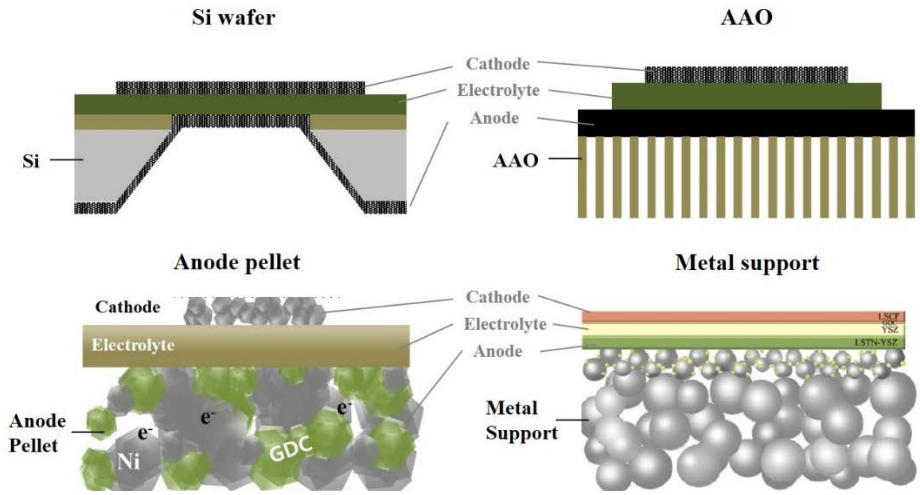

Figure 1.7 Schematic illustration of types of thin-film solid oxide fuel cells depending on substrates.

Furthermore, the active area is limited by a few hundred micrometers due to the structure stability problem. Despite the recent progress in thermo-mechanical stability of si wafer SOFC, the scalability and stability of the cell still need to be much more enhanced[52,66,67].

Anodic aluminum oxide (AAO) has been considered as promising support for thin-film fabrication due to high thermos-mechanical stability and scalability. Uniform nanohole array is formed throughout the substrate. This nano-hole has no tortuosity, which is advantageous for fuel delivery. However, pinhole formation in the electrolyte causes severe performance drop and unstable open circuit voltage issues. Although the pinhole issues are partially resolved by applying hybrid deposition techniques (sputtering and atomic layer deposition etc.) for fabricating

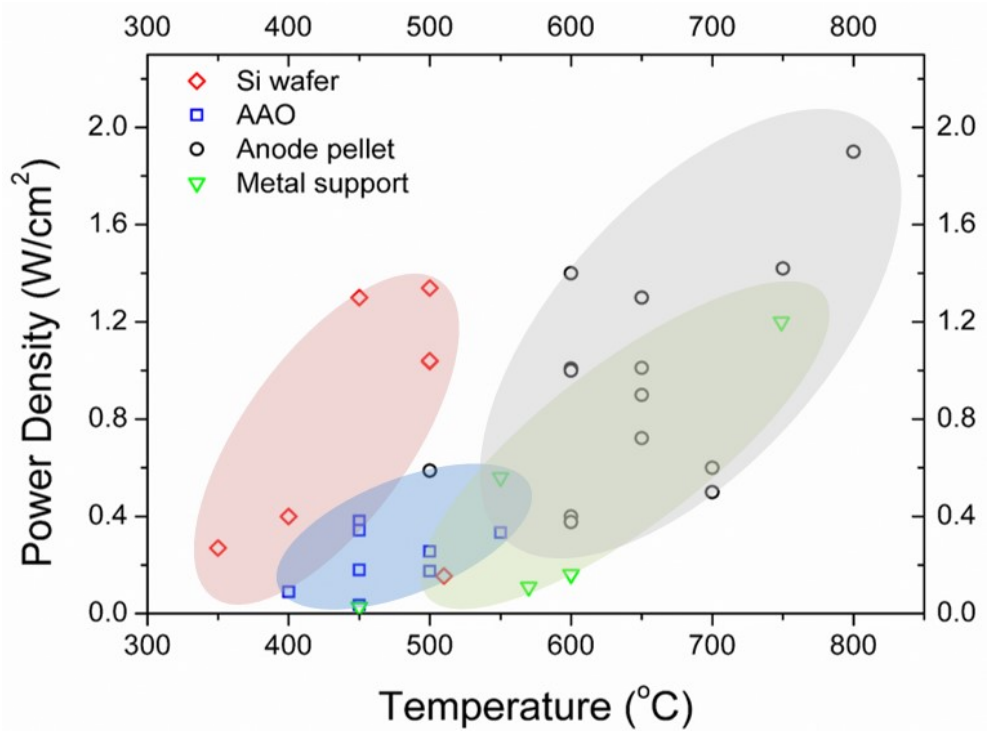

Figure 1.8 Literature data for the peak power density of TF-SOFC depending on types of support.

electrolyte layer, still the peak power density of the cell needs to be enhanced[68,69]. Recently, there is an attempt to apply thin-film fabrication of the anode functional layer or electrolyte to anode pellet and metallic support. However, due to the large pore structure (larger than a few micrometers) and high roughness of the surface structure, physical vapor deposition (PVD) or chemical vapor deposition (CVD) is difficult to be applied to electrode or electrolyte fabrication. Only a few reports have succeeded in developing the process for thin-film deposition on anode pellet or metallic substrate[70,71]. For this reason, high power density of Si wafer and AAO supported TF-SOFCs have are dominant at a temperature under 500℃.

1.4 Hydrocarbon Solid Oxide Fuel Cells

One of the advantages of SOFCs is remarkable fuel flexibility with various utilization methods such as direct electrochemical oxidation, internal steam reforming, and partial oxidation. Direct use of hydrocarbon fuel can benefit to system level. Since external reformer is unnecessary for direct hydrocarbon fuel SOFCs, the system size and complexity are substantially reduced[72–75]. There are various kinds of hydrocarbon fuel such as methane, butane, and propane. In case of use of methane for direct SOFCs, it can be a promising energy source since supplying and storage infrastructure for a major component of the natural gas (over 90% of natural gas is methane) is already existing[76]. It could eliminate the issues of hydrogen storage, which means a large progress in the commercialization of SOFCs to the market. However, significant efforts have to be dedicated to resolving the technical issues for using methane as a fuel for low-temperature SOFCs.

Among various utilization methods for methane, direct internal steam reforming is considered as a promising method for use of methane as a fuel with minimum fuel dilution. Since direct electrochemical oxidation of methane is extremely sluggish at low-temperature, catalytic reforming of methane to carbon monoxide and hydrogen is necessary for generating electric potential[77–79]. Various reactions can happen in steam reforming reactions, and the possible reactions are written below:

$$\text{Steam Reforming: } CH_4 + H_2O \rightarrow CO + 3H_2 \qquad \Delta H = +206\ kJmol^{-1}$$

$$\text{Water Gas Shift: } CO + H_2O \rightarrow CO_2 + H_2 \qquad \Delta H = -41\ kJmol^{-1}$$

In terms of kinetic, hydrogen and carbon monoxide oxidation reaction is much faster than direct oxidation of methane. Therefore, the electrochemical performance of the cell with reformed gas fuel could be higher than that without the reforming process.

The key point of structure design for direct methane SOFCs is that thermally catalytic reforming structure should be located with SOFCs anode structure[80]. When methane fuel is supplied to the anode of SOFCs, without the need of an external reformer, the fuel should be pass through the reforming structure before reaching to TPB at anode side. As mentioned above, without the reforming process, electrochemical performance of low-temperature SOFCs for direct use of methane is significantly reduced. Furthermore, to design direct methane SOFCs structure with high efficiency at low-temperature, steam to carbon ratio (S/C ratio) should be low enough to exclude water management system and minimize fuel dilution. However, a technical breakthrough for nanostructure fabrication is essential for satisfying these structural and operational conditions.

Thermally catalytic steam reforming process of methane is not energetically favored at low operating temperatures (under 500℃). Furthermore, at low S/C ratio operating conditions, thermodynamic calculation shows that carbon coking likely happens at the anode side[81]. It has been reported in the literature about the cell failure due to the massive carbon coking in the anode. To resolve the carbon coking issue and low activity for steam reforming reaction at low-temperature, the activity of the reforming structure should be dramatically enhanced by designing nanostructure with a high density of reaction area. Metallic nanoparticle should well disperse in the ceria oxide support for formation of high catalytic activity. Uniform dispersion with the nano-sized grain structure could be fabricated by the co-sputtering system because of the deposition characteristic of the sputtering principle.

Chapter 2. Background

2.1 Literature Review of AAO supported SOFC

As mentioned in the previous chapter, the AAO substrate has shown a promising characteristic for fabricating thin-film SOFCs due to uniform nano-hole array and scalability. Previous research has focused on the issues related to pinhole formation in the electrolyte during the deposition process. The hybrid deposition method combining sputtering and ALD for electrolyte fabrication is suggested for alleviating the pinhole issue[69]. Development of ALD electrolyte enables open-circuit voltage of AAO-supported TF-SOFC is close to theoretical value at operating temperature even with extremely thin electrolyte layer. Sanghoon Ji et al. reported that 70nm thickness of plasma-enhanced ALD yttria-stabilized zirconia (YSZ) electrolyte shows 1.17V at 500℃[57]. Furthermore, Seongkook Oh et al. reported that electrolyte deposited by using the hybrid deposition method (ALD YSZ and sputtering samarium-doped ceria (SDC)) shows over 500mW/cm^2, which is the highest performance of AAO-supported TF-SOFC at 450℃[82]. Although the significant progress in electrolyte fabrication process, most of the high performing AAO-supported TF-SOFCs still use platinum (Pt)-based anode and cathode. Despite the development of perovskite structure of the oxide cathode, which is considered as a promising candidate for low-temperature cathode materials, catalytic performance of Pt is superior to any other material for operation under 500℃[83]. However, in terms of anode materials, using Pt-based electrode for anode structure is unusual case even for the conventional SOFCs structure. Many research about SOFCs structure fabricated by sintering process (pelletizing, tape casting, screen printing, spray pyrolysis, etc.) uses Ni-based cermet materials for the anode fabrication because of comparable performance of the anode materials to Pt-based materials and feasibility for the commercialization. Nevertheless, the utilization of Ni-based anode structure

for AAO-based SOFCs has been rarely reported. The main reason for that is because of the lack of understanding co-sputtering of Ni-based anode on nanoporous substrate. Not only control of co-sputtered nanostructure but also the thermal effect on nanostructure. In addition, since AAO is electrically non-conductive, current collecting path is through the nanoscale thickness of the anode, which causes unduly high resistance contributed to the ohmic resistance of the full cell. Current collection through in-plane direction of the nanoporous electrode could also cause formation of the dead zone, which is defined as TPB without current connection. We believe that the lack of understanding in this unique structure effect on the cell performance is the major reason for the low power density of Ni-based AAO supported SOFCs at low-temperature considering the nanoscale electrolyte thickness.

To emphasize the strengths of the SOFCs, utilization of hydrocarbon fuel is necessary. Pt is extremely vulnerable to carbon contamination. Without the optimized Ni-based or other material-based anode structure, hydrocarbon fuel can not be used for SOFCs. Although nano-sized grain structure is advantageous for reforming or electrochemical oxidation processes, study on the use of hydrocarbon on AAO supported SOFCs at a temperature under 500°C has not been reported.

2.2 Thesis Outlines

This thesis focuses on two main topics: one is understanding and development of high performing nanostructured Ni-gadolinium doped ceria (GDC) anode fabricated by co-sputtering process. Two is the characterization and development of highly active catalytic reforming nanostructure fabricated by co-sputtering on the AAO substrate. The research is presented in 4 chapters (from chapter 3 to 6). The

detailed contribution and summarization is described below:

- Chapter 3 describes the effect of nanostructured Ni-GDC anode fabricated by co-sputtering on electrochemical performance. As mentioned in the previous chapter, the electrochemical performance of TF-SOFC on AAO substrate is greatly affected by the anode nanostructure. The nanostructure of Ni-GDC deposited by co-sputtering can be controlled by the various parameters of sputtering system. Among those parameters, the major parameters: chamber pressure, thickness of the anode (deposition time), incident angle, which are expected to have a profound effect for the nanostructure, are controlled and comparatively characterized.

- Chapter 4 elaborates the thermal stability of Ni-GDC anode deposited by co-sputtering. The electrochemical performance of Ni-GDC anode is closely related to thermal stability of nanostructure because the operating temperature is around 500℃. It is widely known that Ni is vulnerable to thermal agglomeration due to the high surface energy and diffusion rate at high temperatures. Although the agglomeration tendency depending on Ni grain size and composition of Ni-GDC anode is previously studied, nanostructure change of AAO supported Ni-GDC anode varied with GDC has not been reported. In this chapter, the agglomeration effect on co-sputtered Ni-GDC anode on AAO was characterized by high-resolution field emission microscope (FESEM) and extended time operation.

- Chapter 5 describes the direct methane for co-sputtered Ni-GDC anode varied with GDC composition. Due to the nano-sized grain structure of co-sputtered anode, the catalytic performance for direct oxidation of methane and reforming is higher than the conventional structure. The detailed

electrochemical properties of methane fueled AAO supported SOFCs is demonstrated in the chapter.

- Chapter 6 demonstrates direct methane fueled TF-SOFCs with nanostructure Ru-GDC reforming layer. Since the direct electrochemical oxidation of methane is not energetically favored at low-temperature, the additional reforming structure is essential for achieving high performance. Designing the co-sputtering Ru-GDC reforming structure on AAO supporting system and electrochemical performance of the integrated TF-SOFC is addressed in terms of extended time operation.

Chapter 3. Effect of Nanostructured Ni-based Anode on Performance

3.1 Introduction

Sputtering is known to be advantageous for commercialization due to the capability of uniform large area deposition. For industrial sputtering system, substrate size can be increased up to a few thousand square centimeters. Furthermore, co-sputtering is superior to other deposition methods for mixing two kinds of target materials in nanoscale[84]. Since thin-film deposited by sputtering system consists of the nano-sized grains, theoretical expectation of TPB density in co-sputtered electrode is significantly high. In fact, the performance enhancement with anode functional layer deposited by PLD, which is one kind of PVD method, has been reported in the literature from KIST[85]. However, most of the work on co-sputtering for Ni-based anode on the nanoporous substrate has shown low power density compared to the similar compositional structure of SOFCs at similar operating temperatures. The major reason for the low performance is possibly due to the unique electron conduction path for anode on AAO substrate. AAO is known to be electrically non-conductive structure. Therefore, the electron produced from electrochemical oxidation of the fuel at the anode side should pass through complicated nanoporous structure because the substrate is not conductive. Electron conduction resistance is typically not considered as a concern for ohmic loss or performance of the cell. As demonstrated in this chapter, however, the in-plane connectivity of the nanostructure fabricated by co-sputtering on AAO could be important to achieve high power density.

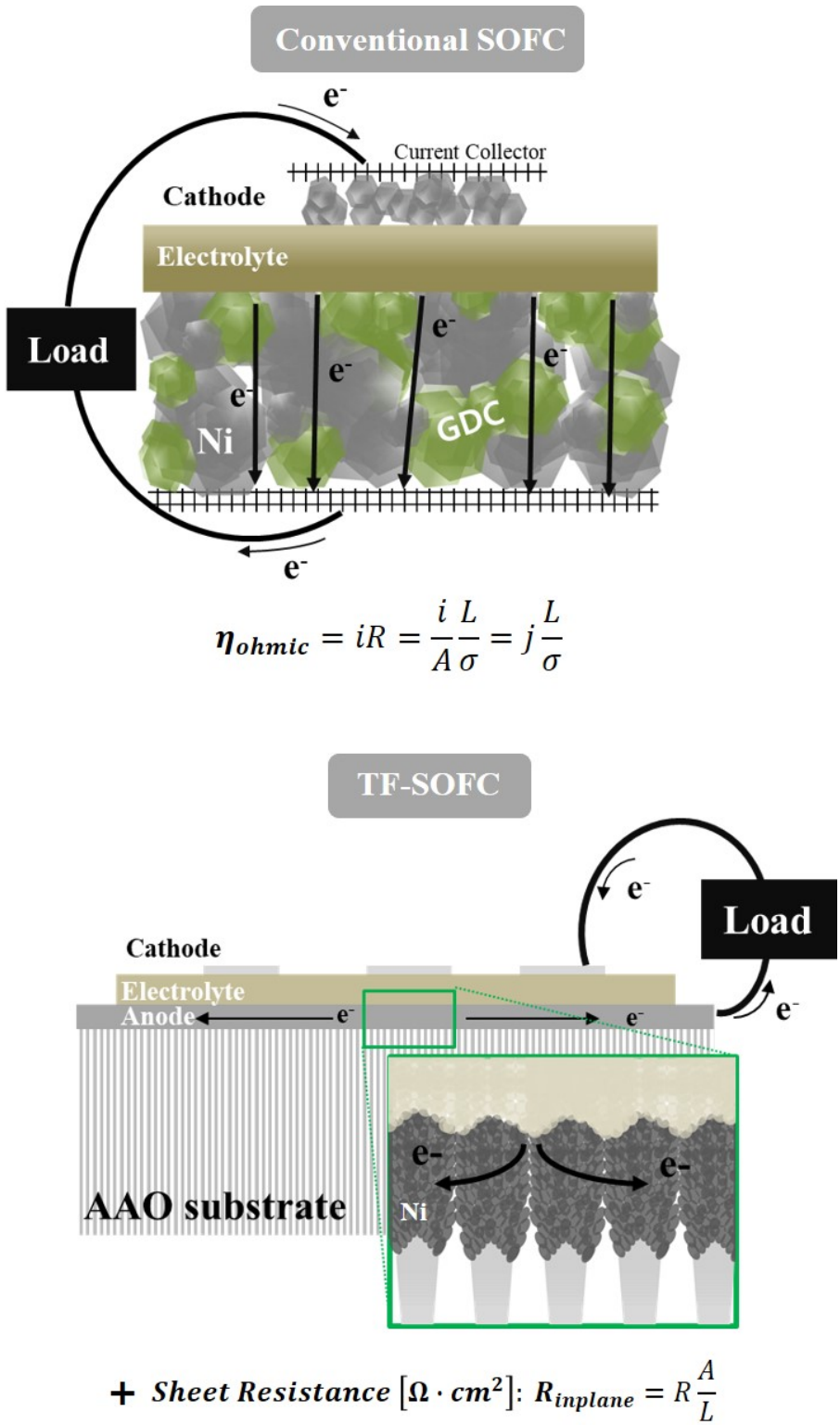

Figure 3.1 Schematic drawing of difference in electron conduction path of conventional anode supported fuel cell and AAO supported thin-film SOFCs.

In this chapter, sputtering parameters are controlled to change the electrochemical properties of the anode structure grown on AAO substrate. First, porosity control by deposition chamber pressure has been previously studied by Dr. Joonho Park. Joonho Park et al. reported that Ni anode deposited with 12 Pa Ar gas showed extensively high porosity compared to the deposition with 0.67 Pa[86]. To reduce variables and select the deposition condition for high density of TPB, deposition pressure for anode structure is fixed to be 8 Pa for all nanostructure fabricated in this chapter. Other

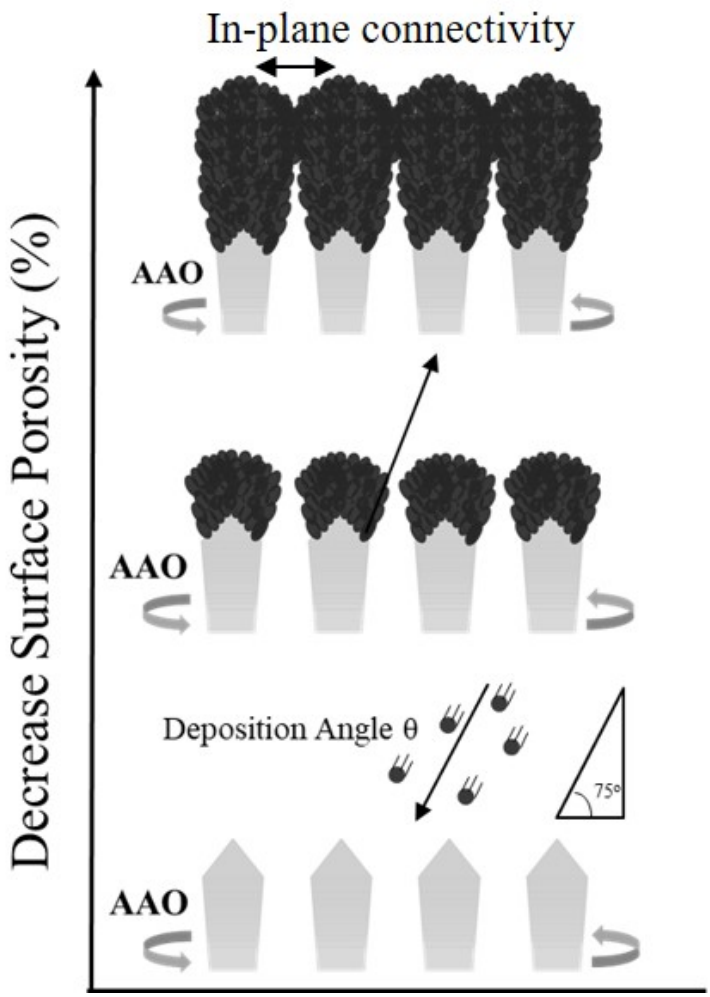

Figure 3.2 Schematic of the growth mechanism of the electrode deposited by sputtering related to surface porosity and the in-plane connectivity.

than deposition pressure, anode thickness is also greatly affecting the surface porosity of the anode deposited on AAO. Figure 3.2 shows schematic of the growing mechanism of co-sputtering anode on AAO. From the schematic, it can be speculated that the columnar structure of the sputtered layer is attributed to the decrease in surface porosity of the anode. Furthermore, not only the surface porosity is affected by the thickness of the anode, but also the in-plane connectivity is influenced by the width of the column structure. Confirmation of high TPB density of the anode deposited with 8 Pa is firstly processed. Secondly, the thickness effect of the Ni-GDC anode is tested by changing the thickness from 300 to 1000nm. Finally, the nano-column structure of Ni anode is controlled by changing incident angle and rotation speed since these two parameters have large impact on the structure change. The result of the electrochemical and microscopic analysis shows insight for designing high performance of nanostructured Ni-GDC anode fabricated by co-sputtering.

3.2 Experimental

For thin-film deposition of the electrodes and electrolyte, AAO substrate with 80nm pore diameter size was used for the support (Inredox, USA). The thickness of the substrate is about 100um. The substrate dimension is 1cm by 1cm. For the deposition of Ni and GDC for the electrode, a commercial sputtering machine (A-Tech System Ltd, South Korea) was used with Ni pure metal target (99.99%) and Gd 20mol% doped ceria target (99.9%). Deposition power control was done by direct current (DC) source and radio frequency (RF) source. DC power is controlled from 50W to 200W for Ni sputtering, and RF power is controlled from 0 to 100W for

GDC sputtering. In case of co-sputtering, the two guns were loaded to the sputtering chamber with the same incident angle for each target. Chamber pressure is determined by the gas flow and pressure controller. For anode and cathode deposition,

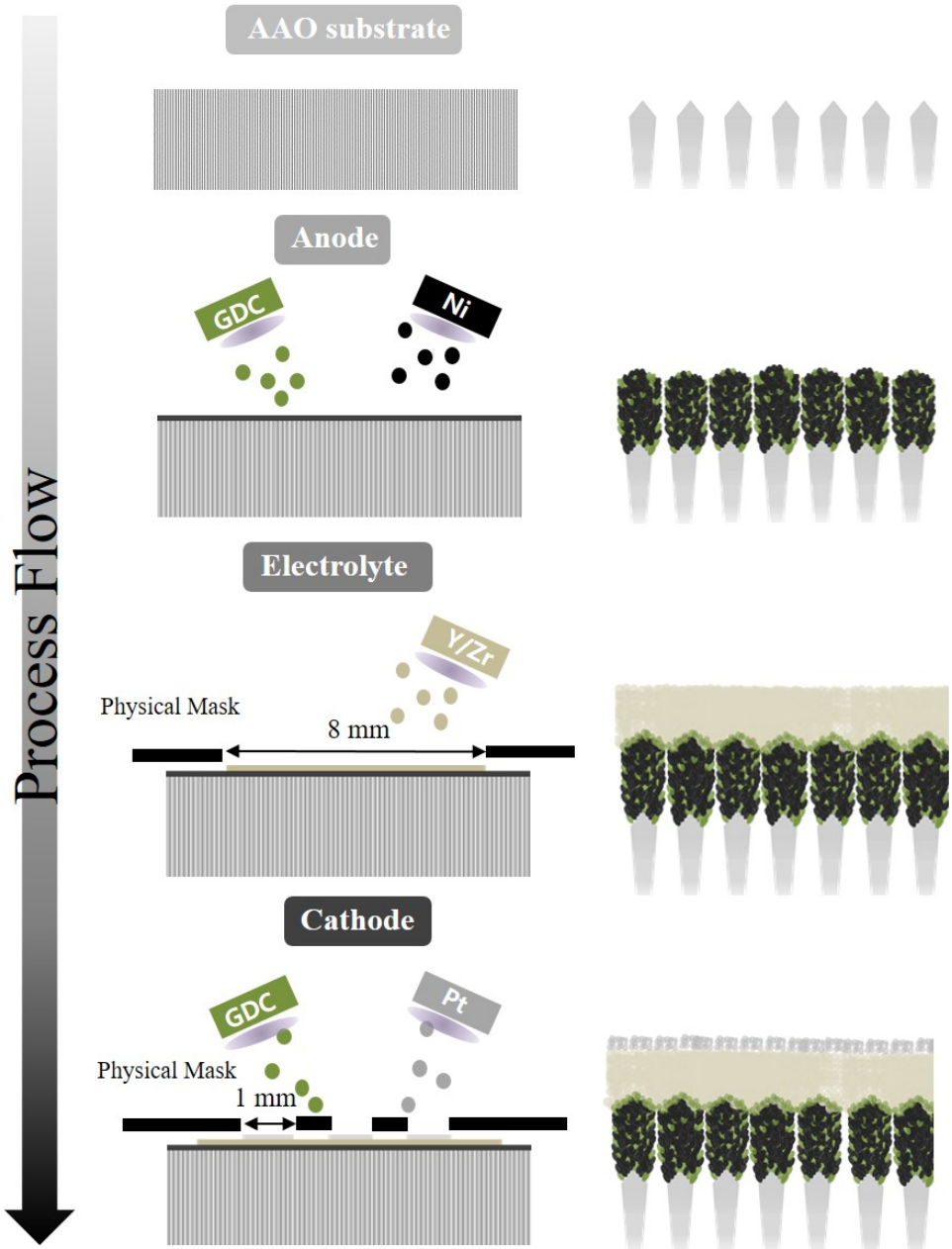

Figure 3.3 Schematic of fabrication process for thin-film SOFCs.

Ar gas atmosphere was used, while Ar/O_2 mixture atmosphere was used for the electrolyte deposition. A thin-film electrolyte is deposited by Y/Zr metal target ($Y_{0.16}Zr_{0.84}$, 99.9%). For reactive sputtering process, chamber atmosphere was controlled by Ar/O_2 mixture gas with 20% O_2. The power is fixed to 200W for YSZ electrolyte deposition. For cathode, Pt metal target (99.9%) and Gd 20mol% doped ceria target (99.9%) were used to deposit Pt-GDC cathode. The deposition power is set to be 100W for Pt and 50W for GDC target. The chamber pressure is also fixed to 12 Pa and applied to every cell fabricated in this thesis.

Thin-film electrolyte and cathode deposition was patterned by physical mask. Considering the substrate dimension, a stainless steel mask with 8mm by 8mm opening was used to deposit the electrolyte. Anode exposed to the air was covered with Ag paste for electrical connection between the anode and the jig. Cathode mask with 1mm by 1mm opening was used to pattern the cathode.

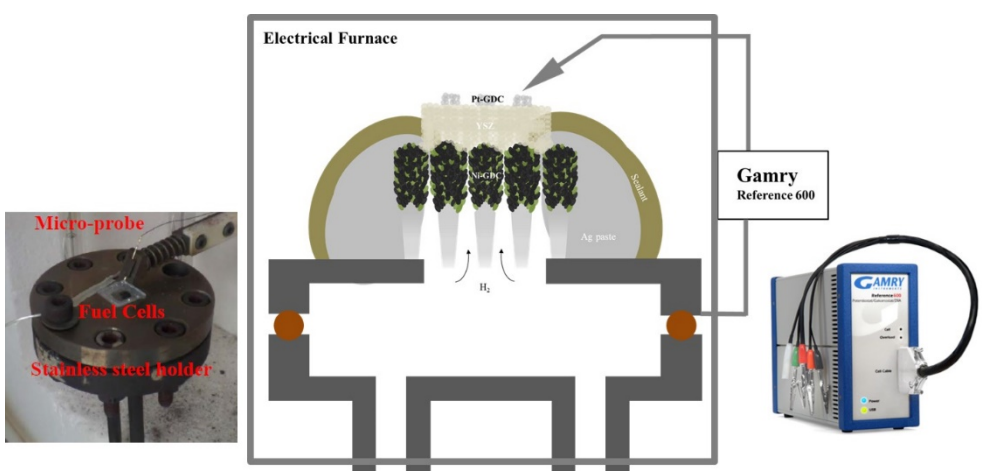

Figure 3.4 Schematic and actual image of a customized test station with TF-SOFCs attached to the stainless steel cell holder (jig).

Thin-film nanostructure was characterized by field emission scanning electron microscope (FESEM) and focused ion beam (FIB) analysis. Magnification of FESEM was varied from 10 to 20000. In addition, the electrochemical performances of the cells were measured by Gamry (Reference 600, Gamry Instrument, USA). TF-SOFCs was attached to the stainless steel jig with Ag paste for electrical connection between the jig and the anode on AAO. After drying process of Ag paste, ceramic sealant was applied on top of dried Ag paste for sealing. TF-SOFCs attached to the jig was dried at ambient air for 4 hours before the testing. The cell was tested in the customized test station consisted of halogen heater. The ramping rate of the temperature was set to be 8℃ per minute. The temperature of the test station was heated up to 100℃ and stayed there for 40min, and sequentially heated up to 500℃ for cell operation. After the temperature of the test station reached the operating temperature, the cathode was contacted with the customized probing tip controlled by X-Y-Z station.

3.3 Results and Discussion

3.3.1 Determination of Deposition Pressure for High Performing Nanostructured Ni-GDC Anode

To verify the porosity effect on Ni-GDC anode deposited by co-sputtering, co-sputtered Ni-GDC was fabricated with 4 Pa and 8 Pa. The surface porosity and the cross-sectional image of the Ni-GDC with 4 Pa and 8 Pa were comparatively shown in figure 3.5. From the surface FESEM images, it is clear that co-sputtered Ni-GDC anode deposited with 8 Pa shows higher porosity. However, even though the grain structure and porosity of the surfaces are different from the nanostructure analysis depending on the chamber pressure, actual electrochemical performance

should be compared by electrochemical impedance spectroscopy (EIS) analysis. In terms of interpretation of EIS graph, the value at the intersection between the graph and the real X-axis at high-frequency region means the ohmic resistance[87]. In addition, it is widely known that the ohmic resistance caused by ion and electron transports is independent of measuring voltage of the cell while the polarization resistance is dependent on the voltage. The size of arc presented in the Nyquist plot is relevant to anode-electrolyte and cathode-electrolyte polarization. Regarding these knowledge, EIS results of Ni-GDC anode varied with deposition pressure indicate that polarization resistance of the Ni-GDC deposited with 8 Pa showed 90% decrease

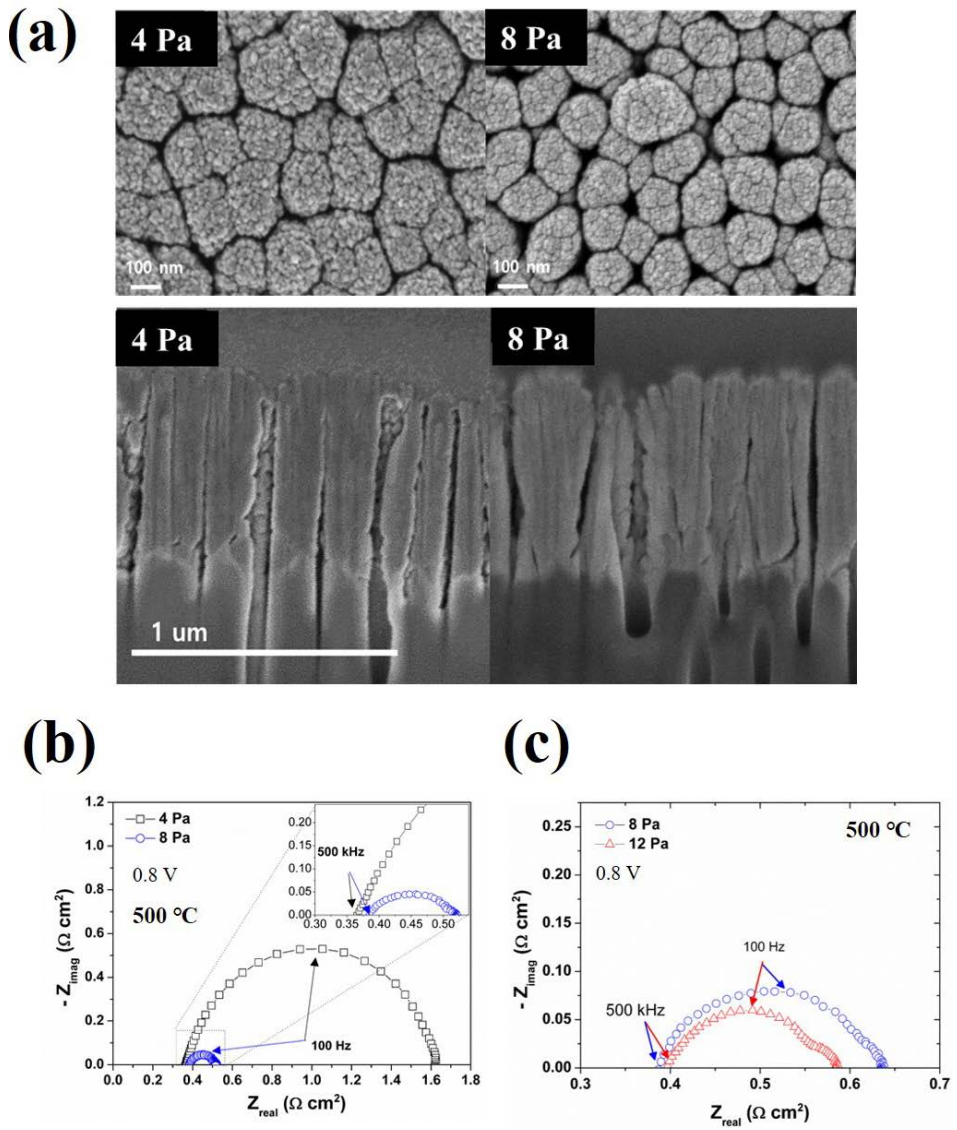

Figure 3.5 (a) Nanostructure change in surface and cross-sectional view varied with deposition pressure (4Pa, 8Pa). (b) Effect of porosity of Ni-GDC varied with 4 and 8 Pa on electrochemical performance measured by EIS.

compared to the one deposited with 4 Pa. Higher chamber pressure (12 Pa) was also suitable condition for fabricating nanostructured anode with high activity confirmed from the EIS graph in figure 3.5 (c). However, the enhancement in polarization resistance was negligible considering 0.8V of measuring voltage for EIS analysis.

Electrolyte and cathode deposition condition was the same for all samples. Therefore, it can be concluded that the difference in polarization resistance of the EIS results is attributed to the difference in anode nanostructure. From these results, we believe that 8 Pa of chamber pressure for highly active Ni-GDC nanostructure is enough to produce high power density at low-temperature. This chamber pressure was used for all other parameter experiments throughout this thesis.

3.3.2 Thickness Effect of Co-sputtered Ni-GDC Anode

Due to the material characteristic of AAO, as previously mentioned, anode thickness of Ni-GDC on AAO should be prominent factor for determining the performance of TF-SOFCs. For an accurate comparison, except for thickness of the anode, composition, electrolyte thickness, and cathode structure were maintained at same condition. GDC contents in the anode were set to be 12.8%, which was controlled by the deposition power of the GDC target (50W). The thickness control of Ni-GDC anode was confirmed from the cross-sectional FIB-SEM images. The thickness was controlled by the deposition time. Current density (j) –voltage (V) - power density (P) curves (polarization curves) were measured for different anode thickness samples. It is noteworthy that the peak power density was increased as the thickness increased up to 800nm. However, as the thickness of the anode was

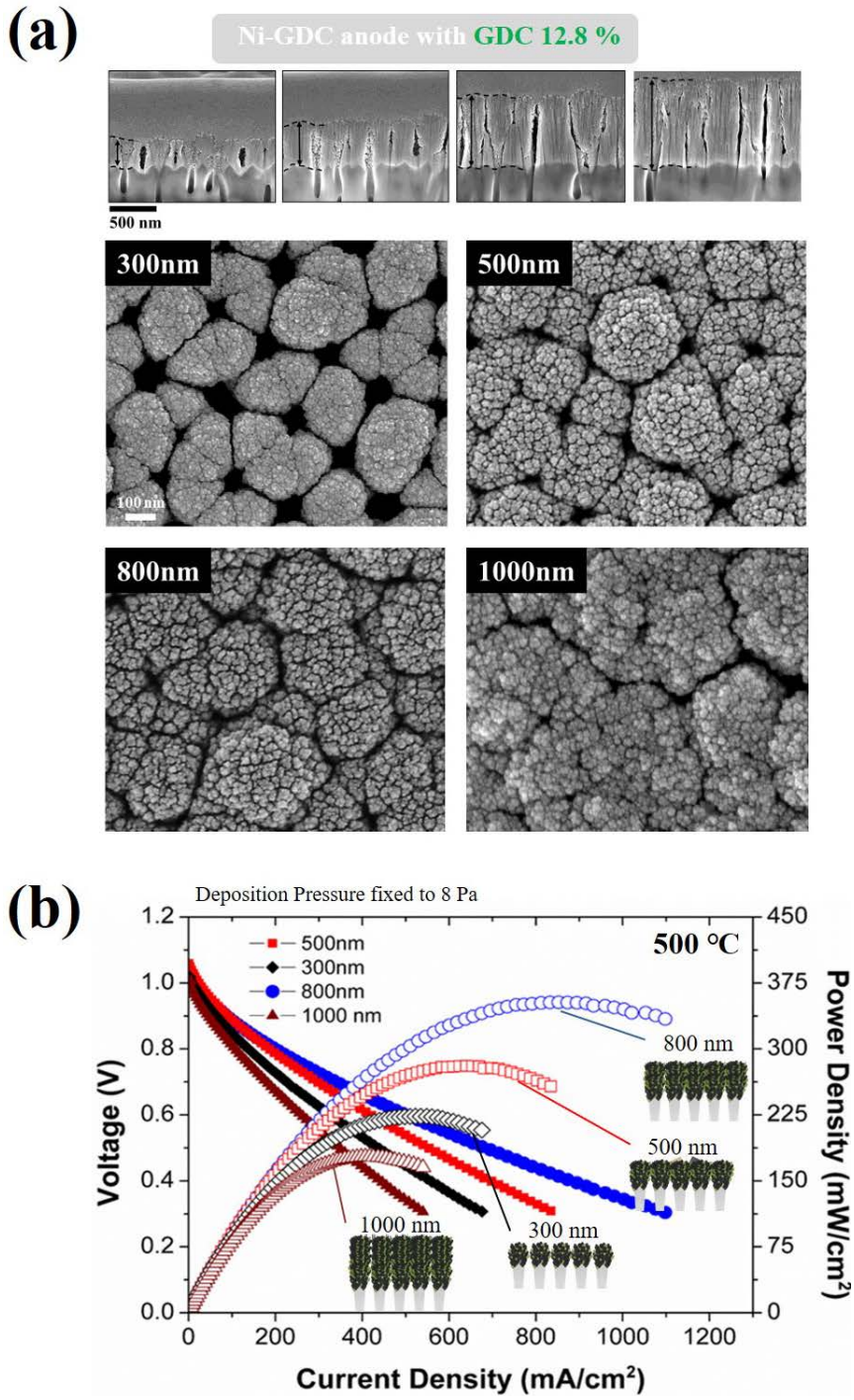

Figure 3.6 (a) Nanostructure surface FESEM and cross-sectional FIB-SEM images of the co-sputtered Ni-GDC anodes with 12.8% GDC content. The anode structure was varied with the thickness from 300 to 1000nm. (b) Current density (j)-voltage (V)-power density (P) of the cells varied with anode thickness was compared.

increased over 1000nm, the performance of TF-SOFCs steeply dropped over 50% from the peak power density of 800nm anode. Detailed contribution to performance difference was analyzed by EIS measurements. Figure 3.7 describes that the performance difference between 300, 500, and 800nm anode structure was attributed to both polarization and ohmic resistance. However, in the range of anode thickness from 500 to 800nm, enhancement in ohmic resistance (over 30% reduction) was

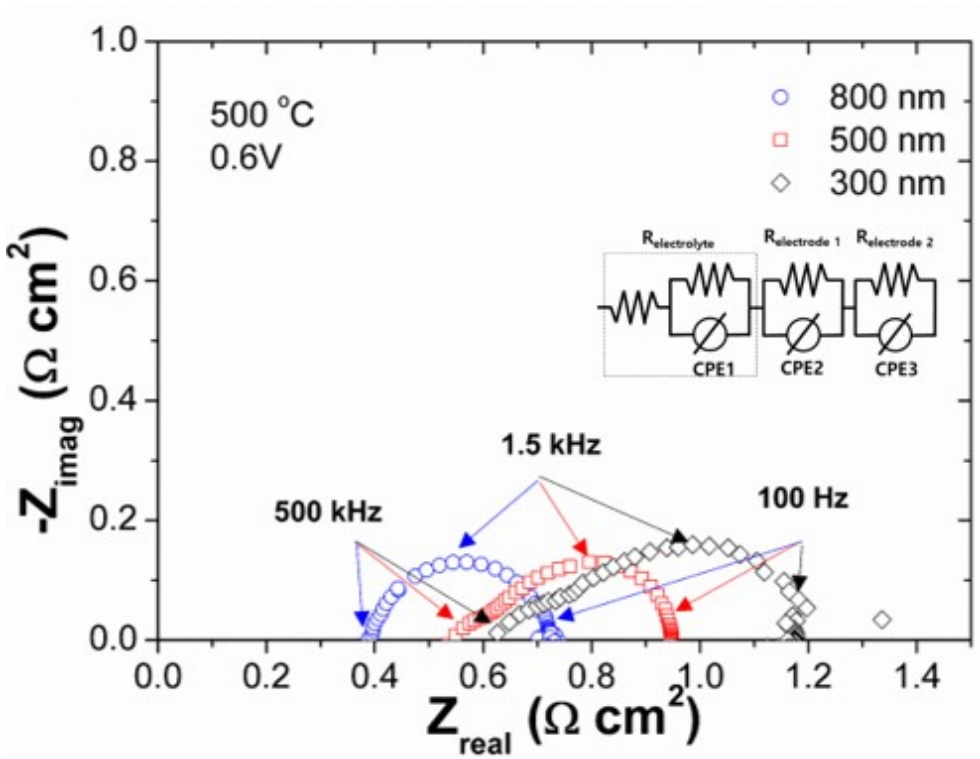

Figure 3.7 EIS results of TF-SOFC with Ni-GDC anode thickness 300, 500, and 800nm measured at 0.6V.

substantially higher than that in polarization resistance (15% reduction). More importantly, anode thickness with 1000nm showed an abrupt increase in polarization resistance compared to 800nm sample, while the ohmic resistance of 1000nm sample was slightly decreased (about 7%). These results indicated that active TPB density of 1000nm sample was decreased significantly. From the nanostructure analysis, it can be speculated that polarization resistance of 1000nm sample was increased due to decrease in surface porosity. As the in-plane connectivity was improved with the thickness increase, density of active reaction sites was also increased, which was consistent with a decreasing tendency of ohmic and polarization resistances. The comparison result of bode plot was also consistent with the speculation. In the frequency range between 10^4 to 10^2 Hz, phase angle of 1000nm sample was clearly higher than that of 800nm sample, which represents surface exchange reaction rate was the major contribution for the difference in polarization resistance. From these results, 800nm thickness of co-sputtered Ni-GDC anode showed the best performance, and the performance could be more enhanced by controlling other parameters.

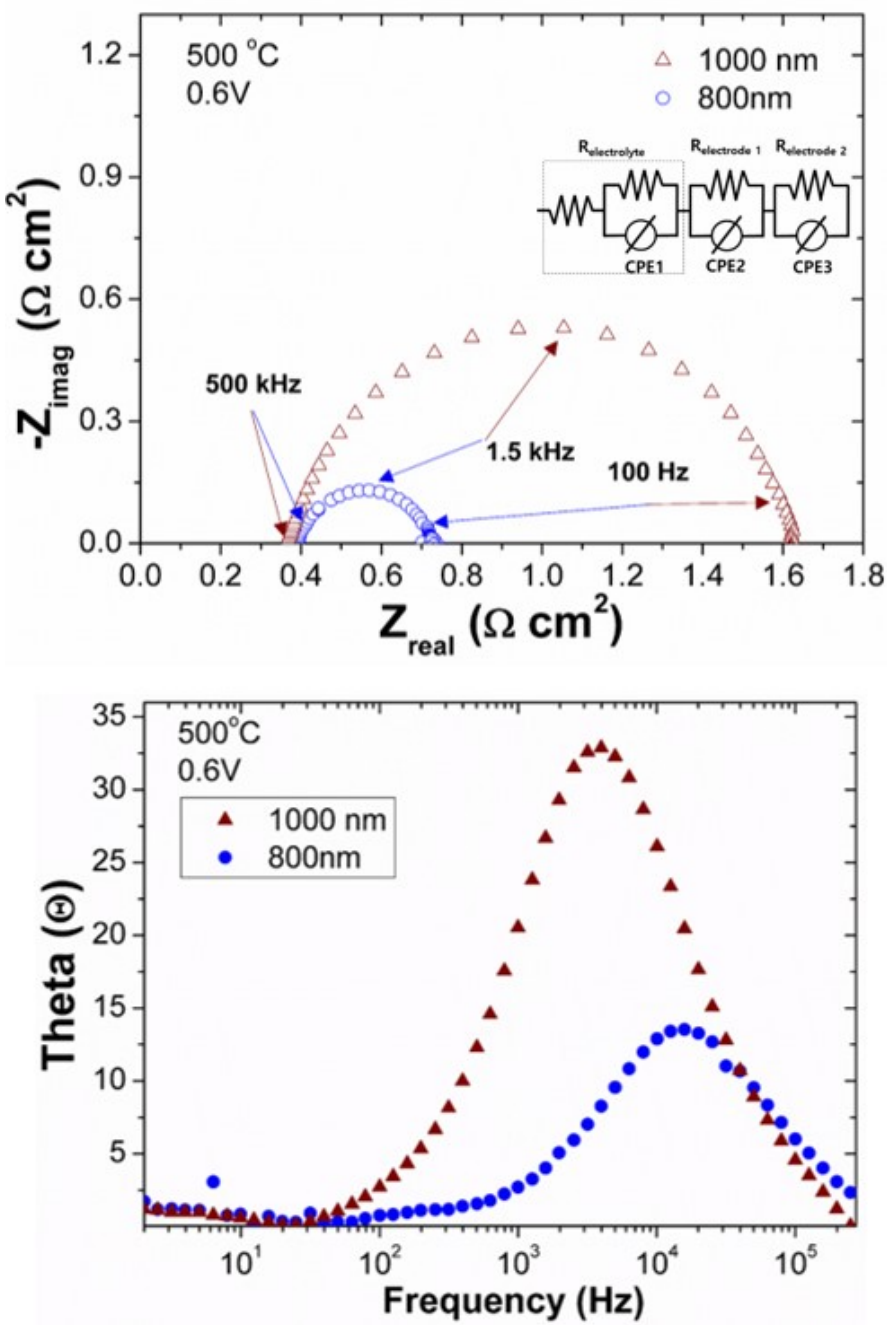

Figure 3.8 EIS and bode plots of Ni-GDC anode thickness varied with 800 and 1000nm. The measurement voltage is 0.6V. The frequency range is from 10^6 to 2 Hz.

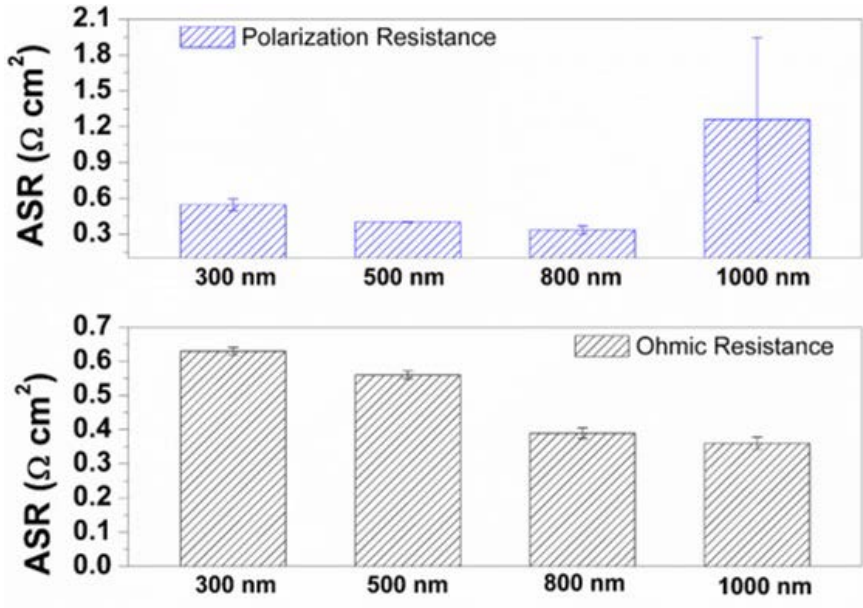

Figure 3.9 EIS equivalent circuit fitting results varied with anode thickness.

Thickness [nm]	300	500	800	1000
R_ohm [ohm·cm²]	0.63	0.56	0.39	0.36
R_pol [ohm·cm²]	0.55	0.40	0.34	1.26

Table 3.1 Area-specific resistance of ohmic and polarization for Ni-GDC anode varied with thickness.

3.3.3 Nano-Column affected by Sputtering Angle & Rotation Speed

From the experimental results for anode thickness change, it can be speculated that in-plan connectivity of the nanoporous anode structure can be the most profound factor for determining the peak power density of TF-SOFCs. At this point, it is essential to consider how the electrical network is connected in side of the nanoporous anode structure on AAO substrate. In figure 3.10, surface structure of bare AAO, 250nm thickness of Ni anode, and 800nm thickness of Ni anode are shown. As the Ni is grown on the nanoporous substrate, the electrical connection

should be formed through the yellow line drawn in figure 3.10. At the early stage of the nanoporous thin-film formation, the film morphology follows the substrate surface shape. As the film has grown over 800nm thickness, the size of the pore is reduced and a few columns are combined into one large column structure. It is notable that the electron produced from the anode-electrolyte interface has no way to go in-plane direction if the TPB is formed at the surface of Ni anode. The electron produced from electrochemical oxidation should be transferred to in-plane direction through the weakly connected Ni grains. Although closely packed Ni grains structure has multiple connections in nanoscale, it can be assumed that the change in the overall in-plane resistance highly depends on the shape of the nano-column. From this assumption, the width of the Ni nano-column was controlled by changing the sputtering incident angle and substrate rotation speed. In addition, the in-plane resistance of the Ni anode on AAO was measured by four-point probes. Consequently, electrochemical performances were measured and compared.

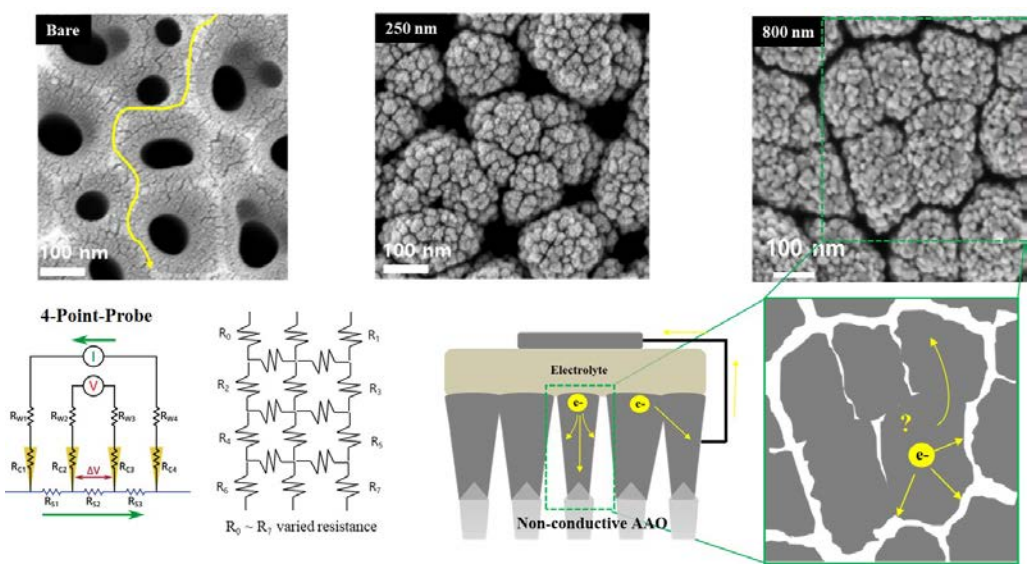

Figure 3.10 Surface nanostructure of bare AAO, 250nm and 800nm thickness of Ni anodes. Schematic illustration of an electron transfer path from TPB. The overall in-plane resistance consisted of multiple nanoscale connections of resistances is measured by 4 point probe.

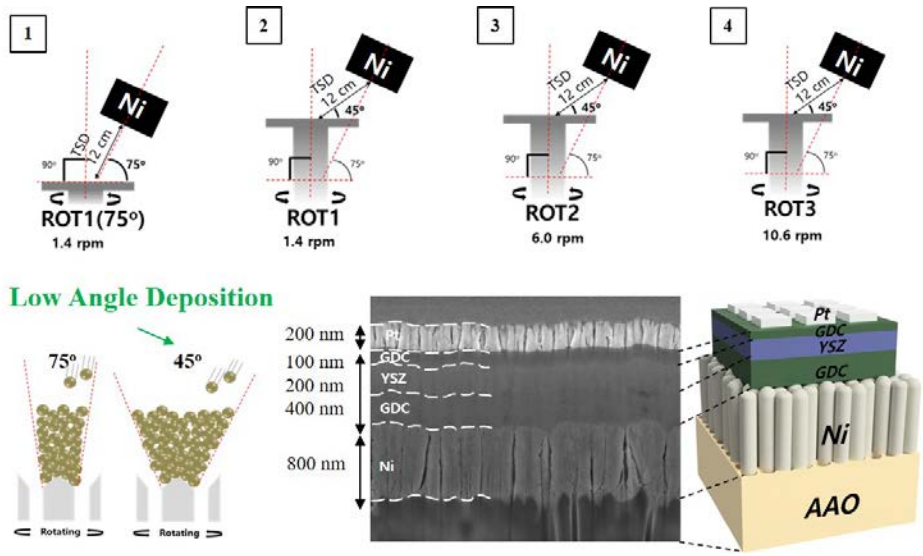

Figure 3.11 Schematic illustration of Ni anode fabrication varied with deposition angle: 75 and 45 degrees. Sample number 1 was deposited with 75 degrees. Sample number 2 was deposited with 45 degrees at rotation speed of 1.4 rpm. Rotation speed was controlled at 1.4, 6, and 10.6 rpm for sample numbers 2, 3, 4. A schematic illustrated in the right side comparatively shows the column structure affected by low angle deposition.

Four kinds of Ni anode samples were fabricated: Sample 1 was deposited by 75º incident angle and rotation speed 1.4 rpm (ROT1). Sample 2, 3, and 4 was deposited by 45º and variation of rotation speed 1.4 (ROT1), 6.0 (ROT2), and 10.6 rpm (ROT3), respectively. On top of the anode structure, 20mol% GDC and YSZ materials were deposited as sandwich structure by O_2 reactive sputtering process. To verify the in-plane resistance of the anode samples 1 and 2, 4-point-probe measurement was used. In figure 3. 12, comparison of the in-plane resistances of ROT1 sample with 75º and 45º was shown. The in-plane resistance of ROT1(75º) sample was higher by a factor of three times compared to that of ROT1(45º). Although the value of the resistance was low, contribution to the ohmic resistance could be large enough to affect the power density. The performance of ROT1(45º) was substantially improved at 450°C. EIS results showed that ohmic resistance of ROT1(45º) was reduced by more than 15% and consequently polarization resistance was also decreased. This reduction of

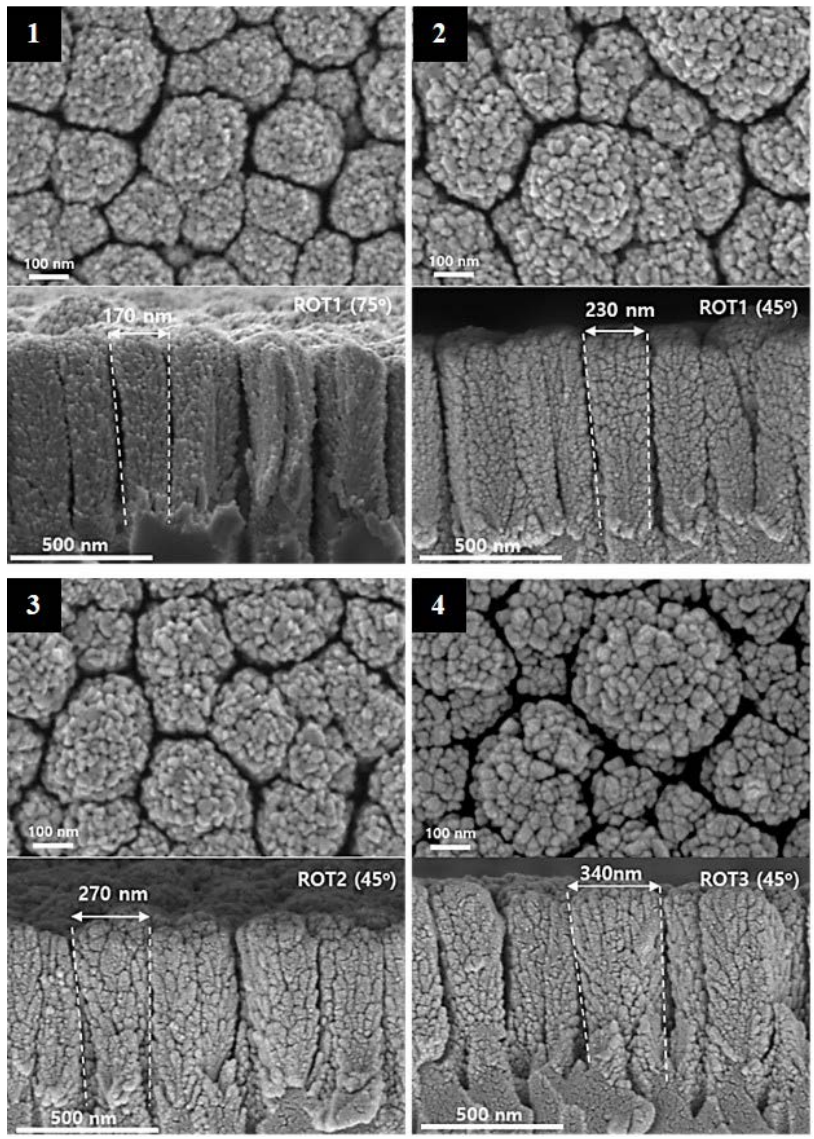

Figure 3.12 Surface nanostructure and cross-sectional FESEM micrographs of Ni anode with deposition conditions of sample numbers 1, 2, 3, and 4.

Sample	ROT1(75°)	ROT1(45°)	ROT2(45°)	ROT3(45°)	Anode Thickness (nm)
Column Width (nm)	170	220	270	340	~ 800

Table 3.2 Column width of sample numbers 1, 2, 3, and 4. Sample 1: ROT1(75°). Sample 2: ROT1(45°). Sample 3: ROT2(45°). Sample 4: ROT3(45°).

the resistances are totally attributed to the anode structure: columnar width. Other than these factors, surface porosity, crystallinity of the anode nanostructure, and the thickness were controlled to be same. Further investigation on the relationship between the nano-column width of the anode and the ohmic resistance was processed by controlling substrate rotation speed. As shown in figure 3.13, the peak power density of TF-SOFCs was steadily increased as the width of the nano-column increases. This tendency is clearly observed in figure 3.13 (c). Resultantly, the peak power density of Ni anode based TF-SOFCs was increased up to 304 mW/cm^2 at 450℃. The high peak power density (477 mW/cm^2) of Ni-based anode TF-SOFCs at 500℃ was obtained by using this Ni anode nanostructure deposited by low angle and high rotation speed. This performance of TF-SOFCs was higher than any other previous reports related to Ni-based anode AAO supported TF-SOFCs. We believe that this improvement, particularly on ohmic resistance, is attributed to the anode nanostructure especially related to column width. The control of the nano-column width by changing the sputtering parameter is the first attempt and contribution in AAO supported TF-SOFCs research field from this thesis.

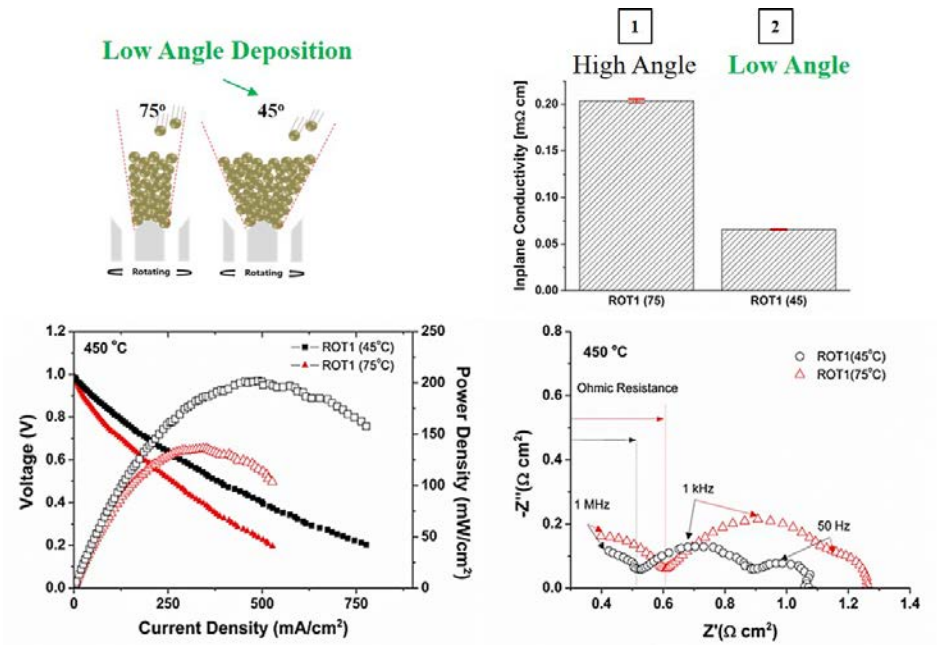

Figure 3.13 Electrochemical performance comparison of ROT1(75º) and ROT1(45º) samples.

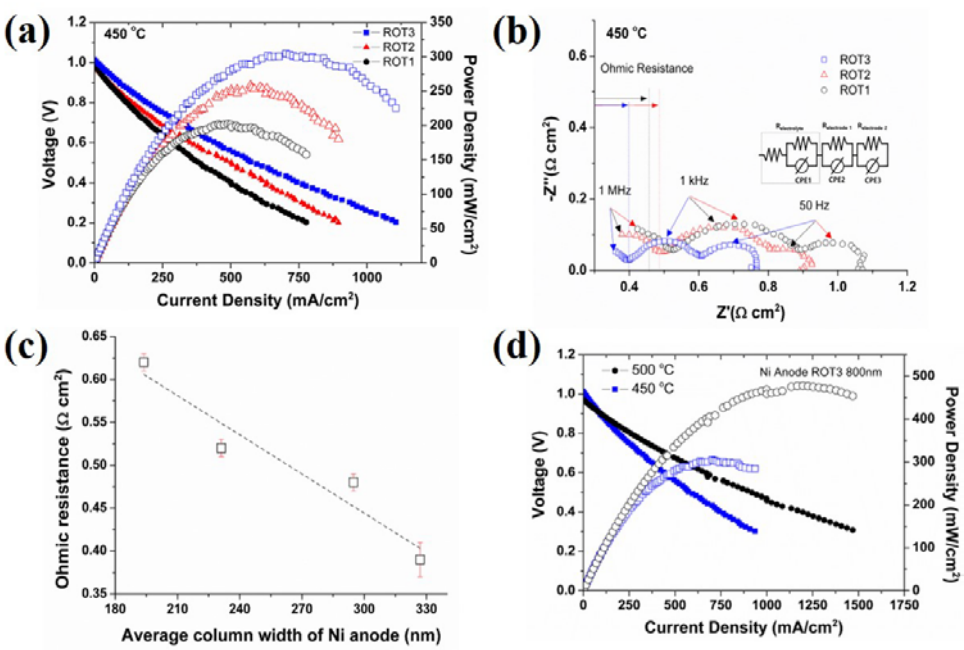

Figure 3.14 (a) j-V-P curves of sputtered Ni anode varied with rotation speed. (b) EIS measurements of ROT1(45º), ROT2(45º), and ROT3(45º) samples. (c) Relationship between nano-column width and ohmic resistance of TF-SOFCs. (d) Performance measurement at two different operating temperatures.

3.3.4 High Performance of Co-sputtered Ni-GDC Anode

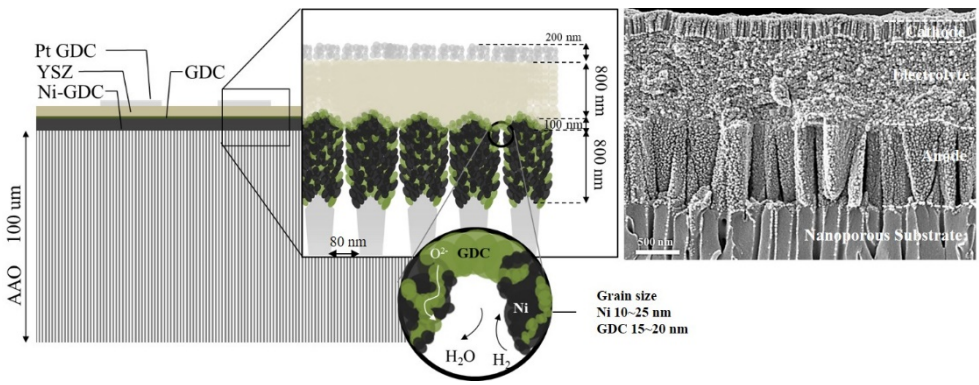

Figure 3.15 Schematic and cross-sectional FESEM images of TF-SOFCs.

Previous experimental results show that the anode nanostructure fabricated by sputtering can be delicately controlled, and the deposition parameter that mostly affects the performance of TF-SOFCs was found from parametric studies. The final process for obtaining high performing nanostructured anode is finding the optimized composition for Ni-GDC anode. Pure Ni anode is vulnerable to thermal agglomeration, and the TPB formation is limited to the interface between the electrolyte and anode. By applying the cermet anode on TF-SOFCs, the performance and the stability of the cell could be greatly enhanced. In co-sputtering process, low angle (45^{o}) and high rotation speed (10.6 rpm) are equally applied for all samples. Therefore, the structural advantage of sputtering anode confirmed from the previous experiments is valid for manufacturing co-sputtered Ni-GDC anode. The GDC composition in the cermet anode was controlled by changing the deposition power for the Ni and GDC targets. The detailed deposition condition for Ni-GDC and GDC composition according to the power control is presented in table 3.3. The volume fraction of GDC was increased from 0 to 27.7%.

Fixed Variable	Ar atmosphere 8 Pa / TSD 8 cm / Incident angle 45°			
Ni Deposition Power [W]	200			
GDC Deposition Power [W]	0	25	50	75
GDC composition in Ni-GDC anode [vol%]	0	3.9	12.8	27.7

Table 3.3 Co-sputtering conditions for nanostructured Ni-GDC anode on AAO.

Since the in-plane conductivity of the nanostructured anode on AAO substrate has great impact on the performance, GDC composition in the cermet anode should affect the performance by blocking the electron conduction path in Ni anode. Although ceria tends to be reduced and show partially electrically conductive at reducing atmosphere, still the electrical conductivity is much less than metal phase such as Ni. Therefore, mixing Ni nanostructure with GDC nano-sized grains could reduce electrical conductivity properties. Before, electrochemical performance measurement, the surface structures of the Ni-GDC anodes were compared because the surface porosity could be attributed to the performance difference. From the surface FESEM images, it is confirmed that the difference in surface porosity depending on GDC volume fraction of Ni-GDC anode was negligible. Therefore, the electrochemical performance difference between the samples should be attributed to the electrical and electrochemical properties of the anode. The samples with 12.8 and 27.7 vol% showed lower electrochemical performance compared to the bare Ni anode sample. Considering GDC contents contribute the formation of TPB density of the anode, it is hard to understand the decreased power density with higher GDC composition. From the EIS results, the performance decrease was mainly because of the increase in ohmic resistance. Although polarization resistance also increased with GDC contents, increase rate of the ohmic resistances was exceptionally high. A possible explanation for this phenomenon is that GDC nanoparticles mixed in Ni-

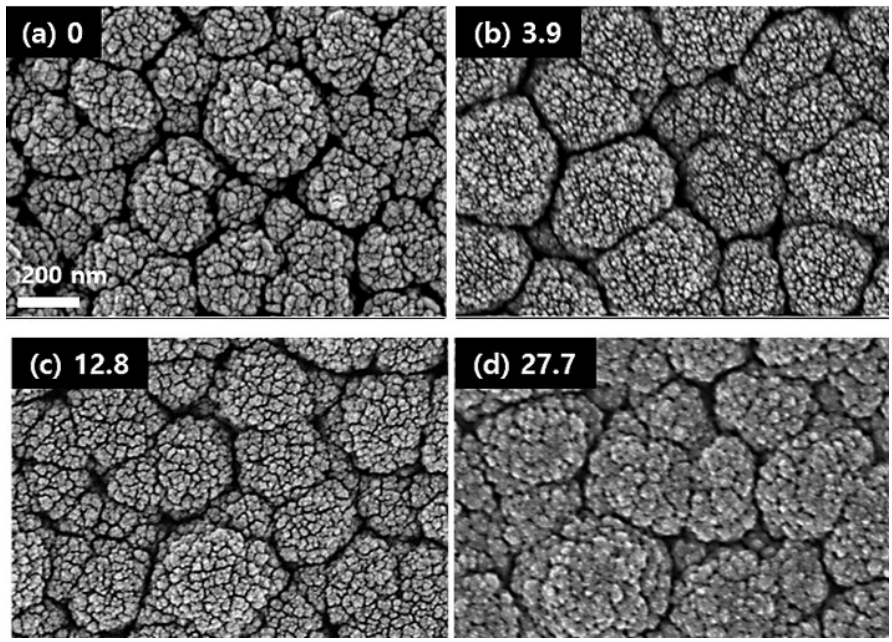

Figure 3.16 Surface nanostructure of Ni-GDC anode depending on GDC composition (a) 0, (b) 3.9, (c) 12.8, and (d) 27.7 vol%.

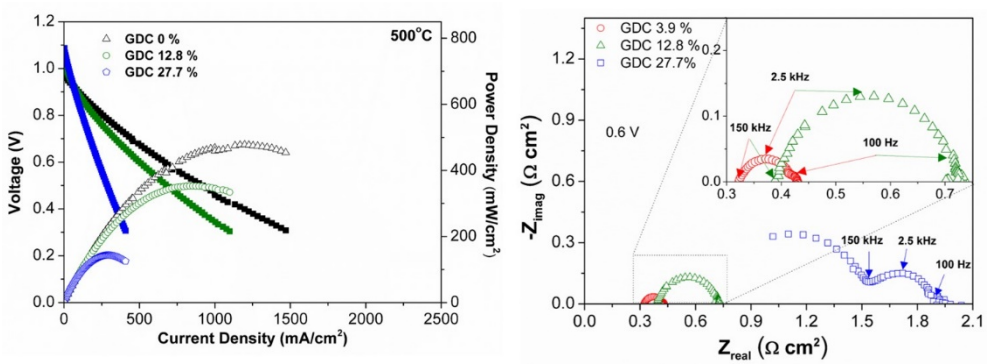

Figure 3.17 Electrochemical performance and EIS results measured at 0.6V of Ni GDC anode varied with GDC contents 0, 12.8, and 27.7 vol%.

GDC anode hinders the electron conduction through the anode. Consequently, deactivation of the reaction sites at the anode side was also increased causing the increase in polarization resistance. More interestingly, the maximum power density was obtained from nanostructured Ni-GDC anode with 3.9 vol% of GDC. Low

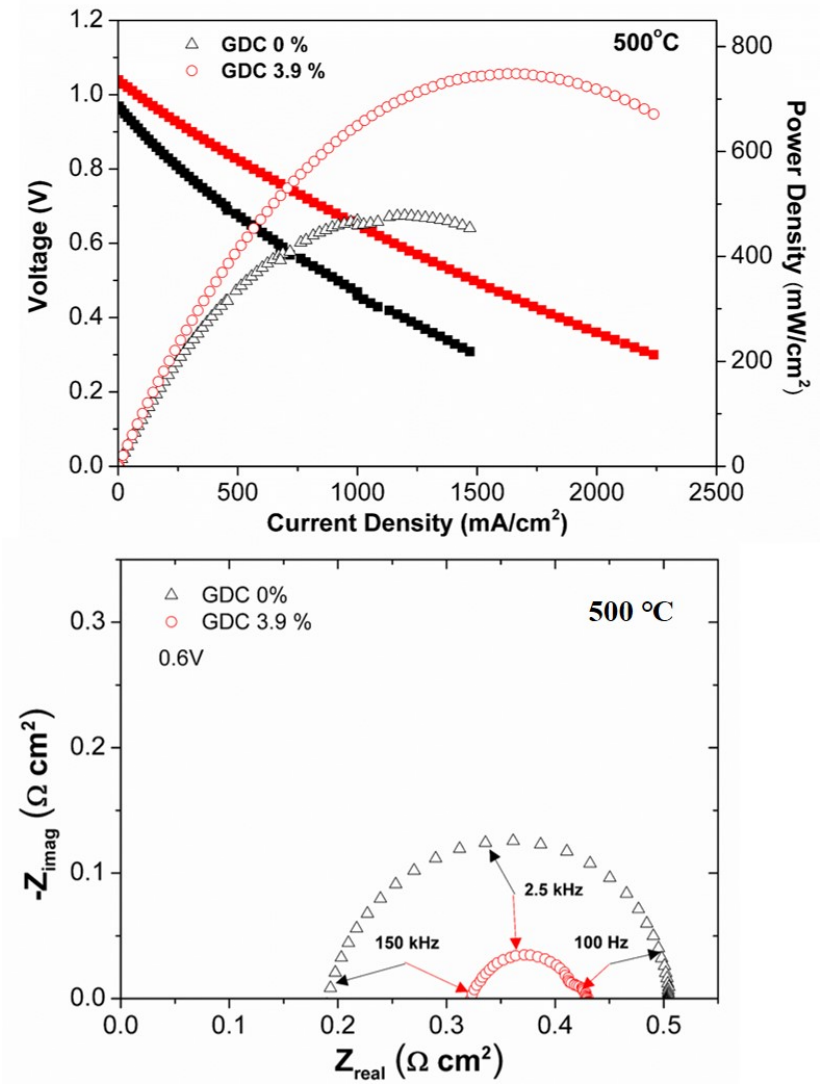

Figure 3.18 Performance comparison of Ni anode with Ni-GDC anode with low loading of GDC (3.9 vol%).

loading of GDC on Ni-GDC anode showed the maximum power density of 749 mW/cm^2 at 500℃. The contributions for the performance analyzed from EIS results indicated that ohmic resistance of the Ni-GDC 3.9vol% sample (0.32 $\Omega \cdot cm^2$) was higher than the pure Ni anode (0.2 $\Omega \cdot cm^2$). However, the increase rate was much intense at polarization resistance. The total area-specific resistance (ASR) of the Ni-GDC anode with 3.9 vol% showed only 0.43 $\Omega \cdot cm^2$ measured at 0.6V. To the best of our knowledge, this power density is the highest performance among AAO-based TF-SOFCs operated under 500℃.

3.4 Conclusion

Intensive research of the effect of the co-sputtering parameter on electrochemical performance of the nanoporous substrate supported TF-SOFCs has been presented for low-temperature. The anode nanostructure fabricated on the AAO was controlled by changing the various deposition parameters such as chamber pressure, deposition power, incident angle, and substrate rotation speed. Although the surface porosity and the thickness of the anode on AAO are known to be critical factors for determining the performance from the previous reports, it has never been confirmed in the co-sputtering system, and the more effective parameters are demonstrated from this chapter.

The early investigation on the effective porosity and the thickness of the co-sputtered anode are determined as 8 Pa and 800nm. Even though the porosity of the film can be more increased if the chamber pressure increase over 8 Pa, 8 Pa was

chosen for the all anode samples fabricated in this chapter because of the reasonable performance with this condition. The thickness of 800nm was optimum value for Ni-GDC co-sputtering anode. This value can be adjusted as the pore diameter of the substrate is changed. Over 800nm thickness of the anode, the polarization resistance was abruptly increased while the ohmic resistance was decreased, which means that the TPB density of the anode was decreased by the blockage of the gas diffusion path. Notable point found in this study is that the in-plane conductivity of the nanostructure deposited on the AAO has a considerable impact on the performance. Unlike the typical SOFCs structure, the electron conduction path in AAO supported anode is limited to the in-plane direction causing a large number of the deactivated zone and the significant ohmic resistance originated from the electron conduction. As the nano-column was controlled by rotation speed and incident angle of the co-sputtering, the peak power density and overall resistances were intensively decreased at low-temperature. The 45 degree of incident angle and 10.6 rpm of high-speed rotation for Ni-GDC co-sputtering presents the high performance in 450 and 500℃.

Finally, with the deposition conditions demonstrated for fabricating Ni-GDC anode, the composition of Ni-GDC anode beneficial for the performance has been presented for low-temperature operation. The excessive contents of GDC composite are negatively affecting in terms of ohmic resistance since the oxide materials could block the electron conduction path. Only 3.9 vol% of GDC in Ni-GDC anode showed the peak power density of 749 mW/cm^2 at 500℃, which is the highest performance among AAO supported TF-SOFCs with Ni-based anode at that temperature.

Chapter 4. Thermal Stability of Ni-GDC Anode deposited by Co-Sputtering

4.1 Introduction

The high surface energy of Ni causing the severe agglomeration at high temperature has always been issue on long term SOFC operation of Ni-based anode. In the literature, it has been reported that the grain size of the Ni and GDC changes the tendency of the agglomeration[88,89]. In addition, variation in GDC composite also greatly affects the structural change during the thermal annealing. From the previous chapter, the performance of Ni-GDC anode with high loading of GDC composite was lower than expectation. Except the in-plane conductivity, the thermal agglomeration effect could be another reason for the performance drop. Based on the knowledge of vulnerability of the nano-sized grain structure for the thermal agglomeration, it can be assumed that the thermal aggregate of Ni-GDC anode has impact on the electrochemical performance even at the very first measurement. To verify the thermal agglomeration tendency of nanostructured Ni-GDC deposited by co-sputtering, structural and operational characteristics were studied in this chapter.

Figure 4.1 Concept of agglomeration at nanostructured Ni-GDC anode.

4.2 Experimental

For various compositions of Ni-GDC anode on AAO substrate, Ni metal, and 20mol% GDC ceramic targets were used to deposit the film. Deposition power for Ni target was varied from 200 to 50W and the RF deposition power was controlled from 0 to 100W. The GDC composition variation was ranging from 0 to 51.3 vol%. Deposition pressure was kept in 8 Pa for fabricating all the samples. In addition, incident angle and rotation speed were sustained with 45 degrees and 10.6 rpm.

For full cell operation test, patterned YSZ electrolyte was deposited for 800nm, and the Pt-GDC cathode was fabricated on top of the electrolyte. Test for extended time operation was done by two kinds of operation. One was under constant voltage of 0.8, and the other one was OCV condition. The electrochemical performance and nanostructure was characterized by the same instruments used in the previous chapter.

The annealing temperature was set to 500℃. The atmosphere of the thermal annealing was sustained at reducing conditions by supplying the gas consisted of 80% hydrogen and 20% nitrogen.

4.2 Results and Discussion

The operational characteristic on extended time for TF-SOFCs varied with GDC composition on Ni-GDC anode was compared in figure 4.2. Samples were named with Ni volume fraction of Ni-GDC anode. The full cell was tested under 0.8V constant voltage at 500℃. The noticeable thing in this result was that the measured

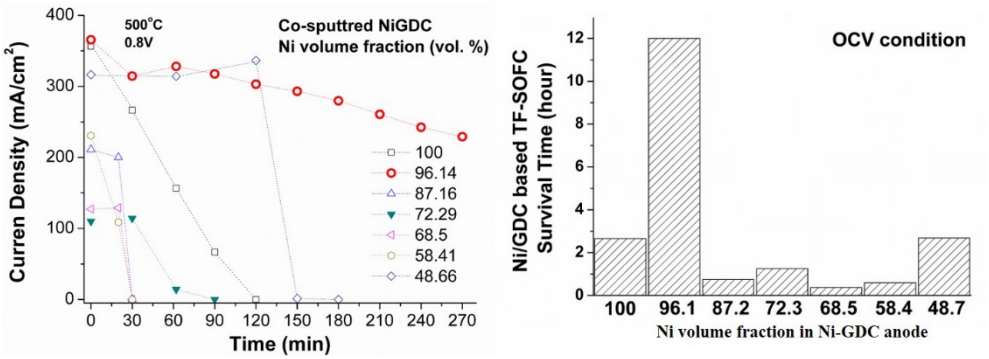

Figure 4.2 Operational characteristic of AAO supported TF-SOFCs with GDC composition variation of nanostructured Ni-GDC anode.

operation lifetimes of TF-SOFCs at constant voltage conditions were less than 180 minutes except for the Ni-GDC anode with 3.9 vol% of GDC (96.1 vol% of Ni). This trend is consistent with operation at OCV condition. Other than Ni-GDC with low contents of GDC, the lifetime was limited under 3 hours. To investigate the cause of the short cell stability of most of AAO supported TF-SOFCs with Ni-GDC anode, the structure change due to thermal annealing at reducing atmosphere was characterized with GDC composition variation. The degree of the agglomeration was intense at pure Ni anode considering the grain size growth. The grain size of as-deposited pure Ni anode was a few tens of nanometer. After annealing process, the grain size of agglomerated Ni anode measured from the high magnification of FESEM image was larger than 500nm, which means more than 20 times increase in grain size. Due to the severe agglomeration, AAO surface was exposed. Not only TPB loss in the anode-electrolyte interface, but also contact between the electrolyte and anode could be damaged. The severe structure change affected by thermal annealing was also observed for higher loading of GDC (over 12.8 vol %) at Ni-GDC anode. Although the agglomerated shape of the nanostructure was different, it can be speculated that Ni nano-sized grain wad diffused and agglomerated to form large grain structure.

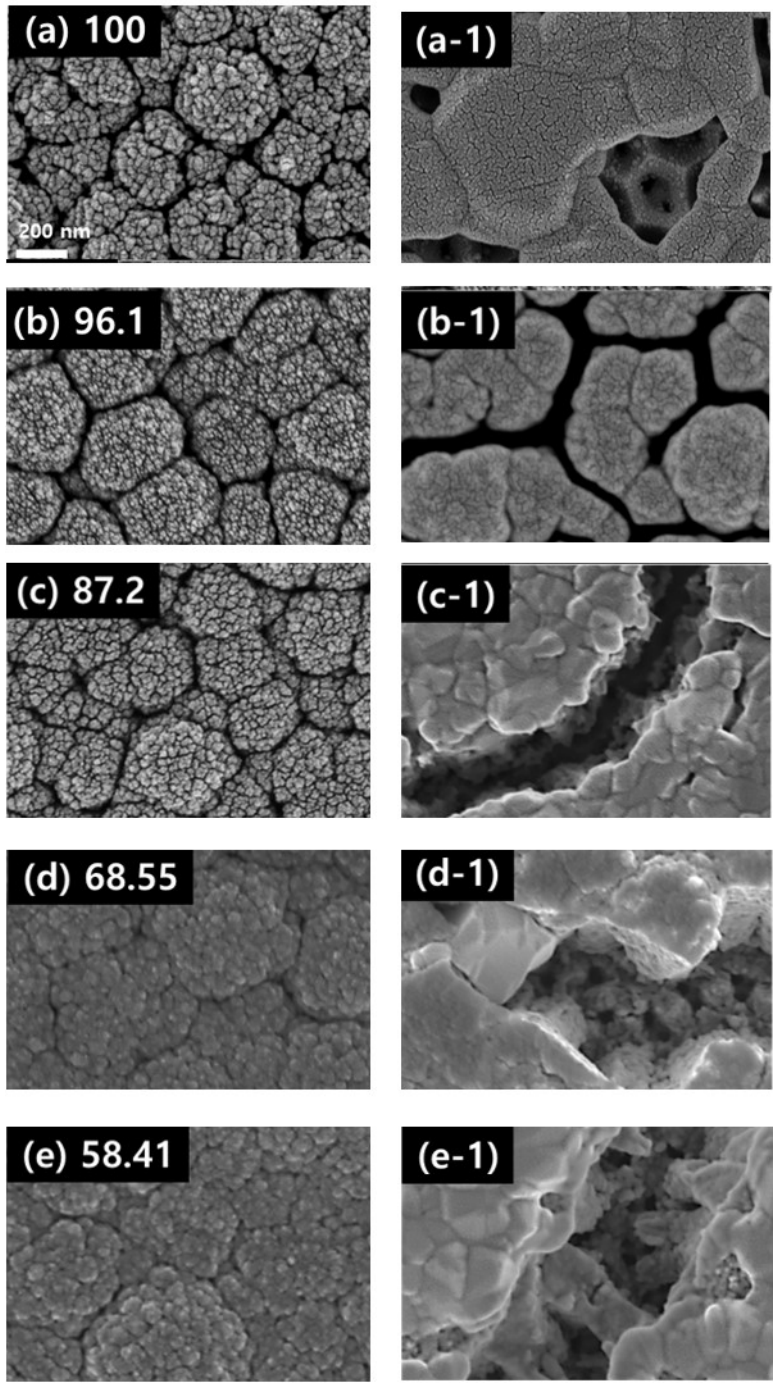

Figure 4.3 Thermal agglomeration of nanostructure depending on Ni volume fraction in Ni-GDC anode (a) 100, (b) 96.1, (c) 87.2, (d) 68.5, (e) 58.4. The samples were agglomerated at 500℃ for 3 hours at reducing atmosphere presented in (a-1), (b-1), (c-1), (d-1), and (e-1) (100sccm H2 through bubbler at room temperature).

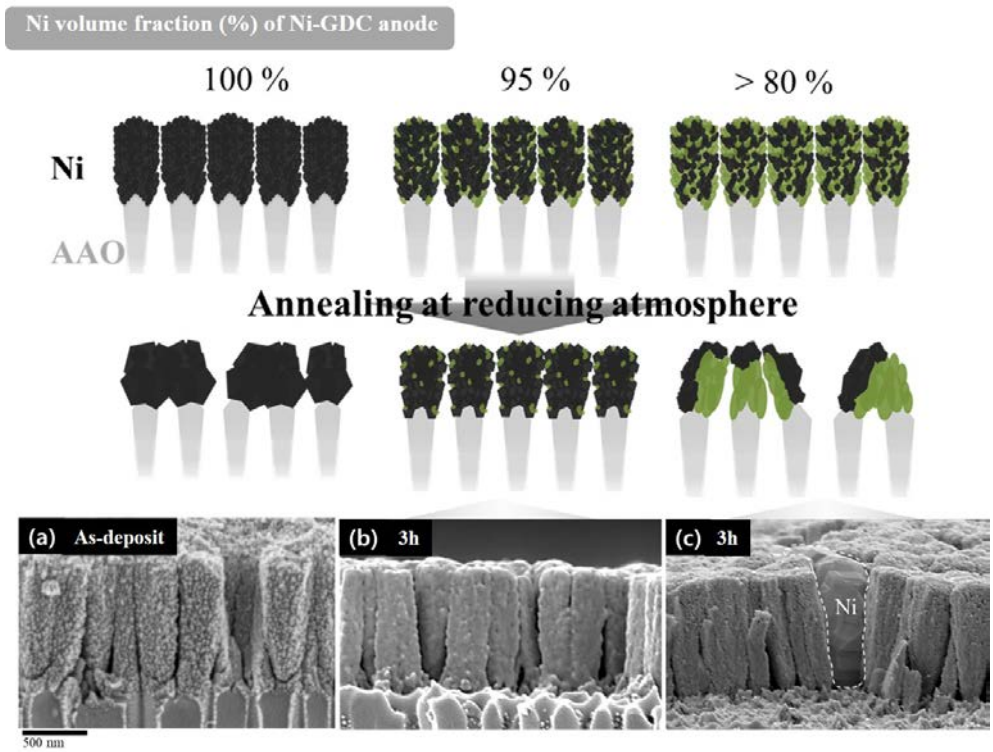

Figure 4.4 Schematic of agglomeration of Ni-GDC on AAO substrate depending on GDC composition. Side view of (a) as-deposit Ni-GDC anode, (b) Ni-GDC with 3.9 vol% of GDC annealed for 3 hours, and (c) Ni-GDC with high loading of GDC annealed for 3 hours. The white dot line is drawn to emphasize the agglomerated Ni grain.

The possibility of delamination at anode-electrolyte interface due to the agglomeration was examined by side view of the agglomerated Ni-GDC anode on AAO substrate. Compared to the as-deposit nanostructure of the Ni-GDC, the nanostructure change of the Ni-GDC with 3.9 vol% of GDC was negligible, only slightly agglomerated of the surface nano-grain. On the other hand, the Ni-GDC with high loading of GDC showed dramatic change in nanostructure. From the side view, it is clear that diffusion of Ni nano grain was the major mechanism for the Ni grain growth. Without the surface diffusion of Ni, the large grain formed inside of nanostructured Ni-GDC anode is impossible because the connection between Ni

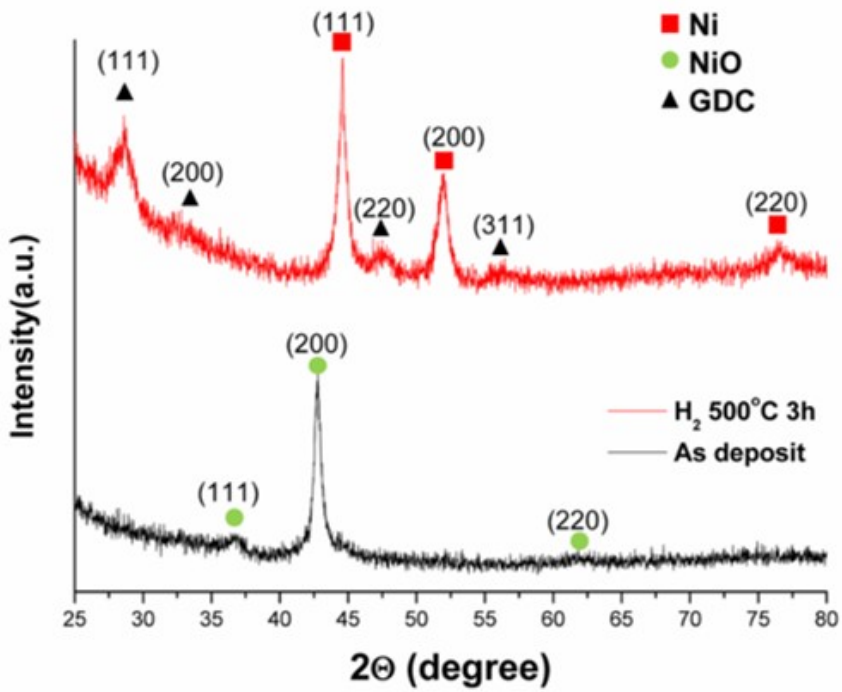

Figure 4.5 Crystallinity of as-deposit and annealed Ni-GDC anode measured by x-ray diffraction (XRD).

grains could be blocked by nanoscale GDC grains at a high level of GDC loading. Enhanced crystallinity of Ni and GDC phase was also consistent with the agglomeration tendency. Since the grain size and density of the structure affect the intensity measured from the XRD, severe agglomeration of Ni-GDC nanostructure was consistent with the change in chemical structure information.

4.4 Conclusion

The agglomeration tendency of Ni-GDC cermet anode fabricated by co-sputtering has been investigated for the different compositions of GDC in Ni-GDC anode. Pure Ni anode is already known to be vulnerable to the thermal agglomeration at 500℃. However, it is interesting that the high concentration of GDC (over 10 vol%) in nanostructured Ni-GDC on AAO support cause even more severe structural change possibly causing the cell failure. The small amount of GDC contents in Ni-GDC anode shows the least agglomerated structure attributed to the thermal protection from GDC nano-grains. The detailed mechanism for agglomeration of nanostructured Ni-GDC has not been demonstrated in this thesis. Nevertheless, it can be assumed from the nanostructure characterization that the high surface energy and diffusion rate of a few tens of nanometer grains could be the major reason for the Ni agglomeration. As confirmed from the side view of the agglomerated Ni-GDC layer, the large grain of Ni is formed in between GDC nano-column by Ni diffusion around GDC nanoparticle and sequentially combining with other Ni grains.

Chapter 5. Ni-GDC Anode for Direct Methane SOFCs

5.1 Introduction

In previous chapters, structural and compositional characteristics of Ni-GDC deposited by co-sputtering have been investigated in terms of electrochemical properties. Consequently, the record-high performance of nanostructured Ni-GDC anode based TF-SOFCs on AAO substrate was achieved due to the improved in-plane conductivity, TPBs density, and the enhanced thermal stability of the nanostructure. The direct utilization of the methane gas fuel could facilitate the commercialization of TF-SOFCs because of the reduced system size and the enhanced overall efficiency of the system[90–92]. Moreover, the existing infrastructure of supplying the natural composed of 90% methane can be beneficial for the practical use of TF-SOFCs as a portable energy source. Therefore, the development of direct methane TF-SOFCs is considered as one of the most imminent issues.

Ni-based anode is the most basic and common structure for reforming and electrochemically oxidizing methane fuel. As mentioned in chapter 1, the direct use of methane to the Ni-GDC anode has several issues. From the thermodynamic ternary diagram for C, H, and O, carbon deposition on the Ni catalyst likely happens at 500℃. On the long term operation with direct methane fuel, the SOFCs are failed due to severe carbon deposition deactivating the reaction sites on the anode. Furthermore, in operational perspective, the low steam to carbon ratio (S/C) is beneficial for the system efficiency due to the low dilution of the fuel[93]. However,

at low S/C ratio, the probability of carbon solid phase formation on metal catalysts is high in terms of thermodynamic point of view. Although the experimental study on direct internal steam reforming for Ni-GDC anode has been frequently demonstrated, the study on the direct use of methane to nanostructured Ni-GDC deposited by co-sputtering has been rarely reported. N. Laosiripojana and K.O. Christensen et al. reported that the nano-sized grain structure of Ni and ceria has resistance properties for carbon coking phenomenon[94,95]. From this literature information, it can be assumed that the co-sputtered Ni-GDC anode could show high catalytic performance for direct internal steam reforming due to the high surface area of the nanostructure even at low-temperature. Therefore, in this chapter, the electrochemical performance of the direct use of SOFCs with the co-sputtered Ni-GDC anode deposited on the scandia stabilized zirconia (ScSZ) pellet substrate was investigated at 500℃.

5.2 Experimental

The ScSZ electrolyte pellet with 150um thickness was used to support the nanostructured Ni-GDC anode for eliminating the possible leakage current through the electrolyte due to the low quality of the electrolyte. Ni-GDC anode deposited by co-sputtering was varied with deposition power. Resultantly, GDC composition of the anodes was controlled for 3.9, 12.8, 31.4, 48.2 volume percentage. The cathode deposition condition was set to be same as the previous experiments in chapter 4.

For the electrochemical measurement of the direct use of methane, methane was supplied to the cell through the bubbler filled with distilled water at room temperature. The methane gas supply was controlled for 50 sccm by mass flow meter

(MFC). For switching the methane fuel to hydrogen gas during the operation, two gas lines were set and controlled by manual valves. The cathode side was exposed to the ambient atmosphere.

The chemical composition before and after operation with a low S/C ratio of methane fuel was analyzed by x-ray photoelectron spectroscopy (XPS). The catalytic performance of nanostructured Ni-GDC anode for the reforming was characterized by measuring OCV of the cell with nearly dry methane.

5.3 Results and Discussion

One of the fundamental indicators of the electrochemical performance with direct methane fuel is the OCV of the cell. Especially, at low-temperature, the reforming kinetic is energetically not favored. Therefore, if the anode is not optimized at composition and structure, the OCV could not be formed with the direct methane fuel. Figure 5.1 shows the OCV of the anode with GDC 3.9 vol% was under 0.2 voltage, which means that the methane was not properly reformed or electrochemically oxidized. As the GDC composition increase in Ni-GDC anode, the OCV of the cell was starting to increase. Over 48.2 vol% of GDC composite in Ni-GDC anode, OCV was close to the theoretical value. This was also confirmed from the J-V-P curves of the cells. The peak power density of the Ni-GDC anode cell with 48.2 vol% showed higher performance compared to the cell with low loading of GDC composite. The major reason for the performance difference was attributed to OCV of the cells. On the other hand, it is noteworthy that current behavior was unstable in the high current region possible related to the reforming rate of the Ni-GDC.

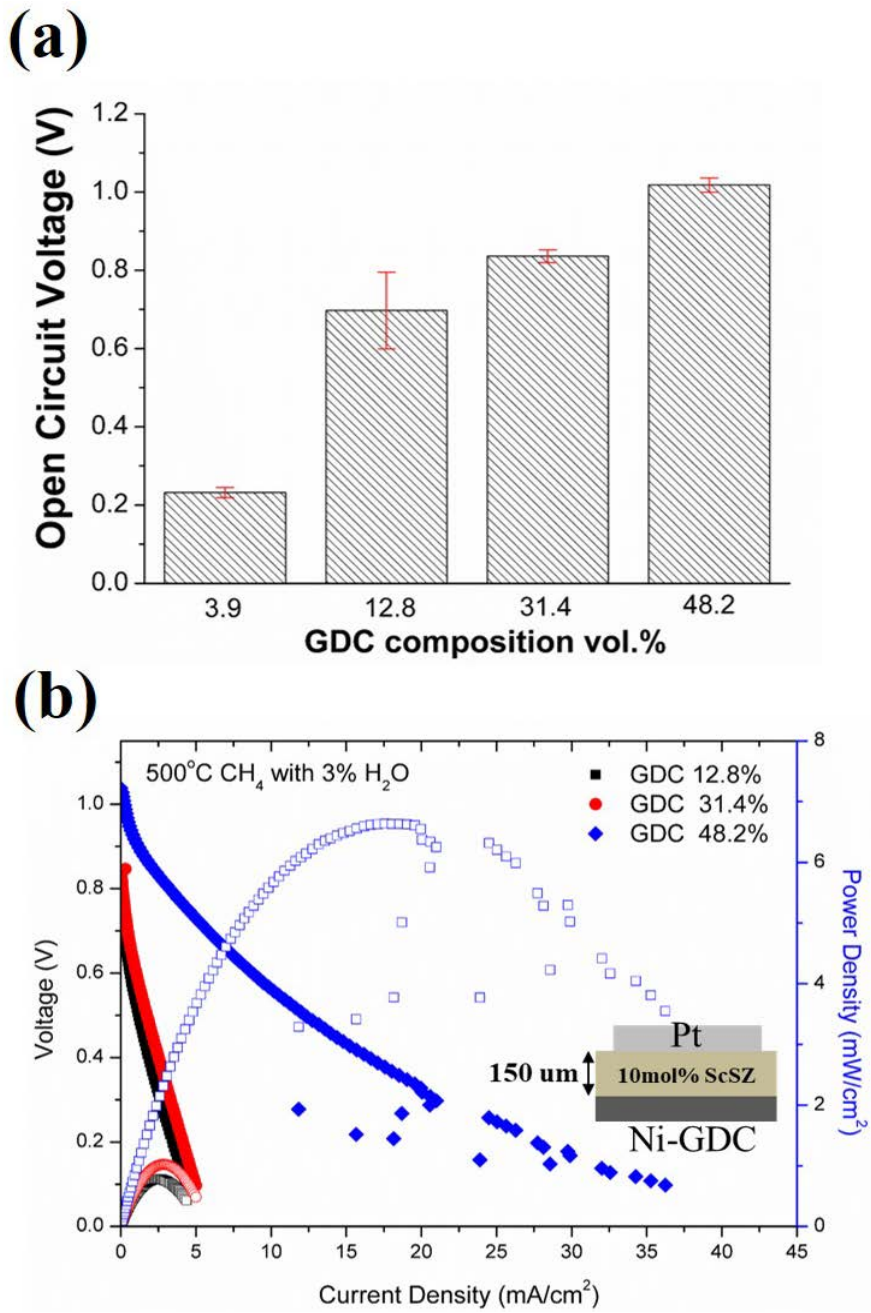

Figure 5.1 (a) Open circuit voltage (OCV) of the Ni-GDC anode on the ScSZ pellet operated with nearly dry methane (3 vol% H_2O). (b) JVP behavior of the Ni-GDC anode varied with 12.8, 31.4, and 48.2 volume percent at 500℃.

As the GDC contents of Ni-GDC anode increase, the TPB density of Ni-GDC anode is increased. This TPB could be acted as reforming sites due to the material characteristic of ceria for reforming. To further investigate the assumption about TPB density effect on reforming kinetic, two different anode structure with different grain size was tested with nearly dry methane at 500℃. The grain size of nanostructured Ni-GDC was less than 50 nm, while that of Ni-GDC fabricated by screen printing was more than 1um, which was more than 20 times larger. The OCV was measured for methane and hydrogen fuel. The results showed that OCV of the nanostructured Ni-GDC anode was over 0.8V with the methane fuel. However, the OCV of the anode fabricated by screen printing method indicated only about 0.2 V for the operation with the methane.

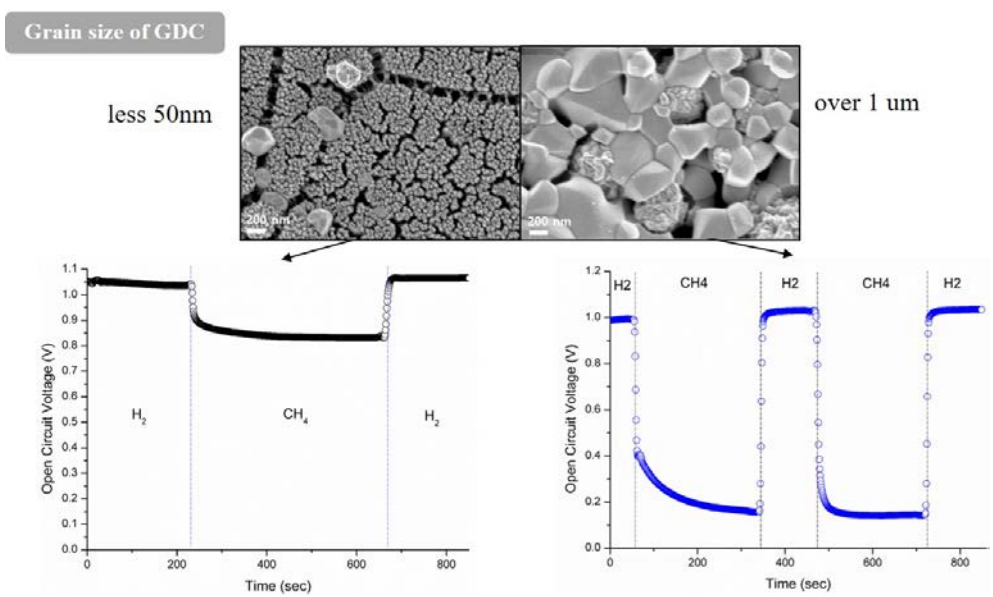

Figure 5.2 Grain size effect of Ni-GDC anode on open-circuit voltage (OCV) of SOFCs operated at 500℃.

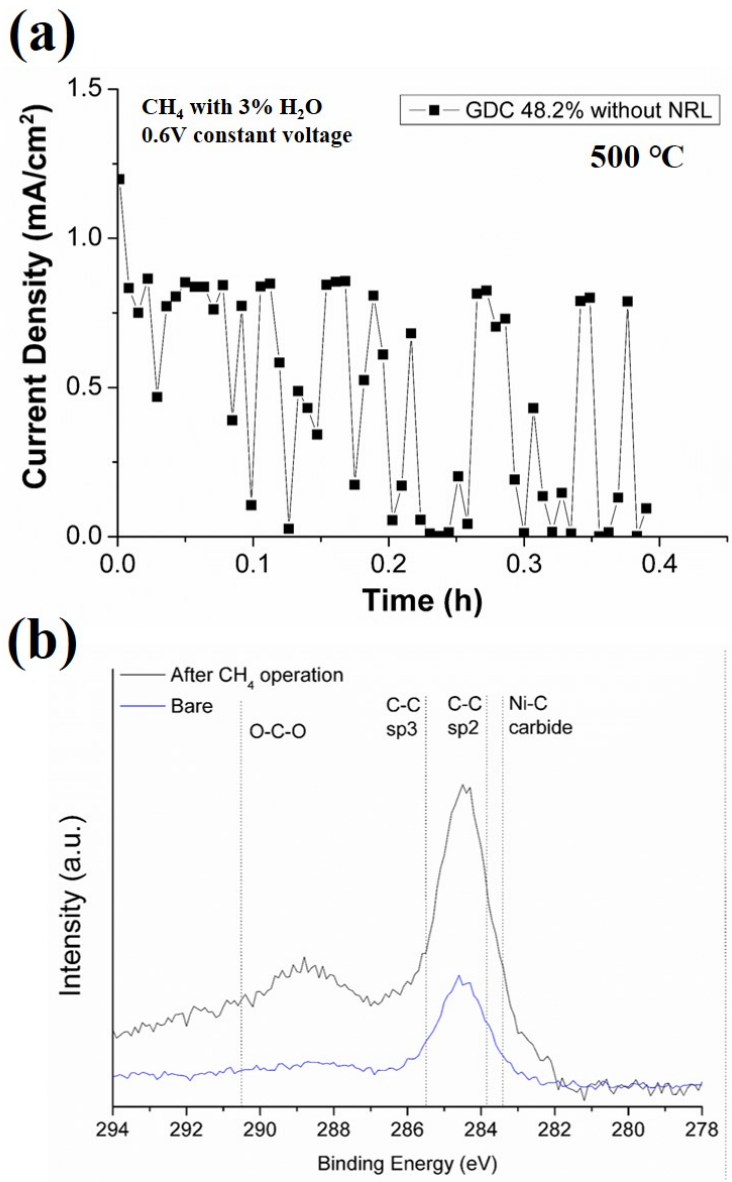

Figure 5.3 (a) Time-dependent characteristic of TF-SOFCs with Ni-GDC anode deposited by co-sputtering at 0.6V. (b) XPS analysis for co-sputtered Ni-GDC anode before and after the operation with CH_4.

Even though the nanostructured Ni-GDC with 48.2 vol% of GDC showed OCV and the performance, the lifetime of the cell was less than 30 minutes. The cause of this short life term was carbon deposition on the Ni metal catalyst of the anode. XPS results showed that Ni-C carbide and C-C binding were detected. Although the carbon was also detected for the bare Ni-GDC anode, the intensity related to the amount of carbon was much higher after methane operation. These results clearly indicated that the co-sputtered Ni-GDC anode was vulnerable to carbon deposition at a low S/C ratio and low-temperature[96]. For extending the operation time of nanostructured Ni-GDC anode, the additional reforming structure should be developed and fabricated on TF-SOFCs.

5.4 Conclusion

The compositional analysis for direct methane fueled TF-SOFCs with Ni-GDC anode is investigated in this chapter. Due to the nano-sized grain of Ni in co-sputtered Ni-GDC anode on ScSZ pellet, the reforming kinetic is greatly enhanced. This was comparatively shown with OCV data of the Ni-GDC fabricated by screen printing method. Even with the same composition of Ni-GDC, the Ni-GDC anode with large grain size (over 1um) showed no discernable OCV at 500℃ for a nearly dry methane fuel. In addition, the GDC volume fraction of co-sputtering Ni-GDC anode should be close to 50 % for producing reasonable OCV. However, the GDC contents of the highest performing Ni-GDC anode for TF-SOFCs was only 3.9 vol%. Therefore, to be operated with low S/C methane fuel, the additional reforming structure is required in TF-SOFCs architecture. The nanostructured reforming layer on TF-SOFCs could be fabricated by co-sputtering. The fabrication process for the reforming layer is investigated in the next chapter.

Chapter 6. Direct Methane Fueled Thin-film SOFCs operated at 500℃

6.1 Introduction

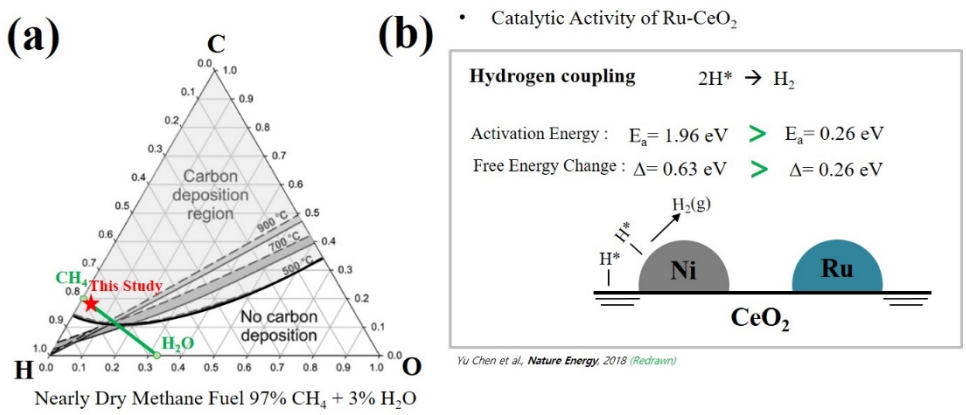

Figure 6.1 (a) Ternary diagram for C-H-O. The fuel composition for TF-SOFCs operation is 97% CH_4 and 3% H_2O. (b) Activation energy and free energy change of hydrogen coupling on Ni and Ru supported by ceria [77].

A low S/C ratio on methane fuel is vulnerable to carbon deposition on metal catalysts in thermodynamic point of view. However, if the metal nano-catalyst is supported with ceria-based materials, carbon species adsorbed on metal can be detached by reacting with lattice oxygen in the support. In addition, the rate of producing hydrogen, hydrogen coupling, depends on the activation energy and free energy change of hydrogen species. According to the report from Yu Chen et al., the hydrogen coupling reaction is thermodynamically and kinetically favored in Ru compared to Ni[77]. In material perspective, the mixture of Ru and ceria support is advantageous for direct methane operation, especially with a low S/C ratio.

Inspired by the recent work related to the thermal catalytic reforming performance of nano-catalyst on ceria support, it is assumed that the nanostructured Ru-GDC reforming layer deposited by co-sputtering could show high performance for methane reforming at low-temperature due to the nano-sized grain enabling the formation of high TPB density[97,98]. Uniformly mixed Ru-GDC reforming layer was fabricated on the bottom of AAO so that the reformed methane fuel could flow into the reaction sites of Ni-GDC anode. The fabrication of reforming layer on the bottom of the substrate is aligned with the state of the art design of the SOFCs structure for the direct methane operation. Even though AAO is electrically non-conductive, Ru-GDC is a thermal catalyst and electrically connected by Ag paste applied to the side.

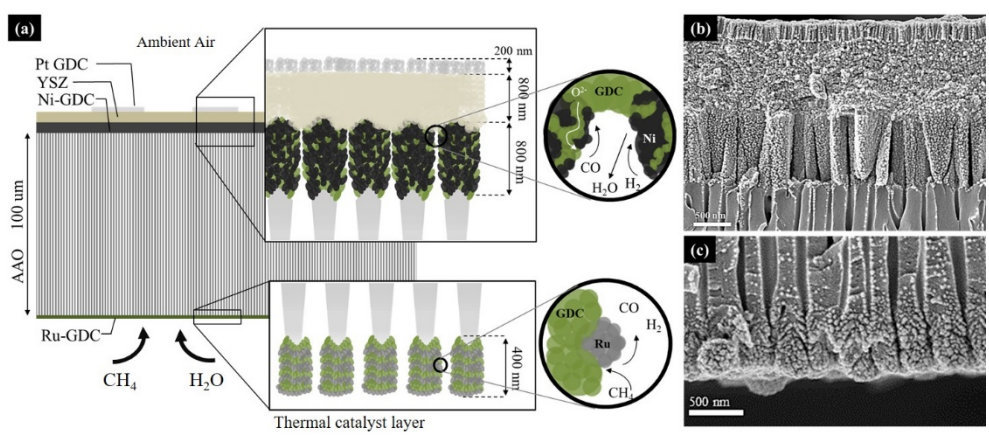

Figure 6.2 (a) Schematic of integrated TF-SOFC with nanostructured Ru-GDC layer. (b) Side view of nanostructured Ni-GDC/GDC/YSZ/Pt-GDC fabricated by magnetron sputtering. (c) 400 nm thickness of Ru-GDC reforming layer deposited by co-sputtering on the bottom of the AAO substrate.

6.2 Experimental

AAO supported TF-SOFCs was fabricated by sputtering. The nanostructure for electrochemical oxidation consisted of Ni-GDC/GDC/YSZ/Pt-GDC. GDC anode interlayer was deposited by ceramic target with O_2 reactive sputtering. For the reactive sputtering, the 80% Ar and 20% O_2 gas were supplied to the chamber to sustain 0.67 Pa. The thickness of GDC interlayer was controlled for 50nm. This role of GDC anode interlayer was inhibiting carbon deposition on Ni by increasing the composition of the GDC at the anode-electrolyte interface. Dense YSZ electrolyte was deposited at 800nm thickness. This thickness of the electrolyte is thicker than the previous research on AAO supported TF-SOFCs to ensure the gas leak from the anode side, which could cause OCV drop. The Ru-GDC reforming layer was deposited on the backside of the AAO. The composition of the Ru-GDC layer was controlled by sequential deposition method. Consequently, the Ru volume percent of Ru-GDC layer was varied by 1.3, 2.0, and 3.3 vol%. The samples with Ru-GDC reforming layer are denoted as RuGDC0.01 for 1.3 vol%, RuGDC0.02 for 2.0 vol%, and RuGDC0.03 for 3.3 vol%, hereafter.

The porosity of Ru-GDC nanostructure was calculated from the surface FESEM images by the image-j program. For the surface chemical analysis, XPS and Raman spectroscopy was used. Furthermore, to investigate the carbon deposition phenomenon for Ni-GDC anode with and without reforming layer, the fixed bed flow reactor was used.

6.3 Results and Discussion

The deposition of Ru-GDC on the AAO substrate was investigated by structural analysis. The side micrograph of Ru sputtering layer on AAO substrate was analyzed by FESEM. Reactive sputtering of Ru metal also showed the nano-column structure, which means that the fabrication of the co-sputtered Ru-GDC reforming layer could form high density of TPB. The crystallinity of Ru-GDC anode

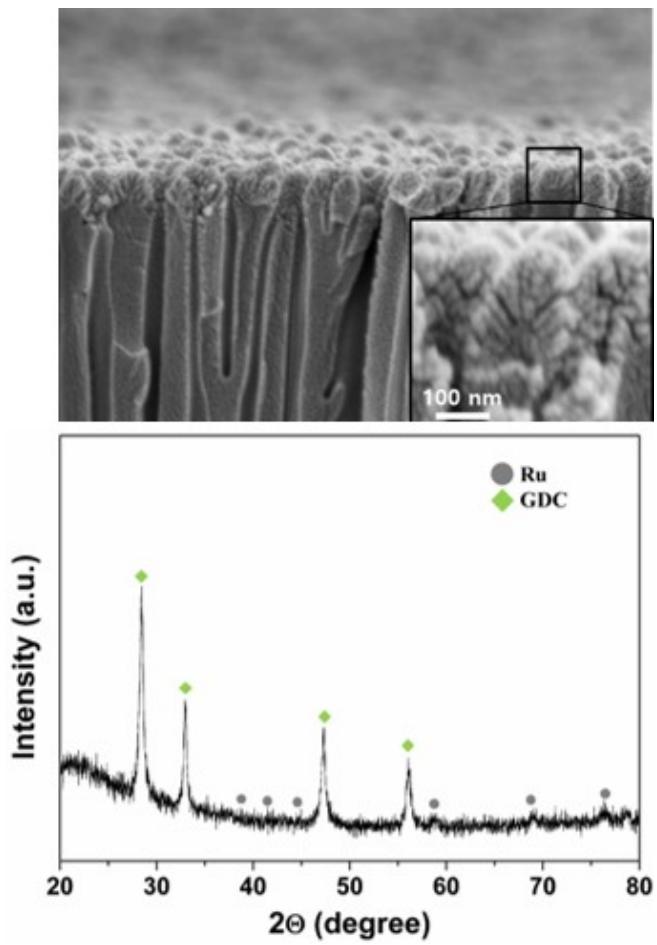

Figure 6.3 (Upper micrograph) Side view of Ru deposited by sputtering on the AAO substrate. (Bottom micrograph) XRD analysis of Ru-GDC fabricated by co-sputtering.

was investigated by XRD analysis. Due to the low contents of Ru, the crystalline peaks were barely detected. However, the peaks were clearly confirmed from the XRD. Since the intensity of the spectrum for the specific crystal structure is proportional to the amount of the structure included in the sample, the results indicate that the contents of the GDC is much more dominant than Ru. The compositional analysis was measured by XPS for the nanostructured Ru-GDC. The XPS spectrum in the range of 100 to 1000 eV shows the photoemission

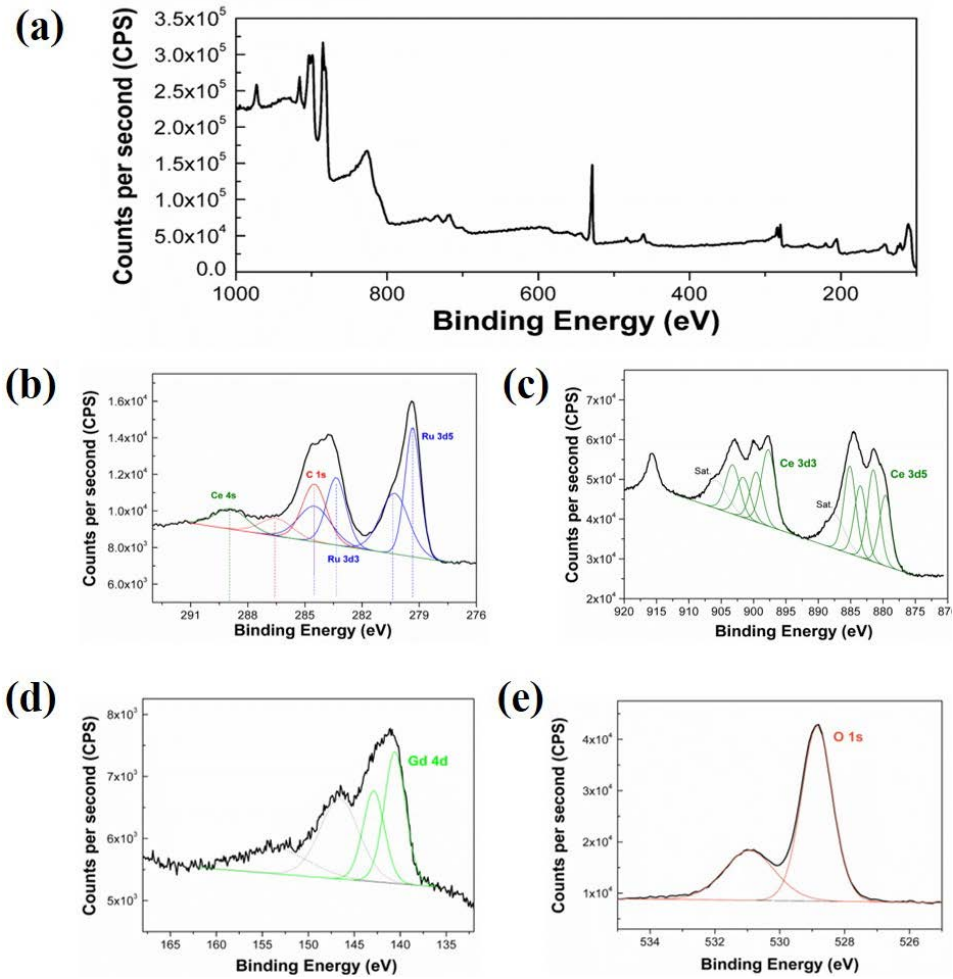

Figure 6.4 XPS analysis for the nanostructured Ru-GDC deposited on AAO substrate. (a) Scan of photoemission properties of Ru-GDC at 100-1000 eV range. (b) The Ru 3d (c) Ce 3d (d) Gd 4d (e) O 1s properties.

properties of Ru 3d, Gd 4d, Ce 3d, and O 1s presented in figure 6.4. The photoemission properties of Ru, Gd, Ce, and O are observed at 276-291eV, 135-166 eV, 870-915 eV, and 526-534 eV. In addition, the peaks measured from XPS analysis at 276-291 eV were deconvoluted into Ru 3d3, 5 and C 1s and Ce 4s. The carbon detected from the XPS results was possibly attributed to the contamination from the ambient air during sample storage. This detection of the contamination is due to the

surface-sensitive characteristic of XPS analysis with only 10nm infiltration of X-ray.

To investigate the compositional effect of the Ru-GDC reforming layer on electrochemical performance, the Ru-GDC layer was fabricated with three different compositions: GDC vol% 1.3, 2.0, and 3.3. In table 6.1, the specific atomic concentration and the volume ratio of Ru was demonstrated. The thickness of the Ru-GDC layer was maintained at 400nm for all samples. Even though Ru contents only changed from 1 to 3 percent, the surface structure could be changed due to the nanoscale thickness of the layer.

Sample	Atomic Conc. (at. %)				Volume Ratio	Volume fraction (vol. %)
	Ru	Gd	Ce	O	V_{Ru}/V_{GDC}	V_{Ru}/V_{Ru+GDC}
RuGDC0.01	2.03	1.07	17.81	58.95	0.013	**1.3**
RuGDC0.02	3.53	2.33	28.35	55.89	0.021	**2.0**
RuGDC0.03	6.16	1.66	35.5	50.81	0.035	**3.3**

Table 6.1 Specific atomic concentration of the nanostructured Ru-GDC reforming layer varied with Ru volume fraction.

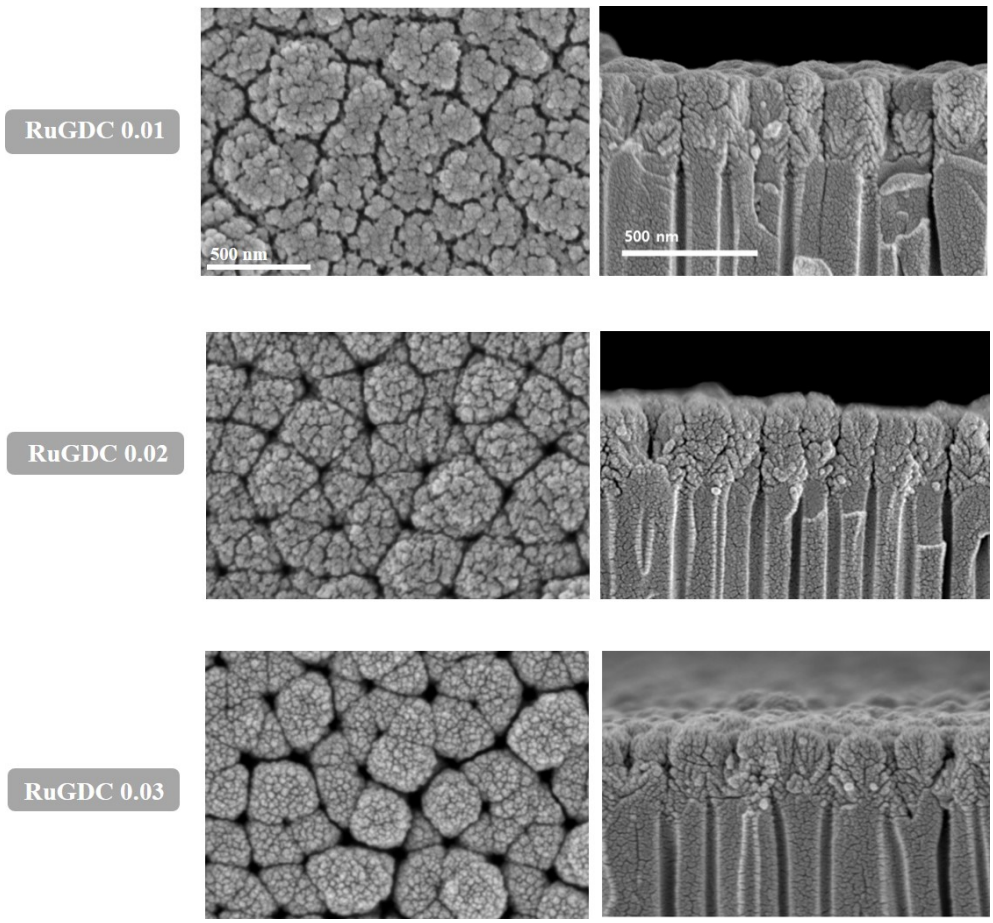

Figure 6.5 Surface and cross-sectional nanostructure of FESEM micrographs for Ru-GDC reforming layer varied with Ru volume fraction.

The surface nanostructure of the co-sputtered layer is sensitive to the growth characteristic of the materials. The high sputtering yield of Ru compared to GDC deposited by ceramic target could be the reason for the difference in the nanostructure even with the small change of the chemical composition. The detailed mechanism of the co-sputtering of Ru-GDC has not been studied. It will be further investigated in future work.

The surface porosity of the Ru-GDC layer was calculated from the FESEM images from figure 6.6. In this figure, the porosity of the RuGDC 0.01 was less than

10 %. As the Ru volume fraction was increased to 3.3%, the porosity of the RuGDC0.03 was also increased over 25%, which is more than twice compared to RuGDC0.01 sample. This structure change affected the OCV tendency of TF-SOFCs with reforming layer. The OCV was measured with nearly dry methane supply at 500℃ for the TF-SOFCs with different compositions of Ru-GDC reforming layer. The composition of Ni-GDC anode was determined as 3.9 vol%, which showed the highest performance compared to other compositions. Due to the low loading of GDC composite, the OCV of the bare TF-SOFCs was close to 0V. This result was consistent with the previous experimental result of chapter 5. As the Ru composition increase for the reforming layer, the OCV was starting to increase and reached to 1.02 V. Although some of the cells with RuGDC0.01 and 0.02 showed higher OCV over 0.8V, the fluctuation was too significant for the stable operation possibly due to unsteady reforming performance. One notable thing in the OCV data was RuGDC 1.6 sample. The high loading of Ru sample showed a little bit lower OCV of TF-SOFCs compared to the cell with RuGDC0.03. This result might indicate that the reforming kinetics are not totally depending on Ru contents. Only when Ru and GDC form a high density of TPB, the Ru-GDC layer could facilitate the high performance of methane reforming. This assumption is supported by the proposed mechanism of steam reforming at the Ru catalyst supported with oxide material[99]. There are several factors for determining the reforming performance. Among those, catalyst activity and resistance characteristics for carbon deposition are the major factors. The role of the catalyst is reducing the activation energy for chemical adsorption of the methane gas species on the metal surface. However, even with the high catalytic performance of the catalyst material, available surface for chemical adsorption could be blocked by the carbon species deposited on the surface. The oxide support is crucial for eliminating the carbon species on the catalyst. According to the proposed mechanism, lattice oxide in the support can react with the carbon species removed

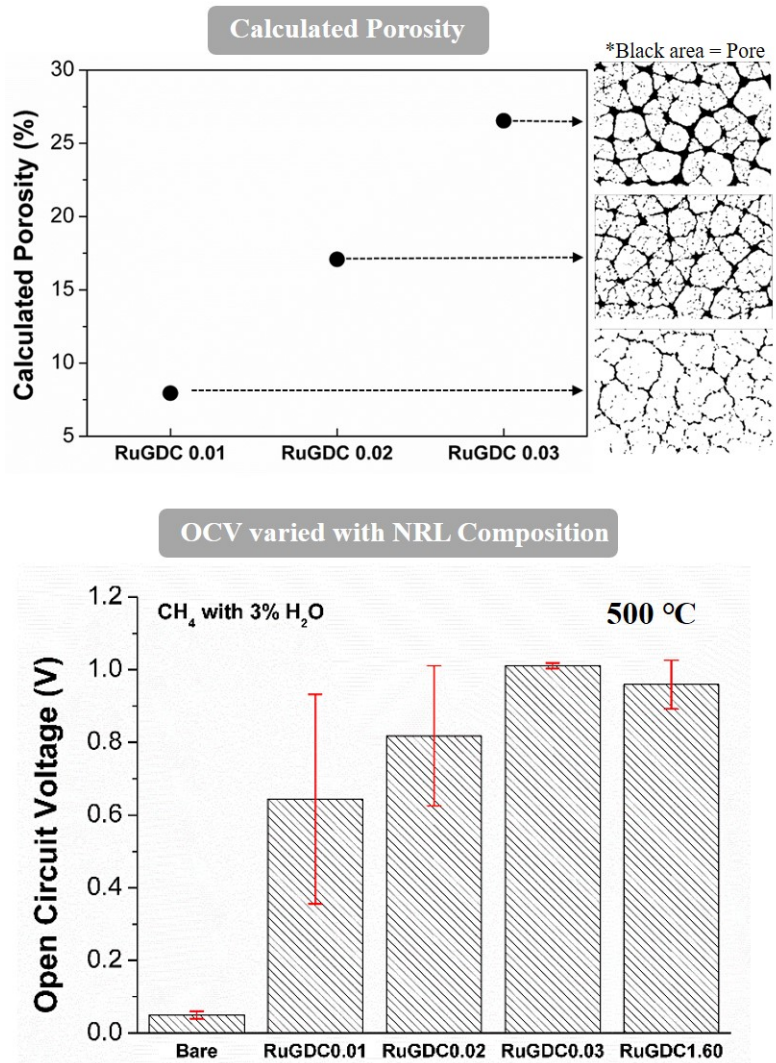

Figure 6.6 The surface porosity of the nanostructured Ru-GDC reforming layer on the AAO substrate. The OCV of TF-SOFC with bare and Ru-GDC reforming layer varied with Ru volume fraction.

by producing carbon monoxide and hydrogen gas. This possibility was also investigated by measuring J-V-P behaviors.

The OCV of TF-SOFC without the Ru-GDC reforming layer was close to zero. To confirm the results, the fuel was switched from hydrogen to methane while measuring the OCV of TF-SOFCs. This result was the same as the pellet based experiments. On the other hand, TF-SOFCs with RuGDC 0.03 samples showed high OCV. The Nernst equation for calculating the theoretical OCV for the temperature ranging from 200 to 700°C. The OCV of TF-SOFCs with RuGDC 0.03 sample was slightly lower than the oxidation of hydrogen and higher than direct oxidation of methane. The accuracy of OCV data of TF-SOFCs could be reduced by the experimental variable such as nanoscale pinhole in the electrolyte or leakage through the sealant, which affecting the OCV by following Nernst equation. Nevertheless, the OCV acquired from this experiment was stable for the extended time operation. Therefore, it is appropriate to assume the major fuel gas species for electrochemical oxidation at anode from the OCV data. Considering this assumption, the primary gas

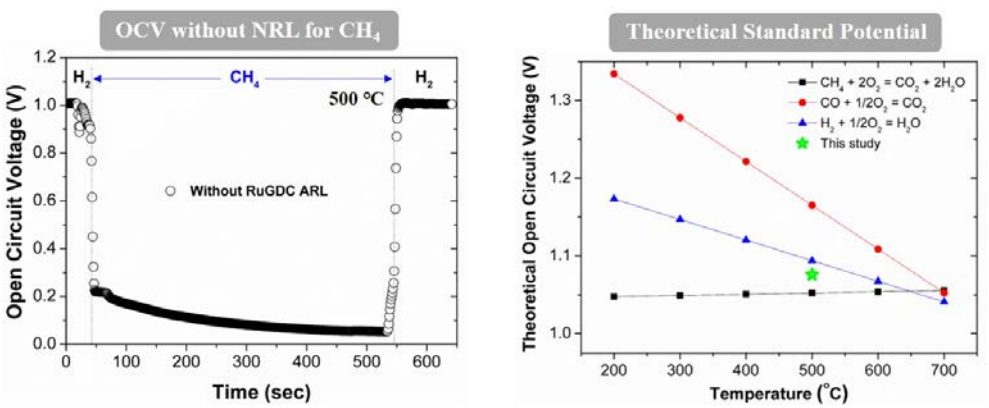

Figure 6.7 OCV without the nanostructure RuGDC reforming layer (NRL) with methane fuel supply. Theoretical standard potential for three electrochemical oxidations compared to OCV of RuGDC 0.03 sample.

component oxidized at the anode was hydrogen and partially methane. The specific gas component at the reaction sites of the anode side could not be realized from this analysis because of the complex reactions of methane and reformed gas oxidation. The reason why it is difficult to know the exact gas composition at the anode reaction sites is that the gas composition is continuously changed by chain reaction. Hydrogen oxidation produces the water vapor, and the water vapor could participate in water gas shift reaction and in reforming reaction because S/C ratio are locally changed at the reaction sites. As mentioned above, the reforming kinetic is enhanced at high level of S/C ratio.

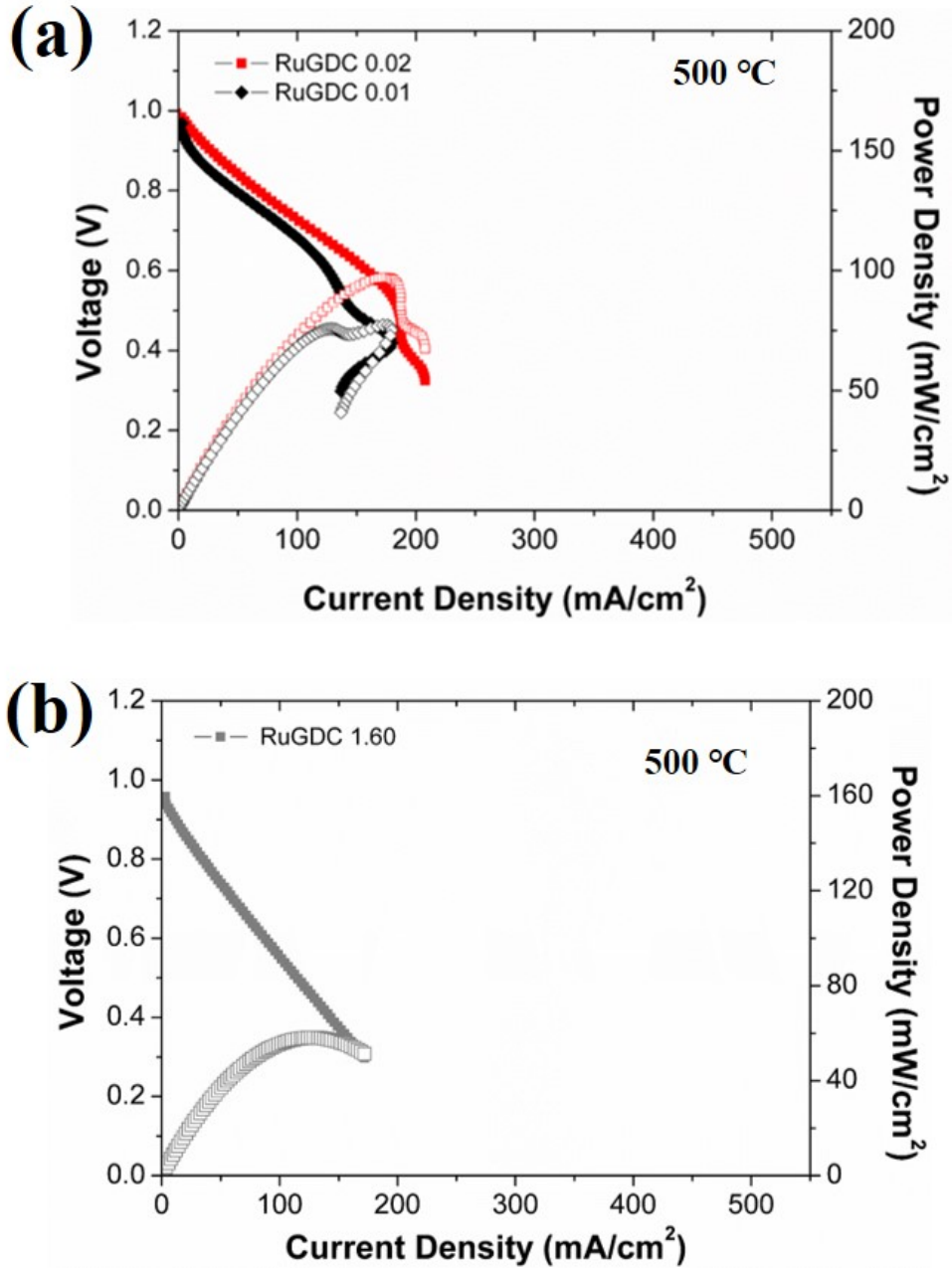

Figure 6.8 (a) JVP behaviors of TF-SOFCs with RuGDC 0.01 and 0.02 NRL samples. (b) JVP behavior of TF-SOFCs with RuGDC 1.60.

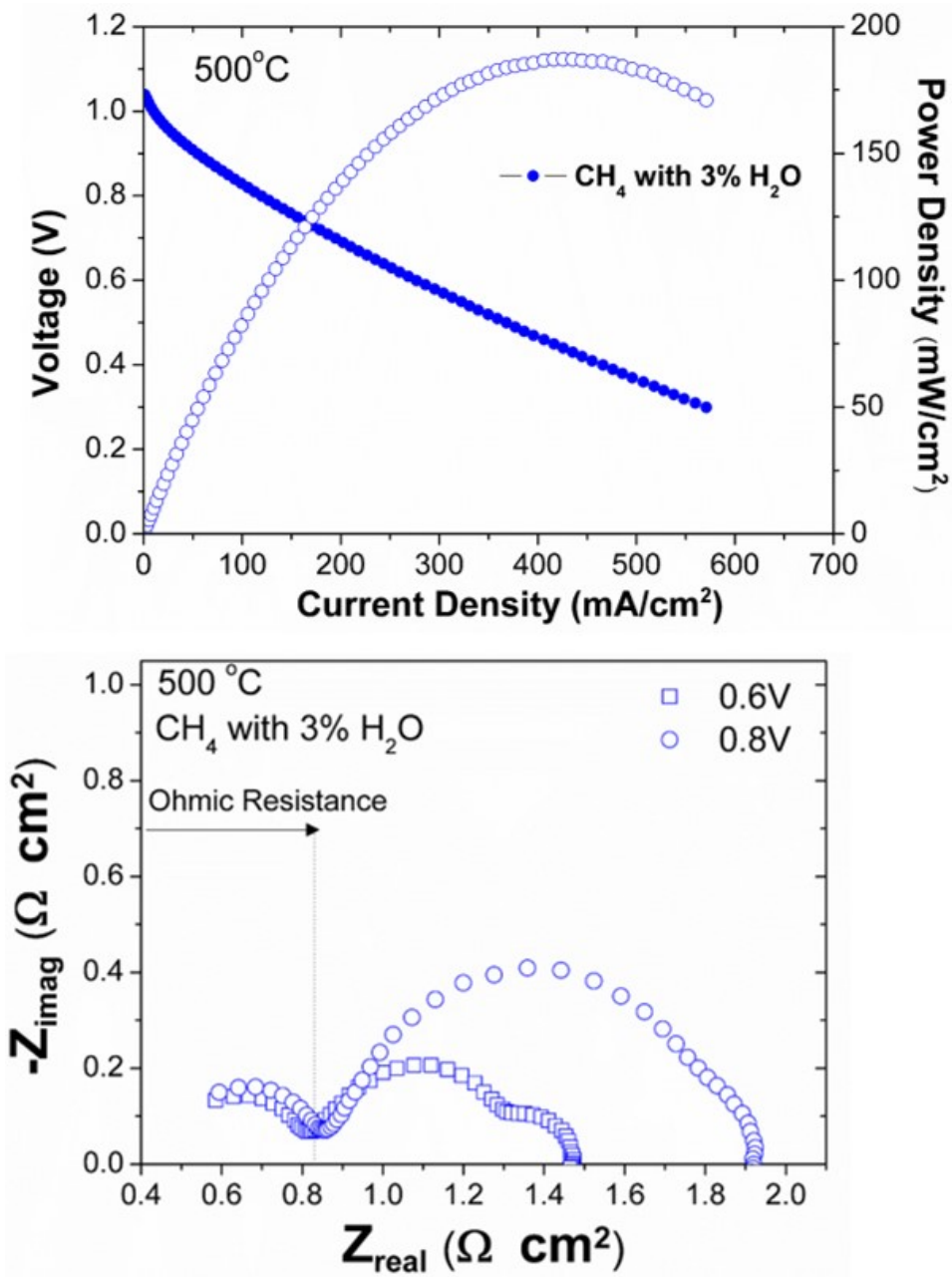

Figure 6.9 The J-V-P curve and the EIS analysis for TF-SOFCs with RuGDC 0.03 NRL measured at 500℃.

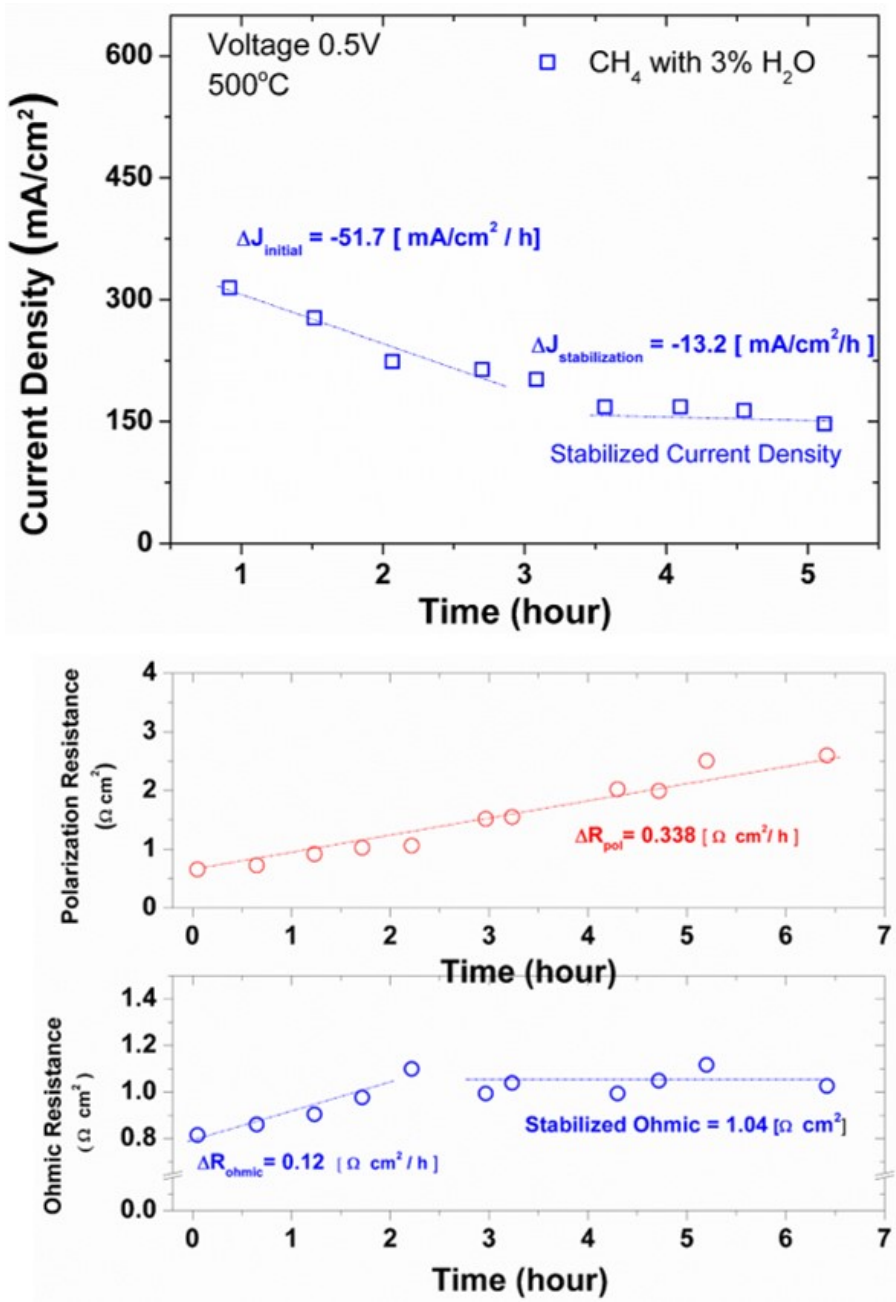

Figure 6.10 The points measurement of TF-SOFC with RuGDC 0.03 NRL for the extended time operation. Current density, polarization resistance, and ohmic resistance were measured during the operation.

The JVP behaviors of RuGDC 0.01, 0.02 and 1.6 samples were measured at 500℃. The current density was unstable at large over-potential region (lower than 0.5V of the cell potential) for both RuGDC 0.01 and 0.02 samples. From the curve shapes, it can be speculated that the hydrogen fuel was insufficient at the anode reaction sites resembling with the concentration loss behavior. Although CO and CH_4 existed at the reaction sites, which were available for oxidation, the electrochemical oxidation of those gas species was too slow to produce high current density. Further optimizing on Ru composition was required. The performance of TF-SOFCs with high loading of Ru was also investigated. The concentration loss or unstable performance was not observed for the samples. However, the peak power density of the cell was under 80 mW/cm^2. Even with the over 50 vol% of Ru contents, the performance was not dramatically improved. This result implies that Ru nanocatalyst itself was not the whole responsibility for the reforming kinetics. The nano-sized grain of Ru on GDC support could be the key factor for high performance for methane reforming. This assumption is consistent with the recent report about singly anchored metal atoms on the ceria support.

Based on the assumption, the performance of TF-SOFC with RuGDC0.03 should be more enhanced. The electrochemical performance of the cell was characterized by JVP behavior and EIS analysis. In figure 6.9, the performance of TF-SOFCs with RuGDC0.03 NRL clearly showed the enhanced power density. The peak power density was reached to the 187 mW/cm^2, which is the highest performance among AAO supported TF-SOFC operated under CH_4 at 500℃. From the EIS analysis, polarization resistance of the cell was much higher compared to the cell with hydrogen fuel. This result was reasonable considering the sluggish reaction of methane or carbon monoxide electrochemical oxidation. Another possible reason

for the considerable polarization resistance was the cell temperature reduction due to the endothermic reaction of methane steam reforming. This could also be the reason for increasing the ohmic resistance of the cell.

The key point of a direct methane operation is time-dependent performance characteristics due to the possibility of carbon formation at the anode reaction sites causing the severe performance degradation and even failure of the cell[100]. Therefore, the investigation of the time-dependent operation is essential in this thesis. Figure 6.10 depicted the current density, polarization, and ohmic resistances changed with the operation time. It was observed that the current density was severely degraded in the early stage of the cell performance at the rate of minus 51.7 mA/cm^2 per hour. After 3 hours operation, the degradation rate was decreased over 70 %. We believe that TF-SOFCs requires the time for the thermal stabilization of the nanostructure. As shown in chapter 4, the Ni-GDC anode showed an agglomerated structure even with the optimized GDC contents. The agglomeration of the anode nanostructure could attribute to the degradation, not only to the polarization but also to the ohmic resistance. By the change of the anode structure, the contact resistance at the anode-electrolyte interface should be affected. After 3 hours, the ohmic resistance was stabilized, unlike the polarization resistance. The steady rise of the polarization resistance could be attributed more to the Pt-based cathode. For further investigation, the constant voltage was applied for the TF-SOFCs with RuGDC 0.03 operated under nearly dry CH_4. The duration of the operation lasted more than 12 hours. Considering the operation time of Ni-GDC deposited on ScSZ pellet with CH_4 was shorter than an hour, this extended operation of AAO supported TF-SOFCs was greatly superior to the previous results. Besides, it has never been reported that the constant voltage measurement of AAO supported TF-SOFCs even with hydrogen fuel. This long operation was attainable due to the thermally enhanced

nanostructured Ni-GDC anode on nanoporous substrate. Nevertheless, the current density of the cell was degraded 4.6 % per hour at 0.8V. This degradation was attributed to the thermal agglomeration of the electrodes, but the cathode agglomeration should be more dominant for the long operation since the hydrogen oxidation is much faster than the oxygen reduction reaction. However, the possibility of the performance degradation by carbon formation on the reaction sites at the anode should be not be ignored since the carbon formation on Ni-GDC anode was confirmed in the previous chapter 5.

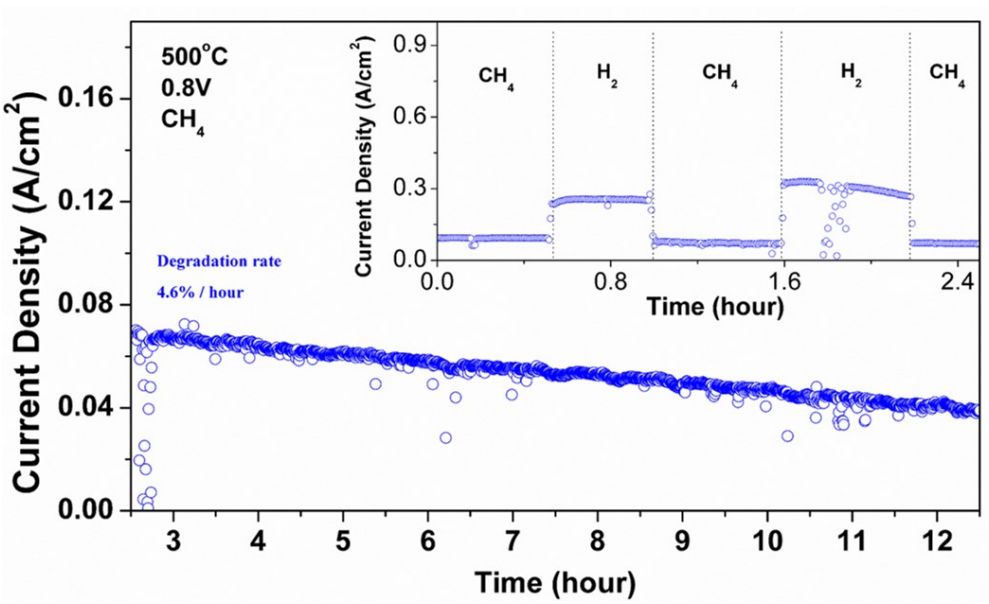

Figure 6.11 The constant voltage measurement of AAO supported TF-SOFC with RuGDC 0.03 operated under nearly dry methane.

To verify the possible carbon coking on the anode nanostructure, the fixed bed flow reactor was used for the nanostructured anode with and without NRL. The Ni-GDC with and without NRL was attached to the SUS jig. The methane passed through the water bubbler was supplied to the AAO substrate. The methane gas was first contacted with Ru-GDC NRL and passed through the nano-channel in the AAO substrate. Sequentially, the gas passed through the nanoporous structure of the Ni-GDC anode. The three kinds of samples were used in this test station: one was Ni-GDC on AAO with the NRL, and the other two were Ni-GDC on AAO without the NRL. After over 12 hours of the exposure, the Ni-GDC anode surfaces of the three samples were analyzed by Raman spectroscopy in the range of 1000 to 2000 cm^{-1} and FESEM.

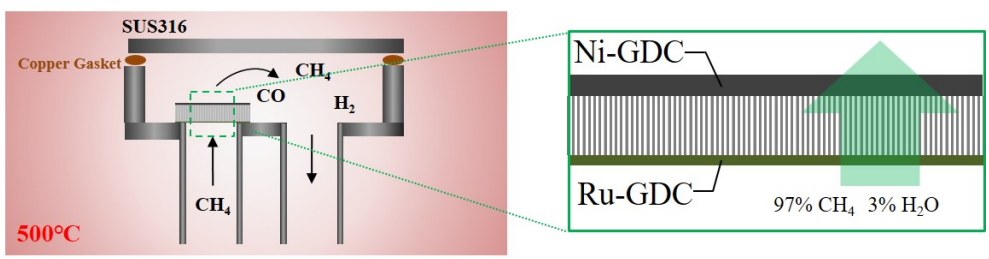

Figure 6.12 Fixed bed flow reactor with hydrogen and methane supply.

From the surface analysis for Ni-GDC with and without the NRL exposed to the CH_4 for more than 12 hours, it is clear that the surface of the Ni-GDC anode with NRL showed no sign of carbon formation. Meanwhile, the carbon nanotube was clearly observed from the high-resolution FESEM surface image. Even with longer exposure time, the sample with NRL showed high resistance characteristics to the carbon coking. To obtain the qualitative information of the surface chemical composition, Raman spectroscopy was applied for the three samples.

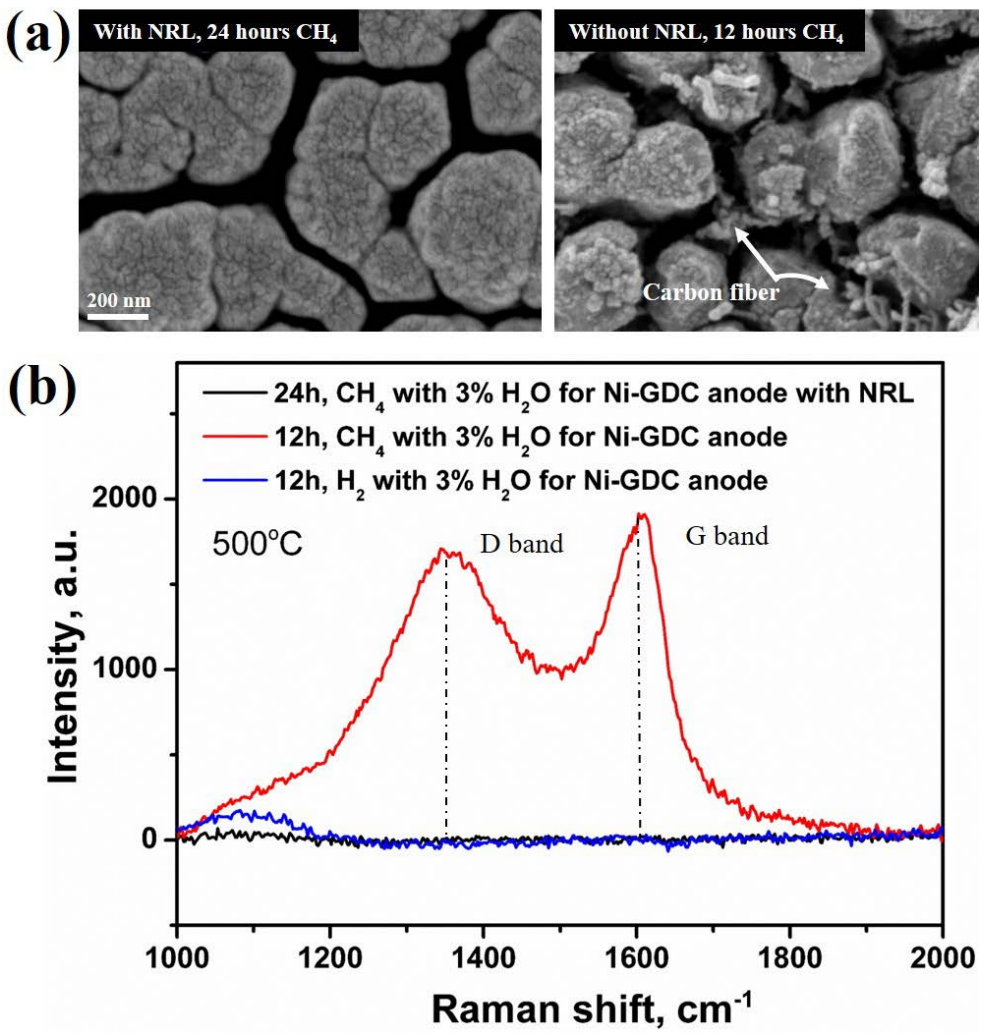

Figure 6.13 (a) Surface nanostructure comparison analyzed by FESEM of Ni-GDC anode exposed to CH_4 97% and H_2O 3% with and without NRL. (b) Raman spectroscopy analysis ranging from 1000 to 2000 cm^{-1} for the three different samples.

Raman spectroscopy results present that there is no signs of carbon for the Ni-GDC anode with NRL exposed to CH_4. It is noteworthy that the spectrum of Ni-GDC with NRL exposed to CH_4 was similar to that of Ni-GDC anode exposed to H_2 for 12 hours, which means both the no detectable carbon formed on the anode and the high reforming performance of the Ru-GDC NRL. On the other hand, in the region between 1500 and 1600 cm^{-1} (G band), in addition, 1320 and 1360 cm^{-1} (D band), the high intensity of the spectrum was detected. It is known that D and G band are indicating the existence of the amorphous carbon sp^2 on the sample surface[101,102]. Furthermore, since the intensity of the Raman spectrum is directly proportional to the concentration of the chemical species, the amount of the amorphous carbon on the surface of the Ni-GDC anode was particularly larger than the sample with NRL. Therefore, it can be concluded that the severe carbon deposition on the nanostructured Ni-GDC anode can be prevented by applying Ru-GDC NRL fabricated by co-sputtering.

6.4 Conclusion

The fabrication process for the nanostructured Ru-GDC layer and the thermal catalytic performance for the methane steam reforming have been demonstrated for low-temperature. The composition and the porosity of the Ru-GDC are realized as critical factors for the performance. The 3.3 vol% of Ru contents showed the OCV over 1V. Furthermore, the peak power density of TF-SOFCs with 3.3 vol% of Ru presented 187 mW/cm^2 at 500°C. The extended time operation of TF-SOFCs with

Ru-GDC reforming layer operated under nearly dry methane showed the degradation rate of 4.6 % per hour possible due to the degradation of Pt-based cathode. Even though the cell suffered from the degradation in the extended time, 12 hours of operation of TF-SOFCs with extremely low S/C methane fuel is the longest time reported in the literature about AAO supported TF-SOFCs.

Chapter 7. Achievements and Future Work

The electrochemical performances of Ni-GDC cermet anode fabricated by co-sputtering were investigated for low operating temperatures. Due to the unique character of the electronic conduction path for the anode, the in-plane conductivity of the Ni-GDC is considered as a critical factor for achieving high performance. The nano-column structure of Ni-GDC anode on AAO substrate has a significant impact on the in-plane conductivity. The nanostructure with the wide width of the nano-column has shown high in-plane conductivity resulting in the low ohmic and polarization resistances. By optimizing the Ni-GDC anode nanostructure, area-specific resistance (ASR) for the charge species conduction is reduced down to 0.3 $\Omega \cdot cm^2$ at 500℃. Furthermore, the effect of GDC volume fraction in Ni-GDC anode on the electrochemical performance was examined. The results indicated that the excessive nano-sized GDC composite in Ni-GDC anode could diminish the peak power density by reducing the in-plane conductivity with the oxide phase of GDC. Consequently, the peak power density of the nanostructured Ni-GDC anode based TF-SOFCs with a low volume fraction of GDC (below 5%) has reached to 749 mW/cm^2. To the best of our knowledge, this result is the highest performance among the AAO supported TF-SOFCs with Ni-based anode reported in the literature.

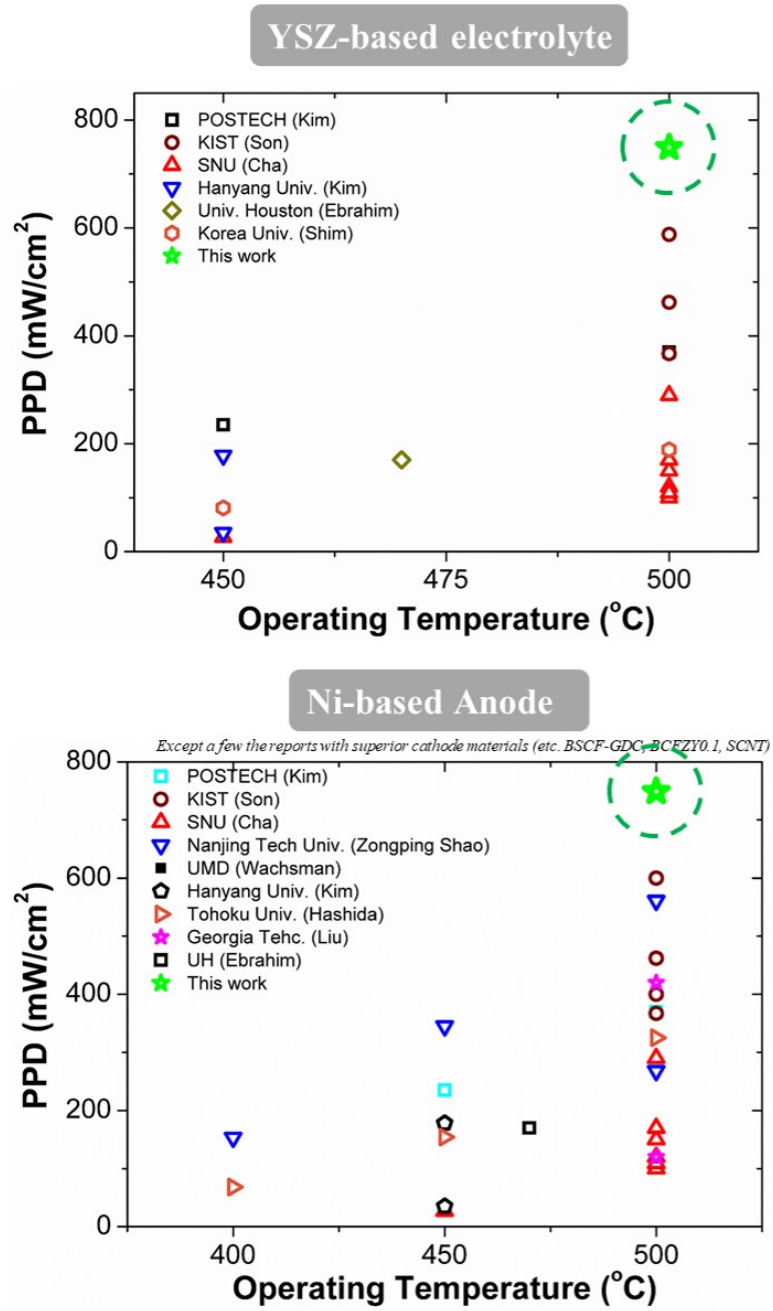

Figure 7.1 Literature data of the peak power density of SOFCs in the range between 400 to 500℃.

For a direct methane SOFCs with extremely low S/C ratio (about 0.03), the co-sputtering fabrication and electrochemical characterization of the nanostructured Ru-GDC reforming layer were investigated. The Ru volume fraction is optimized at 3 %. The nano-sized Ru grains dispersed in nano-grains GDC support is the major contributor to the high catalytic performance for the methane steam reforming at low-temperature. AAO supported TF-SOFCs with the nanostructured Ru-GDC layer has shown the successful operation with the reasonable OCV and high performance for nearly dry methane fuel. Furthermore, the extended time operation of the TF-SOFCs was demonstrated. Although the degradation rate of 4.6 % per hour was shown for the TF-SOFCs, the constant voltage measurement of TF-SOFC with methane fuel for 12 hours is demonstrated for the first time in this thesis.

In this thesis, co-sputtering Ni-GDC anode deposited at room temperature has been examined with the various deposition parameters, as well as with the thermal annealing process. However, the operation time and the degradation rate of TF-SOFCs still needs to be much more enhanced because the state of the art SOFCs usually shows more than 100 hours without the degradation. The experimental results obtained from this thesis give insight for designing the high performance of TF-SOFCs with co-sputtering system. Due to the nano-sized grain of the sputtered layer, the thermal agglomeration of Ni nanoparticles is inevitable at the operating temperature. Therefore, other than Ni-GDC anode with high connectivity, the functional layer of Ni-GDC with high resistance to thermal agglomeration is required. For thermally stable structure, Ni concentration should be limited down to 5%. The TPB density could be high enough to produce high performance even with the low

concentration of Ni because GDC has mixed ionic conductivity at reducing the environment. Further investigation on the nanostructured anode is necessary for the commercialization of TF-SOFCs for low-temperature. Furthermore, the cathode materials should be replaced with oxide based materials such as perovskite structure.

Author’s Related Publication

Nanostructured nickel anode for high performance low temperature solid oxide fuel cell, W. Yu, Y. Lim, S. Lee, A. P, G. Cho, and S.W. Cha, in preparation.

Thickness effect of co-sputtered Ni-GDC anode for anodic aluminum oxide supported low temperature solid oxide fuel cell, W. Yu, S. Lee, G. Cho, and S.W. Cha, in preparation.

Nanostructured Ru-GDC reforming layer for sputtered thin film solid oxide fuel cell with self-steaming mechanism at low temperature, W. Yu, S. Lee, M. Kishimoto, G. Cho, and S.W. Cha, in preparation.

Bibliography

[1] R.P. O'Hayre, S.-W. Cha, W. Colella, F.B. Prinz, Fuel cell fundamentals, John Wiley & Sons New York, 2006.

[2] O. Gröger, H.A. Gasteiger, J.-P. Suchsland, Review—Electromobility: Batteries or Fuel Cells?, J. Electrochem. Soc. 162 (2015) A2605–A2622. doi:10.1149/2.0211514jes.

[3] Z.P. Cano, D. Banham, S. Ye, A. Hintennach, J. Lu, M. Fowler, Z. Chen, Batteries and fuel cells for emerging electric vehicle markets, Nat. Energy. 3 (2018) 279–289. doi:10.1038/s41560-018-0108-1.

[4] T. Yoshida, K. Kojima, Toyota MIRAI fuel cell vehicle and progress toward a future hydrogen society, Electrochem. Soc. Interface. 24 (2015) 45–49. doi:10.1149/2.F03152if.

[5] R. Peters, L. Blum, R. Deja, I. Hoven, W. Tiedemann, S. Küpper, D. Stolten, Operation experience with a 20 kW SOFC system, in: Fuel Cells, John Wiley and Sons Ltd, 2014: pp. 489–499. doi:10.1002/fuce.201300184.

[6] X. Deng, A. Petric, Geometrical modeling of the triple-phase-boundary in solid oxide fuel cells, J. Power Sources. 140 (2005) 297–303. doi:10.1016/J.JPOWSOUR.2004.08.046.

[7] J. Abel, A.A. Kornyshev, W. Lehnert, Correlated resistor network study of porous solid oxide fuel cell anodes, J. Electrochem. Soc. 144 (1997) 4253–4259. doi:10.1149/1.1838174.

[8] R. O'Hayre, D.M. Barnett, F.B. Prinz, The triple phase boundary a mathematical model and experimental investigations for fuel cells, J. Electrochem. Soc. 152 (2005). doi:10.1149/1.1851054.

[9] E.D. Wachsman, K.T. Lee, Lowering the temperature of solid oxide fuel cells., Science. 334 (2011) 935–9. doi:10.1126/science.1204090.

[10] C. Xia, M. Liu, Novel Cathodes for Low-Temperature Solid Oxide Fuel

Cells, Adv. Mater. 14 (2002) 521–523. doi:10.1002/1521-4095(20020404)14:7<521::AID-ADMA521>3.0.CO;2-C.

[11] N.M. Sammes, K. Galloway, M.F. Serincan, T. Suzuki, T. Yamaguchi, M. Awano, W. Colella, Solid oxide fuel cells, in: Handb. Clim. Chang. Mitig., Springer US, 2012: pp. 1703–1727. doi:10.1007/978-1-4419-7991-9_44.

[12] W. He, J. Zou, B. Wang, S. Vilayurganapathy, M. Zhou, X. Lin, K.H.L. Zhang, J. Lin, P. Xu, J.H. Dickerson, Gas transport in porous electrodes of solid oxide fuel cells: A review on diffusion and diffusivity measurement, J. Power Sources. 237 (2013) 64–73. doi:10.1016/j.jpowsour.2013.02.089.

[13] A. Evans, A. Bieberle-Hütter, J.L.M. Rupp, L.J. Gauckler, Review on microfabricated micro-solid oxide fuel cell membranes, J. Power Sources. 194 (2009) 119–129. doi:10.1016/j.jpowsour.2009.03.048.

[14] J.H. Shim, C.-C. Chao, H. Huang, F.B. Prinz, Atomic Layer Deposition of Yttria-Stabilized Zirconia for Solid Oxide Fuel Cells, Chem. Mater. 19 (2007) 3850–3854. doi:10.1021/cm070913t.

[15] C.-C. Chao, C.-M. Hsu, Y. Cui, F.B. Prinz, Improved Solid Oxide Fuel Cell Performance with Nanostructured Electrolytes, ACS Nano. 5 (2011) 5692–5696. doi:10.1021/nn201354p.

[16] D. Beckel, A. Bieberle-Hütter, A. Harvey, A. Infortuna, U.P. Muecke, M. Prestat, J.L.M. Rupp, L.J. Gauckler, Thin films for micro solid oxide fuel cells, J. Power Sources. 173 (2007) 325–345. doi:10.1016/J.JPOWSOUR.2007.04.070.

[17] H.-S. Noh, K.J. Yoon, B.-K. Kim, H.-J. Je, H.-W. Lee, J.-H. Lee, J.-W. Son, Thermo-mechanical stability of multi-scale-architectured thin-film-based solid oxide fuel cells assessed by thermal cycling tests, J. Power Sources. 249 (2014) 125–130. doi:10.1016/J.JPOWSOUR.2013.10.101.

[18] K. Kerman, B.-K. Lai, S. Ramanathan, Pt/Y0.16Zr0.84O1.92/Pt thin film solid oxide fuel cells: Electrode microstructure and stability considerations, J. Power Sources. 196 (2011) 2608–2614.

doi:10.1016/j.jpowsour.2010.10.068.

[19] M. Tsuchiya, B.-K. Lai, S. Ramanathan, Scalable nanostructured membranes for solid-oxide fuel cells, Nat. Nanotechnol. 6 (2011) 282–286. doi:10.1038/nnano.2011.43.

[20] C.-W. Kwon, J.-I. Lee, K.-B. Kim, H.-W. Lee, J.-H. Lee, J.-W. Son, The thermomechanical stability of micro-solid oxide fuel cells fabricated on anodized aluminum oxide membranes, J. Power Sources. 210 (2012) 178–183. doi:10.1016/J.JPOWSOUR.2012.03.020.

[21] S. Hong, J. Bae, B. Koo, Y.-B. Kim, High-performance ultra-thin film solid oxide fuel cell using anodized-aluminum-oxide supporting structure, Electrochem. Commun. 47 (2014) 1–4. doi:10.1016/j.elecom.2014.07.008.

[22] S. Hong, Y. Lim, H. Yang, J. Bae, Y.-B. Kim, Single-chamber fabrication of high-performance low-temperature solid oxide fuel cells with grain-controlled functional layers, J. Mater. Chem. A. 5 (2017) 2029–2036. doi:10.1039/C6TA07237B.

[23] S. Hong, J. Son, Y. Lim, H. Yang, F.B. Prinz, Y.-B. Kim, A homogeneous grain-controlled ScSZ functional layer for high performance low-temperature solid oxide fuel cells, J. Mater. Chem. A. 6 (2018) 16506–16514. doi:10.1039/C8TA05157G.

[24] H.-S. Noh, K.J. Yoon, B.-K. Kim, H.-J. Je, H.-W. Lee, J.-H. Lee, J.-W. Son, Thermo-mechanical stability of multi-scale-architectured thin-film-based solid oxide fuel cells assessed by thermal cycling tests, J. Power Sources. 249 (2014) 125–130. doi:10.1016/J.JPOWSOUR.2013.10.101.

[25] W. Zhou, Z. Shao, R. Ran, W. Jin, N. Xu, A novel efficient oxide electrode for electrocatalytic oxygen reduction at 400–600 °C, Chem. Commun. 0 (2008) 5791. doi:10.1039/b813327a.

[26] E.-O. Oh, C.-M. Whang, Y.-R. Lee, S.-Y. Park, D.H. Prasad, K.J. Yoon, J.-W. Son, J.-H. Lee, H.-W. Lee, Extremely Thin Bilayer Electrolyte for Solid Oxide Fuel Cells (SOFCs) Fabricated by Chemical Solution Deposition

(CSD), Adv. Mater. 24 (2012) 3373–3377. doi:10.1002/adma.201200505.

[27] D.-H. Myung, J. Hwang, J. Hong, H.-W. Lee, B.-K. Kim, J.-H. Lee, J.-W. Son, Pulsed Laser Deposition of La0.6Sr0.4CoO3−δ-Ce0.9Gd0.1O2−δ Nano-Composite and Its Application to Gradient-Structured Thin-film Cathode of SOFC, J. Electrochem. Soc. 158 (2011) B1000. doi:10.1149/1.3599925.

[28] D. Kennouche, J. Hong, H.-S. Noh, J.-W. Son, S.A. Barnett, Three-dimensional microstructure of high-performance pulsed-laser deposited Ni–YSZ SOFC anodes, Phys. Chem. Chem. Phys. 16 (2014) 15249. doi:10.1039/c4cp02251c.

[29] J.-H. Park, W.-S. Hong, G.C. Kim, H.J. Chang, J.-H. Lee, K.J. Yoon, J.-W. Son, The Effect of Post-Annealing on the Properties of a Pulsed-Laser-Deposited $La_{0.6}Sr_{0.4}CoO_{3-\delta}$-$Ce_{0.9}Gd_{0.1}O_{2-\delta}$ Nano-Composite Cathode, J. Electrochem. Soc. 160 (2013) F1027–F1032. doi:10.1149/2.075309jes.

[30] P.-C. Su, C.-C. Chao, J.H. Shim, R. Fasching, F.B. Prinz, Solid Oxide Fuel Cell with Corrugated Thin Film Electrolyte, Nano Lett. 8 (2008) 2289–2292. doi:10.1021/nl800977z.

[31] S. (Rob) Hui, D. Yang, Z. Wang, S. Yick, C. Decès-Petit, W. Qu, A. Tuck, R. Maric, D. Ghosh, Metal-supported solid oxide fuel cell operated at 400–600°C, J. Power Sources. 167 (2007) 336–339. doi:10.1016/j.jpowsour.2007.02.070.

[32] X. Chen, N.J. Wu, L. Smith, A. Ignatiev, Thin-film heterostructure solid oxide fuel cells, Appl. Phys. Lett. 84 (2004) 2700–2702. doi:10.1063/1.1697623.

[33] P. Blennow, J. Hjelm, T. Klemensø, Å.H. Persson, S. Ramousse, M. Mogensen, Planar Metal-Supported SOFC with Novel Cermet Anode, Fuel Cells. 11 (2011) 661–668. doi:10.1002/fuce.201100029.

[34] K.J. Kim, B.H. Park, S.J. Kim, Y. Lee, H. Bae, G.M. Choi, Micro solid oxide fuel cell fabricated on porous stainless steel: a new strategy for

enhanced thermal cycling ability., Sci. Rep. 6 (2016) 22443. doi:10.1038/srep22443.

[35] J.H. Park, S.M. Han, K.J. Yoon, H. Kim, J. Hong, B.-K. Kim, J.-H. Lee, J.-W. Son, Impact of nanostructured anode on low-temperature performance of thin-film-based anode-supported solid oxide fuel cells, J. Power Sources. 315 (2016) 324–330. doi:10.1016/J.JPOWSOUR.2016.03.055.

[36] H.-S. Noh, K.J. Yoon, B.-K. Kim, H.-J. Je, H.-W. Lee, J.-H. Lee, J.-W. Son, Ultimate Performance of Anode-Supported SOFC by Realizing Thin-Film Electrolyte and Nano-Structure Electrode, ECS Trans. 57 (2013) 969–973. doi:10.1149/05701.0969ecst.

[37] J.H. Park, S.M. Han, B.-K. Kim, J.-H. Lee, K.J. Yoon, H. Kim, H.-I. Ji, J.-W. Son, Sintered powder-base cathode over vacuum-deposited thin-film electrolyte of low-temperature solid oxide fuel cell: Performance and stability, Electrochim. Acta. 296 (2019) 1055–1063. doi:10.1016/J.ELECTACTA.2018.11.018.

[38] S. Ji, Y.H. Lee, T. Park, G.Y. Cho, S. Noh, Y. Lee, M. Kim, S. Ha, J. An, S.W. Cha, Doped ceria anode interlayer for low-temperature solid oxide fuel cells with nanothin electrolyte, Thin Solid Films. 591 (2015) 250–254. doi:10.1016/J.TSF.2015.05.005.

[39] S. Kang, I. Chang, Y.-B. Kim, S.W. Cha, Influence of a platinum functional layer on a Ni-Ce0.9Gd0.1O1.95 anode for thin-film solid oxide fuel cells, J. Vac. Sci. Technol. A Vacuum, Surfaces, Film. 33 (2015) 05E120. doi:10.1116/1.4927160.

[40] S. Lee, G.Y. Cho, T. Park, Y.H. Lee, W. Yu, Y. Lee, I. Chang, S.W. Cha, A nanoporous substrate-based low temperature solid oxide fuel cell using a thin film Ni anode, Thin Solid Films. 666 (2018) 177–181. doi:10.1016/J.TSF.2018.09.039.

[41] Z. Fan, J. An, A. Iancu, F.B. Prinz, Thickness effects of yttria-doped ceria interlayers on solid oxide fuel cells, J. Power Sources. 218 (2012) 187–191.

doi:10.1016/j.jpowsour.2012.06.103.

[42] S. Noh, G.Y. Cho, Y.H. Lee, W. Yu, J. An, S.W. Cha, Performance Enhancement in Thin Film Solid Oxide Fuel Cells Using Metal-Mixed Ionic Electronic Conductors Bilayer Anode, Sci. Adv. Mater. 8 (2016) 11–16. doi:10.1166/sam.2016.2589.

[43] Y. Kim, S. Noh, G.Y. Cho, T. Park, Y.H. Lee, W. Yu, Y. Lee, W.H. Tanveer, S.W. Cha, Characterization of thin film solid oxide fuel cells with variations in the thickness of nickel oxide-gadolinia doped ceria anode, Int. J. Precis. Eng. Manuf. 17 (2016) 1079–1083. doi:10.1007/s12541-016-0131-8.

[44] Y. Lee, J. Park, W. Yu, W.H. Tanveer, Y.H. Lee, G.Y. Cho, T. Park, C. Zheng, W. Lee, S.W. Cha, Nickel-based bilayer thin-film anodes for low-temperature solid oxide fuel cells, Energy. 161 (2018) 1133–1138. doi:10.1016/J.ENERGY.2018.07.147.

[45] Y. Lim, H. Lee, S. Hong, Y.-B. Kim, Co-sputtered nanocomposite nickel cermet anode for high-performance low-temperature solid oxide fuel cells, J. Power Sources. 412 (2019) 160–169. doi:10.1016/J.JPOWSOUR.2018.11.025.

[46] Y. Lee, Y.M. Park, G.M. Choi, Micro-solid oxide fuel cell supported on a porous metallic Ni/stainless-steel bi-layer, J. Power Sources. 249 (2014) 79–83. doi:10.1016/J.JPOWSOUR.2013.10.082.

[47] D.Y. Jang, M. Kim, J.W. Kim, K. Bae, J. Son, M.V.F. Schlupp, J.H. Shim, High Performance Anode-Supported Solid Oxide Fuel Cells with Thin Film Yttria-Stabilized Zirconia Membrane Prepared by Aerosol-Assisted Chemical Vapor Deposition, J. Electrochem. Soc. 164 (2017) F484–F490. doi:10.1149/2.0181706jes.

[48] C. Ding, H. Lin, K. Sato, T. Hashida, A simple, rapid spray method for preparing anode-supported solid oxide fuel cells with GDC electrolyte thin films, J. Memb. Sci. 350 (2010) 1–4. doi:10.1016/J.MEMSCI.2009.12.013.

[49] R. Ebrahim, M. Yeleuov, A. Ignatiev, 3D Porous Nickel Anode for Low Temperature Thin Solid Oxide Fuel Cell Applications, Adv. Mater. Technol. 2 (2017) 1700098. doi:10.1002/admt.201700098.

[50] K.T. Lee, N.J. Vito, H.S. Yoon, E.D. Wachsman, Effect of Ni-Gd $_{0.1}$ Ce $_{0.9}$ O $_{1.95}$ Anode Functional Layer Composition on Performance of Lower Temperature SOFCs, J. Electrochem. Soc. 159 (2012) F187–F193. doi:10.1149/2.009207jes.

[51] S. Ji, I. Chang, Y.H. Lee, J. Park, J.Y. Paek, M.H. Lee, S.W. Cha, Fabrication of low-temperature solid oxide fuel cells with a nanothin protective layer by atomic layer deposition, Nanoscale Res. Lett. 8 (n.d.) 48. doi:10.1186/1556-276x-8-48.

[52] J. An, Y.-B. Kim, J. Park, T.M. Gür, F.B. Prinz, Three-Dimensional Nanostructured Bilayer Solid Oxide Fuel Cell with 1.3 W/cm ^{2} at 450 °C, Nano Lett. 13 (2013) 4551–4555. doi:10.1021/nl402661p.

[53] G.D. Han, K.C. Neoh, K. Bae, H.J. Choi, S.W. Park, J.-W. Son, J.H. Shim, Fabrication of lanthanum strontium cobalt ferrite (LSCF) cathodes for high performance solid oxide fuel cells using a low price commercial inkjet printer, J. Power Sources. 306 (2016) 503–509. doi:10.1016/J.JPOWSOUR.2015.12.067.

[54] Z. Zhan, D.M. Bierschenk, J.S. Cronin, S.A. Barnett, A reduced temperature solid oxide fuel cell with nanostructured anodes, Energy Environ. Sci. 4 (2011) 3951. doi:10.1039/c1ee01982a.

[55] Y. Chen, Y. Zhang, J. Baker, P. Majumdar, Z. Yang, M. Han, F. Chen, Hierarchically Oriented Macroporous Anode-Supported Solid Oxide Fuel Cell with Thin Ceria Electrolyte Film, (n.d.). doi:10.1021/am5003662.

[56] S. Ha, P.-C. Su, S.-W. Cha, Combinatorial deposition of a dense nano-thin film YSZ electrolyte for low temperature solid oxide fuel cells, J. Mater. Chem. A. 1 (2013) 9645. doi:10.1039/c3ta11758h.

[57] S. Ji, G.Y. Cho, W. Yu, P.-C. Su, M.H. Lee, S.W. Cha, Plasma-enhanced

atomic layer deposition of nanoscale yttria-stabilized zirconia electrolyte for solid oxide fuel cells with porous substrate., ACS Appl. Mater. Interfaces. 7 (2015) 2998–3002. doi:10.1021/am508710s.

[58] I. Chang, S. Ji, J. Park, M.H. Lee, S.W. Cha, Ultrathin YSZ Coating on Pt Cathode for High Thermal Stability and Enhanced Oxygen Reduction Reaction Activity, Adv. Energy Mater. 5 (2015) n/a-n/a. doi:10.1002/aenm.201402251.

[59] G.Y. Cho, Y.H. Lee, S.W. Hong, J. Bae, J. An, Y.B. Kim, S.W. Cha, High-performance thin film solid oxide fuel cells with scandia-stabilized zirconia (ScSZ) thin film electrolyte, Int. J. Hydrogen Energy. 40 (2015) 15704–15708. doi:10.1016/j.ijhydene.2015.09.124.

[60] J. Park, I. Chang, J.Y. Paek, S. Ji, W. Lee, S.W. Cha, J.-M. Lee, Fabrication of the large area thin-film solid oxide fuel cells, CIRP Ann. - Manuf. Technol. 63 (2014) 513–516. doi:10.1016/j.cirp.2014.03.065.

[61] T. Minami, Present status of transparent conducting oxide thin-film development for Indium-Tin-Oxide (ITO) substitutes, Thin Solid Films. 516 (2008) 5822–5828. doi:10.1016/j.tsf.2007.10.063.

[62] G. Bräuer, B. Szyszka, M. Vergöhl, R. Bandorf, Magnetron sputtering – Milestones of 30 years, Vacuum. 84 (2010) 1354–1359. doi:10.1016/J.VACUUM.2009.12.014.

[63] K. Wasa, I. Kanno, H. Kotera, Handbook of Sputter Deposition Technology: Fundamentals and Applications for Functional Thin Films, Nano-Materials and MEMS: Second Edition, Elsevier Inc., 2012. doi:10.1016/C2010-0-67037-4.

[64] P. Briois, F. Lapostolle, V. Demange, E. Djurado, A. Billard, Structural investigations of YSZ coatings prepared by DC magnetron sputtering, Surf. Coatings Technol. 201 (2007) 6012–6018. doi:10.1016/j.surfcoat.2006.11.016.

[65] E.M. Bringa, R.E. Johnson, Sputtering of nano-grains by energetic ions, in:

Nucl. Instruments Methods Phys. Res. Sect. B Beam Interact. with Mater. Atoms, 2002: pp. 365–370. doi:10.1016/S0168-583X(02)00806-6.

[66] J.D. Baek, Y.-J. Yoon, W. Lee, P.-C. Su, A circular membrane for nano thin film micro solid oxide fuel cells with enhanced mechanical stability, Energy Environ. Sci. 8 (2015) 3374–3380. doi:10.1039/C5EE02328A.

[67] J.D. Baek, K.Y. Liu, P.C. Su, A functional micro-solid oxide fuel cell with a 10 nm-thick freestanding electrolyte, J. Mater. Chem. A. 5 (2017) 18414–18419. doi:10.1039/c7ta05245f.

[68] W. Yu, G.Y. Cho, S. Hong, Y. Lee, PEALD YSZ-based bilayer electrolyte for thin film-solid oxide fuel cells, Nanotechnology. 27 (2016) 1–6. doi:10.1088/0957-4484/27/41/415402.

[69] W. Yu, S. Ji, G.Y. Cho, S. Noh, W.H. Tanveer, J. An, S.W. Cha, Atomic layer deposition of ultrathin blocking layer for low-temperature solid oxide fuel cell on nanoporous substrate, J. Vac. Sci. Technol. A Vacuum, Surfaces, Film. 33 (2015) 01A145. doi:10.1116/1.4904206.

[70] H.-S. Noh, J. Hong, H. Kim, K.J. Yoon, B.-K. Kim, H.-W. Lee, J.-H. Lee, J.-W. Son, Scale-Up of Thin-Film Deposition-Based Solid Oxide Fuel Cell by Sputtering, a Commercially Viable Thin-Film Technology, J. Electrochem. Soc. 163 (2016) F613–F617. doi:10.1149/2.0331607jes.

[71] H.-S. Noh, J.-W. Son, H. Lee, H.-S. Song, H.-W. Lee, J.-H. Lee, Low Temperature Performance Improvement of SOFC with Thin Film Electrolyte and Electrodes Fabricated by Pulsed Laser Deposition, J. Electrochem. Soc. 156 (2009) B1484. doi:10.1149/1.3243859.

[72] S. Park, J. Vohs, R. Gorte, Direct oxidation of hydrocarbons in a solid-oxide fuel cell, Nature. 404 (2000) 265–7. doi:10.1038/35005040.

[73] C. LU, Development of intermediate-temperature solid oxide fuel cells for direct utilization of hydrocarbon fuels, Solid State Ionics. 175 (2004) 47–50. doi:10.1016/j.ssi.2004.09.019.

[74] Z. Zhan, Y. Lin, M. Pillai, I. Kim, S.A. Barnett, High-rate electrochemical

partial oxidation of methane in solid oxide fuel cells, J. Power Sources. 161 (2006) 460–465. doi:10.1016/j.jpowsour.2006.04.139.

[75] E.W. Park, H. Moon, M. Park, S.H. Hyun, Fabrication and characterization of Cu–Ni–YSZ SOFC anodes for direct use of methane via Cu-electroplating, Int. J. Hydrogen Energy. 34 (2009) 5537–5545. doi:10.1016/j.ijhydene.2009.04.060.

[76] X.-M. Ge, S.-H. Chan, Q.-L. Liu, Q. Sun, Solid Oxide Fuel Cell Anode Materials for Direct Hydrocarbon Utilization, Adv. Energy Mater. 2 (2012) 1156–1181. doi:10.1002/aenm.201200342.

[77] Y. Chen, B. deGlee, Y. Tang, Z. Wang, B. Zhao, Y. Wei, L. Zhang, S. Yoo, K. Pei, J.H. Kim, Y. Ding, P. Hu, F.F. Tao, M. Liu, A robust fuel cell operated on nearly dry methane at 500 °C enabled by synergistic thermal catalysis and electrocatalysis, Nat. Energy. 3 (2018) 1042–1050. doi:10.1038/s41560-018-0262-5.

[78] M. Boder, R. Dittmeyer, Catalytic modification of conventional SOFC anodes with a view to reducing their activity for direct internal reforming of natural gas, J. Power Sources. 155 (2006) 13–22. doi:10.1016/j.jpowsour.2004.11.075.

[79] Y.W. Kang, J. Li, G.Y. Cao, H.Y. Tu, J. Li, J. Yang, A reduced 1D dynamic model of a planar direct internal reforming solid oxide fuel cell for system research, J. Power Sources. 188 (2009) 170–176. doi:10.1016/j.jpowsour.2008.11.073.

[80] Z. Shao, S.M. Haile, J. Ahn, P.D. Ronney, Z. Zhan, S. a Barnett, A thermally self-sustained micro solid-oxide fuel-cell stack with high power density., Nature. 435 (2005) 795–798. doi:10.1038/nature03673.

[81] K. Sasaki, Y. Teraoka, Equilibria in Fuel Cell Gases, J. Electrochem. Soc. 150 (2003) A885. doi:10.1149/1.1577338.

[82] S. Oh, J. Park, J.W. Shin, B.C. Yang, J. Zhang, D.Y. Jang, J. An, High performance low-temperature solid oxide fuel cells with atomic layer

deposited-yttria stabilized zirconia embedded thin film electrolyte, J. Mater. Chem. A. 6 (2018) 7401–7408. doi:10.1039/C7TA10678E.

[83] W. Yu, Y. Lee, A. Pandiyan, S. Ji, W.H. Tanveer, S.W. Cha, Enhanced Thermal Stability of Ultrathin Nanostructured Pt cathode by PdO: In Situ Nanodecoration for Low-Temperature Solid Oxide Fuel Cell, ACS Appl. Energy Mater. (2018) acsaem.8b01450. doi:10.1021/acsaem.8b01450.

[84] D. Hegemann, M.M. Hossain, D.J. Balazs, Nanostructured plasma coatings to obtain multifunctional textile surfaces, Prog. Org. Coatings. 58 (2007) 237–240. doi:10.1016/J.PORGCOAT.2006.08.027.

[85] H.-S. Noh, K.J. Yoon, B.-K. Kim, H.-J. Je, H.-W. Lee, J.-H. Lee, J.-W. Son, The potential and challenges of thin-film electrolyte and nanostructured electrode for yttria-stabilized zirconia-base anode-supported solid oxide fuel cells, J. Power Sources. 247 (2014) 105–111. doi:10.1016/j.jpowsour.2013.08.072.

[86] J. Park, Y. Lee, I. Chang, W. Lee, S.W. Cha, Engineering of the electrode structure of thin film solid oxide fuel cells, Thin Solid Films. 584 (2015) 125–129. doi:10.1016/J.TSF.2014.11.018.

[87] J.R.M. (Editor) Evgenij Barsoukov (Editor), Impedance Spectroscopy: Theory, Experiment, and Applications, 2nd Edition - Evgenij Barsoukov, J. Ross Macdonald, 2005. http://eu.wiley.com/WileyCDA/WileyTitle/productCd-0471647497.html (accessed October 18, 2019).

[88] S. Ahn, H. Koo, S.-H. Bae, C. Park, G. Cho, I. Chang, S.-W. Cha, Y.-S. Yoo, Effect of Nickel Contents on the Microstructure of Mesoporous Nickel Oxide/Gadolinium-Doped Ceria, Funct. Mater. Lett. 06 (2013) 1350055. doi:10.1142/S1793604713500550.

[89] U.P. Muecke, S. Graf, U. Rhyner, L.J. Gauckler, Microstructure and electrical conductivity of nanocrystalline nickel- and nickel oxide/gadolinia-doped ceria thin films, Acta Mater. 56 (2008) 677–687.

doi:10.1016/J.ACTAMAT.2007.09.023.

[90] H. He, J.M. Vohs, R.J. Gorte, Carbonaceous deposits in direct utilization hydrocarbon SOFC anode, J. Power Sources. 144 (2005) 135–140. doi:10.1016/j.jpowsour.2004.12.029.

[91] H. Kim, S. Park, J.M. Vohs, R.J. Gorte, Direct Oxidation of Liquid Fuels in a Solid Oxide Fuel Cell, J. Electrochem. Soc. 148 (2001) A693. doi:10.1149/1.1374216.

[92] R.J. Gorte, J.M. Vohs, Catalysis in solid oxide fuel cells., Annu. Rev. Chem. Biomol. Eng. 2 (2011) 9–30. doi:10.1146/annurev-chembioeng-061010-114148.

[93] O. Yamazaki, K. Tomishige, K. Fujimoto, Development of highly stable nickel catalyst for methane-steam reaction under low steam to carbon ratio, Appl. Catal. A Gen. 136 (1996) 49–56. doi:10.1016/0926-860X(95)00268-5.

[94] N. Laosiripojana, S. Assabumrungrat, Catalytic dry reforming of methane over high surface area ceria, Appl. Catal. B Environ. 60 (2005) 107–116. doi:10.1016/J.APCATB.2005.03.001.

[95] K.O. Christensen, D. Chen, R. Lødeng, A. Holmen, Effect of supports and Ni crystal size on carbon formation and sintering during steam methane reforming, Appl. Catal. A Gen. 314 (2006) 9–22. doi:10.1016/J.APCATA.2006.07.028.

[96] D. Fujita, M. Schleberger, S. Tougaard, XPS study of the surface enrichment process of carbon on C-doped Ni(111) using inelastic background analysis, Surf. Sci. 331–333 (1995) 343–348. doi:10.1016/0039-6028(95)00312-6.

[97] O.A. Marina, M. Mogensen, High-temperature conversion of methane on a composite gadolinia-doped ceria - gold electrode, Appl. Catal. A Gen. 189 (1999) 117–126. doi:10.1016/S0926-860X(99)00259-8.

[98] K. Kusakabe, K.I. Sotowa, T. Eda, Y. Iwamoto, Methane steam reforming

over Ce-ZrO2-supported noble metal catalysts at low temperature, Fuel Process. Technol. 86 (2004) 319–326. doi:10.1016/j.fuproc.2004.05.003.

[99] X. Li, M. Liu, J.P. Lee, D. Ding, L.A. Bottomley, S. Park, M. Liu, An operando surface enhanced Raman spectroscopy (SERS) study of carbon deposition on SOFC anodes, Phys. Chem. Chem. Phys. 17 (2015) 21112–21119. doi:10.1039/c4cp05176a.

[100] Y. Choi, E.C. Brown, S.M. Haile, W. Jung, Electrochemically modified, robust solid oxide fuel cell anode for direct-hydrocarbon utilization, Nano Energy. 23 (2016) 161–171. doi:10.1016/J.NANOEN.2016.03.015.

[101] J. Kirtley, A. Singh, D. Halat, T. Oswell, J.M. Hill, R.A. Walker, In situ raman studies of carbon removal from high temperature Ni-YSZ cermet anodes by gas phase reforming agents, J. Phys. Chem. C. 117 (2013) 25908–25916. doi:10.1021/jp408192e.

[102] M. Liu, K.S. Blinn, H. Abernathy, X. Li, M. Liu, L.A. Bottomley, Raman spectroscopic monitoring of carbon deposition on hydrocarbon-fed solid oxide fuel cell anodes, Energy Environ. Sci. 5 (2012) 7913–7917. doi:10.1039/c2ee21499g.

국문 초록

고체 산화물 연료전지는 낮은 오염도, 높은 에너지 효율, 그리고 다양한 연료 활용가능성 때문에 유망한 미래에 에너지 변환 장비로 여겨지고 있다. 이러한 고체산화물 연료전지를 상용화 하기 위해서는 구조적 그리고 연료활용도에 있어서 획기적인 발전이 필요하다. 예를 들어, 구조적인 측면에서, 전해질 두께는 작동 온도를 600 ℃ 미만으로 낮추기에 충분할 정도로 얇아야 한다. 이러한 작동 온도 영역에서 높은 열화율, 고가의 재료 사용, 그리고 긴 초기 작동 시간 같은 고체산화물 연료전지 기술적 문제를 해결할 수 있다. 또한, 연료의 관점에서, 저온 고체산화물 연료전지에 탄화수소 연료 (메탄, 부탄, 프로판 등)를 직접 사용할 수 있다면, 수소 저장 및 큰 시스템 크기의 문제를 제거 할 수 있다. 그러나, 전해질을 제조하기위한 박막 증착 기술은 기판의 증착 조건 및 표면 구조에 크게 의존한다. 스퍼터링 구조와 증착 변수 사이의 상관 관계에 대한 상세한 연구는 전해질 및 전극을 제조하기위한 박막 증착 기술을 상업적으로 적용하기 위해 필수적이다. 또한, 낮은 작동 온도에서, 직접적인 전기 화학적 산화 및 탄화수소 연료의 개질은 매우 느리다. 따라서 낮은 작동 온도에서 높은 활성도를 가진 열 촉매 설계는 필수적이다.

전해질의 두께를 감소시키는 것 외에, 스퍼터링에 의해 증착 된 박막층의 나노 크기의 입자 구조로 인해, 스퍼터링은 고 활성 전극을 설계하는데 이용 될 수 있다. 더욱이, 고성능 열 촉매의 구조는 높은 밀도의 반응영역을 필요로 하기 때문에, 나노 크기의 그레인으로 구성된 코스퍼터링 박막은 저온영역 에서의 직접 메탄 연료사용을 가능하게 할

가능성이 있다. 이 연구에서는 500 ℃에서 작동하는 직접 메탄 SOFC의 개발을 위해 고성능 나노 구조의 Ni-GDC 양극 및 Ru-GDC 개질 층을 제조하기 위해 공동 스퍼터링 기술이 적용되었다.

양극 산화 알루미늄 (AAO)은 균일 한 나노스케일 크기의 나노홀, 높은 열-기계적 안정성 및 확장 성으로 인해 박막 고체산화물 연료전지를 스퍼터링을 이용해 제작하기 위한 기판으로 사용되어왔다. AAO의 전기 비전 도성 특성으로 인해, 전기 화학적 성능은 AAO상의 양극 나노 구조에 의해 크게 영향을 받는다. 전형적인 SOFC구조에서는 집전 저항이 전체 셀 저항에 크게 영향을 미치지 않는다. 그러나, AAO위에 제작된 박막 고체산화물 연료전지에서, 연료극에서 생성된 전자는 기판에 평행한 방향으로만 전도가 가능하며, 이는 전자 집전에서 상당한 손실을 초래한다. 따라서 AAO에서 고성능 Ni-GDC 연료극 구조를 설계하려면 전기 화학적 성능에 대한 나노 구조 효과를 이해해야한다. 증착 챔버 압력, 타겟 과 기판 거리 및 기판 회전 속도와 같은 다양한 증착 파라미터가 양극 두께, 다공도 및 칼럼 구조에 미치는 영향에 대해 연구되었다. 실험 결과는 연료극 나노 구조의 이러한 물리적 특성이 박막 고체산화물 연료전지의 전기 화학적 성능을 결정하는 데 중요한 요소라는 것을 보여 주었다.

AAO위에 공동 스퍼터링에 의해 제조 된 열 촉매 개질 층은 물질 조성과 다공도에 의해 성능이 결정된다. 공동 스퍼터링에 의해 제조 된 Ru-GDC의 조성은 나노 구조의 다공도와 상관 관계가 있다는 것이 주목 할만하다. Ru 및 GDC의 증착 속도의 큰 차이 (90 % 초과)는 조성 변화에 따른 다공도 변화에 기인 할 수 있다. 그러나 이런 물질의 증착률이 나노구조형성에 미치는 영향의 원리는 본 논문의 주제 범위에

속하지 않는다. Ru 3 vol%의 조성비를 가진 Ru-GDC 나노 구조를 활용해 500℃에서 성공적인 개질 성능을 나타냈다. 구조 분석에 따르면 Ru-GDC의 나노 크기 입자 구조가 Ru 함량이 매우 낮음에도 불구하고 직접 메탄 작업을 가능하게 한 것으로 나타났다.

고성능 Ni-GDC 연료극과 Ru-GDC 나노 구조 개질 층 (NRL)의 통합은 건조한 메탄 (3 % H_2O)을 이용해 500 ℃의 저온에서도 상당한 전력 밀도를 생성하는 박막 고체산화물연료전지를 개발했다. 또한, 12시간이 넘는 작동 시간은 문헌에 보고된 AAO기반의 박막 고체산화물 연료전지의 어떤 성능보다 높게 측정되었다. 비록 연료전지가 시간당 4.9 % 열화율을 보였지만, 이는 백금 (Pt) 기반 공기극에 의한 열화에 의한 것으로 보인다. 나노구조분석을 통해 Ni-GDC 연료극에서 탄소 흡착은 확인되지 않았으며, 이는 탄소 흡착이 분해에 주된 기여가 아님을 나타냈다.

주요어: 저온 고체산화물 연료전지, 직접 메탄, 공동 스퍼터링, 니켈(Ni)-가돌리늄 도핑 세리아(GDC) 연료극, 루테늄(Ru)-가돌리늄 도핑 세리아(GDC)

학번: 2014-21846

공학박사 학위논문

Nanostructured Ni-Gd doped Ceria Anode by Co-Sputtering for a Direct Methane Solid Oxide Fuel Cells operated under 500℃

500℃ 이하 작동 직접 메탄 고체산화물 연료전지를 위한 코스퍼터링 니켈-가돌리늄 도핑 세리아 나노구조 연료극

2020년 2월

서울대학교 대학원

기계항공공학부

유 원 종

Nanostructured Ni-Gd doped Ceria Anode by Co-Sputtering for a Direct Methane Solid Oxide Fuel Cells operated under 500℃

By

Wonjong Yu

A Dissertation Submitted in Partial Fulfillment of the

Requirements for the Degree of

Doctor of Philosophy

Department of Mechanical and Aerospace Engineering

Seoul National University

February 2020

Nanostructured Ni-Gd doped Ceria Anode by Co-Sputtering for a Direct Methane Solid Oxide Fuel Cells operated under 500 ℃

지도교수 차 석 원

이 논문을 박사 학위논문으로 제출함
2019년 10월

서울대학교 대학원
기계항공공학부
유 원 종

유원종의 박사 학위논문을 인준함
2019년 12월

위 원 장 _____ (인)

부위원장 _____ (인)

위 원 _____ (인)

위 원 _____ (인)

위 원 _____ (인)

Abstract

Nanostructured Ni-Gd doped Ceria Anode by Co-Sputtering for a Direct Methane Solid Oxide Fuel Cells operated under 500 ℃

Solid oxide fuel cells (SOFCs) are promising energy conversion device converting chemical energy to electric energy with excellent fuel flexibility, high efficiency, and low pollutant. For the commercialization of SOFC, several breakthroughs should be achieved in structure and fuel sections. For example, in terms of structure, electrolyte thickness should be thin enough to reduce the operating temperature down to below 600℃. In these operating temperature region, SOFC technology issues such as high degradation rate, the use of expensive materials, and slow start-up time can be resolved. In addition, in terms of fuel, direct use of hydrocarbon fuel (methane, butane, propane, etc.) to low-temperature SOFCs could eliminate the problem of hydrogen storage and large system size due to external reformer. However, thin-film deposition techniques for fabricating electrolyte is highly dependent on deposition conditions and surface structure of the

substrate. Detailed studies on the correlation between sputtering structure and deposition parameters are essential for commercially applying thin-film deposition techniques for fabricating electrolyte and electrode. In addition, at low operating temperatures, direct electrochemical oxidation and reforming of hydrocarbon fuel are extremely sluggish. Therefore, a highly active thermal catalyst structure at low operating temperatures should be designed and studied.

Due to the nano-sized grain structure of the thin-film layer deposited by sputtering, other than reducing the thickness of electrolyte, sputtering for thin-film fabrication could be utilized for designing highly active electrode. Furthermore, since the requirement for a highly active thermally catalytic reforming layer is providing high density of triple-phase boundary (TPB), co-sputtering for fabricating reforming layer could satisfy the requirement for low-temperature direct hydrocarbon SOFCs. In this study, co-sputtering technique was applied to fabricate high-performance nanostructured Ni-GDC anode and Ru-GDC reforming layer for the development of direct methane SOFCs operated under 500°C.

Anodic aluminum oxide (AAO) has been used as a substrate for thin-film SOFC (TF-SOFC) fabricated by sputtering due to a uniform nano-hole array, high thermo-

mechanical stability, and scalability. Due to electrically non-conductive characteristics of AAO, electrochemical performance is greatly affected by anode nanostructure on AAO. Typical current collecting resistance in anode supported SOFC is negligible to the ohmic resistance of SOFC. In AAO supported TF-SOFC, however, the electron pathway is in-plane direction of nanostructured anode, which results in substantial loss in electron current collecting. Therefore, understanding the nanostructure effect on electrochemical performance is necessary to design high-performance Ni-GDC anode structure on AAO. Various deposition parameters such as deposition chamber pressure, target to substrate distance (TSD), and substrate rotation speed were studied for anode thickness, porosity, and column structure. Experimental results showed that these physical properties of the anode nanostructure are critical factors for determining the electrochemical performance of TF-SOFC.

Thermally catalytic reforming layer fabricated by co-sputtering on AAO depends on composition and porosity. It is noteworthy that the composition of Ru-GDC fabricated by co-sputtering is correlated with the porosity of the nanostructure. It is possible that large difference in deposition rate of Ru and GDC (over 90%) could be attributed to porosity change with composition change. However, a detailed

mechanism is not in this thesis boundary. Nevertheless, Ru 3 volumetric percent showed successful reforming performance at 500℃. The structure analysis indicated that the nano-sized grain structure of Ru-GDC enables the direct methane operation with extremely low contents of Ru.

The integration of high-performance Ni-GDC anode and Ru-GDC nanostructured reforming layer (NRL) could produce substantial power density at 500℃ with nearly dry methane (3% H_2O). Furthermore, operation time is extended to over 12 hours, which is longer than any other experimental data reported in the literature. Although the cell showed 4.9% per hour degradation rate, the platinum (Pt) based cathode is largely attributed to the degradation. Post analysis showed that carbon coking on Ni-GDC anode is negligible, which indicates that the carbon coking is not the main contribution to degradation.

Keyword: low-temperature solid oxide fuel cell, direct methane, co-sputtering, nickel-gadolinium doped ceria (Ni-GDC), ruthenium-gadolinium doped ceria (Ru-GDC)

Student Number: 2014-21846

Acknowledgments

First and foremost, I would like to thank my advisor, Professor Suk Won Cha, who has been a great mentor to me for six years of Ph.D. course. I am deeply indebted to his support and guide during the course of my research and project.

Secondly, I would like to thank the fuel cell group members, Sanghoon Lee, Sangbong Ryu, Inwon Choi, Wonyeop Jeong, Myungsuk Lee, and Jaewon Hwang. Also, I am very thankful to the hybrid vehicle group members, Changbum Kang, Bonhyun Gu, Changhee Song, Donghwan Sung, Jaehyuk Yang, Kyunghyun Kim, and Sunghyun Jang. When I had trouble with the research, the group member gave me a lot of strength and reminded me of the purpose of the Ph.D. course.

I am deeply indebted to my family, father who taught me how to deal with a difficult problem, a mother who improves my mood and mental well-being, and sister who inspire me to further efforts.

Lastly, I would like to give my warmest thanks to my wife Minjae Gil. Without her support and understanding, it would not be possible for me to achieve the goal of my thesis work.

Table of Contents

List of Figures

List of Tables

Chapter 1. Introduction

1.1. Fuel Cell Fundamentals

A fuel cell is an energy conversion device capable of converting chemical species energy to electric energy with high efficiency [1]. The principle of fuel cell operation is similar to battery system. Reactant chemical species are electrochemically oxidized and reduced at anode and cathode, respectively. Electrons produced by electrochemical reaction at electrodes is released to external circuit, and active charge carrier is conducted through electrolyte. The difference between the battery and fuel cell systems is the fuel source. Unlike battery, fuel for the fuel cell is supplied from the external source. Therefore, a fuel cell does not need recharging. With well-designed fuel storage, fuel cells can operate much longer than battery systems at the same weight condition [2,3].

There are various types of fuel cell depending on the chemical properties of the electrolyte. Polymer exchange membrane fuel cell (PEMFC) uses electrolyte fabricated by polymer materials conducting proton through the electrolyte. Solid oxide fuel cells (SOFCs) use solid oxide electrolyte for oxygen ion-conducting. Among many fuel cell type, PEMFC and SOFC are the most advanced fuel cell types close to the commercialization[4,5]. However, there are still critical issues for ensuring economic feasibility.

The fuel cell consists of three mechanical parts: anode, electrolyte, and cathode. Anode and cathode are porous structures so that gaseous fuel passes through the structure. To be electrochemically active, electron conductive solid phase, ionic conducting solid phase, and gas species should be contacted at one boundary, which is called triple-phase boundary (TPB)[6–8]. The electrochemical reactions such as

oxygen reduction or hydrogen oxidation reactions occur in the presence of TPB. Designing the electrode with high density of TPB is important to reduce overall activation loss in fuel cells. On the other hand, the electrolyte structure should be dense enough to block electron. Depending on the electrolyte material and structure, conducting charge carrier species and conductivity are widely varied.

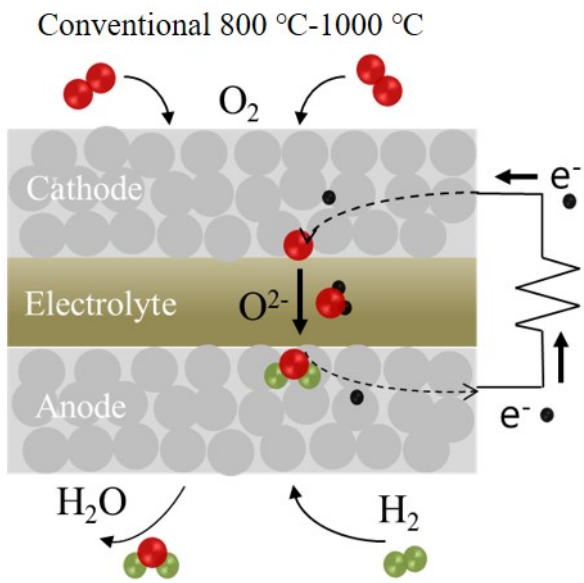

Figure1.1 Demonstration of solid oxide fuel cells working principle.

In the thermodynamic perspective, the maximum energy potential that can be exploited from the electrochemical reactions is theoretically expected by calculating a change in Gibbs free energy of chemical species. The change in the Gibbs free energy change is directly related to electrical work (E).

$$\Delta \hat{g}_f = \ -n \cdot F \cdot E$$

n represents the number of electrons involved in the reaction. F is Faraday's constant. The reversible voltage under standard conditions can be denoted as E^o.

$$E^0 = \frac{-\hat{g}_f}{n \cdot F}$$

However, fuel cells operated under non-standard conditions. Nernst equation accounts for concentration effect on reversible voltage and written by:

$$\mathrm{E} = E^o - \frac{RT}{nF} ln \frac{\Pi a_{products}^{vi}}{\Pi a_{reactants}^{vi}}$$

T is temperature. R is gas constant. *a* is the activity of the gas (for ideal gas, $a_i = p_i/p^o$, p_i is the partial pressure, p^o is the standard pressure).

As fuel cells operate, the ideal voltage can not be sustained due to the various losses from reaction kinetics and activation energy for conduction, and mass transport resistance.

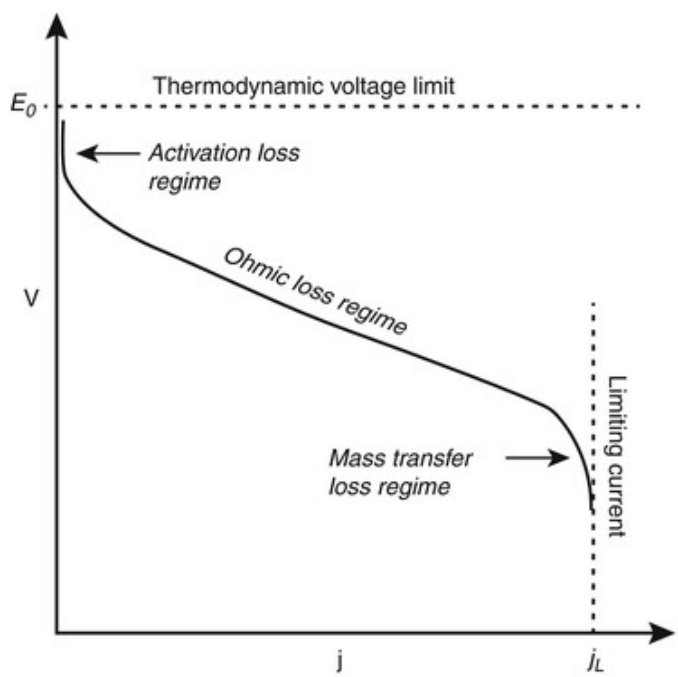

Figure1.2 Schematic of fuel cell i-V curve and three major losses that affect ideal thermodynamic voltage during the operation.

The actual voltage of the fuel cell is affected by three major losses: activation loss (η_{act}), ohmic loss(η_{ohm}), and mass transport loss (η_{mass}). The real voltage is written by:

$$V = E - \eta_{act} - \eta_{ohm} - \eta_{mass}$$

Activation loss is caused by an activation energy barrier from the charge transfer of the electrochemical reaction. Typically, activation loss is dominating at low current region, which is in low over-potential region. The reason for this is because of the activation barrier in reaction kinetics affected by the magnitude of the over-potential. Butler-Volmer equation explains how voltage loss is related to the current produced by the electrochemical reaction in fuel cell and written as:

$$j = j_o^o \left(\frac{C_R^*}{C_R^o} e^{\frac{\alpha n F \eta}{RT}} - \frac{C_P^*}{C_P^o} e^{-\frac{(1-\alpha) n F \eta}{RT}} \right)$$

j is the current density of fuel cells. C_R^* and C_P^* represent actual concentration at the electrode. j_o^o is an exchange current density at standard condition (reference concentration : C_R^o and C_P^o). α is called a transfer coefficient. η represents over-potential in fuel cell operation.

Ohmic loss is originated from charge transport through the electronic path and ionic path. In most cases, electron conduction resistance is negligible compared to ionic conduction. The charge transport resistance follows ohmic's law and can be written as:

$$V = i \left(\frac{L}{A\sigma} \right) = iR$$

L represents the thickness of the electrolyte, length of the ionic conduction path. And A means the area for ionic conduction. σ is the ionic conductivity of the electrolyte.

Last, mass transport loss is caused by depletion of reactant at reaction sites. As the reaction rate increases consuming rate of the reactants at the electrode should

increase. When reactant gas diffusion rate is lower than reaction rate, the current can not be further increased. The relationship between limiting current density (j_L) and diffusivity is presented below:

$$j_L = nFD^{eff}\frac{C_R^o}{\delta}$$

D^{eff} is the effective diffusivity of the reactant gas in the electrode layer. δ is the diffusion layer thickness. This concentration phenomenon affects the Nernst voltage and the expression is written below:

$$\eta_{conc} = \frac{RT}{nF} ln \frac{j_L}{j_L - j}$$

Typically, mass transport is considered as a critical factor for PEMFC system due to the need for water management. Channel design is one of the key aspects for achieving high performance of PEMFC. However, in SOFC system, due to high operating temperature, water management or flow system is considered as less important.

1.2. Solid Oxide Fuel Cells

Oxygen ion conduction through the solid electrolyte is dominated by the hoping mechanism, which is sluggish at low-temperatures (under 600℃). For this reason, operating temperature of conventional SOFCs is in the range between 800 and 1000℃. The unduly high operating temperature (800-1000℃) of conventional SOFCs induces several critical issues such as limited material selection, severe degradation of the cell, and high cost of balance of plant (BOP)[9–11]. For resolving these issues, many research has been focusing on reducing the operating temperature of SOFCs. Major losses of SOFC can be categorized into three parts: activation loss,

ohmic loss, and mass transport loss. Since gas diffusivity at high temperature is sufficiently high, the mass transport loss is typically negligible for SOFCs[12]. Therefore, reducing the activation and ohmic losses is important to achieve high performance of SOFCs at low temperatures.

1.3. Thin-film Solid Oxide Fuel Cells

Thin-film SOFCs (TF-SOFCs) are now one category of SOFCs research field. TF-SOFCs has been drawn significant attention for a decade due to the superior performance enhancement at low operating temperatures [13–16]. As mentioned above, reducing the ohmic and activation resistances is the key factor for SOFCs to be operated at the low-temperature region (under 600℃). Thin-film electrolyte thickness ranging from a few nanometers to micrometer is known to be suitable for lowering ohmic resistance with short ionic conduction path. From the equation related to charge transport resistance, it is clear that electrolyte thickness is proportional to ohmic resistance. Other than reducing the thickness of the electrolyte, thin-film structure has superior characteristics in fabricating the high density of TPB. The thin-film structure typically constitutes of the nano-sized grain structure, which is much smaller than conventional SOFC structure fabricated by chemical sintering methods [17].

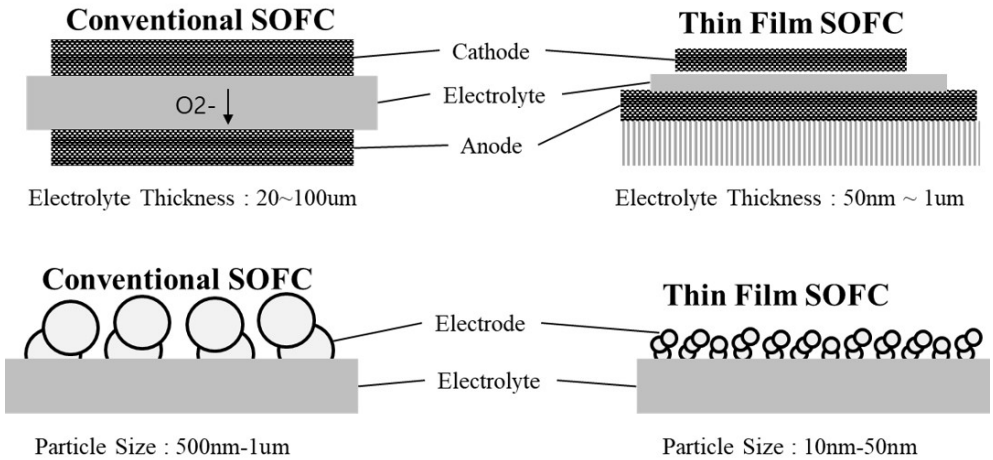

Figure 1.3. Comparative schematics of thin-film SOFC and conventional SOFC.

As the grain size of the electrode reduces, the effective surface area of the electrode, which is potential TPB density for electrochemical reaction, increases. This phenomenon is confirmed from the experimental data reported in the literature. Figure 1.4 represents the working temperature of SOFCs as a function of electrolyte thickness. Black points indicating the reported experimental data of thin-film electrolyte (electrolyte deposited by thin-film deposition techniques: physical or chemical vapor deposition) are clearly located in the low operating temperature compared to the SOFCs with conventional electrolyte (electrolyte fabricated by conventional techniques: sintering process) [10–52].

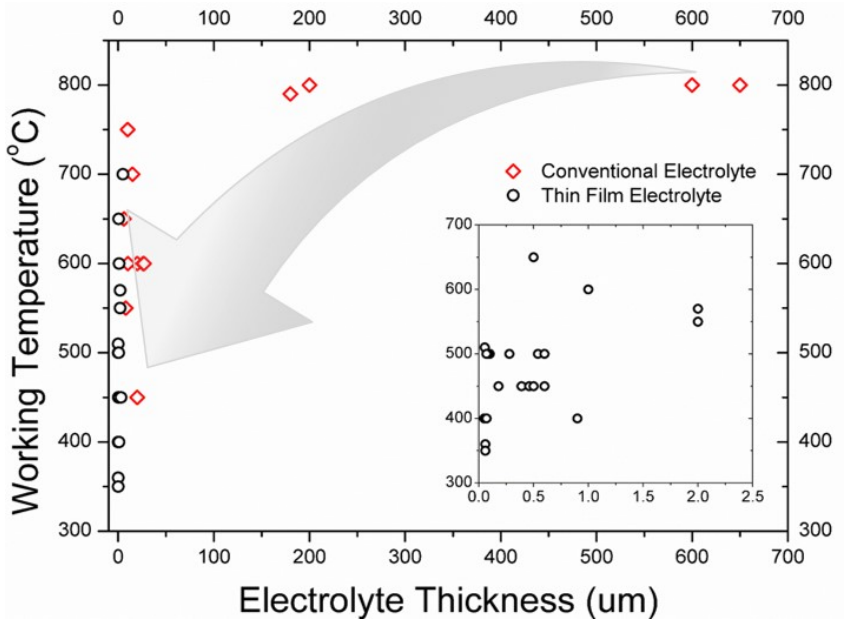

Figure 1.4 Literature experimental data of the working temperature of SOFCs varied with electrolyte thickness. Red: electrolyte fabricated by a conventional process including high-temperature sintering. Black: electrolyte deposited by thin-film deposition techniques including physical or chemical vapor deposition.

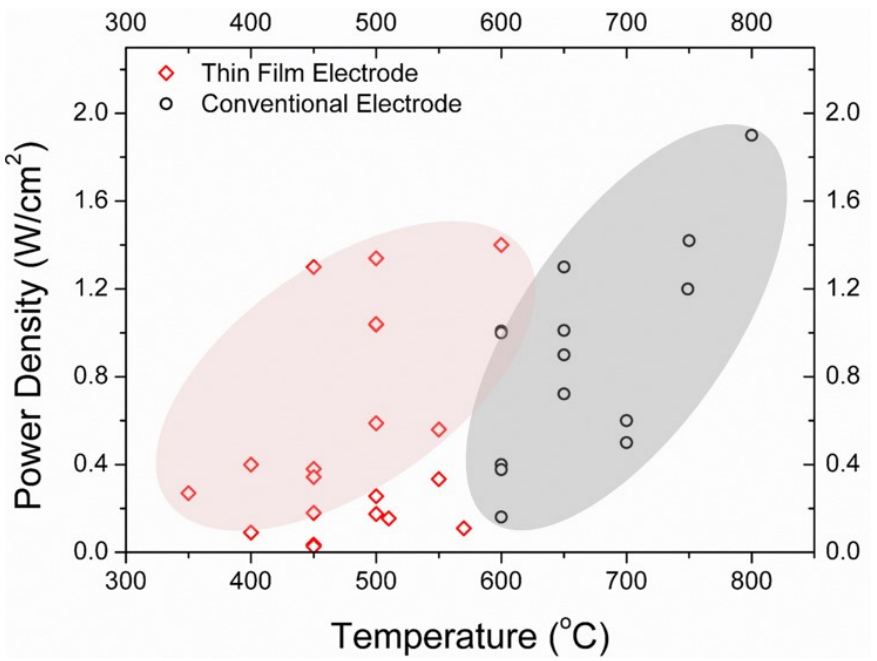

Figure 1.5 Literature experimental data of power density of SOFCs varied with temperature ranging from 350 to 800℃. Red points represent SOFCs with a thin-film electrode fabricated by physical or chemical vapor deposition). Black points represent SOFCs with conventional electrode fabricated by a sintering process.

Figure 1.5 also confirms that SOFCs with thin-film electrode design clearly show high performance in low-temperature regions. Statistic information from the literature indicates that using a thin-film deposition technique for electrode fabrication is beneficial for achieving high performance at low temperatures.

1.3.1 Thin-film Deposition Techniques

Various kinds of thin-film deposition techniques have been used for the fabrication of SOFC components. Magnetron sputtering, pulsed laser deposition (PLD), and thermal evaporation, which are physical vapor deposition (PVD), have been demonstrated as deposition methods for nanostructure fabrication[16]. Chemical vapor deposition (CVD) and atomic layer deposition (ALD) are also extensively used for ultrathin electrolyte and nano-thin surface coating for a nanostructured electrode. Among those techniques, magnetron sputtering has shown superior properties for nanostructure fabrication due to easy control of porosity and nanoscale thickness control[61]. Furthermore, it is already proved that sputtering is commercially viable because of uniform deposition for large area and variety of material selection. The principle of the sputtering is simple. As the large electric potential difference is applied between the target and substrate, a plasma is created by ionizing the sputtering gas species around target materials. Simultaneously, positively charged ionized gas species is dragged into the target surface. The bombardment of the gas species takes off the target material at atomic scale. Ejected atoms from the target flow directly to the substrate. The nucleation and accumulation of the ejected atoms from the target materials result in formation of the nano-sized grain structure of the film on the substrate[62,63].

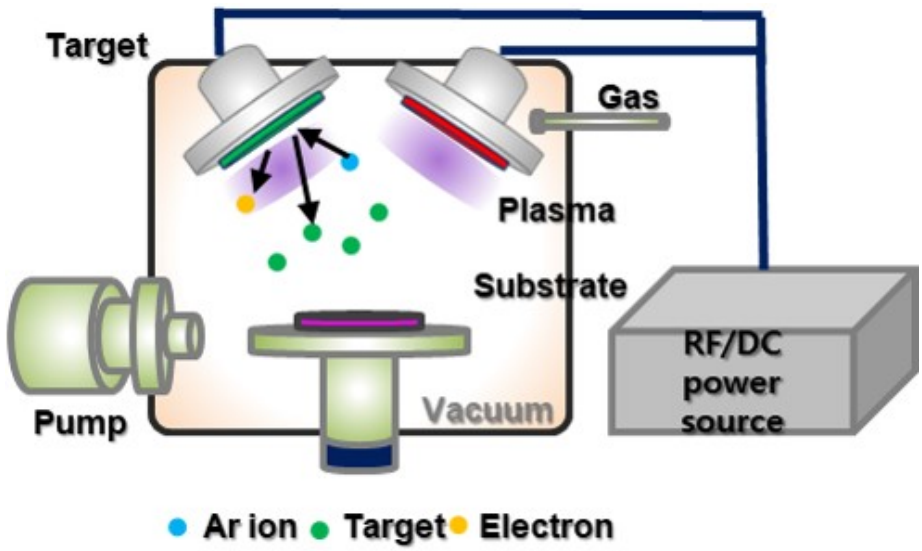

Figure 1.6 Schematic of the sputtering system.

Sputtering has a number of features for controlling the nanostructure of the deposited film. The most dominant and controllable variables for sputtering are sputtering gas species, chamber pressure, target to substrate distance (TSD), sputtering incident angle, and substrate rotation speed. These variables are sensitive for determining the characteristics of the nanostructure such as porosity and column structure. Other than these variables, sputtering power, substrate temperature, and bias voltage can affect the crystallinity and the chemical composition of the deposited film[64].

Thin-film electrolyte fabricated by sputtering has been widely used to reduce the ohmic resistance of SOFC. Meanwhile, nanostructured anode fabricated by sputtering is also promising structure for high performance at low operating temperature due to the high density of triple-phase boundary (TPB) stemmed from

nano-sized grain structure of sputtering layer[65]. However, nanostructure fabricated by sputtering is highly dependent on deposition parameters and substrate structure conditions. To achieve high performance of TF-SOFC fabricated by sputtering, detailed studies on nanostructured sputtering anode affected by deposition parameters are essential. Therefore, various electrode materials such as nickel-gadolinium doped ceria (Ni-GDC) should be studied with various deposition conditions of co-sputtering on the nanoporous substrate.

1.3.2 Types of Thin-film Solid Oxide Fuel Cells

Electrode and electrolyte deposited by the thin-film technique require support (substrate) to be mechanically sustained at nanoscale level. In addition, thin-film structure is highly dependent on surface structure of the support. Therefore, considering the type of substrate for thin-film deposition is the important step for fabricating TF-SOFCs. Type of TF-SOFCs can be categorized into 4: silicon-based freestanding structure, anodic aluminum oxide (AAO) supported structure, anode pellet supported structure, and porous metallic substrate. Si wafer is used as a support for thin-film structure with the lithography etching process. This structure is frequently called as free-standing TF-SOFC due to the characteristic of electrolyte structure. After electrolyte deposition on si wafer, the wafer is etched from the backside to the electrolyte by lithography. Consequently, the electrolyte is sustained by itself without any supporting mechanical structure. For this reason, this type of TF-SOFC suffers severe thermo-mechanical degradation at operating temperature.

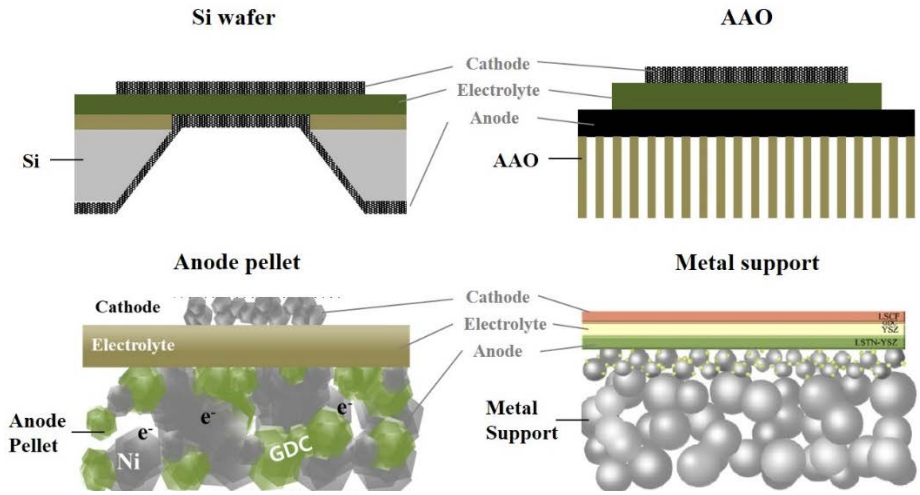

Figure 1.7 Schematic illustration of types of thin-film solid oxide fuel cells depending on substrates.

Furthermore, the active area is limited by a few hundred micrometers due to the structure stability problem. Despite the recent progress in thermo-mechanical stability of si wafer SOFC, the scalability and stability of the cell still need to be much more enhanced[52,66,67].

Anodic aluminum oxide (AAO) has been considered as promising support for thin-film fabrication due to high thermos-mechanical stability and scalability. Uniform nanohole array is formed throughout the substrate. This nano-hole has no tortuosity, which is advantageous for fuel delivery. However, pinhole formation in the electrolyte causes severe performance drop and unstable open circuit voltage issues. Although the pinhole issues are partially resolved by applying hybrid deposition techniques (sputtering and atomic layer deposition etc.) for fabricating

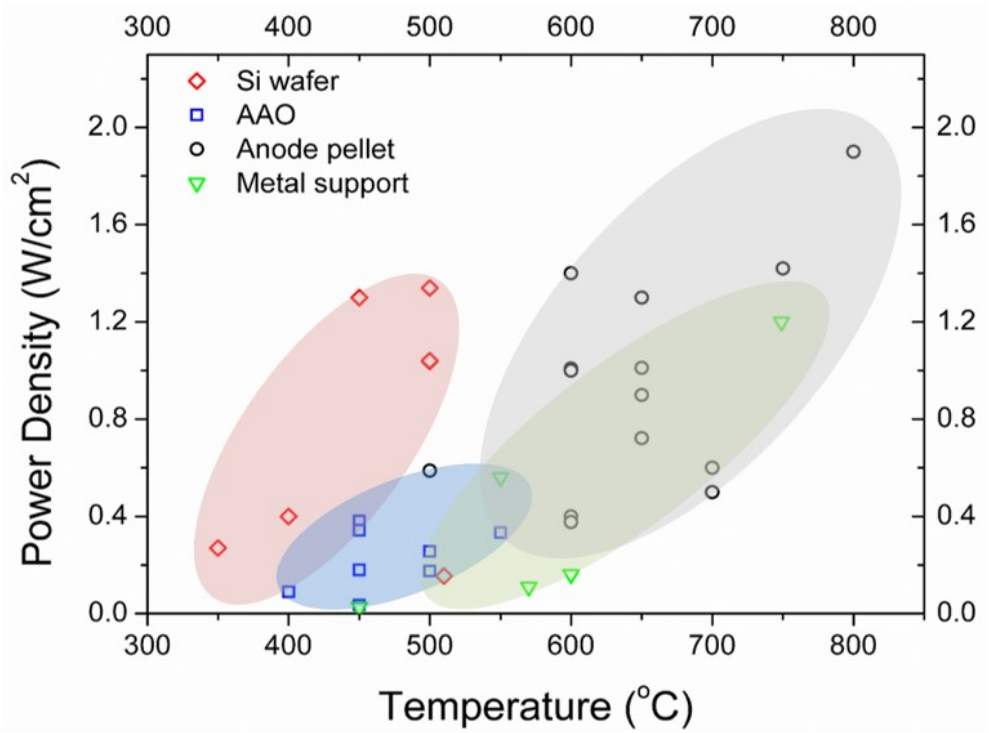

Figure 1.8 Literature data for the peak power density of TF-SOFC depending on types of support.

electrolyte layer, still the peak power density of the cell needs to be enhanced[68,69]. Recently, there is an attempt to apply thin-film fabrication of the anode functional layer or electrolyte to anode pellet and metallic support. However, due to the large pore structure (larger than a few micrometers) and high roughness of the surface structure, physical vapor deposition (PVD) or chemical vapor deposition (CVD) is difficult to be applied to electrode or electrolyte fabrication. Only a few reports have succeeded in developing the process for thin-film deposition on anode pellet or metallic substrate[70,71]. For this reason, high power density of Si wafer and AAO supported TF-SOFCs have are dominant at a temperature under 500℃.

1.4 Hydrocarbon Solid Oxide Fuel Cells

One of the advantages of SOFCs is remarkable fuel flexibility with various utilization methods such as direct electrochemical oxidation, internal steam reforming, and partial oxidation. Direct use of hydrocarbon fuel can benefit to system level. Since external reformer is unnecessary for direct hydrocarbon fuel SOFCs, the system size and complexity are substantially reduced[72–75]. There are various kinds of hydrocarbon fuel such as methane, butane, and propane. In case of use of methane for direct SOFCs, it can be a promising energy source since supplying and storage infrastructure for a major component of the natural gas (over 90% of natural gas is methane) is already existing[76]. It could eliminate the issues of hydrogen storage, which means a large progress in the commercialization of SOFCs to the market. However, significant efforts have to be dedicated to resolving the technical issues for using methane as a fuel for low-temperature SOFCs.

Among various utilization methods for methane, direct internal steam reforming is considered as a promising method for use of methane as a fuel with minimum fuel dilution. Since direct electrochemical oxidation of methane is extremely sluggish at low-temperature, catalytic reforming of methane to carbon monoxide and hydrogen is necessary for generating electric potential[77–79]. Various reactions can happen in steam reforming reactions, and the possible reactions are written below:

$$\text{Steam Reforming: } CH_4 + H_2O \rightarrow CO + 3H_2 \qquad \Delta H = +206\ kJmol^{-1}$$

$$\text{Water Gas Shift: } CO + H_2O \rightarrow CO_2 + H_2 \qquad \Delta H = -41\ kJmol^{-1}$$

In terms of kinetic, hydrogen and carbon monoxide oxidation reaction is much faster than direct oxidation of methane. Therefore, the electrochemical performance of the cell with reformed gas fuel could be higher than that without the reforming process.

The key point of structure design for direct methane SOFCs is that thermally catalytic reforming structure should be located with SOFCs anode structure[80]. When methane fuel is supplied to the anode of SOFCs, without the need of an external reformer, the fuel should be pass through the reforming structure before reaching to TPB at anode side. As mentioned above, without the reforming process, electrochemical performance of low-temperature SOFCs for direct use of methane is significantly reduced. Furthermore, to design direct methane SOFCs structure with high efficiency at low-temperature, steam to carbon ratio (S/C ratio) should be low enough to exclude water management system and minimize fuel dilution. However, a technical breakthrough for nanostructure fabrication is essential for satisfying these structural and operational conditions.

Thermally catalytic steam reforming process of methane is not energetically favored at low operating temperatures (under 500℃). Furthermore, at low S/C ratio operating conditions, thermodynamic calculation shows that carbon coking likely happens at the anode side[81]. It has been reported in the literature about the cell failure due to the massive carbon coking in the anode. To resolve the carbon coking issue and low activity for steam reforming reaction at low-temperature, the activity of the reforming structure should be dramatically enhanced by designing nanostructure with a high density of reaction area. Metallic nanoparticle should well disperse in the ceria oxide support for formation of high catalytic activity. Uniform dispersion with the nano-sized grain structure could be fabricated by the co-sputtering system because of the deposition characteristic of the sputtering principle.

Chapter 2. Background

2.1 Literature Review of AAO supported SOFC

As mentioned in the previous chapter, the AAO substrate has shown a promising characteristic for fabricating thin-film SOFCs due to uniform nano-hole array and scalability. Previous research has focused on the issues related to pinhole formation in the electrolyte during the deposition process. The hybrid deposition method combining sputtering and ALD for electrolyte fabrication is suggested for alleviating the pinhole issue[69]. Development of ALD electrolyte enables open-circuit voltage of AAO-supported TF-SOFC is close to theoretical value at operating temperature even with extremely thin electrolyte layer. Sanghoon Ji et al. reported that 70nm thickness of plasma-enhanced ALD yttria-stabilized zirconia (YSZ) electrolyte shows 1.17V at 500℃[57]. Furthermore, Seongkook Oh et al. reported that electrolyte deposited by using the hybrid deposition method (ALD YSZ and sputtering samarium-doped ceria (SDC)) shows over 500mW/cm^2, which is the highest performance of AAO-supported TF-SOFC at 450℃[82]. Although the significant progress in electrolyte fabrication process, most of the high performing AAO-supported TF-SOFCs still use platinum (Pt)-based anode and cathode. Despite the development of perovskite structure of the oxide cathode, which is considered as a promising candidate for low-temperature cathode materials, catalytic performance of Pt is superior to any other material for operation under 500℃[83]. However, in terms of anode materials, using Pt-based electrode for anode structure is unusual case even for the conventional SOFCs structure. Many research about SOFCs structure fabricated by sintering process (pelletizing, tape casting, screen printing, spray pyrolysis, etc.) uses Ni-based cermet materials for the anode fabrication because of comparable performance of the anode materials to Pt-based materials and feasibility for the commercialization. Nevertheless, the utilization of Ni-based anode structure

for AAO-based SOFCs has been rarely reported. The main reason for that is because of the lack of understanding co-sputtering of Ni-based anode on nanoporous substrate. Not only control of co-sputtered nanostructure but also the thermal effect on nanostructure. In addition, since AAO is electrically non-conductive, current collecting path is through the nanoscale thickness of the anode, which causes unduly high resistance contributed to the ohmic resistance of the full cell. Current collection through in-plane direction of the nanoporous electrode could also cause formation of the dead zone, which is defined as TPB without current connection. We believe that the lack of understanding in this unique structure effect on the cell performance is the major reason for the low power density of Ni-based AAO supported SOFCs at low-temperature considering the nanoscale electrolyte thickness.

To emphasize the strengths of the SOFCs, utilization of hydrocarbon fuel is necessary. Pt is extremely vulnerable to carbon contamination. Without the optimized Ni-based or other material-based anode structure, hydrocarbon fuel can not be used for SOFCs. Although nano-sized grain structure is advantageous for reforming or electrochemical oxidation processes, study on the use of hydrocarbon on AAO supported SOFCs at a temperature under 500°C has not been reported.

2.2 Thesis Outlines

This thesis focuses on two main topics: one is understanding and development of high performing nanostructured Ni-gadolinium doped ceria (GDC) anode fabricated by co-sputtering process. Two is the characterization and development of highly active catalytic reforming nanostructure fabricated by co-sputtering on the AAO substrate. The research is presented in 4 chapters (from chapter 3 to 6). The

detailed contribution and summarization is described below:

- Chapter 3 describes the effect of nanostructured Ni-GDC anode fabricated by co-sputtering on electrochemical performance. As mentioned in the previous chapter, the electrochemical performance of TF-SOFC on AAO substrate is greatly affected by the anode nanostructure. The nanostructure of Ni-GDC deposited by co-sputtering can be controlled by the various parameters of sputtering system. Among those parameters, the major parameters: chamber pressure, thickness of the anode (deposition time), incident angle, which are expected to have a profound effect for the nanostructure, are controlled and comparatively characterized.

- Chapter 4 elaborates the thermal stability of Ni-GDC anode deposited by co-sputtering. The electrochemical performance of Ni-GDC anode is closely related to thermal stability of nanostructure because the operating temperature is around 500℃. It is widely known that Ni is vulnerable to thermal agglomeration due to the high surface energy and diffusion rate at high temperatures. Although the agglomeration tendency depending on Ni grain size and composition of Ni-GDC anode is previously studied, nanostructure change of AAO supported Ni-GDC anode varied with GDC has not been reported. In this chapter, the agglomeration effect on co-sputtered Ni-GDC anode on AAO was characterized by high-resolution field emission microscope (FESEM) and extended time operation.

- Chapter 5 describes the direct methane for co-sputtered Ni-GDC anode varied with GDC composition. Due to the nano-sized grain structure of co-sputtered anode, the catalytic performance for direct oxidation of methane and reforming is higher than the conventional structure. The detailed

electrochemical properties of methane fueled AAO supported SOFCs is demonstrated in the chapter.

- Chapter 6 demonstrates direct methane fueled TF-SOFCs with nanostructure Ru-GDC reforming layer. Since the direct electrochemical oxidation of methane is not energetically favored at low-temperature, the additional reforming structure is essential for achieving high performance. Designing the co-sputtering Ru-GDC reforming structure on AAO supporting system and electrochemical performance of the integrated TF-SOFC is addressed in terms of extended time operation.

Chapter 3. Effect of Nanostructured Ni-based Anode on Performance

3.1 Introduction

Sputtering is known to be advantageous for commercialization due to the capability of uniform large area deposition. For industrial sputtering system, substrate size can be increased up to a few thousand square centimeters. Furthermore, co-sputtering is superior to other deposition methods for mixing two kinds of target materials in nanoscale[84]. Since thin-film deposited by sputtering system consists of the nano-sized grains, theoretical expectation of TPB density in co-sputtered electrode is significantly high. In fact, the performance enhancement with anode functional layer deposited by PLD, which is one kind of PVD method, has been reported in the literature from KIST[85]. However, most of the work on co-sputtering for Ni-based anode on the nanoporous substrate has shown low power density compared to the similar compositional structure of SOFCs at similar operating temperatures. The major reason for the low performance is possibly due to the unique electron conduction path for anode on AAO substrate. AAO is known to be electrically non-conductive structure. Therefore, the electron produced from electrochemical oxidation of the fuel at the anode side should pass through complicated nanoporous structure because the substrate is not conductive. Electron conduction resistance is typically not considered as a concern for ohmic loss or performance of the cell. As demonstrated in this chapter, however, the in-plane connectivity of the nanostructure fabricated by co-sputtering on AAO could be important to achieve high power density.

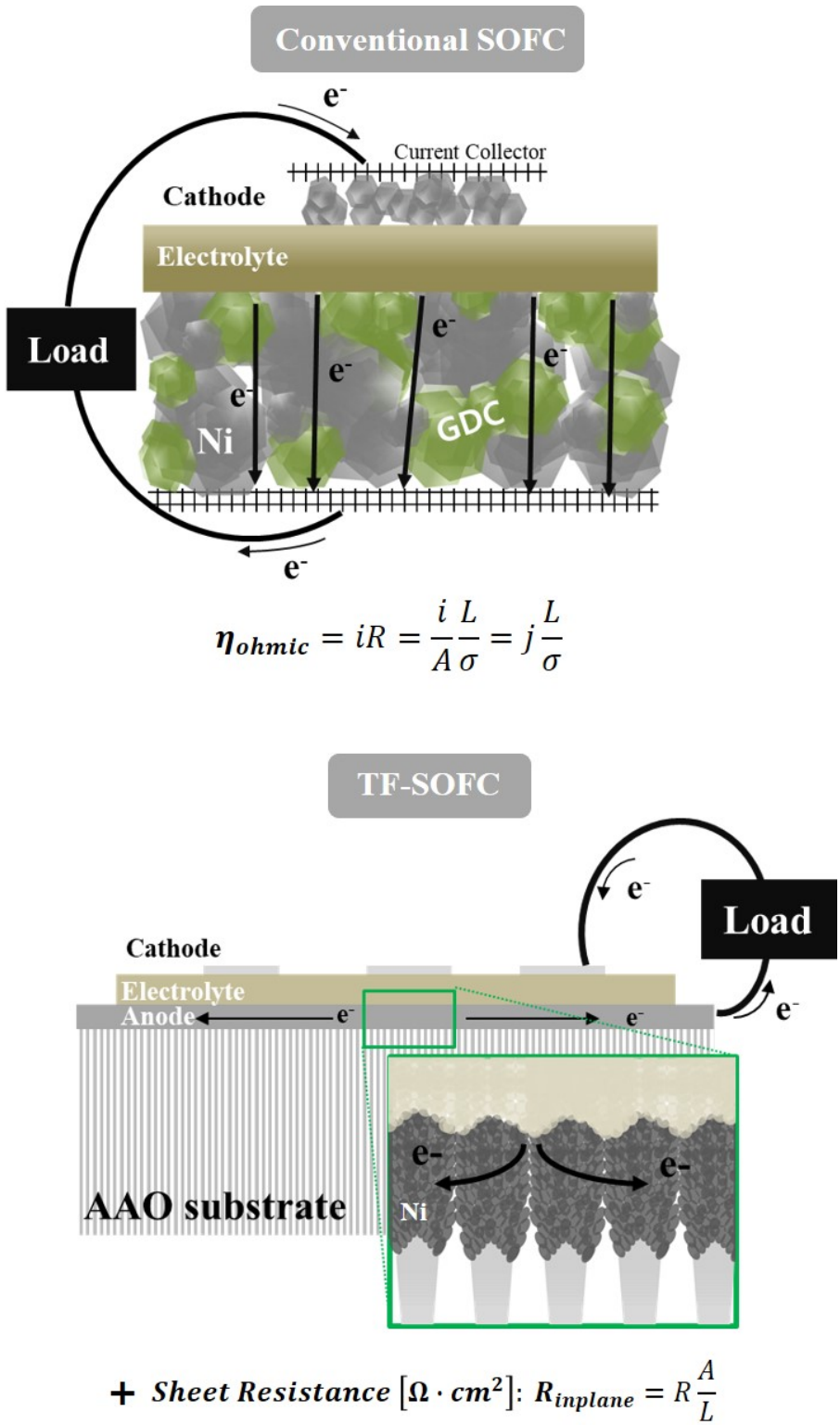

Figure 3.1 Schematic drawing of difference in electron conduction path of conventional anode supported fuel cell and AAO supported thin-film SOFCs.

In this chapter, sputtering parameters are controlled to change the electrochemical properties of the anode structure grown on AAO substrate. First, porosity control by deposition chamber pressure has been previously studied by Dr. Joonho Park. Joonho Park et al. reported that Ni anode deposited with 12 Pa Ar gas showed extensively high porosity compared to the deposition with 0.67 Pa[86]. To reduce variables and select the deposition condition for high density of TPB, deposition pressure for anode structure is fixed to be 8 Pa for all nanostructure fabricated in this chapter. Other

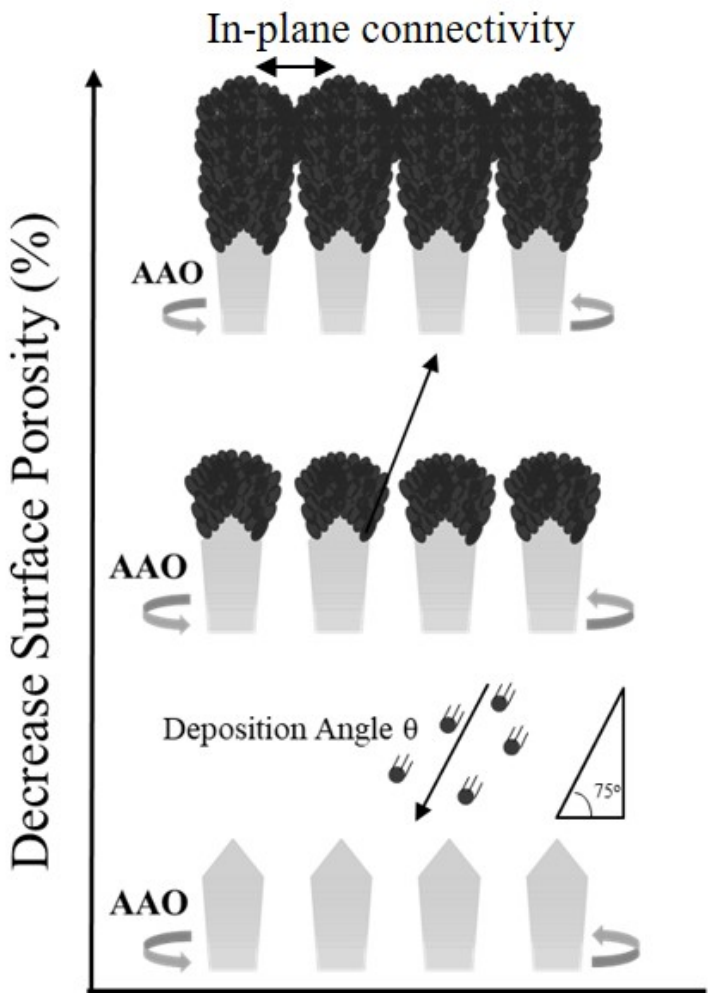

Figure 3.2 Schematic of the growth mechanism of the electrode deposited by sputtering related to surface porosity and the in-plane connectivity.

than deposition pressure, anode thickness is also greatly affecting the surface porosity of the anode deposited on AAO. Figure 3.2 shows schematic of the growing mechanism of co-sputtering anode on AAO. From the schematic, it can be speculated that the columnar structure of the sputtered layer is attributed to the decrease in surface porosity of the anode. Furthermore, not only the surface porosity is affected by the thickness of the anode, but also the in-plane connectivity is influenced by the width of the column structure. Confirmation of high TPB density of the anode deposited with 8 Pa is firstly processed. Secondly, the thickness effect of the Ni-GDC anode is tested by changing the thickness from 300 to 1000nm. Finally, the nano-column structure of Ni anode is controlled by changing incident angle and rotation speed since these two parameters have large impact on the structure change. The result of the electrochemical and microscopic analysis shows insight for designing high performance of nanostructured Ni-GDC anode fabricated by co-sputtering.

3.2 Experimental

For thin-film deposition of the electrodes and electrolyte, AAO substrate with 80nm pore diameter size was used for the support (Inredox, USA). The thickness of the substrate is about 100um. The substrate dimension is 1cm by 1cm. For the deposition of Ni and GDC for the electrode, a commercial sputtering machine (A-Tech System Ltd, South Korea) was used with Ni pure metal target (99.99%) and Gd 20mol% doped ceria target (99.9%). Deposition power control was done by direct current (DC) source and radio frequency (RF) source. DC power is controlled from 50W to 200W for Ni sputtering, and RF power is controlled from 0 to 100W for

GDC sputtering. In case of co-sputtering, the two guns were loaded to the sputtering chamber with the same incident angle for each target. Chamber pressure is determined by the gas flow and pressure controller. For anode and cathode deposition,

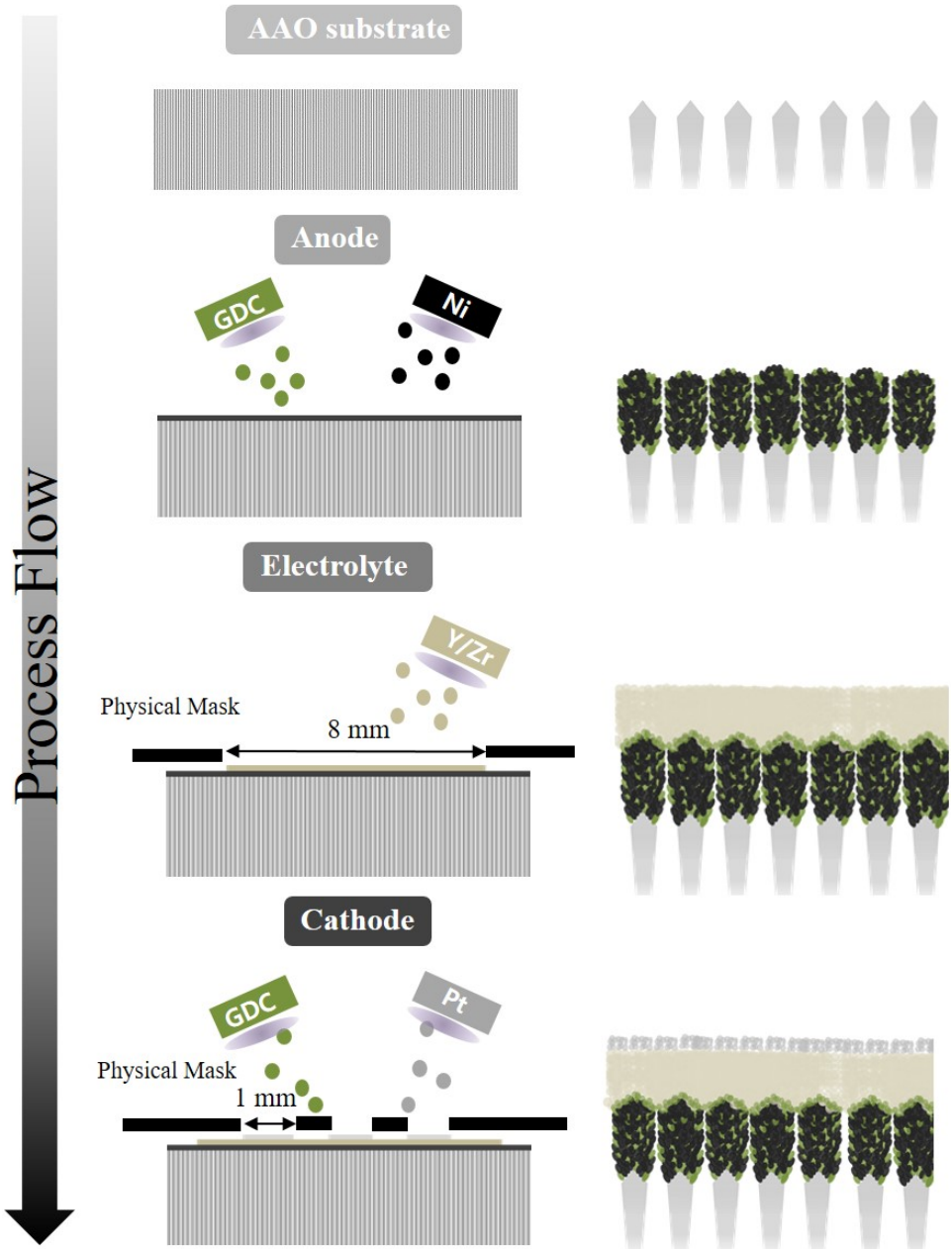

Figure 3.3 Schematic of fabrication process for thin-film SOFCs.

Ar gas atmosphere was used, while Ar/O_2 mixture atmosphere was used for the electrolyte deposition. A thin-film electrolyte is deposited by Y/Zr metal target ($Y_{0.16}Zr_{0.84}$, 99.9%). For reactive sputtering process, chamber atmosphere was controlled by Ar/O_2 mixture gas with 20% O_2. The power is fixed to 200W for YSZ electrolyte deposition. For cathode, Pt metal target (99.9%) and Gd 20mol% doped ceria target (99.9%) were used to deposit Pt-GDC cathode. The deposition power is set to be 100W for Pt and 50W for GDC target. The chamber pressure is also fixed to 12 Pa and applied to every cell fabricated in this thesis.

Thin-film electrolyte and cathode deposition was patterned by physical mask. Considering the substrate dimension, a stainless steel mask with 8mm by 8mm opening was used to deposit the electrolyte. Anode exposed to the air was covered with Ag paste for electrical connection between the anode and the jig. Cathode mask with 1mm by 1mm opening was used to pattern the cathode.

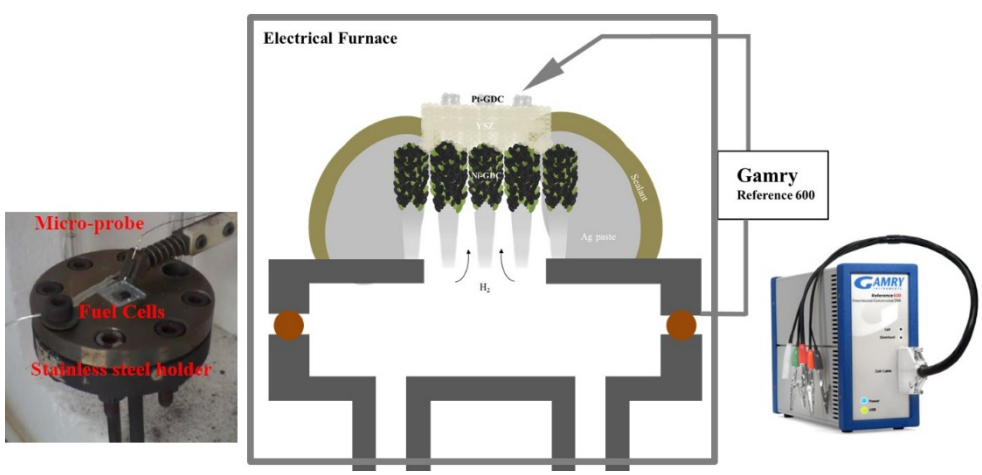

Figure 3.4 Schematic and actual image of a customized test station with TF-SOFCs attached to the stainless steel cell holder (jig).

Thin-film nanostructure was characterized by field emission scanning electron microscope (FESEM) and focused ion beam (FIB) analysis. Magnification of FESEM was varied from 10 to 20000. In addition, the electrochemical performances of the cells were measured by Gamry (Reference 600, Gamry Instrument, USA). TF-SOFCs was attached to the stainless steel jig with Ag paste for electrical connection between the jig and the anode on AAO. After drying process of Ag paste, ceramic sealant was applied on top of dried Ag paste for sealing. TF-SOFCs attached to the jig was dried at ambient air for 4 hours before the testing. The cell was tested in the customized test station consisted of halogen heater. The ramping rate of the temperature was set to be 8℃ per minute. The temperature of the test station was heated up to 100℃ and stayed there for 40min, and sequentially heated up to 500℃ for cell operation. After the temperature of the test station reached the operating temperature, the cathode was contacted with the customized probing tip controlled by X-Y-Z station.

3.3 Results and Discussion

3.3.1 Determination of Deposition Pressure for High Performing Nanostructured Ni-GDC Anode

To verify the porosity effect on Ni-GDC anode deposited by co-sputtering, co-sputtered Ni-GDC was fabricated with 4 Pa and 8 Pa. The surface porosity and the cross-sectional image of the Ni-GDC with 4 Pa and 8 Pa were comparatively shown in figure 3.5. From the surface FESEM images, it is clear that co-sputtered Ni-GDC anode deposited with 8 Pa shows higher porosity. However, even though the grain structure and porosity of the surfaces are different from the nanostructure analysis depending on the chamber pressure, actual electrochemical performance

should be compared by electrochemical impedance spectroscopy (EIS) analysis. In terms of interpretation of EIS graph, the value at the intersection between the graph and the real X-axis at high-frequency region means the ohmic resistance[87]. In addition, it is widely known that the ohmic resistance caused by ion and electron transports is independent of measuring voltage of the cell while the polarization resistance is dependent on the voltage. The size of arc presented in the Nyquist plot is relevant to anode-electrolyte and cathode-electrolyte polarization. Regarding these knowledge, EIS results of Ni-GDC anode varied with deposition pressure indicate that polarization resistance of the Ni-GDC deposited with 8 Pa showed 90% decrease

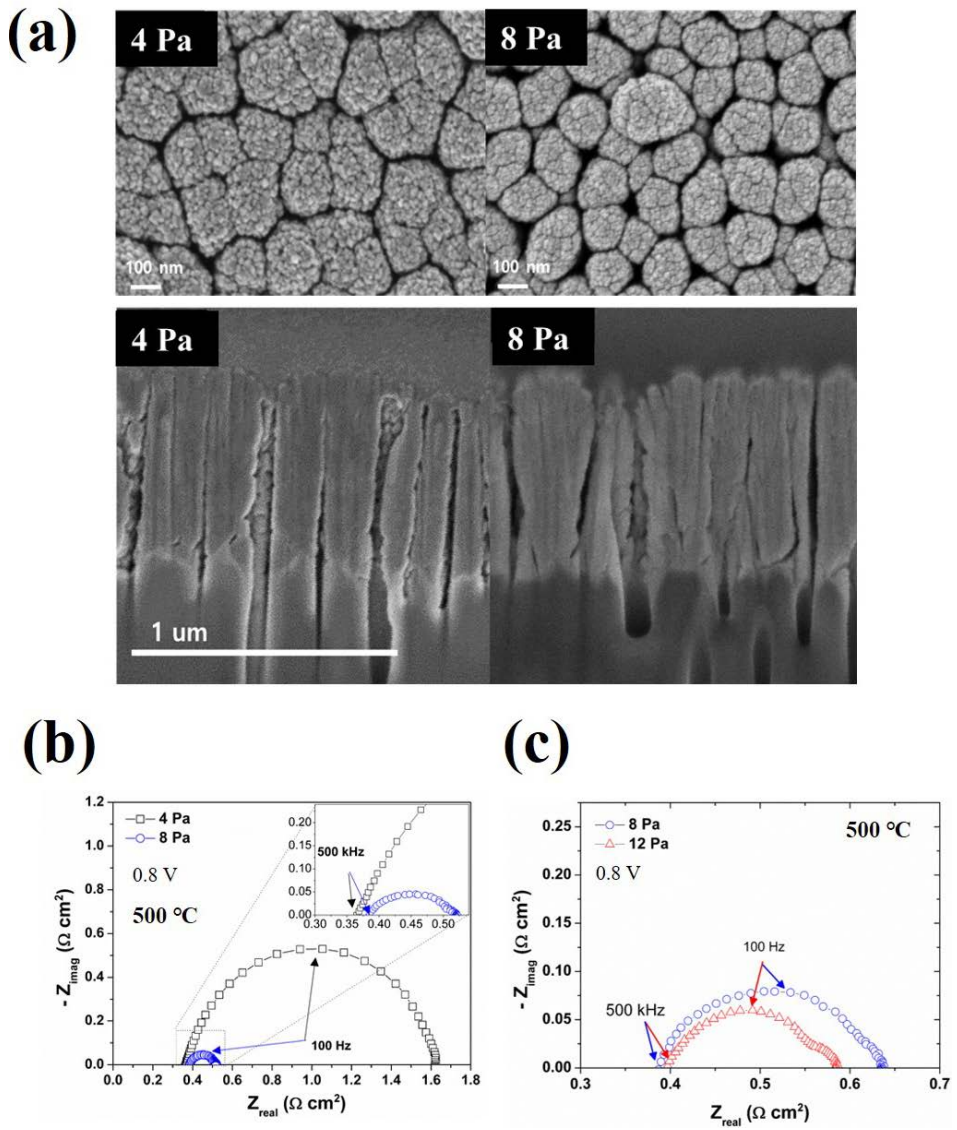

Figure 3.5 (a) Nanostructure change in surface and cross-sectional view varied with deposition pressure (4Pa, 8Pa). (b) Effect of porosity of Ni-GDC varied with 4 and 8 Pa on electrochemical performance measured by EIS.

compared to the one deposited with 4 Pa. Higher chamber pressure (12 Pa) was also suitable condition for fabricating nanostructured anode with high activity confirmed from the EIS graph in figure 3.5 (c). However, the enhancement in polarization resistance was negligible considering 0.8V of measuring voltage for EIS analysis.

Electrolyte and cathode deposition condition was the same for all samples. Therefore, it can be concluded that the difference in polarization resistance of the EIS results is attributed to the difference in anode nanostructure. From these results, we believe that 8 Pa of chamber pressure for highly active Ni-GDC nanostructure is enough to produce high power density at low-temperature. This chamber pressure was used for all other parameter experiments throughout this thesis.

3.3.2 Thickness Effect of Co-sputtered Ni-GDC Anode

Due to the material characteristic of AAO, as previously mentioned, anode thickness of Ni-GDC on AAO should be prominent factor for determining the performance of TF-SOFCs. For an accurate comparison, except for thickness of the anode, composition, electrolyte thickness, and cathode structure were maintained at same condition. GDC contents in the anode were set to be 12.8%, which was controlled by the deposition power of the GDC target (50W). The thickness control of Ni-GDC anode was confirmed from the cross-sectional FIB-SEM images. The thickness was controlled by the deposition time. Current density (j) –voltage (V) - power density (P) curves (polarization curves) were measured for different anode thickness samples. It is noteworthy that the peak power density was increased as the thickness increased up to 800nm. However, as the thickness of the anode was

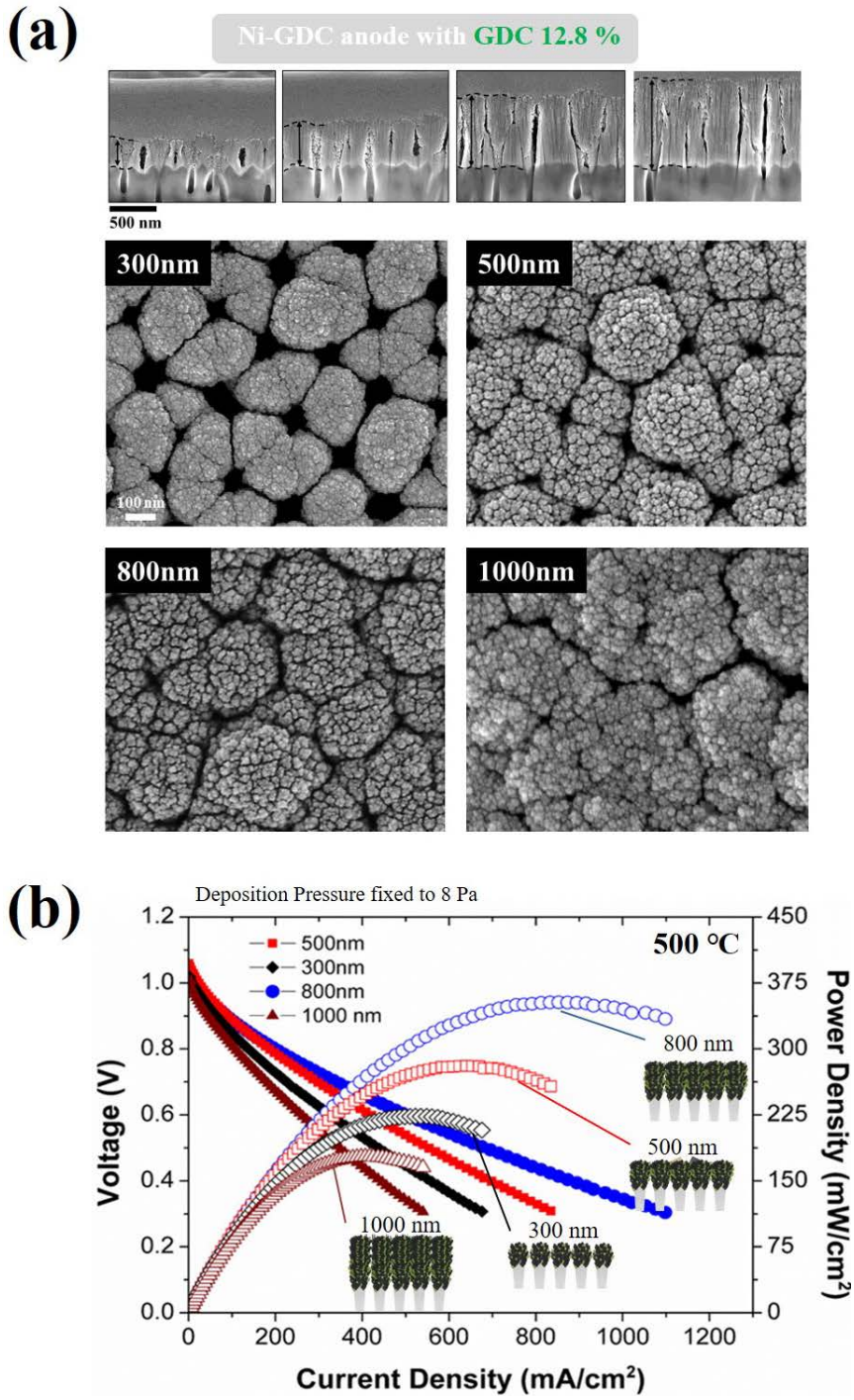

Figure 3.6 (a) Nanostructure surface FESEM and cross-sectional FIB-SEM images of the co-sputtered Ni-GDC anodes with 12.8% GDC content. The anode structure was varied with the thickness from 300 to 1000nm. (b) Current density (j)-voltage (V)-power density (P) of the cells varied with anode thickness was compared.

increased over 1000nm, the performance of TF-SOFCs steeply dropped over 50% from the peak power density of 800nm anode. Detailed contribution to performance difference was analyzed by EIS measurements. Figure 3.7 describes that the performance difference between 300, 500, and 800nm anode structure was attributed to both polarization and ohmic resistance. However, in the range of anode thickness from 500 to 800nm, enhancement in ohmic resistance (over 30% reduction) was

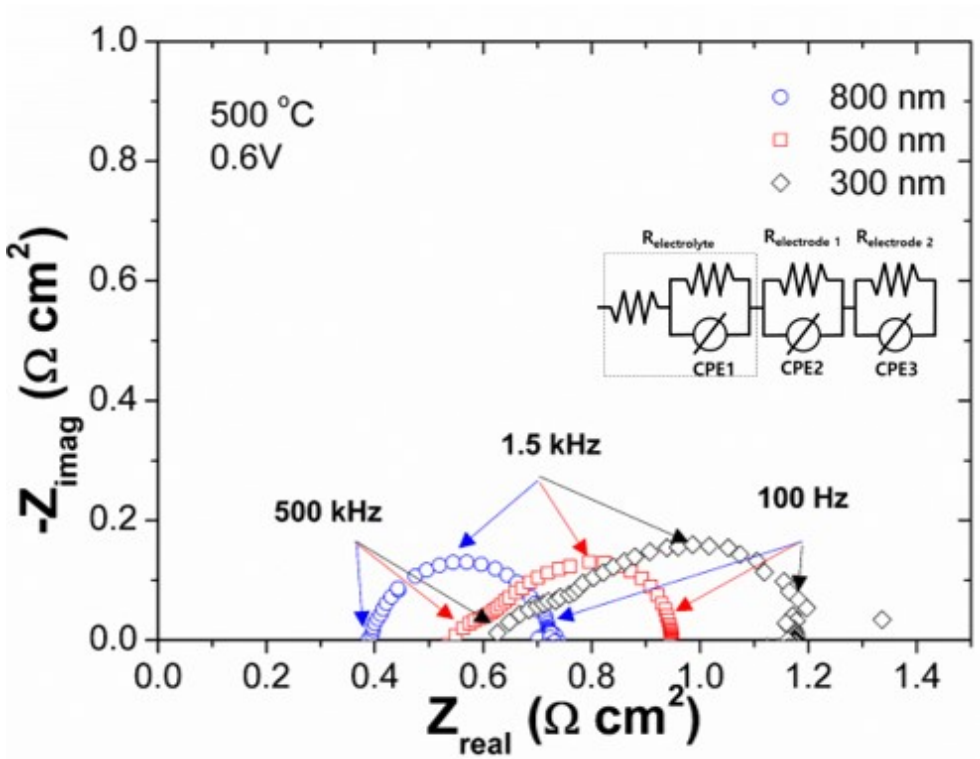

Figure 3.7 EIS results of TF-SOFC with Ni-GDC anode thickness 300, 500, and 800nm measured at 0.6V.

substantially higher than that in polarization resistance (15% reduction). More importantly, anode thickness with 1000nm showed an abrupt increase in polarization resistance compared to 800nm sample, while the ohmic resistance of 1000nm sample was slightly decreased (about 7%). These results indicated that active TPB density of 1000nm sample was decreased significantly. From the nanostructure analysis, it can be speculated that polarization resistance of 1000nm sample was increased due to decrease in surface porosity. As the in-plane connectivity was improved with the thickness increase, density of active reaction sites was also increased, which was consistent with a decreasing tendency of ohmic and polarization resistances. The comparison result of bode plot was also consistent with the speculation. In the frequency range between 10^4 to 10^2 Hz, phase angle of 1000nm sample was clearly higher than that of 800nm sample, which represents surface exchange reaction rate was the major contribution for the difference in polarization resistance. From these results, 800nm thickness of co-sputtered Ni-GDC anode showed the best performance, and the performance could be more enhanced by controlling other parameters.

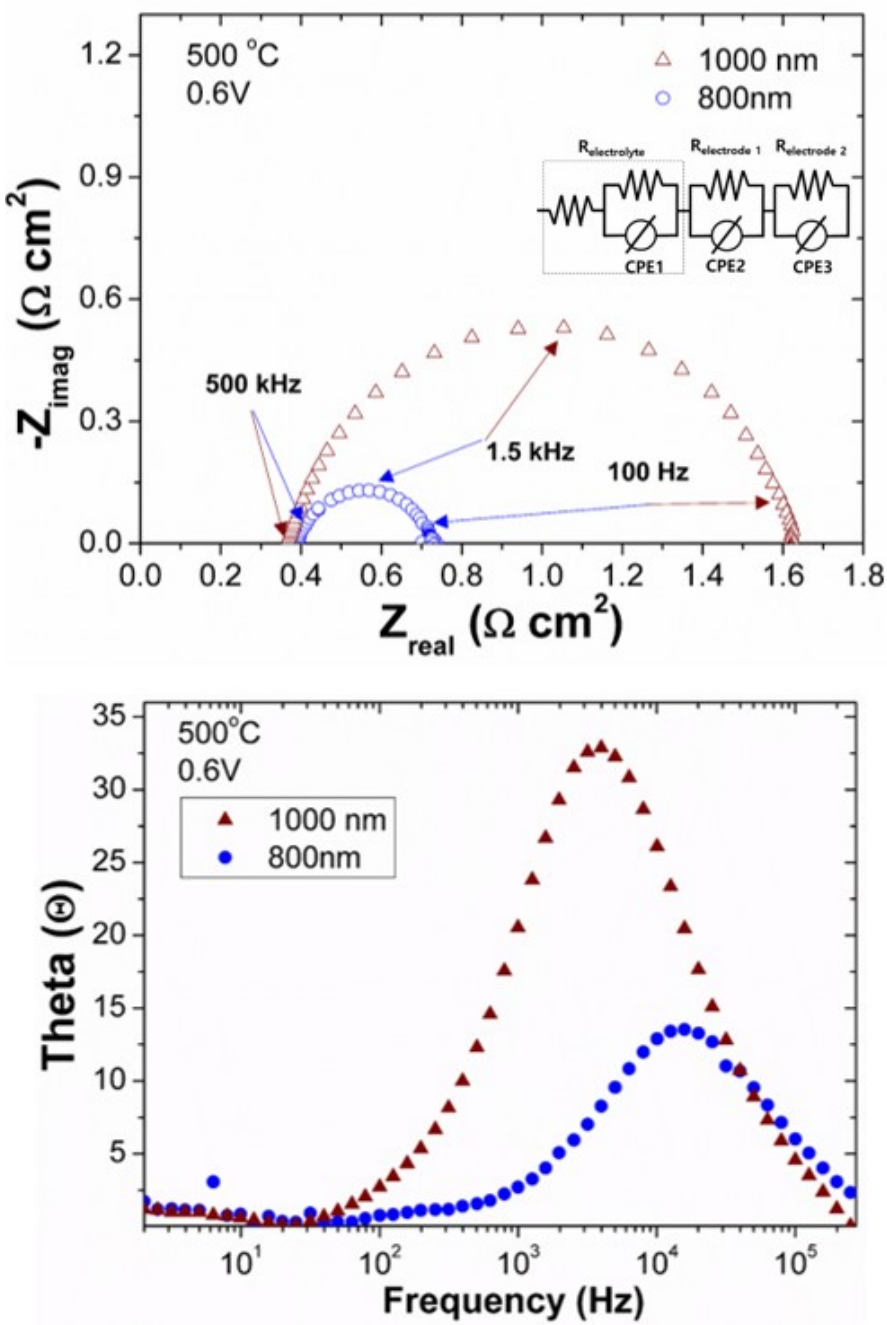

Figure 3.8 EIS and bode plots of Ni-GDC anode thickness varied with 800 and 1000nm. The measurement voltage is 0.6V. The frequency range is from 10^6 to 2 Hz.

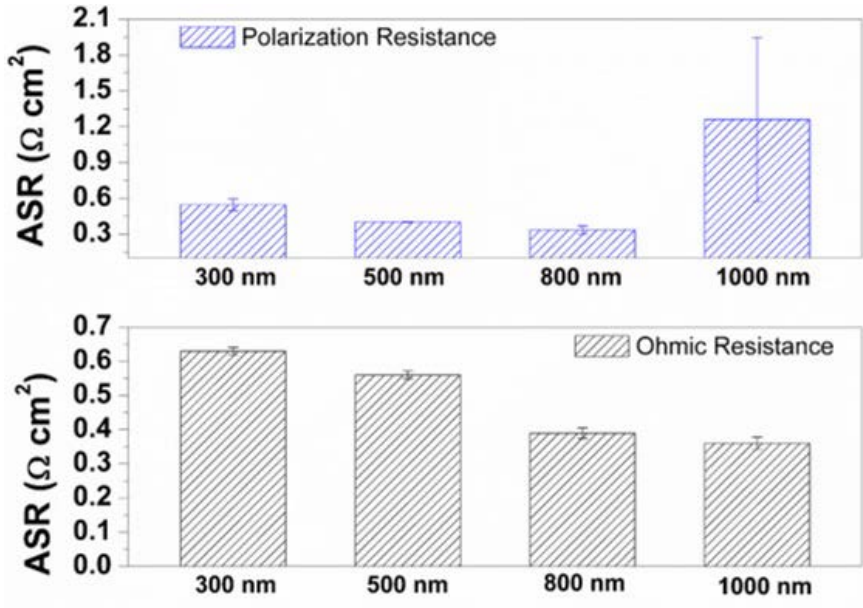

Figure 3.9 EIS equivalent circuit fitting results varied with anode thickness.

Thickness [nm]	300	500	800	1000
R_ohm [ohm·cm²]	0.63	0.56	0.39	0.36
R_pol [ohm·cm²]	0.55	0.40	0.34	1.26

Table 3.1 Area-specific resistance of ohmic and polarization for Ni-GDC anode varied with thickness.

3.3.3 Nano-Column affected by Sputtering Angle & Rotation Speed

From the experimental results for anode thickness change, it can be speculated that in-plan connectivity of the nanoporous anode structure can be the most profound factor for determining the peak power density of TF-SOFCs. At this point, it is essential to consider how the electrical network is connected in side of the nanoporous anode structure on AAO substrate. In figure 3.10, surface structure of bare AAO, 250nm thickness of Ni anode, and 800nm thickness of Ni anode are shown. As the Ni is grown on the nanoporous substrate, the electrical connection

should be formed through the yellow line drawn in figure 3.10. At the early stage of the nanoporous thin-film formation, the film morphology follows the substrate surface shape. As the film has grown over 800nm thickness, the size of the pore is reduced and a few columns are combined into one large column structure. It is notable that the electron produced from the anode-electrolyte interface has no way to go in-plane direction if the TPB is formed at the surface of Ni anode. The electron produced from electrochemical oxidation should be transferred to in-plane direction through the weakly connected Ni grains. Although closely packed Ni grains structure has multiple connections in nanoscale, it can be assumed that the change in the overall in-plane resistance highly depends on the shape of the nano-column. From this assumption, the width of the Ni nano-column was controlled by changing the sputtering incident angle and substrate rotation speed. In addition, the in-plane resistance of the Ni anode on AAO was measured by four-point probes. Consequently, electrochemical performances were measured and compared.

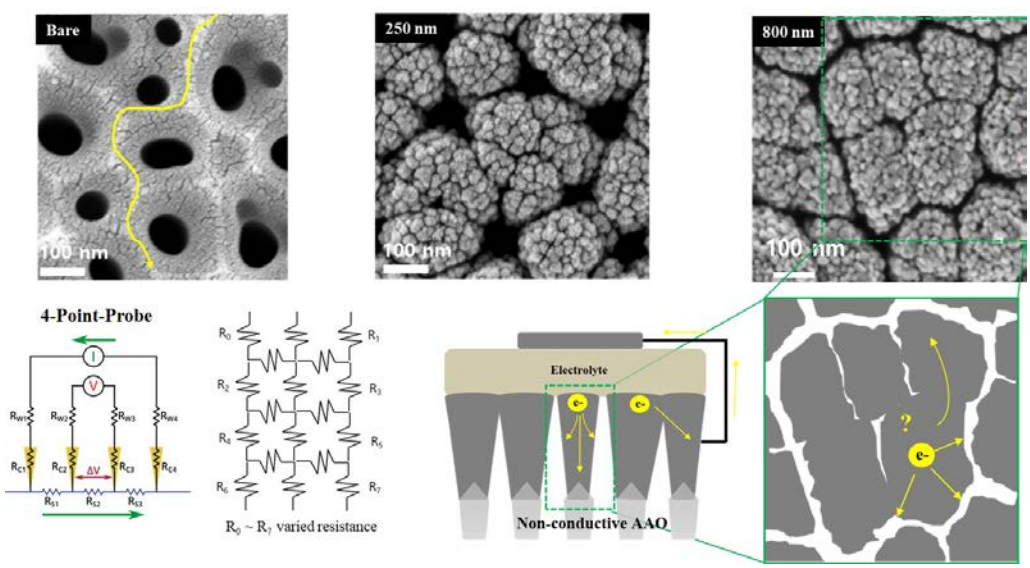

Figure 3.10 Surface nanostructure of bare AAO, 250nm and 800nm thickness of Ni anodes. Schematic illustration of an electron transfer path from TPB. The overall in-plane resistance consisted of multiple nanoscale connections of resistances is measured by 4 point probe.

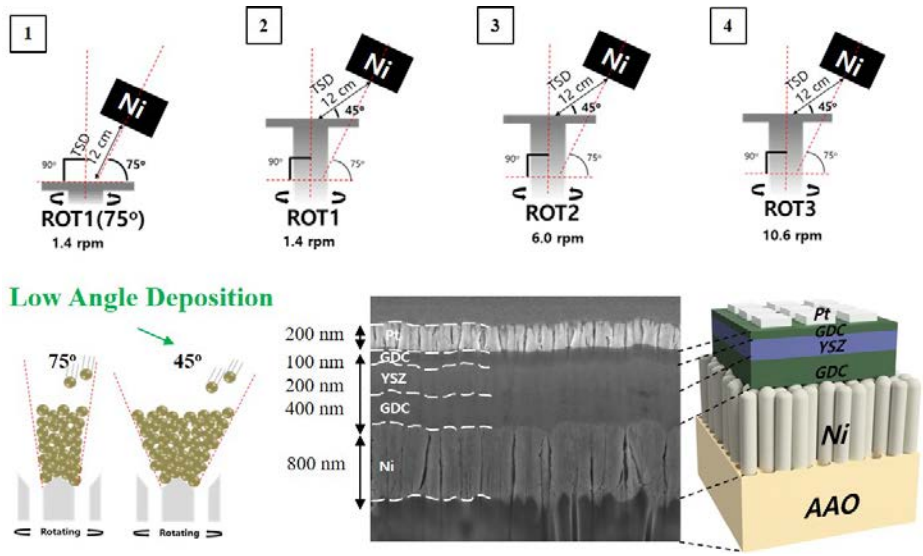

Figure 3.11 Schematic illustration of Ni anode fabrication varied with deposition angle: 75 and 45 degrees. Sample number 1 was deposited with 75 degrees. Sample number 2 was deposited with 45 degrees at rotation speed of 1.4 rpm. Rotation speed was controlled at 1.4, 6, and 10.6 rpm for sample numbers 2, 3, 4. A schematic illustrated in the right side comparatively shows the column structure affected by low angle deposition.

Four kinds of Ni anode samples were fabricated: Sample 1 was deposited by 75º incident angle and rotation speed 1.4 rpm (ROT1). Sample 2, 3, and 4 was deposited by 45º and variation of rotation speed 1.4 (ROT1), 6.0 (ROT2), and 10.6 rpm (ROT3), respectively. On top of the anode structure, 20mol% GDC and YSZ materials were deposited as sandwich structure by O_2 reactive sputtering process. To verify the in-plane resistance of the anode samples 1 and 2, 4-point-probe measurement was used. In figure 3. 12, comparison of the in-plane resistances of ROT1 sample with 75º and 45º was shown. The in-plane resistance of ROT1(75º) sample was higher by a factor of three times compared to that of ROT1(45º). Although the value of the resistance was low, contribution to the ohmic resistance could be large enough to affect the power density. The performance of ROT1(45º) was substantially improved at 450°C. EIS results showed that ohmic resistance of ROT1(45º) was reduced by more than 15% and consequently polarization resistance was also decreased. This reduction of

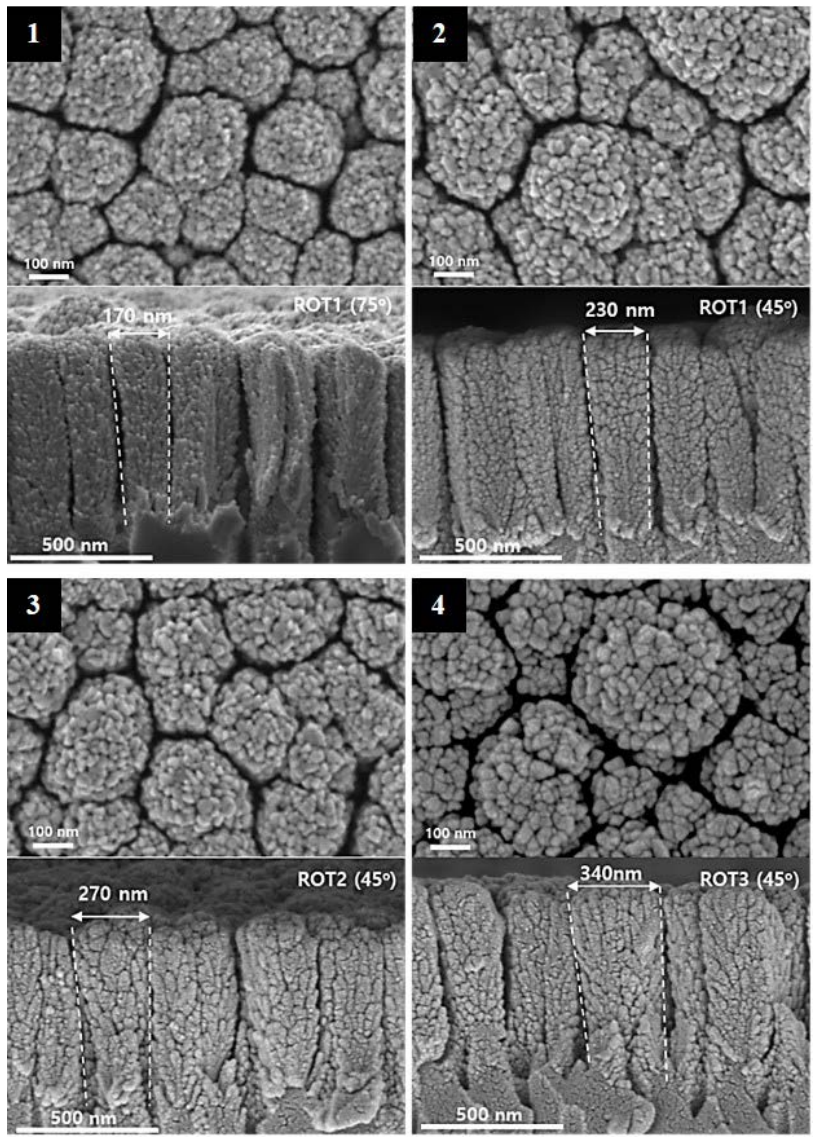

Figure 3.12 Surface nanostructure and cross-sectional FESEM micrographs of Ni anode with deposition conditions of sample numbers 1, 2, 3, and 4.

Sample	ROT1(75°)	ROT1(45°)	ROT2(45°)	ROT3(45°)	Anode Thickness (nm)
Column Width (nm)	170	220	270	340	~ 800

Table 3.2 Column width of sample numbers 1, 2, 3, and 4. Sample 1: ROT1(75°). Sample 2: ROT1(45°). Sample 3: ROT2(45°). Sample 4: ROT3(45°).

the resistances are totally attributed to the anode structure: columnar width. Other than these factors, surface porosity, crystallinity of the anode nanostructure, and the thickness were controlled to be same. Further investigation on the relationship between the nano-column width of the anode and the ohmic resistance was processed by controlling substrate rotation speed. As shown in figure 3.13, the peak power density of TF-SOFCs was steadily increased as the width of the nano-column increases. This tendency is clearly observed in figure 3.13 (c). Resultantly, the peak power density of Ni anode based TF-SOFCs was increased up to 304 mW/cm^2 at 450℃. The high peak power density (477 mW/cm^2) of Ni-based anode TF-SOFCs at 500℃ was obtained by using this Ni anode nanostructure deposited by low angle and high rotation speed. This performance of TF-SOFCs was higher than any other previous reports related to Ni-based anode AAO supported TF-SOFCs. We believe that this improvement, particularly on ohmic resistance, is attributed to the anode nanostructure especially related to column width. The control of the nano-column width by changing the sputtering parameter is the first attempt and contribution in AAO supported TF-SOFCs research field from this thesis.

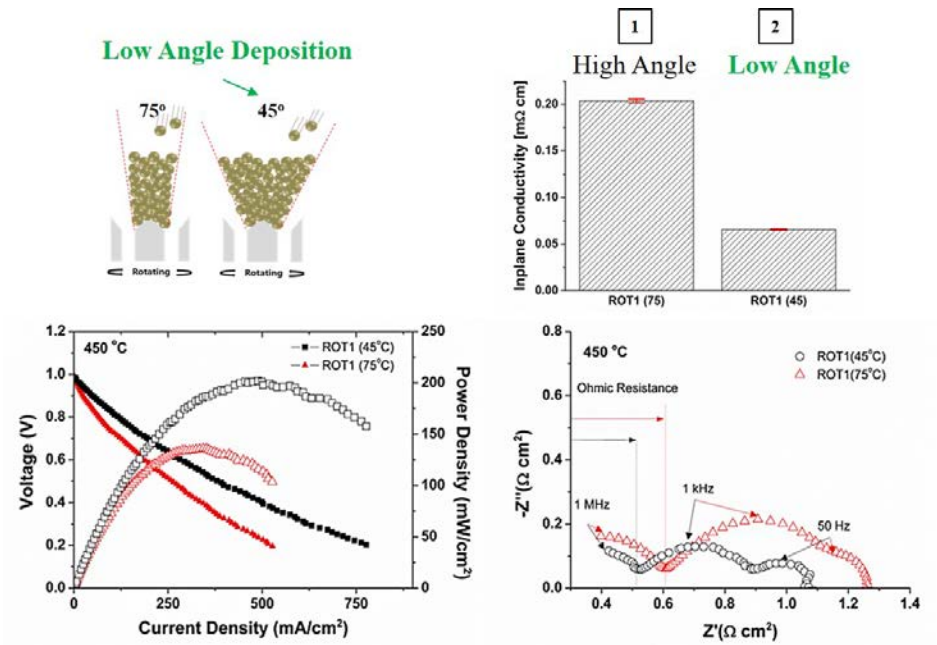

Figure 3.13 Electrochemical performance comparison of ROT1(75º) and ROT1(45º) samples.

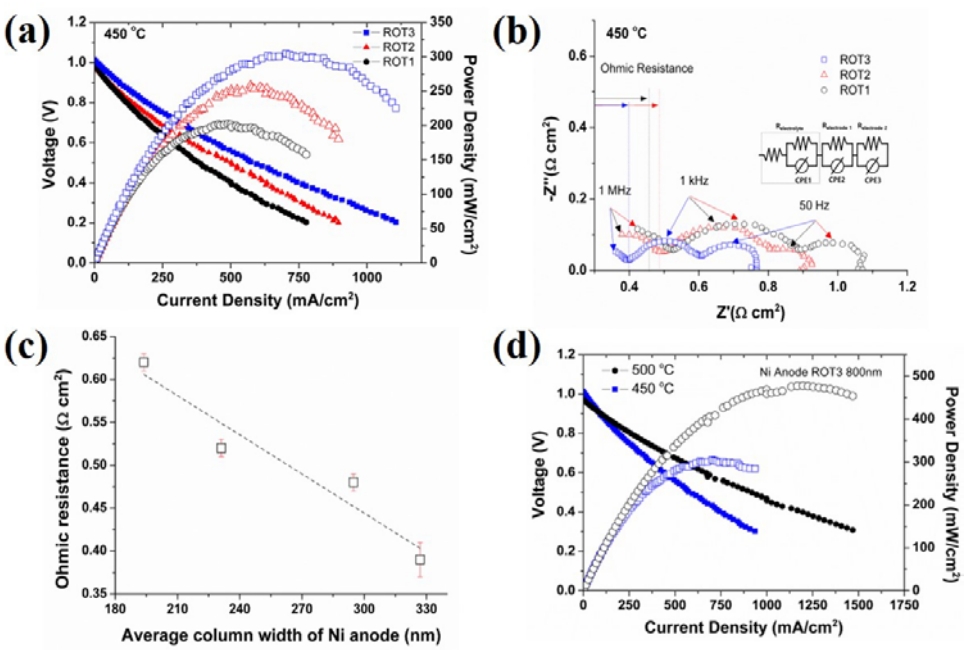

Figure 3.14 (a) j-V-P curves of sputtered Ni anode varied with rotation speed. (b) EIS measurements of ROT1(45º), ROT2(45º), and ROT3(45º) samples. (c) Relationship between nano-column width and ohmic resistance of TF-SOFCs. (d) Performance measurement at two different operating temperatures.

3.3.4 High Performance of Co-sputtered Ni-GDC Anode

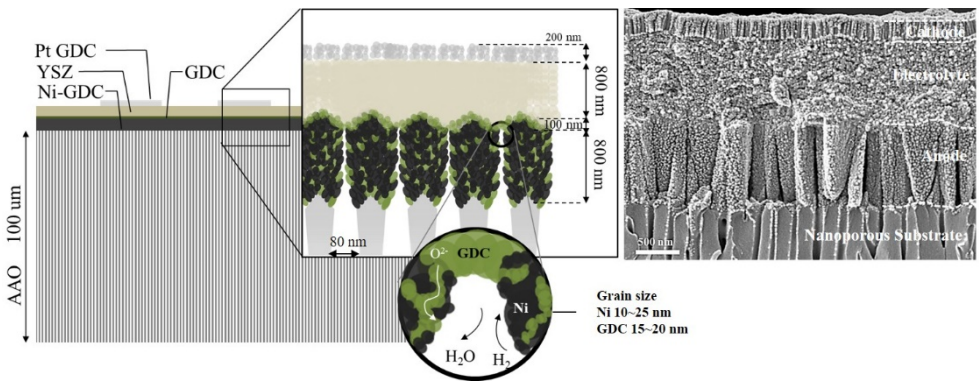

Figure 3.15 Schematic and cross-sectional FESEM images of TF-SOFCs.

Previous experimental results show that the anode nanostructure fabricated by sputtering can be delicately controlled, and the deposition parameter that mostly affects the performance of TF-SOFCs was found from parametric studies. The final process for obtaining high performing nanostructured anode is finding the optimized composition for Ni-GDC anode. Pure Ni anode is vulnerable to thermal agglomeration, and the TPB formation is limited to the interface between the electrolyte and anode. By applying the cermet anode on TF-SOFCs, the performance and the stability of the cell could be greatly enhanced. In co-sputtering process, low angle (45^{o}) and high rotation speed (10.6 rpm) are equally applied for all samples. Therefore, the structural advantage of sputtering anode confirmed from the previous experiments is valid for manufacturing co-sputtered Ni-GDC anode. The GDC composition in the cermet anode was controlled by changing the deposition power for the Ni and GDC targets. The detailed deposition condition for Ni-GDC and GDC composition according to the power control is presented in table 3.3. The volume fraction of GDC was increased from 0 to 27.7%.

Fixed Variable	Ar atmosphere 8 Pa / TSD 8 cm / Incident angle 45°			
Ni Deposition Power [W]	200			
GDC Deposition Power [W]	0	25	50	75
GDC composition in Ni-GDC anode [vol%]	0	3.9	12.8	27.7

Table 3.3 Co-sputtering conditions for nanostructured Ni-GDC anode on AAO.

Since the in-plane conductivity of the nanostructured anode on AAO substrate has great impact on the performance, GDC composition in the cermet anode should affect the performance by blocking the electron conduction path in Ni anode. Although ceria tends to be reduced and show partially electrically conductive at reducing atmosphere, still the electrical conductivity is much less than metal phase such as Ni. Therefore, mixing Ni nanostructure with GDC nano-sized grains could reduce electrical conductivity properties. Before, electrochemical performance measurement, the surface structures of the Ni-GDC anodes were compared because the surface porosity could be attributed to the performance difference. From the surface FESEM images, it is confirmed that the difference in surface porosity depending on GDC volume fraction of Ni-GDC anode was negligible. Therefore, the electrochemical performance difference between the samples should be attributed to the electrical and electrochemical properties of the anode. The samples with 12.8 and 27.7 vol% showed lower electrochemical performance compared to the bare Ni anode sample. Considering GDC contents contribute the formation of TPB density of the anode, it is hard to understand the decreased power density with higher GDC composition. From the EIS results, the performance decrease was mainly because of the increase in ohmic resistance. Although polarization resistance also increased with GDC contents, increase rate of the ohmic resistances was exceptionally high. A possible explanation for this phenomenon is that GDC nanoparticles mixed in Ni-

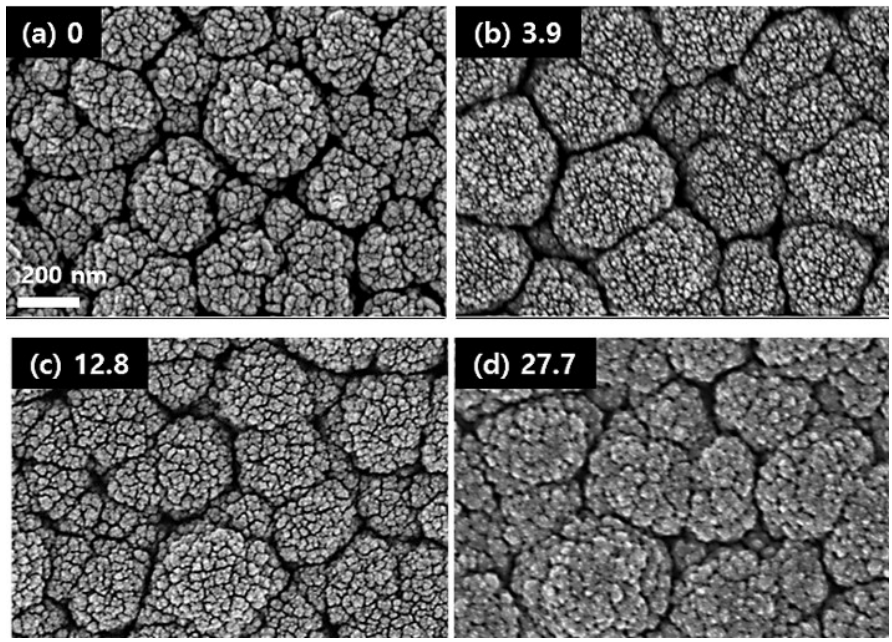

Figure 3.16 Surface nanostructure of Ni-GDC anode depending on GDC composition (a) 0, (b) 3.9, (c) 12.8, and (d) 27.7 vol%.

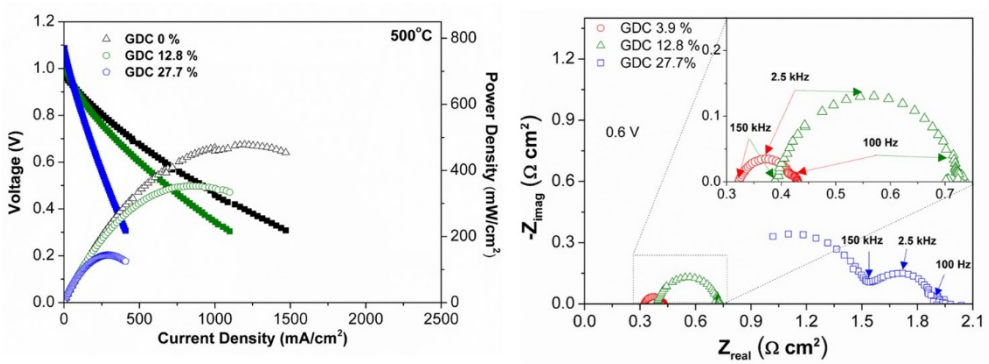

Figure 3.17 Electrochemical performance and EIS results measured at 0.6V of Ni GDC anode varied with GDC contents 0, 12.8, and 27.7 vol%.

GDC anode hinders the electron conduction through the anode. Consequently, deactivation of the reaction sites at the anode side was also increased causing the increase in polarization resistance. More interestingly, the maximum power density was obtained from nanostructured Ni-GDC anode with 3.9 vol% of GDC. Low

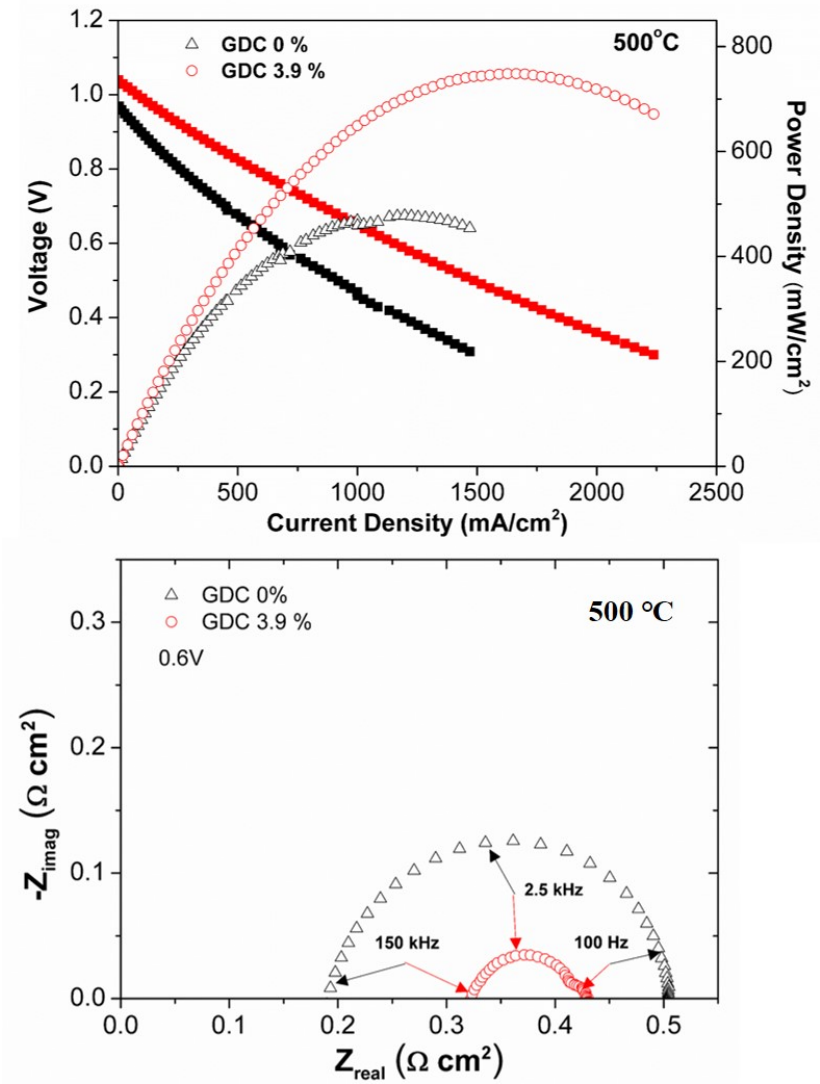

Figure 3.18 Performance comparison of Ni anode with Ni-GDC anode with low loading of GDC (3.9 vol%).

loading of GDC on Ni-GDC anode showed the maximum power density of 749 mW/cm^2 at 500℃. The contributions for the performance analyzed from EIS results indicated that ohmic resistance of the Ni-GDC 3.9vol% sample (0.32 $\Omega \cdot cm^2$) was higher than the pure Ni anode (0.2 $\Omega \cdot cm^2$). However, the increase rate was much intense at polarization resistance. The total area-specific resistance (ASR) of the Ni-GDC anode with 3.9 vol% showed only 0.43 $\Omega \cdot cm^2$ measured at 0.6V. To the best of our knowledge, this power density is the highest performance among AAO-based TF-SOFCs operated under 500℃.

3.4 Conclusion

Intensive research of the effect of the co-sputtering parameter on electrochemical performance of the nanoporous substrate supported TF-SOFCs has been presented for low-temperature. The anode nanostructure fabricated on the AAO was controlled by changing the various deposition parameters such as chamber pressure, deposition power, incident angle, and substrate rotation speed. Although the surface porosity and the thickness of the anode on AAO are known to be critical factors for determining the performance from the previous reports, it has never been confirmed in the co-sputtering system, and the more effective parameters are demonstrated from this chapter.

The early investigation on the effective porosity and the thickness of the co-sputtered anode are determined as 8 Pa and 800nm. Even though the porosity of the film can be more increased if the chamber pressure increase over 8 Pa, 8 Pa was

chosen for the all anode samples fabricated in this chapter because of the reasonable performance with this condition. The thickness of 800nm was optimum value for Ni-GDC co-sputtering anode. This value can be adjusted as the pore diameter of the substrate is changed. Over 800nm thickness of the anode, the polarization resistance was abruptly increased while the ohmic resistance was decreased, which means that the TPB density of the anode was decreased by the blockage of the gas diffusion path. Notable point found in this study is that the in-plane conductivity of the nanostructure deposited on the AAO has a considerable impact on the performance. Unlike the typical SOFCs structure, the electron conduction path in AAO supported anode is limited to the in-plane direction causing a large number of the deactivated zone and the significant ohmic resistance originated from the electron conduction. As the nano-column was controlled by rotation speed and incident angle of the co-sputtering, the peak power density and overall resistances were intensively decreased at low-temperature. The 45 degree of incident angle and 10.6 rpm of high-speed rotation for Ni-GDC co-sputtering presents the high performance in 450 and 500℃.

Finally, with the deposition conditions demonstrated for fabricating Ni-GDC anode, the composition of Ni-GDC anode beneficial for the performance has been presented for low-temperature operation. The excessive contents of GDC composite are negatively affecting in terms of ohmic resistance since the oxide materials could block the electron conduction path. Only 3.9 vol% of GDC in Ni-GDC anode showed the peak power density of 749 mW/cm^2 at 500℃, which is the highest performance among AAO supported TF-SOFCs with Ni-based anode at that temperature.

Chapter 4. Thermal Stability of Ni-GDC Anode deposited by Co-Sputtering

4.1 Introduction

The high surface energy of Ni causing the severe agglomeration at high temperature has always been issue on long term SOFC operation of Ni-based anode. In the literature, it has been reported that the grain size of the Ni and GDC changes the tendency of the agglomeration[88,89]. In addition, variation in GDC composite also greatly affects the structural change during the thermal annealing. From the previous chapter, the performance of Ni-GDC anode with high loading of GDC composite was lower than expectation. Except the in-plane conductivity, the thermal agglomeration effect could be another reason for the performance drop. Based on the knowledge of vulnerability of the nano-sized grain structure for the thermal agglomeration, it can be assumed that the thermal aggregate of Ni-GDC anode has impact on the electrochemical performance even at the very first measurement. To verify the thermal agglomeration tendency of nanostructured Ni-GDC deposited by co-sputtering, structural and operational characteristics were studied in this chapter.

Figure 4.1 Concept of agglomeration at nanostructured Ni-GDC anode.

4.2 Experimental

For various compositions of Ni-GDC anode on AAO substrate, Ni metal, and 20mol% GDC ceramic targets were used to deposit the film. Deposition power for Ni target was varied from 200 to 50W and the RF deposition power was controlled from 0 to 100W. The GDC composition variation was ranging from 0 to 51.3 vol%. Deposition pressure was kept in 8 Pa for fabricating all the samples. In addition, incident angle and rotation speed were sustained with 45 degrees and 10.6 rpm.

For full cell operation test, patterned YSZ electrolyte was deposited for 800nm, and the Pt-GDC cathode was fabricated on top of the electrolyte. Test for extended time operation was done by two kinds of operation. One was under constant voltage of 0.8, and the other one was OCV condition. The electrochemical performance and nanostructure was characterized by the same instruments used in the previous chapter.

The annealing temperature was set to 500℃. The atmosphere of the thermal annealing was sustained at reducing conditions by supplying the gas consisted of 80% hydrogen and 20% nitrogen.

4.2 Results and Discussion

The operational characteristic on extended time for TF-SOFCs varied with GDC composition on Ni-GDC anode was compared in figure 4.2. Samples were named with Ni volume fraction of Ni-GDC anode. The full cell was tested under 0.8V constant voltage at 500℃. The noticeable thing in this result was that the measured

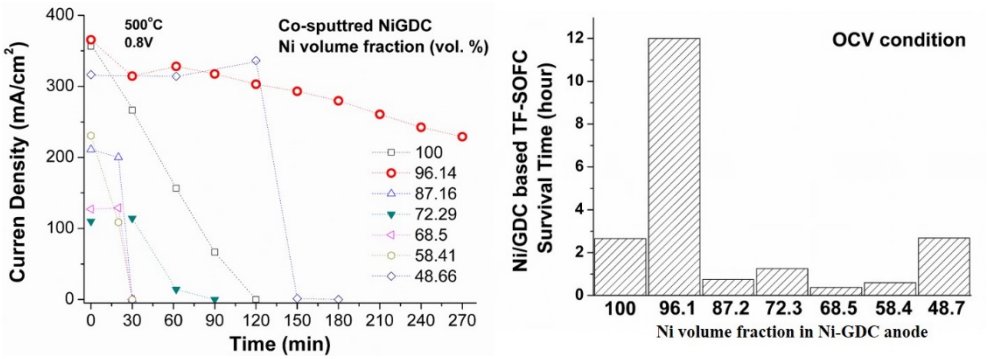

Figure 4.2 Operational characteristic of AAO supported TF-SOFCs with GDC composition variation of nanostructured Ni-GDC anode.

operation lifetimes of TF-SOFCs at constant voltage conditions were less than 180 minutes except for the Ni-GDC anode with 3.9 vol% of GDC (96.1 vol% of Ni). This trend is consistent with operation at OCV condition. Other than Ni-GDC with low contents of GDC, the lifetime was limited under 3 hours. To investigate the cause of the short cell stability of most of AAO supported TF-SOFCs with Ni-GDC anode, the structure change due to thermal annealing at reducing atmosphere was characterized with GDC composition variation. The degree of the agglomeration was intense at pure Ni anode considering the grain size growth. The grain size of as-deposited pure Ni anode was a few tens of nanometer. After annealing process, the grain size of agglomerated Ni anode measured from the high magnification of FESEM image was larger than 500nm, which means more than 20 times increase in grain size. Due to the severe agglomeration, AAO surface was exposed. Not only TPB loss in the anode-electrolyte interface, but also contact between the electrolyte and anode could be damaged. The severe structure change affected by thermal annealing was also observed for higher loading of GDC (over 12.8 vol %) at Ni-GDC anode. Although the agglomerated shape of the nanostructure was different, it can be speculated that Ni nano-sized grain wad diffused and agglomerated to form large grain structure.

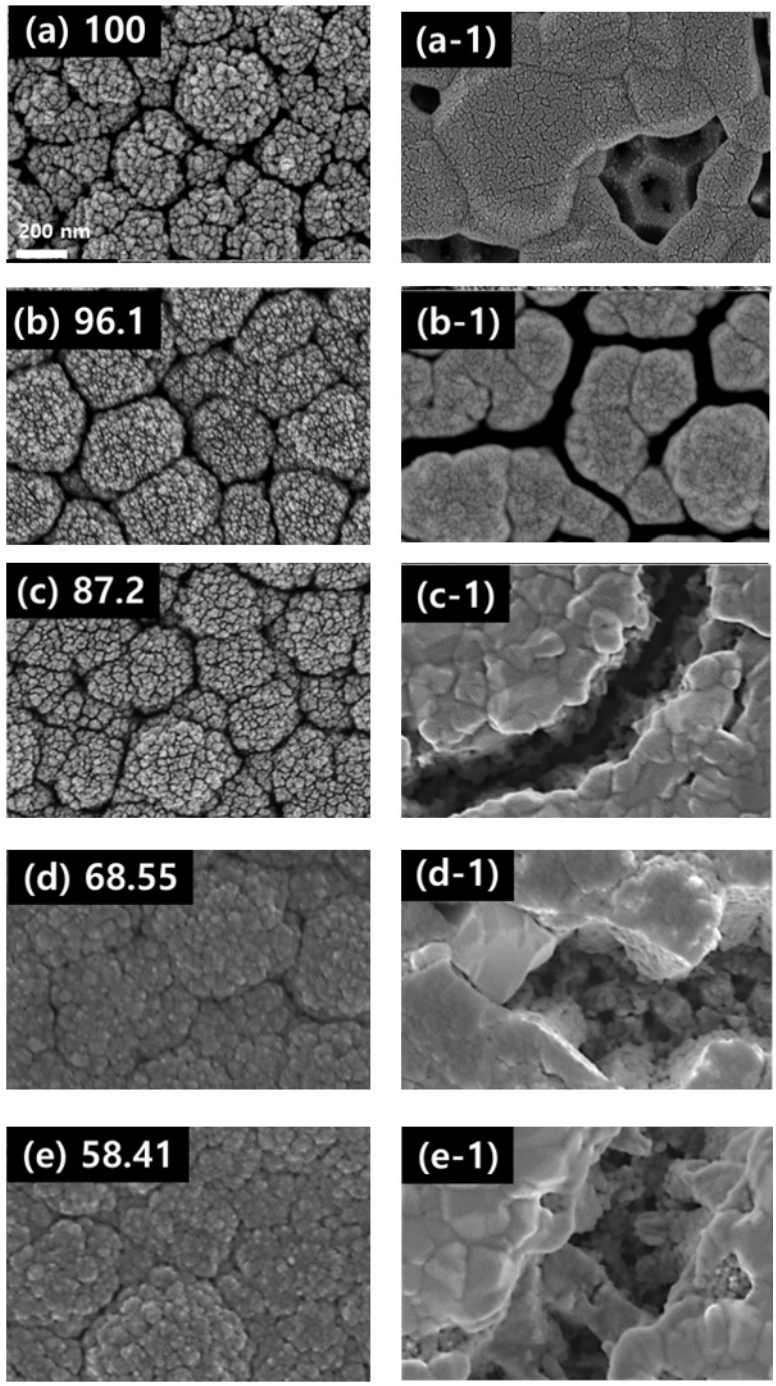

Figure 4.3 Thermal agglomeration of nanostructure depending on Ni volume fraction in Ni-GDC anode (a) 100, (b) 96.1, (c) 87.2, (d) 68.5, (e) 58.4. The samples were agglomerated at 500℃ for 3 hours at reducing atmosphere presented in (a-1), (b-1), (c-1), (d-1), and (e-1) (100sccm H2 through bubbler at room temperature).

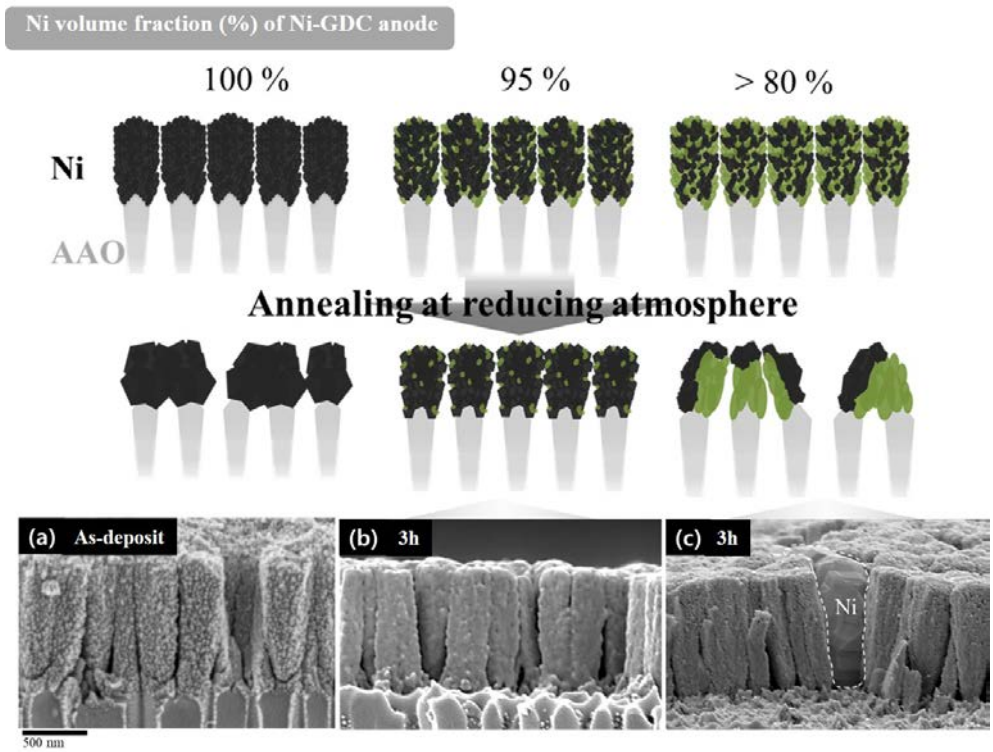

Figure 4.4 Schematic of agglomeration of Ni-GDC on AAO substrate depending on GDC composition. Side view of (a) as-deposit Ni-GDC anode, (b) Ni-GDC with 3.9 vol% of GDC annealed for 3 hours, and (c) Ni-GDC with high loading of GDC annealed for 3 hours. The white dot line is drawn to emphasize the agglomerated Ni grain.

The possibility of delamination at anode-electrolyte interface due to the agglomeration was examined by side view of the agglomerated Ni-GDC anode on AAO substrate. Compared to the as-deposit nanostructure of the Ni-GDC, the nanostructure change of the Ni-GDC with 3.9 vol% of GDC was negligible, only slightly agglomerated of the surface nano-grain. On the other hand, the Ni-GDC with high loading of GDC showed dramatic change in nanostructure. From the side view, it is clear that diffusion of Ni nano grain was the major mechanism for the Ni grain growth. Without the surface diffusion of Ni, the large grain formed inside of nanostructured Ni-GDC anode is impossible because the connection between Ni

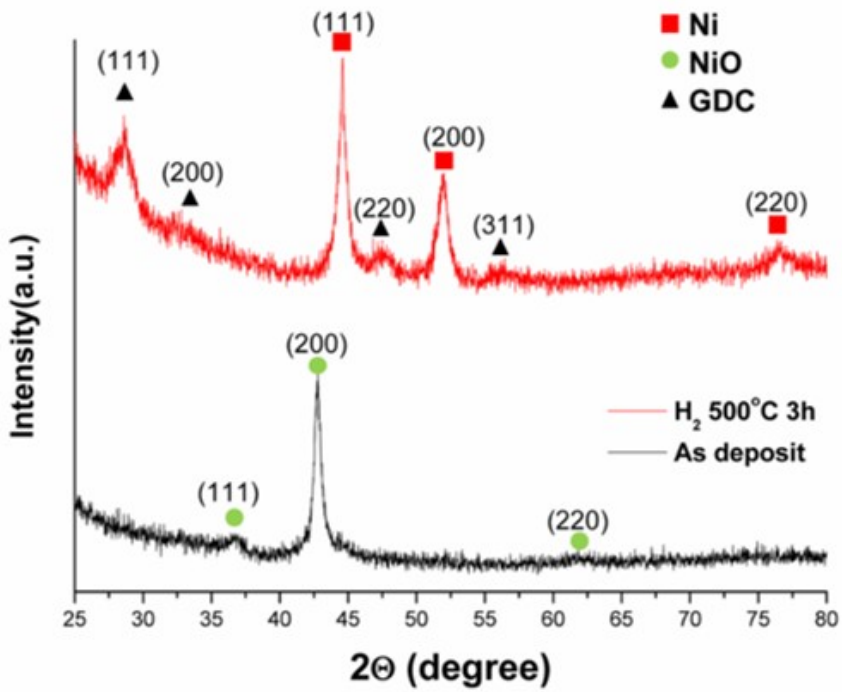

Figure 4.5 Crystallinity of as-deposit and annealed Ni-GDC anode measured by x-ray diffraction (XRD).

grains could be blocked by nanoscale GDC grains at a high level of GDC loading. Enhanced crystallinity of Ni and GDC phase was also consistent with the agglomeration tendency. Since the grain size and density of the structure affect the intensity measured from the XRD, severe agglomeration of Ni-GDC nanostructure was consistent with the change in chemical structure information.

4.4 Conclusion

The agglomeration tendency of Ni-GDC cermet anode fabricated by co-sputtering has been investigated for the different compositions of GDC in Ni-GDC anode. Pure Ni anode is already known to be vulnerable to the thermal agglomeration at 500℃. However, it is interesting that the high concentration of GDC (over 10 vol%) in nanostructured Ni-GDC on AAO support cause even more severe structural change possibly causing the cell failure. The small amount of GDC contents in Ni-GDC anode shows the least agglomerated structure attributed to the thermal protection from GDC nano-grains. The detailed mechanism for agglomeration of nanostructured Ni-GDC has not been demonstrated in this thesis. Nevertheless, it can be assumed from the nanostructure characterization that the high surface energy and diffusion rate of a few tens of nanometer grains could be the major reason for the Ni agglomeration. As confirmed from the side view of the agglomerated Ni-GDC layer, the large grain of Ni is formed in between GDC nano-column by Ni diffusion around GDC nanoparticle and sequentially combining with other Ni grains.

Chapter 5. Ni-GDC Anode for Direct Methane SOFCs

5.1 Introduction

In previous chapters, structural and compositional characteristics of Ni-GDC deposited by co-sputtering have been investigated in terms of electrochemical properties. Consequently, the record-high performance of nanostructured Ni-GDC anode based TF-SOFCs on AAO substrate was achieved due to the improved in-plane conductivity, TPBs density, and the enhanced thermal stability of the nanostructure. The direct utilization of the methane gas fuel could facilitate the commercialization of TF-SOFCs because of the reduced system size and the enhanced overall efficiency of the system[90–92]. Moreover, the existing infrastructure of supplying the natural composed of 90% methane can be beneficial for the practical use of TF-SOFCs as a portable energy source. Therefore, the development of direct methane TF-SOFCs is considered as one of the most imminent issues.

Ni-based anode is the most basic and common structure for reforming and electrochemically oxidizing methane fuel. As mentioned in chapter 1, the direct use of methane to the Ni-GDC anode has several issues. From the thermodynamic ternary diagram for C, H, and O, carbon deposition on the Ni catalyst likely happens at 500℃. On the long term operation with direct methane fuel, the SOFCs are failed due to severe carbon deposition deactivating the reaction sites on the anode. Furthermore, in operational perspective, the low steam to carbon ratio (S/C) is beneficial for the system efficiency due to the low dilution of the fuel[93]. However,

at low S/C ratio, the probability of carbon solid phase formation on metal catalysts is high in terms of thermodynamic point of view. Although the experimental study on direct internal steam reforming for Ni-GDC anode has been frequently demonstrated, the study on the direct use of methane to nanostructured Ni-GDC deposited by co-sputtering has been rarely reported. N. Laosiripojana and K.O. Christensen et al. reported that the nano-sized grain structure of Ni and ceria has resistance properties for carbon coking phenomenon[94,95]. From this literature information, it can be assumed that the co-sputtered Ni-GDC anode could show high catalytic performance for direct internal steam reforming due to the high surface area of the nanostructure even at low-temperature. Therefore, in this chapter, the electrochemical performance of the direct use of SOFCs with the co-sputtered Ni-GDC anode deposited on the scandia stabilized zirconia (ScSZ) pellet substrate was investigated at 500℃.

5.2 Experimental

The ScSZ electrolyte pellet with 150um thickness was used to support the nanostructured Ni-GDC anode for eliminating the possible leakage current through the electrolyte due to the low quality of the electrolyte. Ni-GDC anode deposited by co-sputtering was varied with deposition power. Resultantly, GDC composition of the anodes was controlled for 3.9, 12.8, 31.4, 48.2 volume percentage. The cathode deposition condition was set to be same as the previous experiments in chapter 4.

For the electrochemical measurement of the direct use of methane, methane was supplied to the cell through the bubbler filled with distilled water at room temperature. The methane gas supply was controlled for 50 sccm by mass flow meter

(MFC). For switching the methane fuel to hydrogen gas during the operation, two gas lines were set and controlled by manual valves. The cathode side was exposed to the ambient atmosphere.

The chemical composition before and after operation with a low S/C ratio of methane fuel was analyzed by x-ray photoelectron spectroscopy (XPS). The catalytic performance of nanostructured Ni-GDC anode for the reforming was characterized by measuring OCV of the cell with nearly dry methane.

5.3 Results and Discussion

One of the fundamental indicators of the electrochemical performance with direct methane fuel is the OCV of the cell. Especially, at low-temperature, the reforming kinetic is energetically not favored. Therefore, if the anode is not optimized at composition and structure, the OCV could not be formed with the direct methane fuel. Figure 5.1 shows the OCV of the anode with GDC 3.9 vol% was under 0.2 voltage, which means that the methane was not properly reformed or electrochemically oxidized. As the GDC composition increase in Ni-GDC anode, the OCV of the cell was starting to increase. Over 48.2 vol% of GDC composite in Ni-GDC anode, OCV was close to the theoretical value. This was also confirmed from the J-V-P curves of the cells. The peak power density of the Ni-GDC anode cell with 48.2 vol% showed higher performance compared to the cell with low loading of GDC composite. The major reason for the performance difference was attributed to OCV of the cells. On the other hand, it is noteworthy that current behavior was unstable in the high current region possible related to the reforming rate of the Ni-GDC.

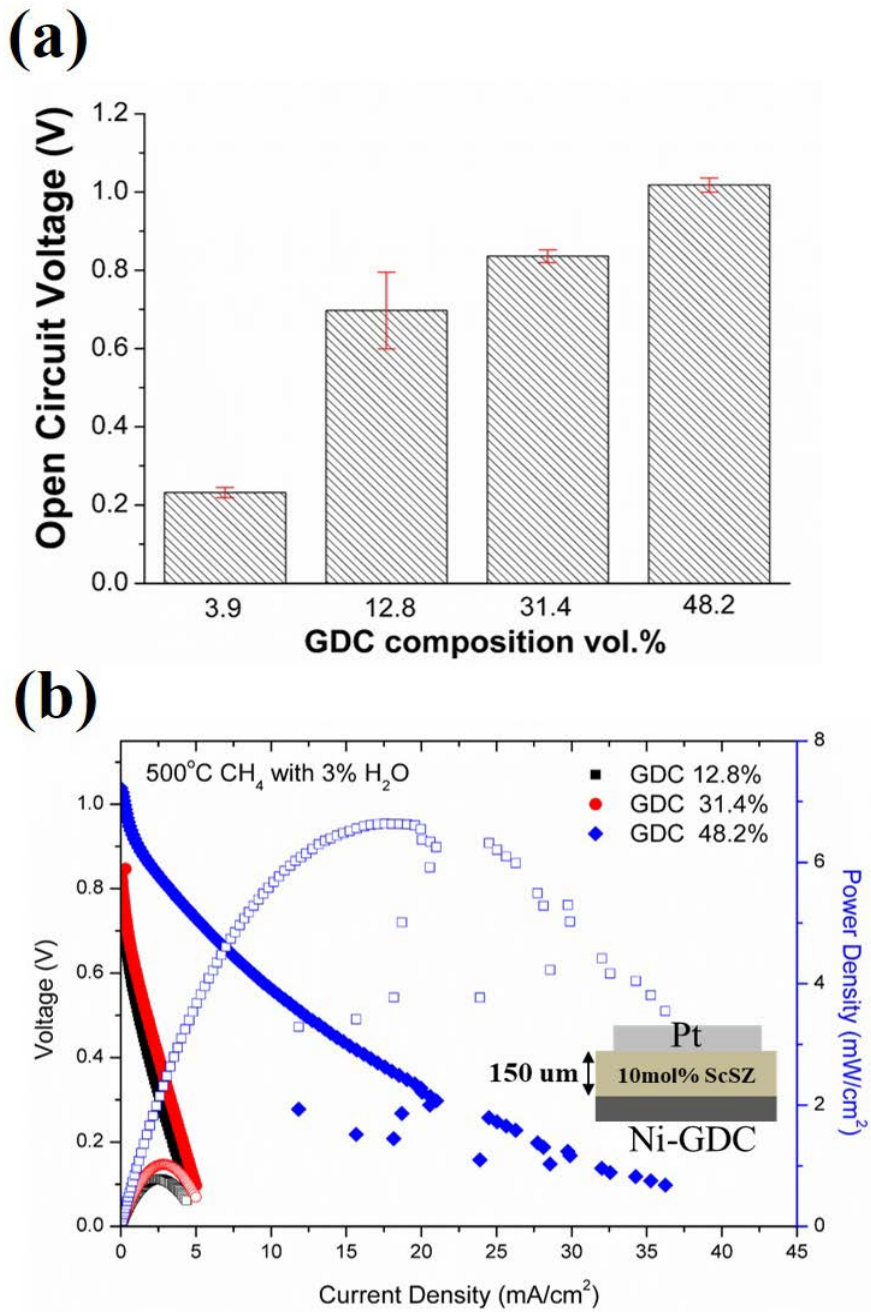

Figure 5.1 (a) Open circuit voltage (OCV) of the Ni-GDC anode on the ScSZ pellet operated with nearly dry methane (3 vol% H_2O). (b) JVP behavior of the Ni-GDC anode varied with 12.8, 31.4, and 48.2 volume percent at 500℃.

As the GDC contents of Ni-GDC anode increase, the TPB density of Ni-GDC anode is increased. This TPB could be acted as reforming sites due to the material characteristic of ceria for reforming. To further investigate the assumption about TPB density effect on reforming kinetic, two different anode structure with different grain size was tested with nearly dry methane at 500℃. The grain size of nanostructured Ni-GDC was less than 50 nm, while that of Ni-GDC fabricated by screen printing was more than 1um, which was more than 20 times larger. The OCV was measured for methane and hydrogen fuel. The results showed that OCV of the nanostructured Ni-GDC anode was over 0.8V with the methane fuel. However, the OCV of the anode fabricated by screen printing method indicated only about 0.2 V for the operation with the methane.

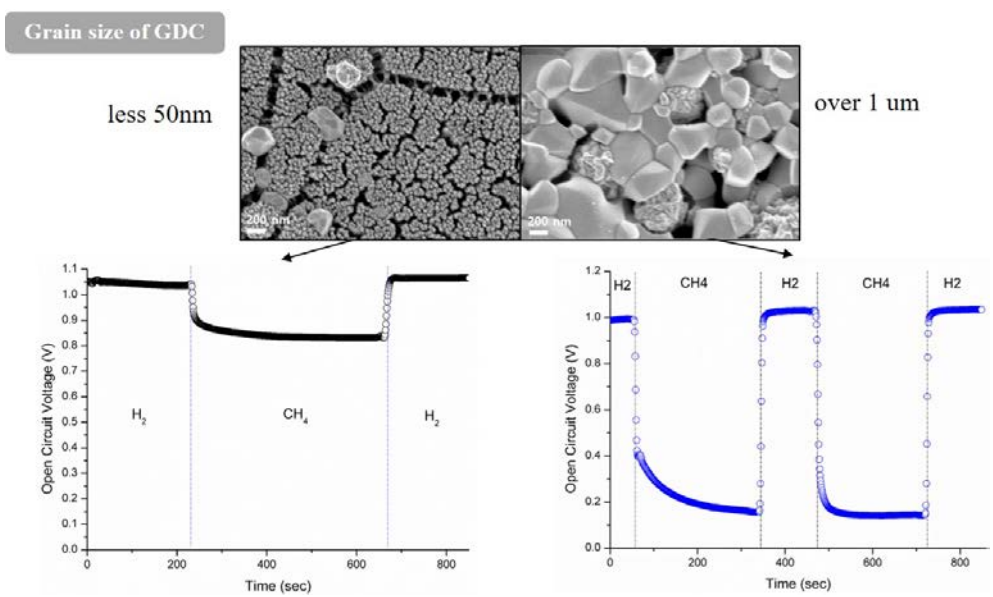

Figure 5.2 Grain size effect of Ni-GDC anode on open-circuit voltage (OCV) of SOFCs operated at 500℃.

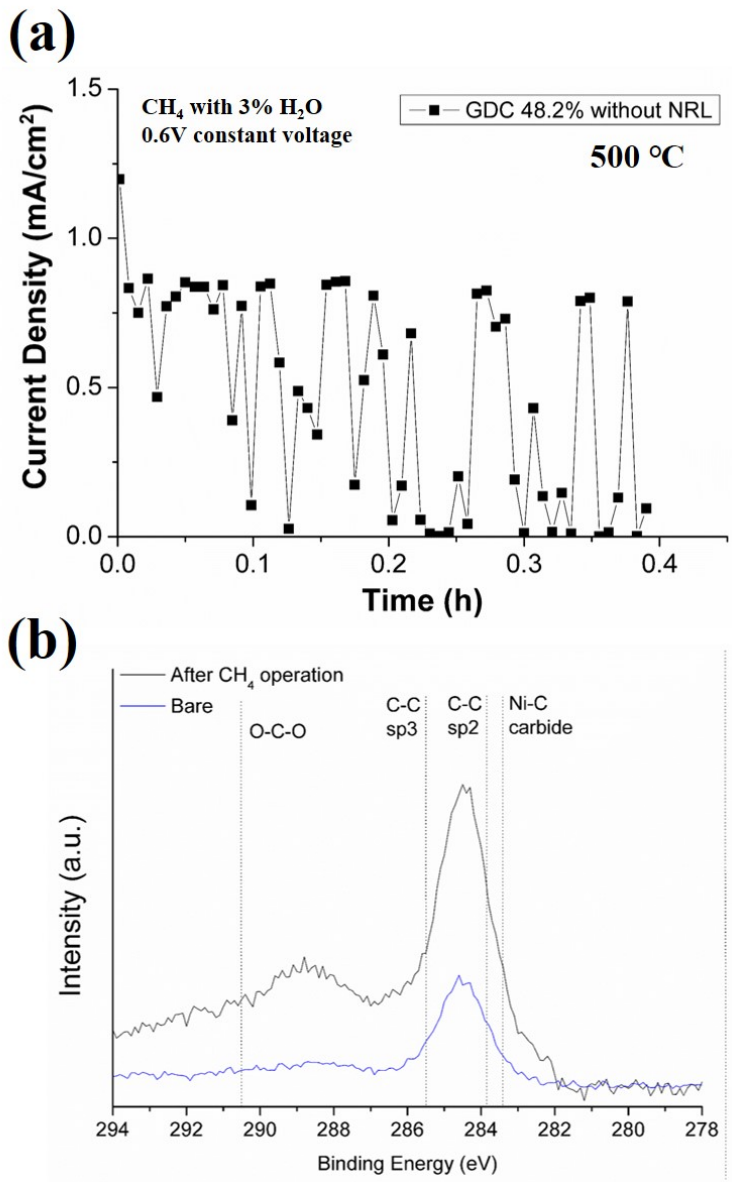

Figure 5.3 (a) Time-dependent characteristic of TF-SOFCs with Ni-GDC anode deposited by co-sputtering at 0.6V. (b) XPS analysis for co-sputtered Ni-GDC anode before and after the operation with CH_4.

Even though the nanostructured Ni-GDC with 48.2 vol% of GDC showed OCV and the performance, the lifetime of the cell was less than 30 minutes. The cause of this short life term was carbon deposition on the Ni metal catalyst of the anode. XPS results showed that Ni-C carbide and C-C binding were detected. Although the carbon was also detected for the bare Ni-GDC anode, the intensity related to the amount of carbon was much higher after methane operation. These results clearly indicated that the co-sputtered Ni-GDC anode was vulnerable to carbon deposition at a low S/C ratio and low-temperature[96]. For extending the operation time of nanostructured Ni-GDC anode, the additional reforming structure should be developed and fabricated on TF-SOFCs.

5.4 Conclusion

The compositional analysis for direct methane fueled TF-SOFCs with Ni-GDC anode is investigated in this chapter. Due to the nano-sized grain of Ni in co-sputtered Ni-GDC anode on ScSZ pellet, the reforming kinetic is greatly enhanced. This was comparatively shown with OCV data of the Ni-GDC fabricated by screen printing method. Even with the same composition of Ni-GDC, the Ni-GDC anode with large grain size (over 1um) showed no discernable OCV at 500℃ for a nearly dry methane fuel. In addition, the GDC volume fraction of co-sputtering Ni-GDC anode should be close to 50 % for producing reasonable OCV. However, the GDC contents of the highest performing Ni-GDC anode for TF-SOFCs was only 3.9 vol%. Therefore, to be operated with low S/C methane fuel, the additional reforming structure is required in TF-SOFCs architecture. The nanostructured reforming layer on TF-SOFCs could be fabricated by co-sputtering. The fabrication process for the reforming layer is investigated in the next chapter.

Chapter 6. Direct Methane Fueled Thin-film SOFCs operated at 500℃

6.1 Introduction

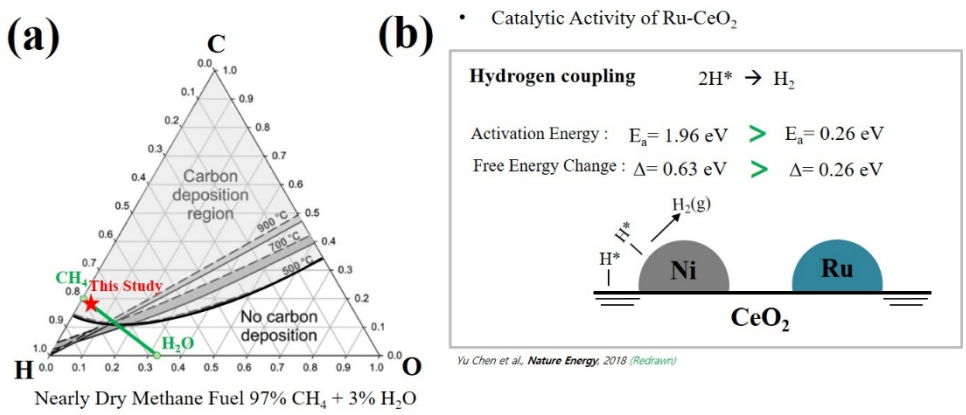

Figure 6.1 (a) Ternary diagram for C-H-O. The fuel composition for TF-SOFCs operation is 97% CH_4 and 3% H_2O. (b) Activation energy and free energy change of hydrogen coupling on Ni and Ru supported by ceria [77].

A low S/C ratio on methane fuel is vulnerable to carbon deposition on metal catalysts in thermodynamic point of view. However, if the metal nano-catalyst is supported with ceria-based materials, carbon species adsorbed on metal can be detached by reacting with lattice oxygen in the support. In addition, the rate of producing hydrogen, hydrogen coupling, depends on the activation energy and free energy change of hydrogen species. According to the report from Yu Chen et al., the hydrogen coupling reaction is thermodynamically and kinetically favored in Ru compared to Ni[77]. In material perspective, the mixture of Ru and ceria support is advantageous for direct methane operation, especially with a low S/C ratio.

Inspired by the recent work related to the thermal catalytic reforming performance of nano-catalyst on ceria support, it is assumed that the nanostructured Ru-GDC reforming layer deposited by co-sputtering could show high performance for methane reforming at low-temperature due to the nano-sized grain enabling the formation of high TPB density[97,98]. Uniformly mixed Ru-GDC reforming layer was fabricated on the bottom of AAO so that the reformed methane fuel could flow into the reaction sites of Ni-GDC anode. The fabrication of reforming layer on the bottom of the substrate is aligned with the state of the art design of the SOFCs structure for the direct methane operation. Even though AAO is electrically non-conductive, Ru-GDC is a thermal catalyst and electrically connected by Ag paste applied to the side.

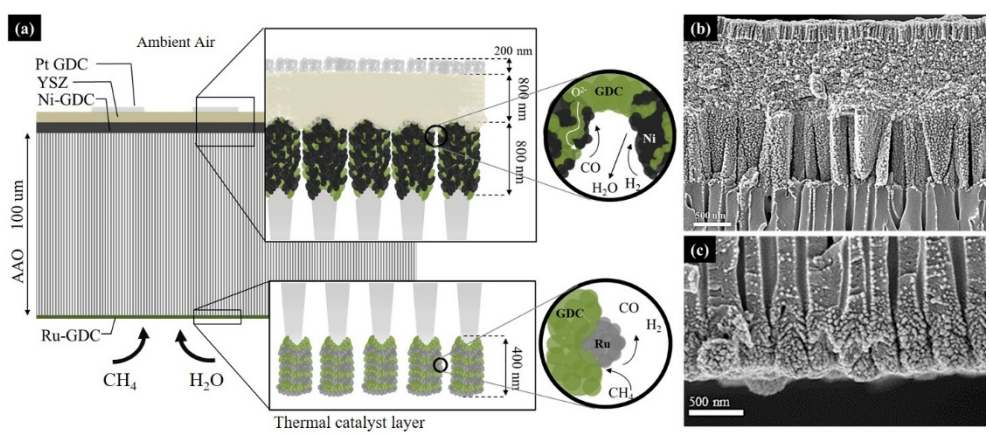

Figure 6.2 (a) Schematic of integrated TF-SOFC with nanostructured Ru-GDC layer. (b) Side view of nanostructured Ni-GDC/GDC/YSZ/Pt-GDC fabricated by magnetron sputtering. (c) 400 nm thickness of Ru-GDC reforming layer deposited by co-sputtering on the bottom of the AAO substrate.

6.2 Experimental

AAO supported TF-SOFCs was fabricated by sputtering. The nanostructure for electrochemical oxidation consisted of Ni-GDC/GDC/YSZ/Pt-GDC. GDC anode interlayer was deposited by ceramic target with O_2 reactive sputtering. For the reactive sputtering, the 80% Ar and 20% O_2 gas were supplied to the chamber to sustain 0.67 Pa. The thickness of GDC interlayer was controlled for 50nm. This role of GDC anode interlayer was inhibiting carbon deposition on Ni by increasing the composition of the GDC at the anode-electrolyte interface. Dense YSZ electrolyte was deposited at 800nm thickness. This thickness of the electrolyte is thicker than the previous research on AAO supported TF-SOFCs to ensure the gas leak from the anode side, which could cause OCV drop. The Ru-GDC reforming layer was deposited on the backside of the AAO. The composition of the Ru-GDC layer was controlled by sequential deposition method. Consequently, the Ru volume percent of Ru-GDC layer was varied by 1.3, 2.0, and 3.3 vol%. The samples with Ru-GDC reforming layer are denoted as RuGDC0.01 for 1.3 vol%, RuGDC0.02 for 2.0 vol%, and RuGDC0.03 for 3.3 vol%, hereafter.

The porosity of Ru-GDC nanostructure was calculated from the surface FESEM images by the image-j program. For the surface chemical analysis, XPS and Raman spectroscopy was used. Furthermore, to investigate the carbon deposition phenomenon for Ni-GDC anode with and without reforming layer, the fixed bed flow reactor was used.

6.3 Results and Discussion

The deposition of Ru-GDC on the AAO substrate was investigated by structural analysis. The side micrograph of Ru sputtering layer on AAO substrate was analyzed by FESEM. Reactive sputtering of Ru metal also showed the nano-column structure, which means that the fabrication of the co-sputtered Ru-GDC reforming layer could form high density of TPB. The crystallinity of Ru-GDC anode

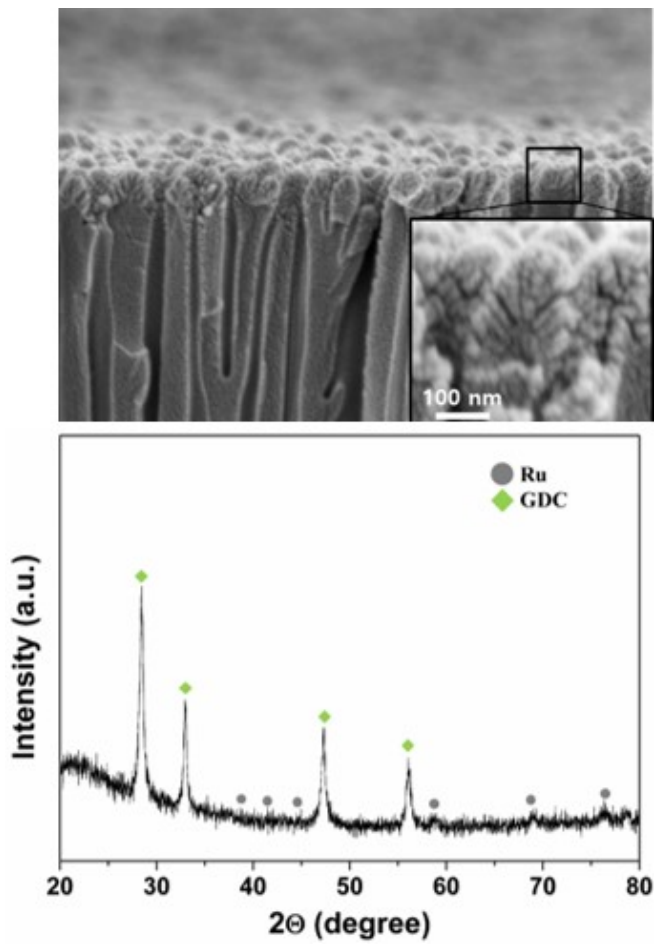

Figure 6.3 (Upper micrograph) Side view of Ru deposited by sputtering on the AAO substrate. (Bottom micrograph) XRD analysis of Ru-GDC fabricated by co-sputtering.

was investigated by XRD analysis. Due to the low contents of Ru, the crystalline peaks were barely detected. However, the peaks were clearly confirmed from the XRD. Since the intensity of the spectrum for the specific crystal structure is proportional to the amount of the structure included in the sample, the results indicate that the contents of the GDC is much more dominant than Ru. The compositional analysis was measured by XPS for the nanostructured Ru-GDC. The XPS spectrum in the range of 100 to 1000 eV shows the photoemission

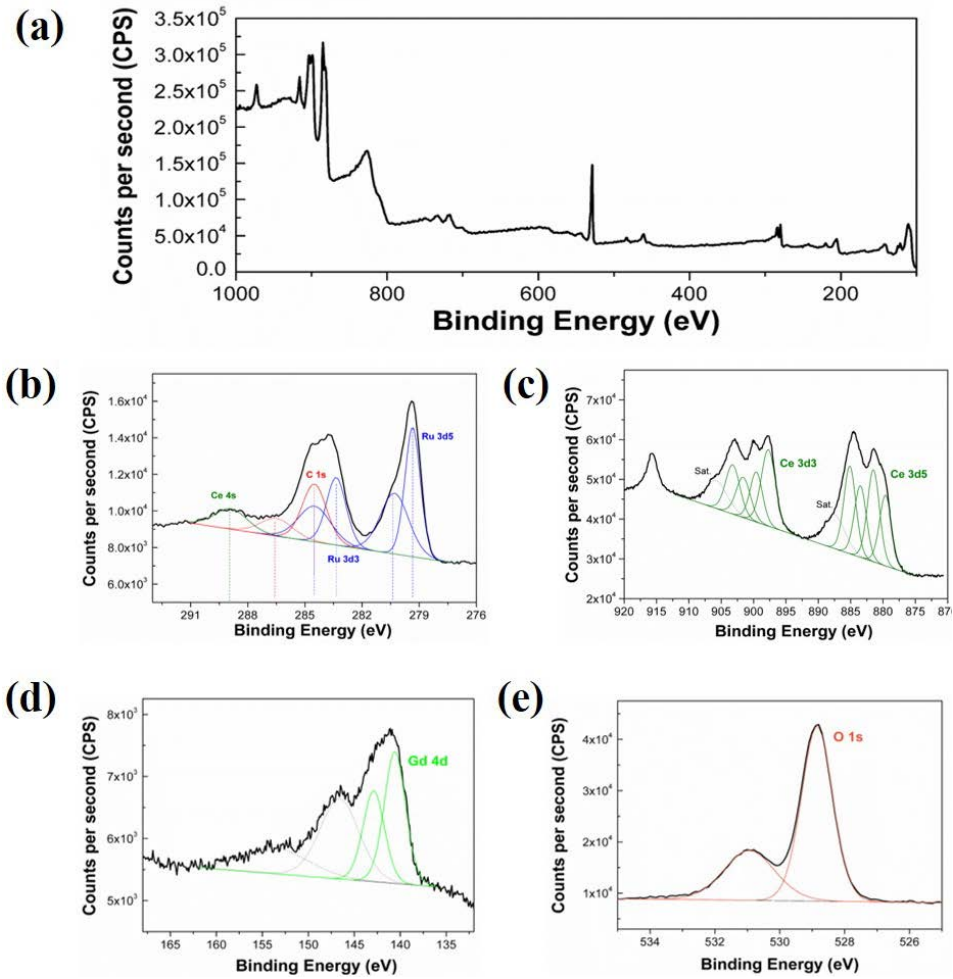

Figure 6.4 XPS analysis for the nanostructured Ru-GDC deposited on AAO substrate. (a) Scan of photoemission properties of Ru-GDC at 100-1000 eV range. (b) The Ru 3d (c) Ce 3d (d) Gd 4d (e) O 1s properties.

properties of Ru 3d, Gd 4d, Ce 3d, and O 1s presented in figure 6.4. The photoemission properties of Ru, Gd, Ce, and O are observed at 276-291eV, 135-166 eV, 870-915 eV, and 526-534 eV. In addition, the peaks measured from XPS analysis at 276-291 eV were deconvoluted into Ru 3d3, 5 and C 1s and Ce 4s. The carbon detected from the XPS results was possibly attributed to the contamination from the ambient air during sample storage. This detection of the contamination is due to the

surface-sensitive characteristic of XPS analysis with only 10nm infiltration of X-ray.

To investigate the compositional effect of the Ru-GDC reforming layer on electrochemical performance, the Ru-GDC layer was fabricated with three different compositions: GDC vol% 1.3, 2.0, and 3.3. In table 6.1, the specific atomic concentration and the volume ratio of Ru was demonstrated. The thickness of the Ru-GDC layer was maintained at 400nm for all samples. Even though Ru contents only changed from 1 to 3 percent, the surface structure could be changed due to the nanoscale thickness of the layer.

Sample	Atomic Conc. (at. %)				Volume Ratio	Volume fraction (vol. %)
	Ru	Gd	Ce	O	V_{Ru}/V_{GDC}	V_{Ru}/V_{Ru+GDC}
RuGDC0.01	2.03	1.07	17.81	58.95	0.013	**1.3**
RuGDC0.02	3.53	2.33	28.35	55.89	0.021	**2.0**
RuGDC0.03	6.16	1.66	35.5	50.81	0.035	**3.3**

Table 6.1 Specific atomic concentration of the nanostructured Ru-GDC reforming layer varied with Ru volume fraction.

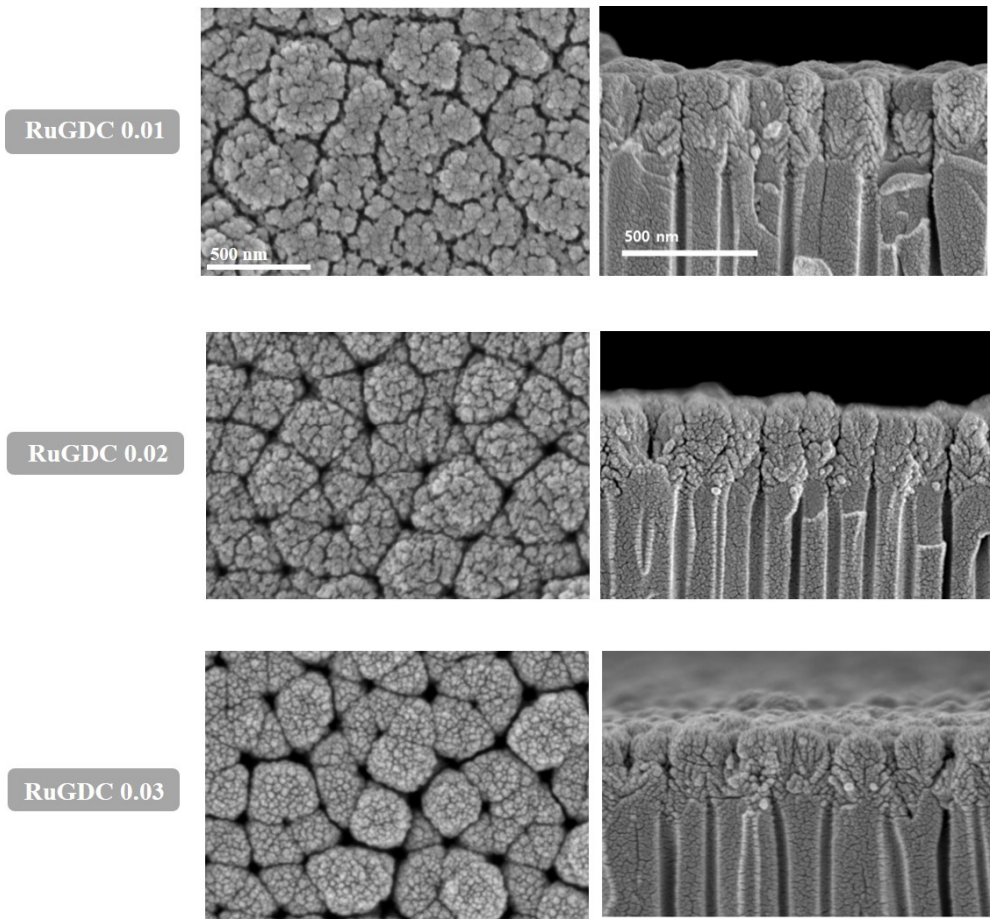

Figure 6.5 Surface and cross-sectional nanostructure of FESEM micrographs for Ru-GDC reforming layer varied with Ru volume fraction.

The surface nanostructure of the co-sputtered layer is sensitive to the growth characteristic of the materials. The high sputtering yield of Ru compared to GDC deposited by ceramic target could be the reason for the difference in the nanostructure even with the small change of the chemical composition. The detailed mechanism of the co-sputtering of Ru-GDC has not been studied. It will be further investigated in future work.

The surface porosity of the Ru-GDC layer was calculated from the FESEM images from figure 6.6. In this figure, the porosity of the RuGDC 0.01 was less than

10 %. As the Ru volume fraction was increased to 3.3%, the porosity of the RuGDC0.03 was also increased over 25%, which is more than twice compared to RuGDC0.01 sample. This structure change affected the OCV tendency of TF-SOFCs with reforming layer. The OCV was measured with nearly dry methane supply at 500℃ for the TF-SOFCs with different compositions of Ru-GDC reforming layer. The composition of Ni-GDC anode was determined as 3.9 vol%, which showed the highest performance compared to other compositions. Due to the low loading of GDC composite, the OCV of the bare TF-SOFCs was close to 0V. This result was consistent with the previous experimental result of chapter 5. As the Ru composition increase for the reforming layer, the OCV was starting to increase and reached to 1.02 V. Although some of the cells with RuGDC0.01 and 0.02 showed higher OCV over 0.8V, the fluctuation was too significant for the stable operation possibly due to unsteady reforming performance. One notable thing in the OCV data was RuGDC 1.6 sample. The high loading of Ru sample showed a little bit lower OCV of TF-SOFCs compared to the cell with RuGDC0.03. This result might indicate that the reforming kinetics are not totally depending on Ru contents. Only when Ru and GDC form a high density of TPB, the Ru-GDC layer could facilitate the high performance of methane reforming. This assumption is supported by the proposed mechanism of steam reforming at the Ru catalyst supported with oxide material[99]. There are several factors for determining the reforming performance. Among those, catalyst activity and resistance characteristics for carbon deposition are the major factors. The role of the catalyst is reducing the activation energy for chemical adsorption of the methane gas species on the metal surface. However, even with the high catalytic performance of the catalyst material, available surface for chemical adsorption could be blocked by the carbon species deposited on the surface. The oxide support is crucial for eliminating the carbon species on the catalyst. According to the proposed mechanism, lattice oxide in the support can react with the carbon species removed

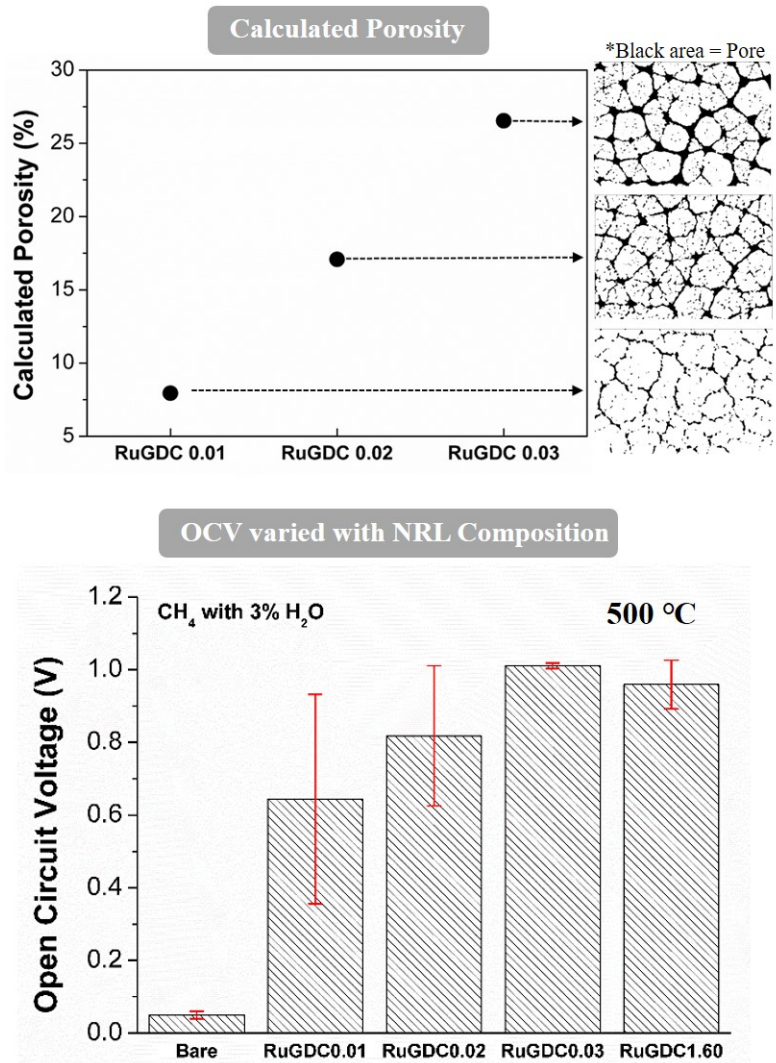

Figure 6.6 The surface porosity of the nanostructured Ru-GDC reforming layer on the AAO substrate. The OCV of TF-SOFC with bare and Ru-GDC reforming layer varied with Ru volume fraction.

by producing carbon monoxide and hydrogen gas. This possibility was also investigated by measuring J-V-P behaviors.

The OCV of TF-SOFC without the Ru-GDC reforming layer was close to zero. To confirm the results, the fuel was switched from hydrogen to methane while measuring the OCV of TF-SOFCs. This result was the same as the pellet based experiments. On the other hand, TF-SOFCs with RuGDC 0.03 samples showed high OCV. The Nernst equation for calculating the theoretical OCV for the temperature ranging from 200 to 700°C. The OCV of TF-SOFCs with RuGDC 0.03 sample was slightly lower than the oxidation of hydrogen and higher than direct oxidation of methane. The accuracy of OCV data of TF-SOFCs could be reduced by the experimental variable such as nanoscale pinhole in the electrolyte or leakage through the sealant, which affecting the OCV by following Nernst equation. Nevertheless, the OCV acquired from this experiment was stable for the extended time operation. Therefore, it is appropriate to assume the major fuel gas species for electrochemical oxidation at anode from the OCV data. Considering this assumption, the primary gas

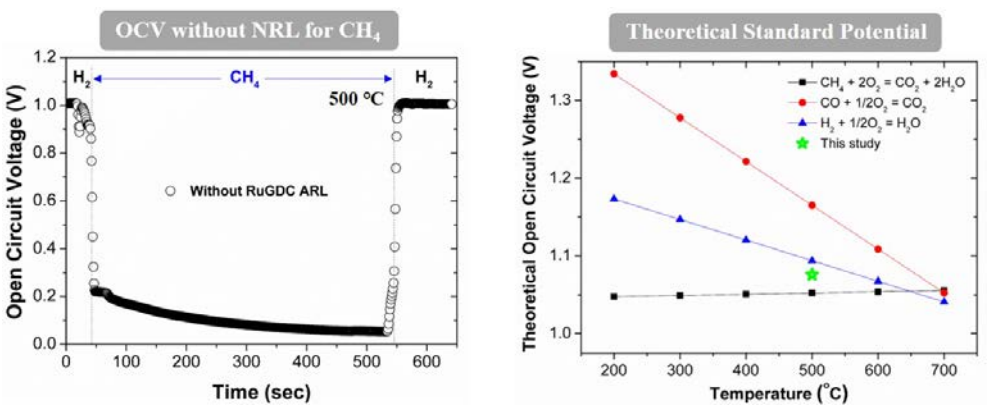

Figure 6.7 OCV without the nanostructure RuGDC reforming layer (NRL) with methane fuel supply. Theoretical standard potential for three electrochemical oxidations compared to OCV of RuGDC 0.03 sample.

component oxidized at the anode was hydrogen and partially methane. The specific gas component at the reaction sites of the anode side could not be realized from this analysis because of the complex reactions of methane and reformed gas oxidation. The reason why it is difficult to know the exact gas composition at the anode reaction sites is that the gas composition is continuously changed by chain reaction. Hydrogen oxidation produces the water vapor, and the water vapor could participate in water gas shift reaction and in reforming reaction because S/C ratio are locally changed at the reaction sites. As mentioned above, the reforming kinetic is enhanced at high level of S/C ratio.

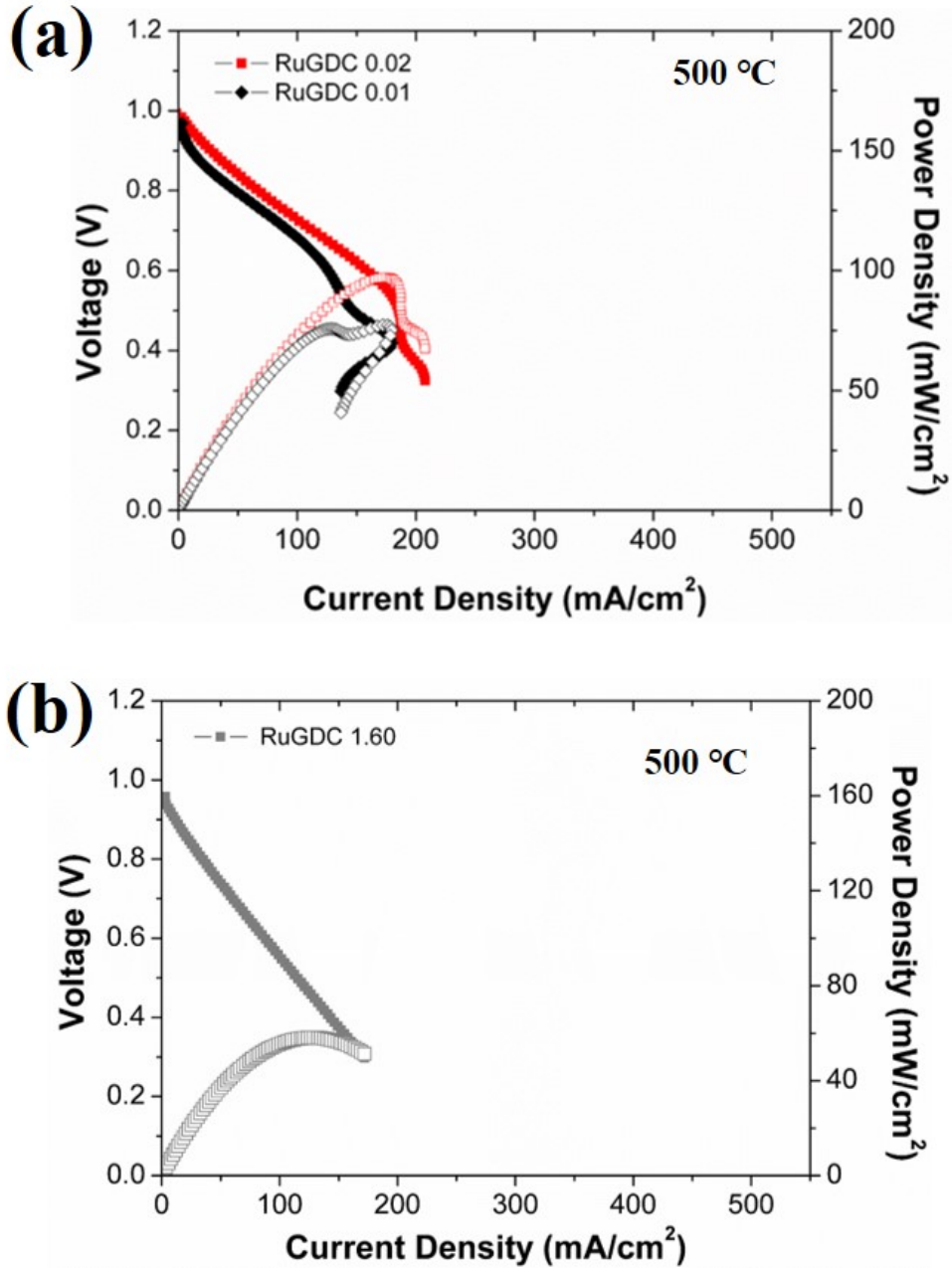

Figure 6.8 (a) JVP behaviors of TF-SOFCs with RuGDC 0.01 and 0.02 NRL samples. (b) JVP behavior of TF-SOFCs with RuGDC 1.60.

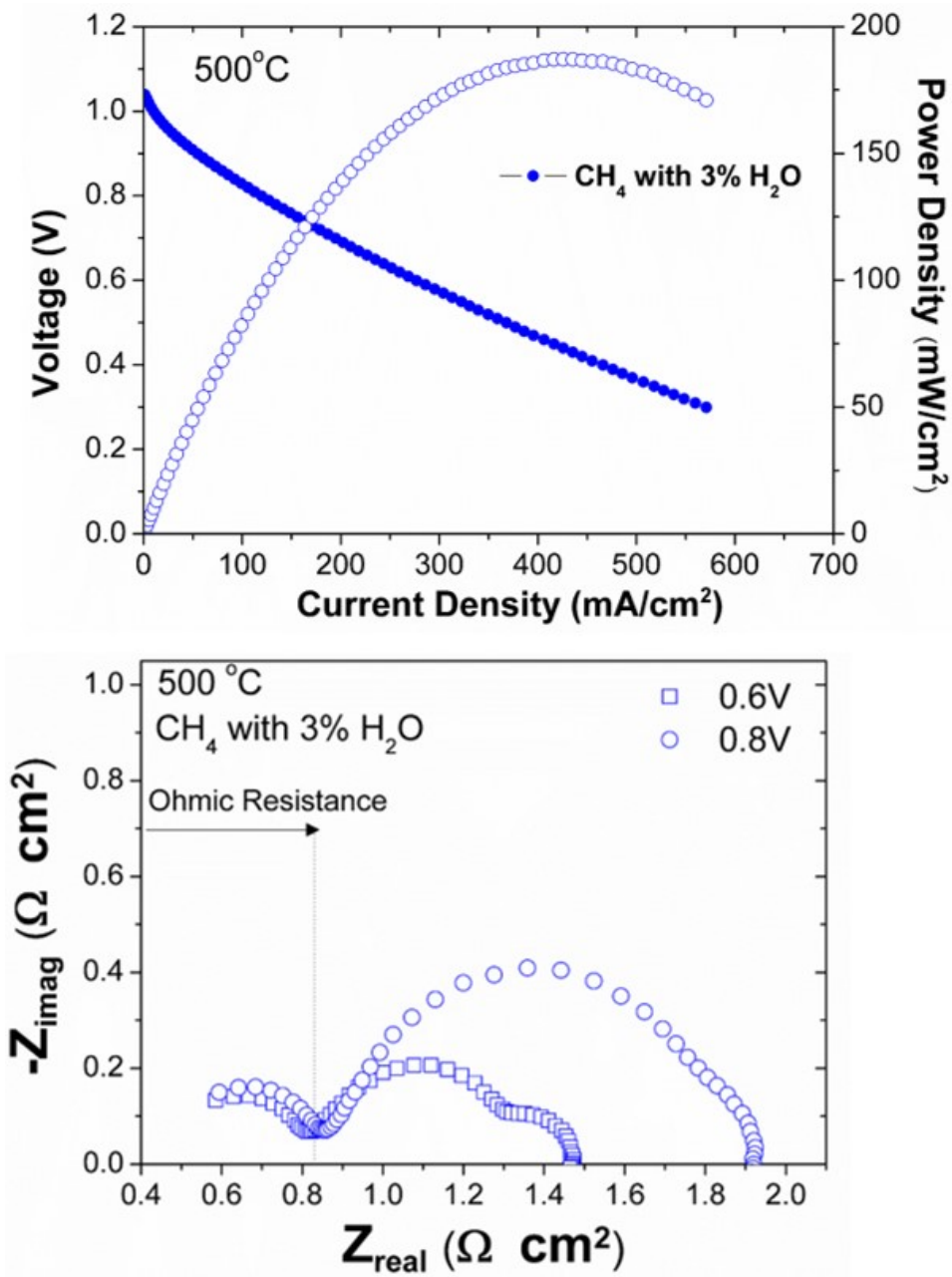

Figure 6.9 The J-V-P curve and the EIS analysis for TF-SOFCs with RuGDC 0.03 NRL measured at 500℃.

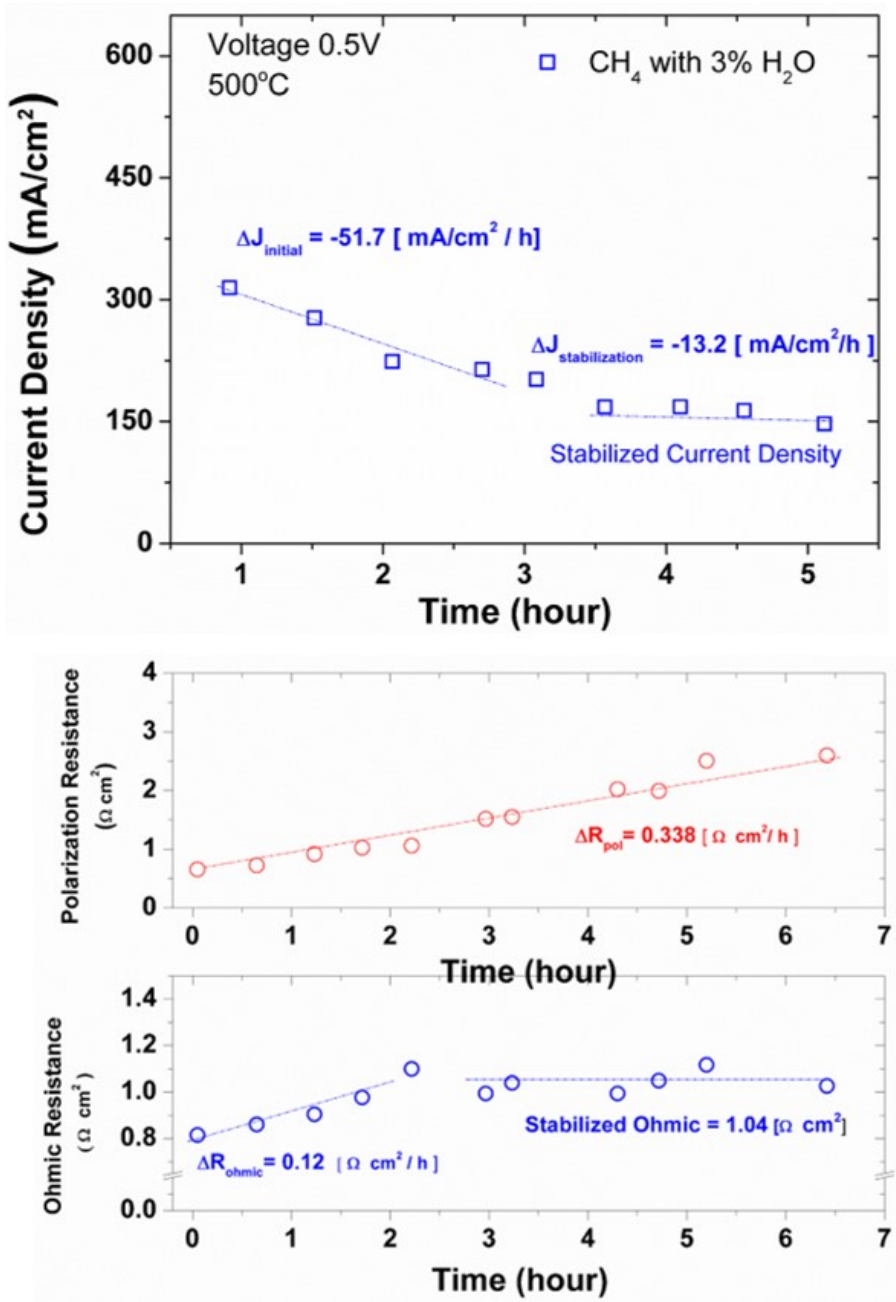

Figure 6.10 The points measurement of TF-SOFC with RuGDC 0.03 NRL for the extended time operation. Current density, polarization resistance, and ohmic resistance were measured during the operation.

The JVP behaviors of RuGDC 0.01, 0.02 and 1.6 samples were measured at 500℃. The current density was unstable at large over-potential region (lower than 0.5V of the cell potential) for both RuGDC 0.01 and 0.02 samples. From the curve shapes, it can be speculated that the hydrogen fuel was insufficient at the anode reaction sites resembling with the concentration loss behavior. Although CO and CH_4 existed at the reaction sites, which were available for oxidation, the electrochemical oxidation of those gas species was too slow to produce high current density. Further optimizing on Ru composition was required. The performance of TF-SOFCs with high loading of Ru was also investigated. The concentration loss or unstable performance was not observed for the samples. However, the peak power density of the cell was under 80 mW/cm^2. Even with the over 50 vol% of Ru contents, the performance was not dramatically improved. This result implies that Ru nanocatalyst itself was not the whole responsibility for the reforming kinetics. The nano-sized grain of Ru on GDC support could be the key factor for high performance for methane reforming. This assumption is consistent with the recent report about singly anchored metal atoms on the ceria support.

Based on the assumption, the performance of TF-SOFC with RuGDC0.03 should be more enhanced. The electrochemical performance of the cell was characterized by JVP behavior and EIS analysis. In figure 6.9, the performance of TF-SOFCs with RuGDC0.03 NRL clearly showed the enhanced power density. The peak power density was reached to the 187 mW/cm^2, which is the highest performance among AAO supported TF-SOFC operated under CH_4 at 500℃. From the EIS analysis, polarization resistance of the cell was much higher compared to the cell with hydrogen fuel. This result was reasonable considering the sluggish reaction of methane or carbon monoxide electrochemical oxidation. Another possible reason

for the considerable polarization resistance was the cell temperature reduction due to the endothermic reaction of methane steam reforming. This could also be the reason for increasing the ohmic resistance of the cell.

The key point of a direct methane operation is time-dependent performance characteristics due to the possibility of carbon formation at the anode reaction sites causing the severe performance degradation and even failure of the cell[100]. Therefore, the investigation of the time-dependent operation is essential in this thesis. Figure 6.10 depicted the current density, polarization, and ohmic resistances changed with the operation time. It was observed that the current density was severely degraded in the early stage of the cell performance at the rate of minus 51.7 mA/cm^2 per hour. After 3 hours operation, the degradation rate was decreased over 70 %. We believe that TF-SOFCs requires the time for the thermal stabilization of the nanostructure. As shown in chapter 4, the Ni-GDC anode showed an agglomerated structure even with the optimized GDC contents. The agglomeration of the anode nanostructure could attribute to the degradation, not only to the polarization but also to the ohmic resistance. By the change of the anode structure, the contact resistance at the anode-electrolyte interface should be affected. After 3 hours, the ohmic resistance was stabilized, unlike the polarization resistance. The steady rise of the polarization resistance could be attributed more to the Pt-based cathode. For further investigation, the constant voltage was applied for the TF-SOFCs with RuGDC 0.03 operated under nearly dry CH_4. The duration of the operation lasted more than 12 hours. Considering the operation time of Ni-GDC deposited on ScSZ pellet with CH_4 was shorter than an hour, this extended operation of AAO supported TF-SOFCs was greatly superior to the previous results. Besides, it has never been reported that the constant voltage measurement of AAO supported TF-SOFCs even with hydrogen fuel. This long operation was attainable due to the thermally enhanced

nanostructured Ni-GDC anode on nanoporous substrate. Nevertheless, the current density of the cell was degraded 4.6 % per hour at 0.8V. This degradation was attributed to the thermal agglomeration of the electrodes, but the cathode agglomeration should be more dominant for the long operation since the hydrogen oxidation is much faster than the oxygen reduction reaction. However, the possibility of the performance degradation by carbon formation on the reaction sites at the anode should be not be ignored since the carbon formation on Ni-GDC anode was confirmed in the previous chapter 5.

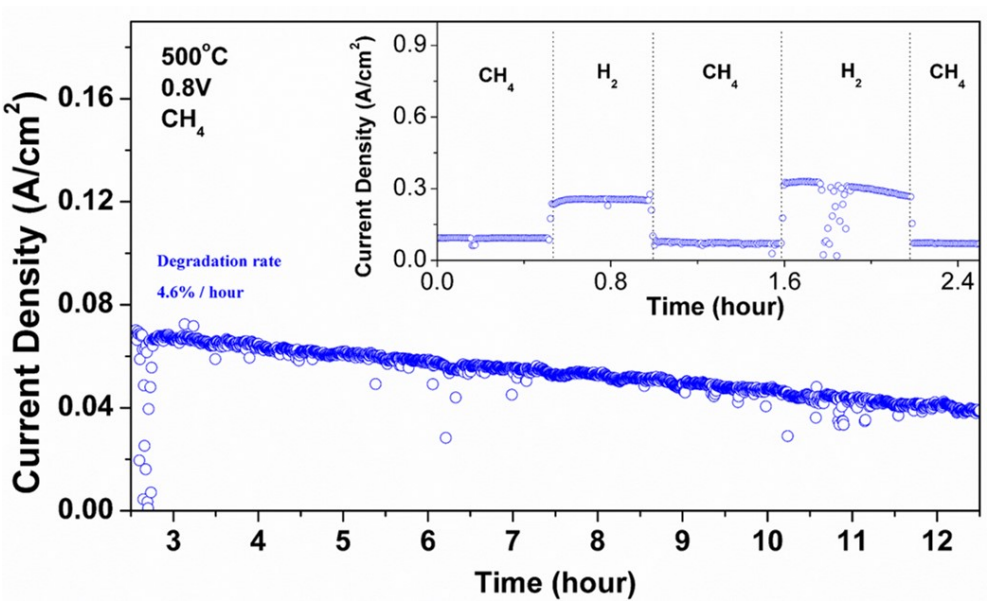

Figure 6.11 The constant voltage measurement of AAO supported TF-SOFC with RuGDC 0.03 operated under nearly dry methane.

To verify the possible carbon coking on the anode nanostructure, the fixed bed flow reactor was used for the nanostructured anode with and without NRL. The Ni-GDC with and without NRL was attached to the SUS jig. The methane passed through the water bubbler was supplied to the AAO substrate. The methane gas was first contacted with Ru-GDC NRL and passed through the nano-channel in the AAO substrate. Sequentially, the gas passed through the nanoporous structure of the Ni-GDC anode. The three kinds of samples were used in this test station: one was Ni-GDC on AAO with the NRL, and the other two were Ni-GDC on AAO without the NRL. After over 12 hours of the exposure, the Ni-GDC anode surfaces of the three samples were analyzed by Raman spectroscopy in the range of 1000 to 2000 cm^{-1} and FESEM.

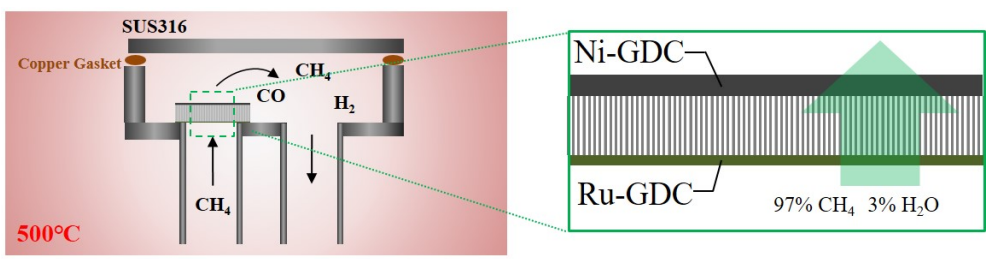

Figure 6.12 Fixed bed flow reactor with hydrogen and methane supply.

From the surface analysis for Ni-GDC with and without the NRL exposed to the CH_4 for more than 12 hours, it is clear that the surface of the Ni-GDC anode with NRL showed no sign of carbon formation. Meanwhile, the carbon nanotube was clearly observed from the high-resolution FESEM surface image. Even with longer exposure time, the sample with NRL showed high resistance characteristics to the carbon coking. To obtain the qualitative information of the surface chemical composition, Raman spectroscopy was applied for the three samples.

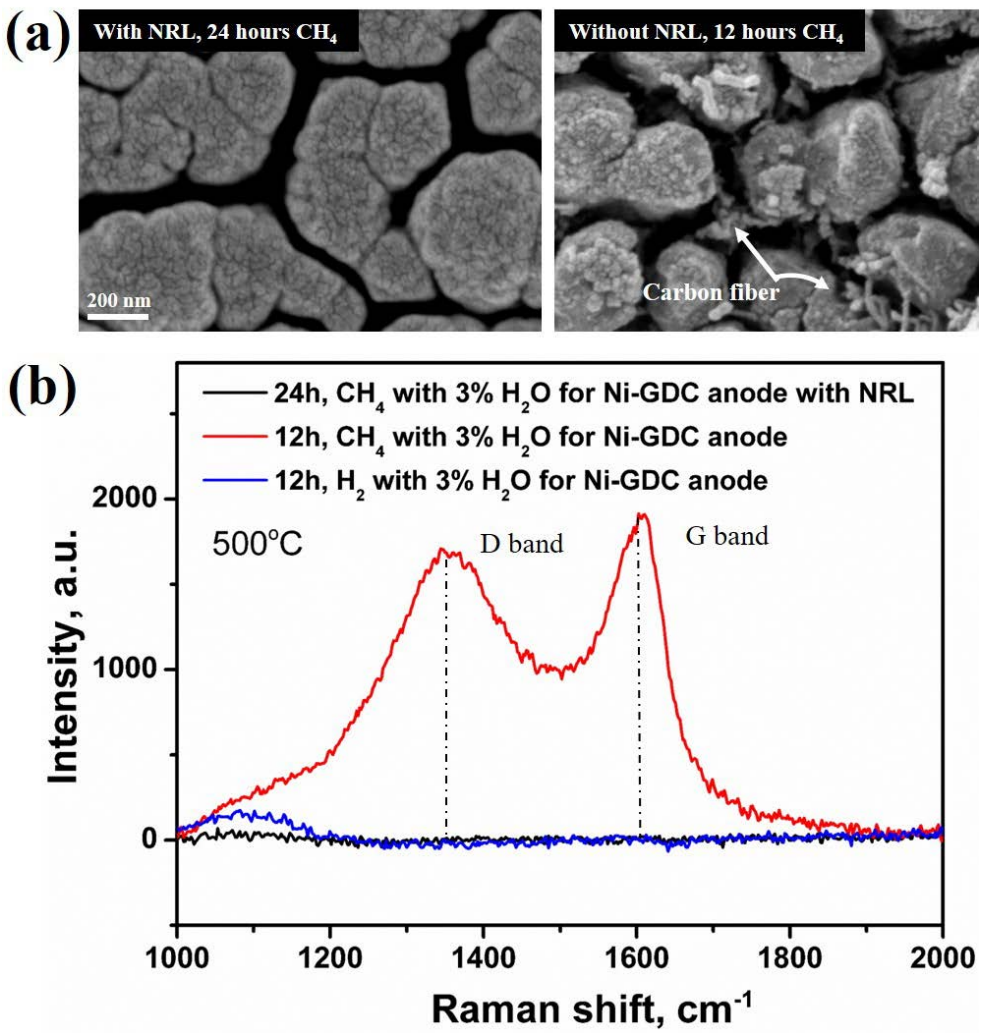

Figure 6.13 (a) Surface nanostructure comparison analyzed by FESEM of Ni-GDC anode exposed to CH_4 97% and H_2O 3% with and without NRL. (b) Raman spectroscopy analysis ranging from 1000 to 2000 cm^{-1} for the three different samples.

Raman spectroscopy results present that there is no signs of carbon for the Ni-GDC anode with NRL exposed to CH_4. It is noteworthy that the spectrum of Ni-GDC with NRL exposed to CH_4 was similar to that of Ni-GDC anode exposed to H_2 for 12 hours, which means both the no detectable carbon formed on the anode and the high reforming performance of the Ru-GDC NRL. On the other hand, in the region between 1500 and 1600 cm^{-1} (G band), in addition, 1320 and 1360 cm^{-1} (D band), the high intensity of the spectrum was detected. It is known that D and G band are indicating the existence of the amorphous carbon sp^2 on the sample surface[101,102]. Furthermore, since the intensity of the Raman spectrum is directly proportional to the concentration of the chemical species, the amount of the amorphous carbon on the surface of the Ni-GDC anode was particularly larger than the sample with NRL. Therefore, it can be concluded that the severe carbon deposition on the nanostructured Ni-GDC anode can be prevented by applying Ru-GDC NRL fabricated by co-sputtering.

6.4 Conclusion

The fabrication process for the nanostructured Ru-GDC layer and the thermal catalytic performance for the methane steam reforming have been demonstrated for low-temperature. The composition and the porosity of the Ru-GDC are realized as critical factors for the performance. The 3.3 vol% of Ru contents showed the OCV over 1V. Furthermore, the peak power density of TF-SOFCs with 3.3 vol% of Ru presented 187 mW/cm^2 at 500°C. The extended time operation of TF-SOFCs with

Ru-GDC reforming layer operated under nearly dry methane showed the degradation rate of 4.6 % per hour possible due to the degradation of Pt-based cathode. Even though the cell suffered from the degradation in the extended time, 12 hours of operation of TF-SOFCs with extremely low S/C methane fuel is the longest time reported in the literature about AAO supported TF-SOFCs.

Chapter 7. Achievements and Future Work

The electrochemical performances of Ni-GDC cermet anode fabricated by co-sputtering were investigated for low operating temperatures. Due to the unique character of the electronic conduction path for the anode, the in-plane conductivity of the Ni-GDC is considered as a critical factor for achieving high performance. The nano-column structure of Ni-GDC anode on AAO substrate has a significant impact on the in-plane conductivity. The nanostructure with the wide width of the nano-column has shown high in-plane conductivity resulting in the low ohmic and polarization resistances. By optimizing the Ni-GDC anode nanostructure, area-specific resistance (ASR) for the charge species conduction is reduced down to 0.3 $\Omega \cdot cm^2$ at 500℃. Furthermore, the effect of GDC volume fraction in Ni-GDC anode on the electrochemical performance was examined. The results indicated that the excessive nano-sized GDC composite in Ni-GDC anode could diminish the peak power density by reducing the in-plane conductivity with the oxide phase of GDC. Consequently, the peak power density of the nanostructured Ni-GDC anode based TF-SOFCs with a low volume fraction of GDC (below 5%) has reached to 749 mW/cm^2. To the best of our knowledge, this result is the highest performance among the AAO supported TF-SOFCs with Ni-based anode reported in the literature.

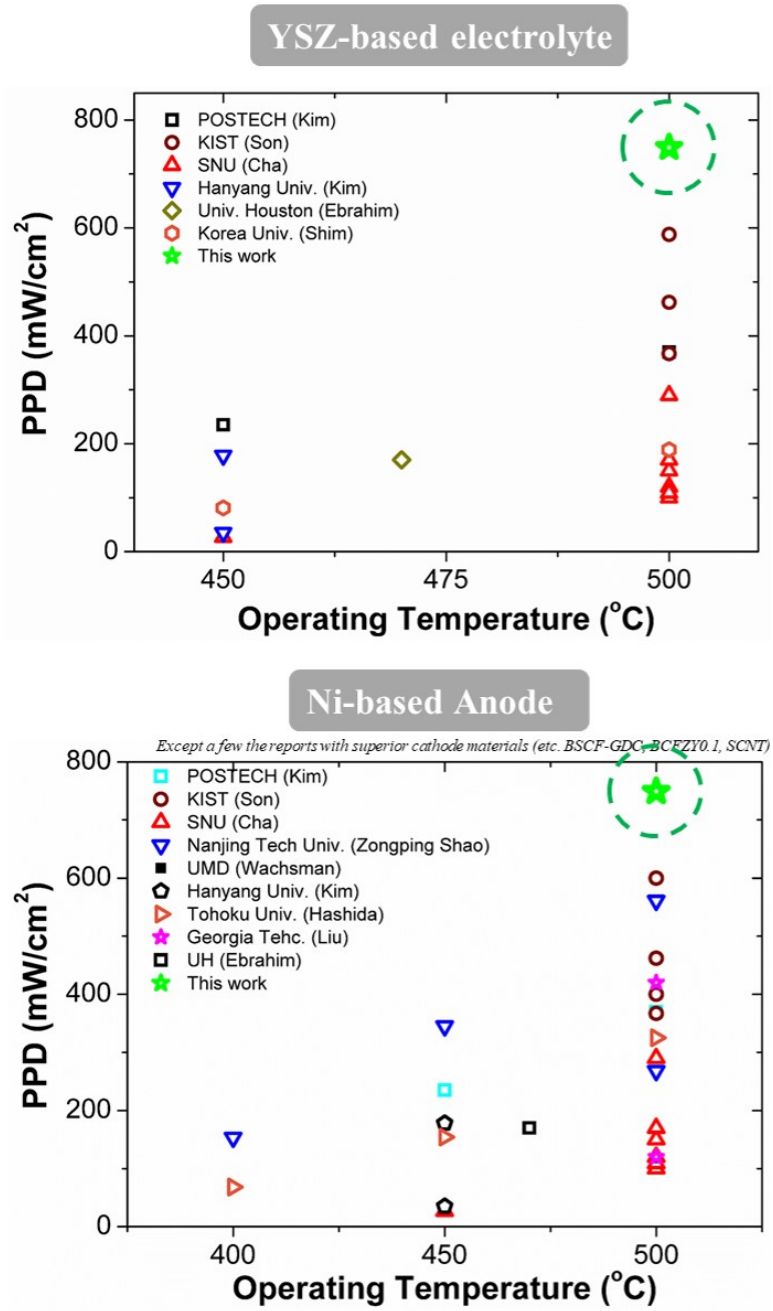

Figure 7.1 Literature data of the peak power density of SOFCs in the range between 400 to 500℃.

For a direct methane SOFCs with extremely low S/C ratio (about 0.03), the co-sputtering fabrication and electrochemical characterization of the nanostructured Ru-GDC reforming layer were investigated. The Ru volume fraction is optimized at 3 %. The nano-sized Ru grains dispersed in nano-grains GDC support is the major contributor to the high catalytic performance for the methane steam reforming at low-temperature. AAO supported TF-SOFCs with the nanostructured Ru-GDC layer has shown the successful operation with the reasonable OCV and high performance for nearly dry methane fuel. Furthermore, the extended time operation of the TF-SOFCs was demonstrated. Although the degradation rate of 4.6 % per hour was shown for the TF-SOFCs, the constant voltage measurement of TF-SOFC with methane fuel for 12 hours is demonstrated for the first time in this thesis.

In this thesis, co-sputtering Ni-GDC anode deposited at room temperature has been examined with the various deposition parameters, as well as with the thermal annealing process. However, the operation time and the degradation rate of TF-SOFCs still needs to be much more enhanced because the state of the art SOFCs usually shows more than 100 hours without the degradation. The experimental results obtained from this thesis give insight for designing the high performance of TF-SOFCs with co-sputtering system. Due to the nano-sized grain of the sputtered layer, the thermal agglomeration of Ni nanoparticles is inevitable at the operating temperature. Therefore, other than Ni-GDC anode with high connectivity, the functional layer of Ni-GDC with high resistance to thermal agglomeration is required. For thermally stable structure, Ni concentration should be limited down to 5%. The TPB density could be high enough to produce high performance even with the low

concentration of Ni because GDC has mixed ionic conductivity at reducing the environment. Further investigation on the nanostructured anode is necessary for the commercialization of TF-SOFCs for low-temperature. Furthermore, the cathode materials should be replaced with oxide based materials such as perovskite structure.

Author’s Related Publication

Nanostructured nickel anode for high performance low temperature solid oxide fuel cell, W. Yu, Y. Lim, S. Lee, A. P, G. Cho, and S.W. Cha, in preparation.

Thickness effect of co-sputtered Ni-GDC anode for anodic aluminum oxide supported low temperature solid oxide fuel cell, W. Yu, S. Lee, G. Cho, and S.W. Cha, in preparation.

Nanostructured Ru-GDC reforming layer for sputtered thin film solid oxide fuel cell with self-steaming mechanism at low temperature, W. Yu, S. Lee, M. Kishimoto, G. Cho, and S.W. Cha, in preparation.

Bibliography

[1] R.P. O'Hayre, S.-W. Cha, W. Colella, F.B. Prinz, Fuel cell fundamentals, John Wiley & Sons New York, 2006.

[2] O. Gröger, H.A. Gasteiger, J.-P. Suchsland, Review—Electromobility: Batteries or Fuel Cells?, J. Electrochem. Soc. 162 (2015) A2605–A2622. doi:10.1149/2.0211514jes.

[3] Z.P. Cano, D. Banham, S. Ye, A. Hintennach, J. Lu, M. Fowler, Z. Chen, Batteries and fuel cells for emerging electric vehicle markets, Nat. Energy. 3 (2018) 279–289. doi:10.1038/s41560-018-0108-1.

[4] T. Yoshida, K. Kojima, Toyota MIRAI fuel cell vehicle and progress toward a future hydrogen society, Electrochem. Soc. Interface. 24 (2015) 45–49. doi:10.1149/2.F03152if.

[5] R. Peters, L. Blum, R. Deja, I. Hoven, W. Tiedemann, S. Küpper, D. Stolten, Operation experience with a 20 kW SOFC system, in: Fuel Cells, John Wiley and Sons Ltd, 2014: pp. 489–499. doi:10.1002/fuce.201300184.

[6] X. Deng, A. Petric, Geometrical modeling of the triple-phase-boundary in solid oxide fuel cells, J. Power Sources. 140 (2005) 297–303. doi:10.1016/J.JPOWSOUR.2004.08.046.

[7] J. Abel, A.A. Kornyshev, W. Lehnert, Correlated resistor network study of porous solid oxide fuel cell anodes, J. Electrochem. Soc. 144 (1997) 4253–4259. doi:10.1149/1.1838174.

[8] R. O'Hayre, D.M. Barnett, F.B. Prinz, The triple phase boundary a mathematical model and experimental investigations for fuel cells, J. Electrochem. Soc. 152 (2005). doi:10.1149/1.1851054.

[9] E.D. Wachsman, K.T. Lee, Lowering the temperature of solid oxide fuel cells., Science. 334 (2011) 935–9. doi:10.1126/science.1204090.

[10] C. Xia, M. Liu, Novel Cathodes for Low-Temperature Solid Oxide Fuel

Cells, Adv. Mater. 14 (2002) 521–523. doi:10.1002/1521-4095(20020404)14:7<521::AID-ADMA521>3.0.CO;2-C.

[11] N.M. Sammes, K. Galloway, M.F. Serincan, T. Suzuki, T. Yamaguchi, M. Awano, W. Colella, Solid oxide fuel cells, in: Handb. Clim. Chang. Mitig., Springer US, 2012: pp. 1703–1727. doi:10.1007/978-1-4419-7991-9_44.

[12] W. He, J. Zou, B. Wang, S. Vilayurganapathy, M. Zhou, X. Lin, K.H.L. Zhang, J. Lin, P. Xu, J.H. Dickerson, Gas transport in porous electrodes of solid oxide fuel cells: A review on diffusion and diffusivity measurement, J. Power Sources. 237 (2013) 64–73. doi:10.1016/j.jpowsour.2013.02.089.

[13] A. Evans, A. Bieberle-Hütter, J.L.M. Rupp, L.J. Gauckler, Review on microfabricated micro-solid oxide fuel cell membranes, J. Power Sources. 194 (2009) 119–129. doi:10.1016/j.jpowsour.2009.03.048.

[14] J.H. Shim, C.-C. Chao, H. Huang, F.B. Prinz, Atomic Layer Deposition of Yttria-Stabilized Zirconia for Solid Oxide Fuel Cells, Chem. Mater. 19 (2007) 3850–3854. doi:10.1021/cm070913t.

[15] C.-C. Chao, C.-M. Hsu, Y. Cui, F.B. Prinz, Improved Solid Oxide Fuel Cell Performance with Nanostructured Electrolytes, ACS Nano. 5 (2011) 5692–5696. doi:10.1021/nn201354p.

[16] D. Beckel, A. Bieberle-Hütter, A. Harvey, A. Infortuna, U.P. Muecke, M. Prestat, J.L.M. Rupp, L.J. Gauckler, Thin films for micro solid oxide fuel cells, J. Power Sources. 173 (2007) 325–345. doi:10.1016/J.JPOWSOUR.2007.04.070.

[17] H.-S. Noh, K.J. Yoon, B.-K. Kim, H.-J. Je, H.-W. Lee, J.-H. Lee, J.-W. Son, Thermo-mechanical stability of multi-scale-architectured thin-film-based solid oxide fuel cells assessed by thermal cycling tests, J. Power Sources. 249 (2014) 125–130. doi:10.1016/J.JPOWSOUR.2013.10.101.

[18] K. Kerman, B.-K. Lai, S. Ramanathan, Pt/Y0.16Zr0.84O1.92/Pt thin film solid oxide fuel cells: Electrode microstructure and stability considerations, J. Power Sources. 196 (2011) 2608–2614.

doi:10.1016/j.jpowsour.2010.10.068.

[19] M. Tsuchiya, B.-K. Lai, S. Ramanathan, Scalable nanostructured membranes for solid-oxide fuel cells, Nat. Nanotechnol. 6 (2011) 282–286. doi:10.1038/nnano.2011.43.

[20] C.-W. Kwon, J.-I. Lee, K.-B. Kim, H.-W. Lee, J.-H. Lee, J.-W. Son, The thermomechanical stability of micro-solid oxide fuel cells fabricated on anodized aluminum oxide membranes, J. Power Sources. 210 (2012) 178–183. doi:10.1016/J.JPOWSOUR.2012.03.020.

[21] S. Hong, J. Bae, B. Koo, Y.-B. Kim, High-performance ultra-thin film solid oxide fuel cell using anodized-aluminum-oxide supporting structure, Electrochem. Commun. 47 (2014) 1–4. doi:10.1016/j.elecom.2014.07.008.

[22] S. Hong, Y. Lim, H. Yang, J. Bae, Y.-B. Kim, Single-chamber fabrication of high-performance low-temperature solid oxide fuel cells with grain-controlled functional layers, J. Mater. Chem. A. 5 (2017) 2029–2036. doi:10.1039/C6TA07237B.

[23] S. Hong, J. Son, Y. Lim, H. Yang, F.B. Prinz, Y.-B. Kim, A homogeneous grain-controlled ScSZ functional layer for high performance low-temperature solid oxide fuel cells, J. Mater. Chem. A. 6 (2018) 16506–16514. doi:10.1039/C8TA05157G.

[24] H.-S. Noh, K.J. Yoon, B.-K. Kim, H.-J. Je, H.-W. Lee, J.-H. Lee, J.-W. Son, Thermo-mechanical stability of multi-scale-architectured thin-film-based solid oxide fuel cells assessed by thermal cycling tests, J. Power Sources. 249 (2014) 125–130. doi:10.1016/J.JPOWSOUR.2013.10.101.

[25] W. Zhou, Z. Shao, R. Ran, W. Jin, N. Xu, A novel efficient oxide electrode for electrocatalytic oxygen reduction at 400–600 °C, Chem. Commun. 0 (2008) 5791. doi:10.1039/b813327a.

[26] E.-O. Oh, C.-M. Whang, Y.-R. Lee, S.-Y. Park, D.H. Prasad, K.J. Yoon, J.-W. Son, J.-H. Lee, H.-W. Lee, Extremely Thin Bilayer Electrolyte for Solid Oxide Fuel Cells (SOFCs) Fabricated by Chemical Solution Deposition

(CSD), Adv. Mater. 24 (2012) 3373–3377. doi:10.1002/adma.201200505.

[27] D.-H. Myung, J. Hwang, J. Hong, H.-W. Lee, B.-K. Kim, J.-H. Lee, J.-W. Son, Pulsed Laser Deposition of La0.6Sr0.4CoO3−δ-Ce0.9Gd0.1O2−δ Nano-Composite and Its Application to Gradient-Structured Thin-film Cathode of SOFC, J. Electrochem. Soc. 158 (2011) B1000. doi:10.1149/1.3599925.

[28] D. Kennouche, J. Hong, H.-S. Noh, J.-W. Son, S.A. Barnett, Three-dimensional microstructure of high-performance pulsed-laser deposited Ni–YSZ SOFC anodes, Phys. Chem. Chem. Phys. 16 (2014) 15249. doi:10.1039/c4cp02251c.

[29] J.-H. Park, W.-S. Hong, G.C. Kim, H.J. Chang, J.-H. Lee, K.J. Yoon, J.-W. Son, The Effect of Post-Annealing on the Properties of a Pulsed-Laser-Deposited $La_{0.6}Sr_{0.4}CoO_{3-\delta}$-$Ce_{0.9}Gd_{0.1}O_{2-\delta}$ Nano-Composite Cathode, J. Electrochem. Soc. 160 (2013) F1027–F1032. doi:10.1149/2.075309jes.

[30] P.-C. Su, C.-C. Chao, J.H. Shim, R. Fasching, F.B. Prinz, Solid Oxide Fuel Cell with Corrugated Thin Film Electrolyte, Nano Lett. 8 (2008) 2289–2292. doi:10.1021/nl800977z.

[31] S. (Rob) Hui, D. Yang, Z. Wang, S. Yick, C. Decès-Petit, W. Qu, A. Tuck, R. Maric, D. Ghosh, Metal-supported solid oxide fuel cell operated at 400–600°C, J. Power Sources. 167 (2007) 336–339. doi:10.1016/j.jpowsour.2007.02.070.

[32] X. Chen, N.J. Wu, L. Smith, A. Ignatiev, Thin-film heterostructure solid oxide fuel cells, Appl. Phys. Lett. 84 (2004) 2700–2702. doi:10.1063/1.1697623.

[33] P. Blennow, J. Hjelm, T. Klemensø, Å.H. Persson, S. Ramousse, M. Mogensen, Planar Metal-Supported SOFC with Novel Cermet Anode, Fuel Cells. 11 (2011) 661–668. doi:10.1002/fuce.201100029.

[34] K.J. Kim, B.H. Park, S.J. Kim, Y. Lee, H. Bae, G.M. Choi, Micro solid oxide fuel cell fabricated on porous stainless steel: a new strategy for

enhanced thermal cycling ability., Sci. Rep. 6 (2016) 22443. doi:10.1038/srep22443.

[35] J.H. Park, S.M. Han, K.J. Yoon, H. Kim, J. Hong, B.-K. Kim, J.-H. Lee, J.-W. Son, Impact of nanostructured anode on low-temperature performance of thin-film-based anode-supported solid oxide fuel cells, J. Power Sources. 315 (2016) 324–330. doi:10.1016/J.JPOWSOUR.2016.03.055.

[36] H.-S. Noh, K.J. Yoon, B.-K. Kim, H.-J. Je, H.-W. Lee, J.-H. Lee, J.-W. Son, Ultimate Performance of Anode-Supported SOFC by Realizing Thin-Film Electrolyte and Nano-Structure Electrode, ECS Trans. 57 (2013) 969–973. doi:10.1149/05701.0969ecst.

[37] J.H. Park, S.M. Han, B.-K. Kim, J.-H. Lee, K.J. Yoon, H. Kim, H.-I. Ji, J.-W. Son, Sintered powder-base cathode over vacuum-deposited thin-film electrolyte of low-temperature solid oxide fuel cell: Performance and stability, Electrochim. Acta. 296 (2019) 1055–1063. doi:10.1016/J.ELECTACTA.2018.11.018.

[38] S. Ji, Y.H. Lee, T. Park, G.Y. Cho, S. Noh, Y. Lee, M. Kim, S. Ha, J. An, S.W. Cha, Doped ceria anode interlayer for low-temperature solid oxide fuel cells with nanothin electrolyte, Thin Solid Films. 591 (2015) 250–254. doi:10.1016/J.TSF.2015.05.005.

[39] S. Kang, I. Chang, Y.-B. Kim, S.W. Cha, Influence of a platinum functional layer on a Ni-Ce0.9Gd0.1O1.95 anode for thin-film solid oxide fuel cells, J. Vac. Sci. Technol. A Vacuum, Surfaces, Film. 33 (2015) 05E120. doi:10.1116/1.4927160.

[40] S. Lee, G.Y. Cho, T. Park, Y.H. Lee, W. Yu, Y. Lee, I. Chang, S.W. Cha, A nanoporous substrate-based low temperature solid oxide fuel cell using a thin film Ni anode, Thin Solid Films. 666 (2018) 177–181. doi:10.1016/J.TSF.2018.09.039.

[41] Z. Fan, J. An, A. Iancu, F.B. Prinz, Thickness effects of yttria-doped ceria interlayers on solid oxide fuel cells, J. Power Sources. 218 (2012) 187–191.

doi:10.1016/j.jpowsour.2012.06.103.

[42] S. Noh, G.Y. Cho, Y.H. Lee, W. Yu, J. An, S.W. Cha, Performance Enhancement in Thin Film Solid Oxide Fuel Cells Using Metal-Mixed Ionic Electronic Conductors Bilayer Anode, Sci. Adv. Mater. 8 (2016) 11–16. doi:10.1166/sam.2016.2589.

[43] Y. Kim, S. Noh, G.Y. Cho, T. Park, Y.H. Lee, W. Yu, Y. Lee, W.H. Tanveer, S.W. Cha, Characterization of thin film solid oxide fuel cells with variations in the thickness of nickel oxide-gadolinia doped ceria anode, Int. J. Precis. Eng. Manuf. 17 (2016) 1079–1083. doi:10.1007/s12541-016-0131-8.

[44] Y. Lee, J. Park, W. Yu, W.H. Tanveer, Y.H. Lee, G.Y. Cho, T. Park, C. Zheng, W. Lee, S.W. Cha, Nickel-based bilayer thin-film anodes for low-temperature solid oxide fuel cells, Energy. 161 (2018) 1133–1138. doi:10.1016/J.ENERGY.2018.07.147.

[45] Y. Lim, H. Lee, S. Hong, Y.-B. Kim, Co-sputtered nanocomposite nickel cermet anode for high-performance low-temperature solid oxide fuel cells, J. Power Sources. 412 (2019) 160–169. doi:10.1016/J.JPOWSOUR.2018.11.025.

[46] Y. Lee, Y.M. Park, G.M. Choi, Micro-solid oxide fuel cell supported on a porous metallic Ni/stainless-steel bi-layer, J. Power Sources. 249 (2014) 79–83. doi:10.1016/J.JPOWSOUR.2013.10.082.

[47] D.Y. Jang, M. Kim, J.W. Kim, K. Bae, J. Son, M.V.F. Schlupp, J.H. Shim, High Performance Anode-Supported Solid Oxide Fuel Cells with Thin Film Yttria-Stabilized Zirconia Membrane Prepared by Aerosol-Assisted Chemical Vapor Deposition, J. Electrochem. Soc. 164 (2017) F484–F490. doi:10.1149/2.0181706jes.

[48] C. Ding, H. Lin, K. Sato, T. Hashida, A simple, rapid spray method for preparing anode-supported solid oxide fuel cells with GDC electrolyte thin films, J. Memb. Sci. 350 (2010) 1–4. doi:10.1016/J.MEMSCI.2009.12.013.

[49] R. Ebrahim, M. Yeleuov, A. Ignatiev, 3D Porous Nickel Anode for Low Temperature Thin Solid Oxide Fuel Cell Applications, Adv. Mater. Technol. 2 (2017) 1700098. doi:10.1002/admt.201700098.

[50] K.T. Lee, N.J. Vito, H.S. Yoon, E.D. Wachsman, Effect of Ni-Gd $_{0.1}$ Ce $_{0.9}$ O $_{1.95}$ Anode Functional Layer Composition on Performance of Lower Temperature SOFCs, J. Electrochem. Soc. 159 (2012) F187–F193. doi:10.1149/2.009207jes.

[51] S. Ji, I. Chang, Y.H. Lee, J. Park, J.Y. Paek, M.H. Lee, S.W. Cha, Fabrication of low-temperature solid oxide fuel cells with a nanothin protective layer by atomic layer deposition, Nanoscale Res. Lett. 8 (n.d.) 48. doi:10.1186/1556-276x-8-48.

[52] J. An, Y.-B. Kim, J. Park, T.M. Gür, F.B. Prinz, Three-Dimensional Nanostructured Bilayer Solid Oxide Fuel Cell with 1.3 W/cm ^{2} at 450 °C, Nano Lett. 13 (2013) 4551–4555. doi:10.1021/nl402661p.

[53] G.D. Han, K.C. Neoh, K. Bae, H.J. Choi, S.W. Park, J.-W. Son, J.H. Shim, Fabrication of lanthanum strontium cobalt ferrite (LSCF) cathodes for high performance solid oxide fuel cells using a low price commercial inkjet printer, J. Power Sources. 306 (2016) 503–509. doi:10.1016/J.JPOWSOUR.2015.12.067.

[54] Z. Zhan, D.M. Bierschenk, J.S. Cronin, S.A. Barnett, A reduced temperature solid oxide fuel cell with nanostructured anodes, Energy Environ. Sci. 4 (2011) 3951. doi:10.1039/c1ee01982a.

[55] Y. Chen, Y. Zhang, J. Baker, P. Majumdar, Z. Yang, M. Han, F. Chen, Hierarchically Oriented Macroporous Anode-Supported Solid Oxide Fuel Cell with Thin Ceria Electrolyte Film, (n.d.). doi:10.1021/am5003662.

[56] S. Ha, P.-C. Su, S.-W. Cha, Combinatorial deposition of a dense nano-thin film YSZ electrolyte for low temperature solid oxide fuel cells, J. Mater. Chem. A. 1 (2013) 9645. doi:10.1039/c3ta11758h.

[57] S. Ji, G.Y. Cho, W. Yu, P.-C. Su, M.H. Lee, S.W. Cha, Plasma-enhanced

atomic layer deposition of nanoscale yttria-stabilized zirconia electrolyte for solid oxide fuel cells with porous substrate., ACS Appl. Mater. Interfaces. 7 (2015) 2998–3002. doi:10.1021/am508710s.

[58] I. Chang, S. Ji, J. Park, M.H. Lee, S.W. Cha, Ultrathin YSZ Coating on Pt Cathode for High Thermal Stability and Enhanced Oxygen Reduction Reaction Activity, Adv. Energy Mater. 5 (2015) n/a-n/a. doi:10.1002/aenm.201402251.

[59] G.Y. Cho, Y.H. Lee, S.W. Hong, J. Bae, J. An, Y.B. Kim, S.W. Cha, High-performance thin film solid oxide fuel cells with scandia-stabilized zirconia (ScSZ) thin film electrolyte, Int. J. Hydrogen Energy. 40 (2015) 15704–15708. doi:10.1016/j.ijhydene.2015.09.124.

[60] J. Park, I. Chang, J.Y. Paek, S. Ji, W. Lee, S.W. Cha, J.-M. Lee, Fabrication of the large area thin-film solid oxide fuel cells, CIRP Ann. - Manuf. Technol. 63 (2014) 513–516. doi:10.1016/j.cirp.2014.03.065.

[61] T. Minami, Present status of transparent conducting oxide thin-film development for Indium-Tin-Oxide (ITO) substitutes, Thin Solid Films. 516 (2008) 5822–5828. doi:10.1016/j.tsf.2007.10.063.

[62] G. Bräuer, B. Szyszka, M. Vergöhl, R. Bandorf, Magnetron sputtering – Milestones of 30 years, Vacuum. 84 (2010) 1354–1359. doi:10.1016/J.VACUUM.2009.12.014.

[63] K. Wasa, I. Kanno, H. Kotera, Handbook of Sputter Deposition Technology: Fundamentals and Applications for Functional Thin Films, Nano-Materials and MEMS: Second Edition, Elsevier Inc., 2012. doi:10.1016/C2010-0-67037-4.

[64] P. Briois, F. Lapostolle, V. Demange, E. Djurado, A. Billard, Structural investigations of YSZ coatings prepared by DC magnetron sputtering, Surf. Coatings Technol. 201 (2007) 6012–6018. doi:10.1016/j.surfcoat.2006.11.016.

[65] E.M. Bringa, R.E. Johnson, Sputtering of nano-grains by energetic ions, in:

Nucl. Instruments Methods Phys. Res. Sect. B Beam Interact. with Mater. Atoms, 2002: pp. 365–370. doi:10.1016/S0168-583X(02)00806-6.

[66] J.D. Baek, Y.-J. Yoon, W. Lee, P.-C. Su, A circular membrane for nano thin film micro solid oxide fuel cells with enhanced mechanical stability, Energy Environ. Sci. 8 (2015) 3374–3380. doi:10.1039/C5EE02328A.

[67] J.D. Baek, K.Y. Liu, P.C. Su, A functional micro-solid oxide fuel cell with a 10 nm-thick freestanding electrolyte, J. Mater. Chem. A. 5 (2017) 18414–18419. doi:10.1039/c7ta05245f.

[68] W. Yu, G.Y. Cho, S. Hong, Y. Lee, PEALD YSZ-based bilayer electrolyte for thin film-solid oxide fuel cells, Nanotechnology. 27 (2016) 1–6. doi:10.1088/0957-4484/27/41/415402.

[69] W. Yu, S. Ji, G.Y. Cho, S. Noh, W.H. Tanveer, J. An, S.W. Cha, Atomic layer deposition of ultrathin blocking layer for low-temperature solid oxide fuel cell on nanoporous substrate, J. Vac. Sci. Technol. A Vacuum, Surfaces, Film. 33 (2015) 01A145. doi:10.1116/1.4904206.

[70] H.-S. Noh, J. Hong, H. Kim, K.J. Yoon, B.-K. Kim, H.-W. Lee, J.-H. Lee, J.-W. Son, Scale-Up of Thin-Film Deposition-Based Solid Oxide Fuel Cell by Sputtering, a Commercially Viable Thin-Film Technology, J. Electrochem. Soc. 163 (2016) F613–F617. doi:10.1149/2.0331607jes.

[71] H.-S. Noh, J.-W. Son, H. Lee, H.-S. Song, H.-W. Lee, J.-H. Lee, Low Temperature Performance Improvement of SOFC with Thin Film Electrolyte and Electrodes Fabricated by Pulsed Laser Deposition, J. Electrochem. Soc. 156 (2009) B1484. doi:10.1149/1.3243859.

[72] S. Park, J. Vohs, R. Gorte, Direct oxidation of hydrocarbons in a solid-oxide fuel cell, Nature. 404 (2000) 265–7. doi:10.1038/35005040.

[73] C. LU, Development of intermediate-temperature solid oxide fuel cells for direct utilization of hydrocarbon fuels, Solid State Ionics. 175 (2004) 47–50. doi:10.1016/j.ssi.2004.09.019.

[74] Z. Zhan, Y. Lin, M. Pillai, I. Kim, S.A. Barnett, High-rate electrochemical

partial oxidation of methane in solid oxide fuel cells, J. Power Sources. 161 (2006) 460–465. doi:10.1016/j.jpowsour.2006.04.139.

[75] E.W. Park, H. Moon, M. Park, S.H. Hyun, Fabrication and characterization of Cu–Ni–YSZ SOFC anodes for direct use of methane via Cu-electroplating, Int. J. Hydrogen Energy. 34 (2009) 5537–5545. doi:10.1016/j.ijhydene.2009.04.060.

[76] X.-M. Ge, S.-H. Chan, Q.-L. Liu, Q. Sun, Solid Oxide Fuel Cell Anode Materials for Direct Hydrocarbon Utilization, Adv. Energy Mater. 2 (2012) 1156–1181. doi:10.1002/aenm.201200342.

[77] Y. Chen, B. deGlee, Y. Tang, Z. Wang, B. Zhao, Y. Wei, L. Zhang, S. Yoo, K. Pei, J.H. Kim, Y. Ding, P. Hu, F.F. Tao, M. Liu, A robust fuel cell operated on nearly dry methane at 500 °C enabled by synergistic thermal catalysis and electrocatalysis, Nat. Energy. 3 (2018) 1042–1050. doi:10.1038/s41560-018-0262-5.

[78] M. Boder, R. Dittmeyer, Catalytic modification of conventional SOFC anodes with a view to reducing their activity for direct internal reforming of natural gas, J. Power Sources. 155 (2006) 13–22. doi:10.1016/j.jpowsour.2004.11.075.

[79] Y.W. Kang, J. Li, G.Y. Cao, H.Y. Tu, J. Li, J. Yang, A reduced 1D dynamic model of a planar direct internal reforming solid oxide fuel cell for system research, J. Power Sources. 188 (2009) 170–176. doi:10.1016/j.jpowsour.2008.11.073.

[80] Z. Shao, S.M. Haile, J. Ahn, P.D. Ronney, Z. Zhan, S. a Barnett, A thermally self-sustained micro solid-oxide fuel-cell stack with high power density., Nature. 435 (2005) 795–798. doi:10.1038/nature03673.

[81] K. Sasaki, Y. Teraoka, Equilibria in Fuel Cell Gases, J. Electrochem. Soc. 150 (2003) A885. doi:10.1149/1.1577338.

[82] S. Oh, J. Park, J.W. Shin, B.C. Yang, J. Zhang, D.Y. Jang, J. An, High performance low-temperature solid oxide fuel cells with atomic layer

deposited-yttria stabilized zirconia embedded thin film electrolyte, J. Mater. Chem. A. 6 (2018) 7401–7408. doi:10.1039/C7TA10678E.

[83] W. Yu, Y. Lee, A. Pandiyan, S. Ji, W.H. Tanveer, S.W. Cha, Enhanced Thermal Stability of Ultrathin Nanostructured Pt cathode by PdO: In Situ Nanodecoration for Low-Temperature Solid Oxide Fuel Cell, ACS Appl. Energy Mater. (2018) acsaem.8b01450. doi:10.1021/acsaem.8b01450.

[84] D. Hegemann, M.M. Hossain, D.J. Balazs, Nanostructured plasma coatings to obtain multifunctional textile surfaces, Prog. Org. Coatings. 58 (2007) 237–240. doi:10.1016/J.PORGCOAT.2006.08.027.

[85] H.-S. Noh, K.J. Yoon, B.-K. Kim, H.-J. Je, H.-W. Lee, J.-H. Lee, J.-W. Son, The potential and challenges of thin-film electrolyte and nanostructured electrode for yttria-stabilized zirconia-base anode-supported solid oxide fuel cells, J. Power Sources. 247 (2014) 105–111. doi:10.1016/j.jpowsour.2013.08.072.

[86] J. Park, Y. Lee, I. Chang, W. Lee, S.W. Cha, Engineering of the electrode structure of thin film solid oxide fuel cells, Thin Solid Films. 584 (2015) 125–129. doi:10.1016/J.TSF.2014.11.018.

[87] J.R.M. (Editor) Evgenij Barsoukov (Editor), Impedance Spectroscopy: Theory, Experiment, and Applications, 2nd Edition - Evgenij Barsoukov, J. Ross Macdonald, 2005. http://eu.wiley.com/WileyCDA/WileyTitle/productCd-0471647497.html (accessed October 18, 2019).

[88] S. Ahn, H. Koo, S.-H. Bae, C. Park, G. Cho, I. Chang, S.-W. Cha, Y.-S. Yoo, Effect of Nickel Contents on the Microstructure of Mesoporous Nickel Oxide/Gadolinium-Doped Ceria, Funct. Mater. Lett. 06 (2013) 1350055. doi:10.1142/S1793604713500550.

[89] U.P. Muecke, S. Graf, U. Rhyner, L.J. Gauckler, Microstructure and electrical conductivity of nanocrystalline nickel- and nickel oxide/gadolinia-doped ceria thin films, Acta Mater. 56 (2008) 677–687.

doi:10.1016/J.ACTAMAT.2007.09.023.

[90] H. He, J.M. Vohs, R.J. Gorte, Carbonaceous deposits in direct utilization hydrocarbon SOFC anode, J. Power Sources. 144 (2005) 135–140. doi:10.1016/j.jpowsour.2004.12.029.

[91] H. Kim, S. Park, J.M. Vohs, R.J. Gorte, Direct Oxidation of Liquid Fuels in a Solid Oxide Fuel Cell, J. Electrochem. Soc. 148 (2001) A693. doi:10.1149/1.1374216.

[92] R.J. Gorte, J.M. Vohs, Catalysis in solid oxide fuel cells., Annu. Rev. Chem. Biomol. Eng. 2 (2011) 9–30. doi:10.1146/annurev-chembioeng-061010-114148.

[93] O. Yamazaki, K. Tomishige, K. Fujimoto, Development of highly stable nickel catalyst for methane-steam reaction under low steam to carbon ratio, Appl. Catal. A Gen. 136 (1996) 49–56. doi:10.1016/0926-860X(95)00268-5.

[94] N. Laosiripojana, S. Assabumrungrat, Catalytic dry reforming of methane over high surface area ceria, Appl. Catal. B Environ. 60 (2005) 107–116. doi:10.1016/J.APCATB.2005.03.001.

[95] K.O. Christensen, D. Chen, R. Lødeng, A. Holmen, Effect of supports and Ni crystal size on carbon formation and sintering during steam methane reforming, Appl. Catal. A Gen. 314 (2006) 9–22. doi:10.1016/J.APCATA.2006.07.028.

[96] D. Fujita, M. Schleberger, S. Tougaard, XPS study of the surface enrichment process of carbon on C-doped Ni(111) using inelastic background analysis, Surf. Sci. 331–333 (1995) 343–348. doi:10.1016/0039-6028(95)00312-6.

[97] O.A. Marina, M. Mogensen, High-temperature conversion of methane on a composite gadolinia-doped ceria - gold electrode, Appl. Catal. A Gen. 189 (1999) 117–126. doi:10.1016/S0926-860X(99)00259-8.

[98] K. Kusakabe, K.I. Sotowa, T. Eda, Y. Iwamoto, Methane steam reforming

over Ce-ZrO2-supported noble metal catalysts at low temperature, Fuel Process. Technol. 86 (2004) 319–326. doi:10.1016/j.fuproc.2004.05.003.

[99] X. Li, M. Liu, J.P. Lee, D. Ding, L.A. Bottomley, S. Park, M. Liu, An operando surface enhanced Raman spectroscopy (SERS) study of carbon deposition on SOFC anodes, Phys. Chem. Chem. Phys. 17 (2015) 21112–21119. doi:10.1039/c4cp05176a.

[100] Y. Choi, E.C. Brown, S.M. Haile, W. Jung, Electrochemically modified, robust solid oxide fuel cell anode for direct-hydrocarbon utilization, Nano Energy. 23 (2016) 161–171. doi:10.1016/J.NANOEN.2016.03.015.

[101] J. Kirtley, A. Singh, D. Halat, T. Oswell, J.M. Hill, R.A. Walker, In situ raman studies of carbon removal from high temperature Ni-YSZ cermet anodes by gas phase reforming agents, J. Phys. Chem. C. 117 (2013) 25908–25916. doi:10.1021/jp408192e.

[102] M. Liu, K.S. Blinn, H. Abernathy, X. Li, M. Liu, L.A. Bottomley, Raman spectroscopic monitoring of carbon deposition on hydrocarbon-fed solid oxide fuel cell anodes, Energy Environ. Sci. 5 (2012) 7913–7917. doi:10.1039/c2ee21499g.

국문 초록

고체 산화물 연료전지는 낮은 오염도, 높은 에너지 효율, 그리고 다양한 연료 활용가능성 때문에 유망한 미래에 에너지 변환 장비로 여겨지고 있다. 이러한 고체산화물 연료전지를 상용화 하기 위해서는 구조적 그리고 연료활용도에 있어서 획기적인 발전이 필요하다. 예를 들어, 구조적인 측면에서, 전해질 두께는 작동 온도를 600 ℃ 미만으로 낮추기에 충분할 정도로 얇아야 한다. 이러한 작동 온도 영역에서 높은 열화율, 고가의 재료 사용, 그리고 긴 초기 작동 시간 같은 고체산화물 연료전지 기술적 문제를 해결할 수 있다. 또한, 연료의 관점에서, 저온 고체산화물 연료전지에 탄화수소 연료 (메탄, 부탄, 프로판 등)를 직접 사용할 수 있다면, 수소 저장 및 큰 시스템 크기의 문제를 제거 할 수 있다. 그러나, 전해질을 제조하기위한 박막 증착 기술은 기판의 증착 조건 및 표면 구조에 크게 의존한다. 스퍼터링 구조와 증착 변수 사이의 상관 관계에 대한 상세한 연구는 전해질 및 전극을 제조하기위한 박막 증착 기술을 상업적으로 적용하기 위해 필수적이다. 또한, 낮은 작동 온도에서, 직접적인 전기 화학적 산화 및 탄화수소 연료의 개질은 매우 느리다. 따라서 낮은 작동 온도에서 높은 활성도를 가진 열 촉매 설계는 필수적이다.

전해질의 두께를 감소시키는 것 외에, 스퍼터링에 의해 증착 된 박막층의 나노 크기의 입자 구조로 인해, 스퍼터링은 고 활성 전극을 설계하는데 이용 될 수 있다. 더욱이, 고성능 열 촉매의 구조는 높은 밀도의 반응영역을 필요로 하기 때문에, 나노 크기의 그레인으로 구성된 코스퍼터링 박막은 저온영역 에서의 직접 메탄 연료사용을 가능하게 할

가능성이 있다. 이 연구에서는 500 ℃에서 작동하는 직접 메탄 SOFC의 개발을 위해 고성능 나노 구조의 Ni-GDC 양극 및 Ru-GDC 개질 층을 제조하기 위해 공동 스퍼터링 기술이 적용되었다.

양극 산화 알루미늄 (AAO)은 균일 한 나노스케일 크기의 나노홀, 높은 열-기계적 안정성 및 확장 성으로 인해 박막 고체산화물 연료전지를 스퍼터링을 이용해 제작하기 위한 기판으로 사용되어왔다. AAO의 전기 비전 도성 특성으로 인해, 전기 화학적 성능은 AAO상의 양극 나노 구조에 의해 크게 영향을 받는다. 전형적인 SOFC구조에서는 집전 저항이 전체 셀 저항에 크게 영향을 미치지 않는다. 그러나, AAO위에 제작된 박막 고체산화물 연료전지에서, 연료극에서 생성된 전자는 기판에 평행한 방향으로만 전도가 가능하며, 이는 전자 집전에서 상당한 손실을 초래한다. 따라서 AAO에서 고성능 Ni-GDC 연료극 구조를 설계하려면 전기 화학적 성능에 대한 나노 구조 효과를 이해해야한다. 증착 챔버 압력, 타겟 과 기판 거리 및 기판 회전 속도와 같은 다양한 증착 파라미터가 양극 두께, 다공도 및 칼럼 구조에 미치는 영향에 대해 연구되었다. 실험 결과는 연료극 나노 구조의 이러한 물리적 특성이 박막 고체산화물 연료전지의 전기 화학적 성능을 결정하는 데 중요한 요소라는 것을 보여 주었다.

AAO위에 공동 스퍼터링에 의해 제조 된 열 촉매 개질 층은 물질 조성과 다공도에 의해 성능이 결정된다. 공동 스퍼터링에 의해 제조 된 Ru-GDC의 조성은 나노 구조의 다공도와 상관 관계가 있다는 것이 주목 할만하다. Ru 및 GDC의 증착 속도의 큰 차이 (90 % 초과)는 조성 변화에 따른 다공도 변화에 기인 할 수 있다. 그러나 이런 물질의 증착률이 나노구조형성에 미치는 영향의 원리는 본 논문의 주제 범위에

속하지 않는다. Ru 3 vol%의 조성비를 가진 Ru-GDC 나노 구조를 활용해 500℃에서 성공적인 개질 성능을 나타냈다. 구조 분석에 따르면 Ru-GDC의 나노 크기 입자 구조가 Ru 함량이 매우 낮음에도 불구하고 직접 메탄 작업을 가능하게 한 것으로 나타났다.

고성능 Ni-GDC 연료극과 Ru-GDC 나노 구조 개질 층 (NRL)의 통합은 건조한 메탄 (3 % H_2O)을 이용해 500 ℃의 저온에서도 상당한 전력 밀도를 생성하는 박막 고체산화물연료전지를 개발했다. 또한, 12시간이 넘는 작동 시간은 문헌에 보고된 AAO기반의 박막 고체산화물 연료전지의 어떤 성능보다 높게 측정되었다. 비록 연료전지가 시간당 4.9 % 열화율을 보였지만, 이는 백금 (Pt) 기반 공기극에 의한 열화에 의한 것으로 보인다. 나노구조분석을 통해 Ni-GDC 연료극에서 탄소 흡착은 확인되지 않았으며, 이는 탄소 흡착이 분해에 주된 기여가 아님을 나타냈다.

주요어: 저온 고체산화물 연료전지, 직접 메탄, 공동 스퍼터링, 니켈(Ni)-가돌리늄 도핑 세리아(GDC) 연료극, 루테늄(Ru)-가돌리늄 도핑 세리아(GDC)

학번: 2014-21846